UNIVERSITY OF LEEDS

Impact of steering flow on tropical cyclone predictability

John Edward Ashcroft

Submitted in accordance with the requirements for the degree of

Doctor of Philosophy

The University of Leeds
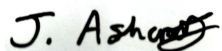
Centre for Doctoral Training in Fluid Dynamics

September 2020

Intellectual Property

The candidate confirms that the work submitted is his own and that appropriate credit has been given where reference has been made to the work of others.

This copy has been supplied on the understanding that it is copyright material and that no quotation from the thesis may be published without proper acknowledgement.

Signed   J. Ashcroft

Acknowledgements

First and foremost, I would like to thank my supervisors, Juliane Schwendike, Andrew Ross, Stephen Griffiths and Chris Short for their guidance, support, patience and encouragement over the past four years. I have thoroughly enjoyed working with each one of my supervisors during my research project. I am particularly grateful of the many opportunities I have been provided with to engage with the wider research community, facilitating both my professional and academic development.

I am appreciative of the involvement of the Met Office in this project. My short spells spent in Exeter working with Chris and witnessing the work the Met Office do has been inspiring.

I am grateful to EPSRC for providing me the funding to undertake this research as part of the Leeds Centre of Doctoral Training in Fluid Dynamics.

I would also like to thank my peers for creating a stimulating environment throughout my research project (both in person and, when that was no longer possible, virtually).

Thank you to Zara, without whom I would not have made it to the end.

Finally, I want to thank my parents for their unwavering support and for not getting too stressed on my behalf in the final few months.

Abstract

Although tropical cyclone (TC) track forecasts in numerical weather prediction models have improved considerably over the past few decades, there remain cases with large uncertainty. Typhoon Haiyan (2013) and Typhoon Hagupit (2014) are examples of two high-impact storms where, despite similarities in the observed track and intensity, the predictability of the storms differed greatly. Ensemble forecasts showed large uncertainty in the track of Hagupit, whereas the ensemble spread for Haiyan was considerably less.

Using the Met Office's Unified Model, 5-day global and convection permitting (CP) ensemble forecasts are analysed for both storms. Global forecasts show Haiyan was located on the southern periphery of the subtropical high and embedded in a strong easterly flow. In contrast, the steering flow of Hagupit was weak as the TC became located between two anticyclones. We show that Hagupit's position between the anticyclones, the strength of the anticyclones, the interactions between the TC outflow and its environment, and the upper-level geopotential height directly to the south of the TC contributed to whether Hagupit would make landfall over the Philippines or turn to the north.

The track forecasts in the CP ensembles of both storms produced errors which were not present in the global forecasts. For Haiyan, CP forecasts predicted the motion of the TC to be too slow, whilst for Hagupit the CP forecasts predicted the TC to make a systematic south-west turn, away from the actual storm path. For a third high-impact TC, Hurricane Florence (2018), CP forecasts predicted the storm to move too far to the west before turning north. Analysis of these forecast busts shows differences in how TCs interact with upper-level steering winds, particularly

in periods of strong vertical wind shear, can cause differences in the global and CP track forecasts.

Contents

List of Figures

List of Abbreviations

AMSR2	Advanced Microwave Scanning Radiometer 2
CP	Convection Permitting
DPE	Direct Positional Error
ECMWF	European Centre for Medium-Range Weather Forecasting
ETKF	Ensemble Transform Kalman Filter
GA	Global Atmosphere
GMI	Global Precipitation Measurement Microwave Imager
GPM	Global Precipitation Measurement
HWRF	Hurricane Weather Research and Forecasting
IBTrACS	International Best-Track Archive for Climate Stewardship
MetUM	Met Office's Unified Model
MOGREPS-G	Met Office Global and Regional Ensemble System - Global
NRL-MRY	National Research Laboratory Monterey Marine Division
RA1-T	Regional Atmosphere 1 - Tropical
SKEB	Stochastic Kinetic Energy Backscatter
SSM/I	Special Sensor Microwave/Imager
SST	Sea Surface Temperature
TC	Topical Cyclone

WRF   Weather Research and Forecasting

Chapter 1

Introduction

For many communities around the world, accurately predicting the weather is imperative to their safety, infrastructure and economy. However, weather forecasting is not straightforward. Lorenz (1972) famously described how a flap of a butterfly's wings could cause a tornado on the other side of the world. Whilst this is a metaphoric example, the idea is important. Weather is chaotic and thus small errors early in a weather forecast can amplify in time to large errors. When predicting high-impact weather events such as tropical cyclones (TCs), these large errors can have devastating consequences.

Tropical cyclones are both fascinating and extremely dangerous. Approximately 80 TCs form globally each year (Ramsay, 2017). Through their strong winds, high precipitation rates and large storm surges, TCs have the potential to devastate countries in which they make landfall (Emanuel et al., 2005). Whilst future projections of TCs remain uncertain, a greater proportion of intense storms along with increased TC-related flooding due to sea level rise could make the impacts of TCs even more severe in the future (Knutson et al., 2020). Predicting the motion and strength of TCs is critical for stakeholders to make suitable decisions to mitigate against the impacts (Bauer et al., 2015). Further, complex dynamical and thermodynamical processes which occur across multiple spatial scales in TCs provide many interesting scientific challenges (Emanuel, 2003; Montgomery and Smith, 2017).
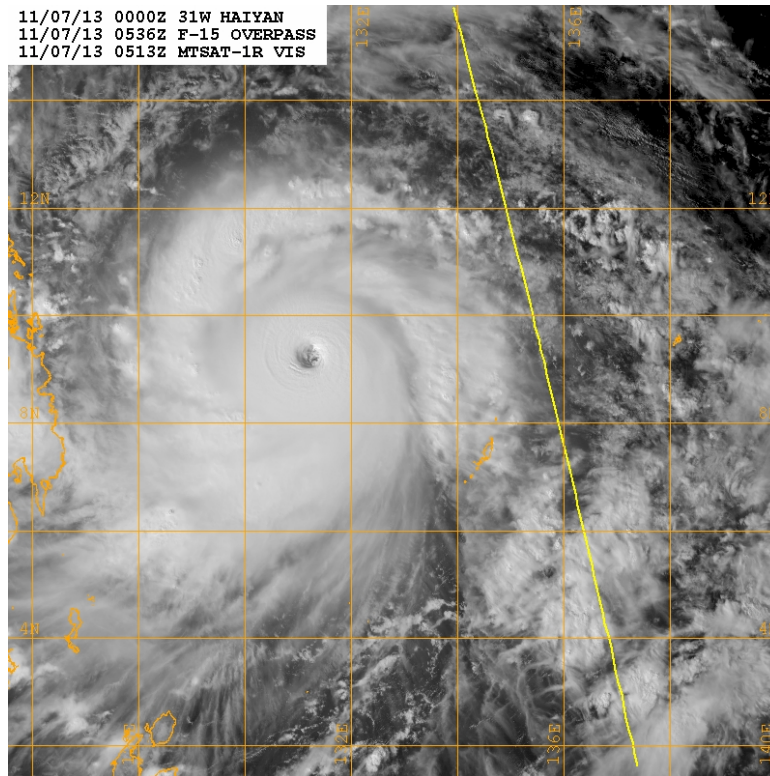
Figure 1.1: Visible satellite image taken of Typhoon Haiyan at 0536 UTC 7 November 2013 from the SSM/I satellite, showing the storm 10 hours prior to peak intensity. Image taken from NRL-MYL.

Tropical cyclones are vast, intense, rotating storms which form over the world's warmest oceans. The cloud-free centre of an intense TC (the *eye*) makes them instantly recognisable from satellite images (e.g. Figure 1.1). The eye, which has a typical radius of about 15-50 km (Weatherford and Gray, 1988), is surrounded by the *eyewall*, an area of deep convective clouds which extend outwards a further 20-50 km. Both the highest precipitation rates and strongest winds can be found in the eyewall, with the wind strength gradually decreasing with increasing radius from the storm centre and becoming indistinguishable from the environmental winds at a typical radius of 100-1000 km from the TC centre (Emanuel, 2003).

A TC is categorised by its maximum wind speed (defined as the 1-minute sustained wind at a height of 10 m). A TC with maximum wind speeds less than $17 \, \mathrm{m \, s^{-1}}$ is a *tropical depression*; TCs with maximum wind speeds between $17 \, \mathrm{m \, s^{-1}}$ and $32 \, \mathrm{m \, s^{-1}}$ are *tropical storms* and TCs with winds greater than $32 \, \mathrm{m \, s^{-1}}$ are *hurricanes* in the North Atlantic or eastern North Pacific, *typhoons* in the western North Pacific or *severe tropical cyclones* elsewhere. The Saffir-Simpson scale can be used to further

classify TCs with winds greater than $32\,\mathrm{m\,s^{-1}}$. According to the Saffir-Simpson scale the strongest TC is a category-5 storm and has 1-minute sustained winds greater than $70\,\mathrm{m\,s^{-1}}$.

Track forecasts for TCs have improved greatly over the past few decades (Figure 1.2). This has largely been due to the advancement of numerical weather prediction (NWP) models, which are used throughout the world for both global and regional weather forecasts. Mean global model track errors for a 72 hour forecast are now comparable to those of a 12 hour forecast 25 years ago (Yamaguchi et al., 2017). For example, in the western North Pacific, the Met Office's Unified Model (MetUM) average 72 hour track forecast error has decreased from over 600 km to under 200 km since 1992 (Heming, 2016), whilst the 48 hour average TC track forecast error is approximately 100 km (Short and Petch, 2018; Emanuel, 2018; Hodges and Klingaman, 2019). Despite the improvements, it has been suggested that we are approaching the intrinsic limits of track predictability (Landsea and Cangialosi, 2018). Furthermore, although there have been consistent improvements in track forecasts, there remain cases when a TC forecast has large errors (Yamaguchi et al., 2017). These cases are problematic for decision makers whose job is to protect lives and infrastructure in the communities in which TCs make landfall. This thesis is motivated by the crucial need to understand what causes some TC track forecasts to be uncertain, and thus reduce the impact of future cases.

Ensemble forecasts use a set of individual forecasts with perturbed initial conditions and perturbed model physics. The perturbed initial conditions account for potential errors in the observations, whilst the perturbed model physics account for uncertainties in the model. The ensemble is designed in such a way that each individual forecast (i.e. each ensemble member) is equally likely to occur. Therefore, the rate at which the ensemble members diverge from one another informs the forecaster of the uncertainty in the forecast and thus provides a tool for assessing the probability of errors in any one of the individual forecasts. The MetUM is routinely used to provide TC ensemble forecasts in many parts of the world, including the western North Pacific.
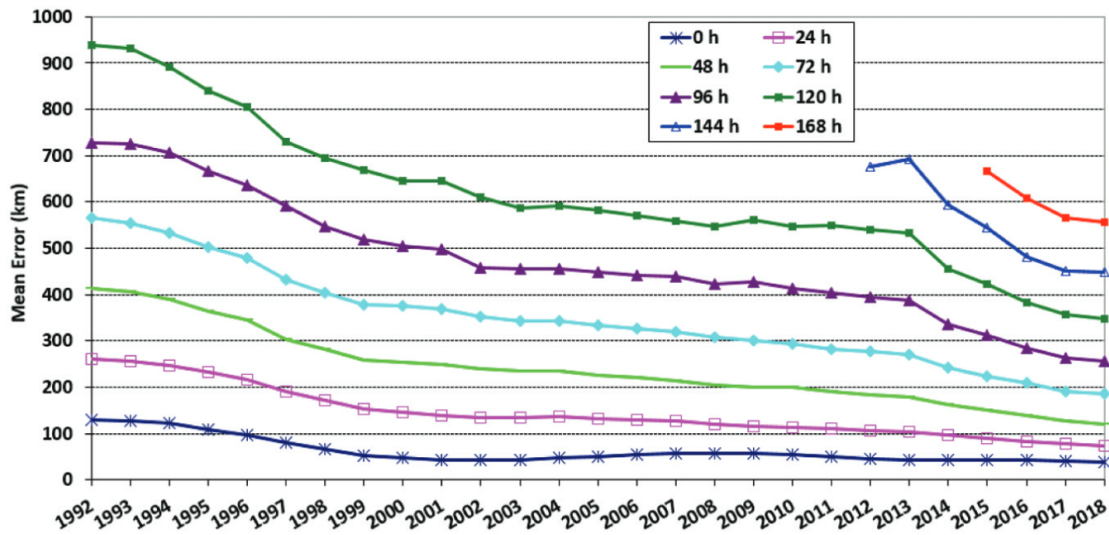
Figure 1.2: Met Office global 5-year running mean track errors for TCs in the northern hemisphere. Image taken from Heming et al. (2019).

The western North Pacific basin has the highest number of TCs every year compared to other tropical ocean basins, with a maximum between the months of July and October (Figure 1.3). Many of these TCs cause substantial damage to countries in the area such as the Philippines. Annually, the Philippines has on average 9 landfalling TCs (Cinco et al., 2016). As an island nation with dense population and widespread poverty, the Philippines is particularly vulnerable to TCs and is one of the most at-risk nations to natural disasters (Eckstein et al., 2019).

Two particularly strong TCs to make landfall over the Philippines were Typhoon Haiyan in 2013 and Typhoon Hagupit in 2014. Haiyan made landfall close to peak intensity with winds of over $83\,\mathrm{m\,s^{-1}}$, at the time the highest winds of any storm that had made landfall since records began. Over 6,200 people died with a further 4.1 million having to leave their homes. The total damage is estimated to have cost US $2.1 billion (Food and Agriculture Organization, 2014; Lum and Margesson, 2014). Hagupit reached similar intensities to Haiyan, but weakened before making landfall in the Philippines. Around the time of landfall the maximum 10-minute-sustained winds were $46\,\mathrm{m\,s^{-1}}$. The storm lead to 18 deaths and caused US $114 million of damage (OCHA, 2014).

The track forecasts for Hagupit and Haiyan, two seemingly similar storms in terms of position, intensity and size, were different. For Haiyan the track was predicted
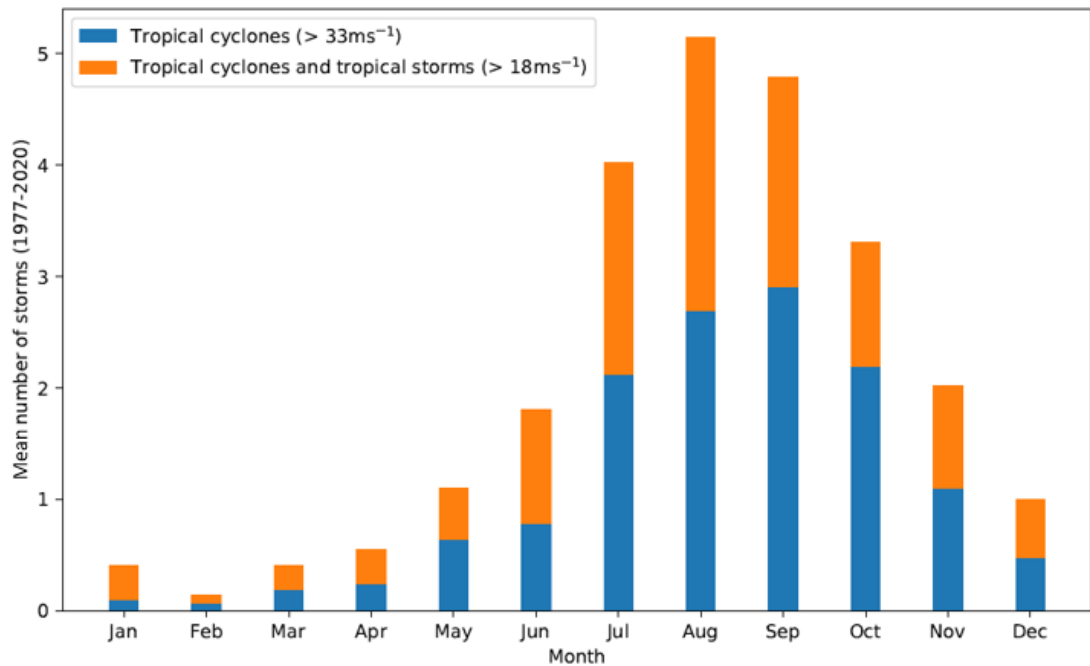
Figure 1.3: Yearly mean number of tropical storms and tropical cyclones for each month in the western North Pacific between 1977 and 2020. Data taken from IBTrACS.

with a high degree of certainty (Figure 1.4), whilst for Hagupit there was much more uncertainty in the track forecast (Figure 1.5). Comparing Figures 1.4 and 1.5, one of the main questions that comes to mind is: Why do the different tracks of Hagupit cover a much broader region than those of Haiyan? Comparing the forecasts of both storms can provide insight into the key differences between the storms and their environments which may have lead to the differences in track predictability.

Current global models are limited by their coarse resolution and thus do not resolve processes such as convection explicitly. Convection permitting (CP) weather forecasts provide a step-change for forecasting convective storms (Clark et al., 2016). Unlike current global models, CP forecasts are run at a resolution high enough to permit convection to develop independently in the model, rather than to use a parameterisation scheme. As technological advances continue, CP forecasts will eventually become the norm for global forecasting (Bauer et al., 2015).

The Met Office use a limited-area, CP configuration over the western North Pacific, with one of the aims to improve TC forecasts in the area. Evaluation of the CP forecasts indicates that, compared to the global forecasts, they are successful at
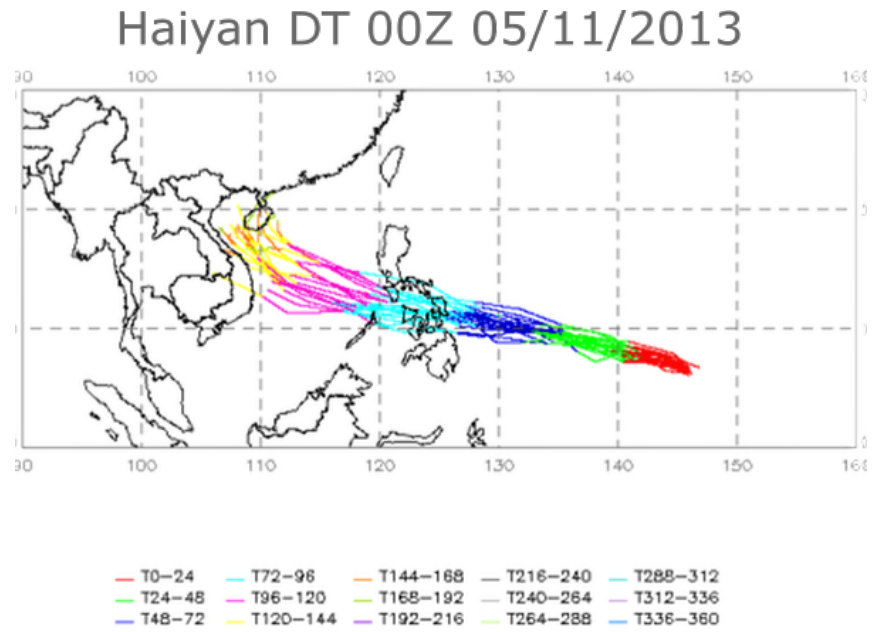
Figure 1.4: Met Office global 7-day track forecast for Typhoon Haiyan initialised at 0000 UTC 5 November 2013. Image courtesy: Helen Titley, Met Office.
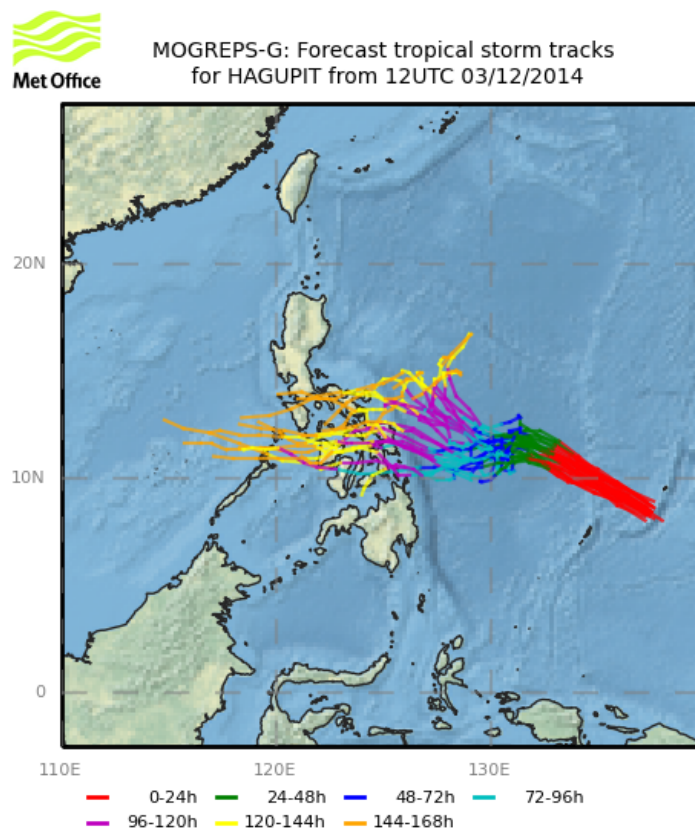
Figure 1.5: Met Office global 7-day track forecast for Typhoon Hagupit initialised at 1200 UTC 3 December 2014. Image courtesy: Helen Titley, Met Office.

improving intensity and precipitation predictions for TCs (Short and Petch, 2018). Despite these improvements, the mean track error has remained the same, as shown by comparing the orange and green lines in Figure 1.6. Although the mean error is similar, there is a significant positional difference between the global and CP forecasts (i.e. the black line in Figure 1.6). This suggests there are differences in TC motion in the CP simulations compared to the global simulations (in some instances the CP forecasts must perform better than the global, and in other instances the global forecasts must perform better than the CP). Figure 1.6 also shows that, over the western North Pacific and during the evaluation period, the European Centre for Medium-Range Weather Forecasts (ECMWF) operational global forecasts perform better at predicting TC tracks, whilst the CP Hurricane Weather Research and Forecast (HWRF) has the largest positional errors. At a lead time of T+120, the ECMWF forecasts average error decreases compared to earlier lead times. This decrease in error is likely a result of the small case sample size at T+120 (approximately 25 cases).

The difference in TC track forecasts between global and CP configurations of the MetUM is worth investigating as it may provide insight into potential causes of TC track errors. The regional, CP configuration is one-way nested. This means that whilst it takes boundary conditions from the global forecasts, the CP simulations do not feedback to the global forecasts. Therefore, differences between the two configurations come from the increased resolution in the limited area domain and the different scientific configurations used within that domain. Understanding the cause of these differences can aid future model development and improve our fundamental understanding of TC motion. This is particularly important in cases in which the global forecasts perform better than the CP forecasts at predicting the track of a TC. Whilst CP simulations will undoubtedly contribute to improved intensity forecasts in the future, it is important not to reduce the skill in the track forecasts.

This thesis aims to improve our understanding of TC track predictability in both global and CP configurations of the MetUM. In particular some of the key questions are:
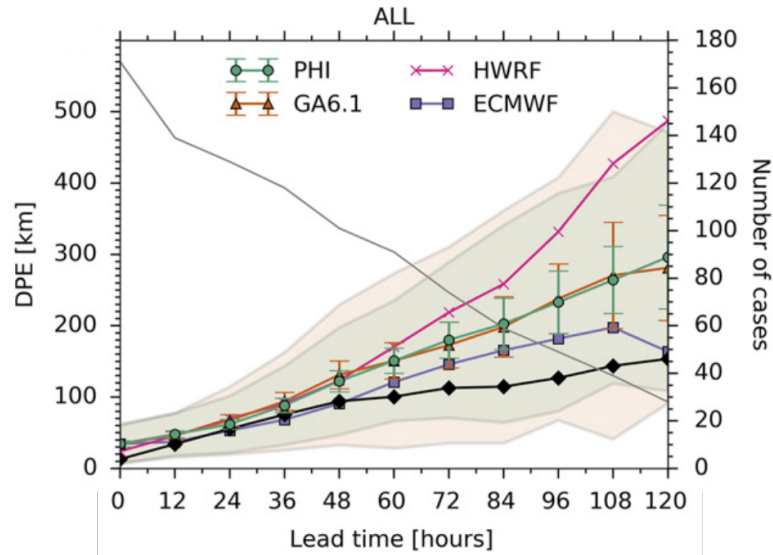
Figure 1.6: Track forecast errors of TCs in the western North Pacific between 4 November 2014 to 15 March 2016. Error is calculated as the direct positional error (DPE) between the forecast and the observed storm position. The solid line with error bars is the mean and 95% confidence interval, respectively. The shaded regions are one standard deviation about the mean. The figure compare the Met Office global forecasts (GA6.1), the Met Office's regional CP forecast (PHI), operational ECMWF forecasts and operational HWRF forecasts. The solid black line shows the mean distance between the GA6.1 and PHI forecasts at each lead time. Figure taken from Short and Petch (2018).

- Why were the track forecasts for Typhoon Haiyan and Typhoon Hagupit so different?

- How do Haiyan and Hagupit interact with their environment, and what impact does this interaction have on their tracks?

- What causes the differences in track forecasts between the global and CP simulations?

To address the first two questions, a number of global ensemble forecasts of Haiyan and Hagupit are analysed in detail using the MetUM. For the final question, CP forecasts of Haiyan, Hagupit and a third TC, Hurricane Florence (2018), are analysed and compared to the global forecasts. Hurricane Florence is included in this analysis as it was a high-impact TC which caught the eye of Met Office model developers due to CP forecasts inaccurately forecasting Florence's motion. After making landfall over North Carolina, Florence travelled west and moved inland before making a northwards turn. Whilst the global ensemble members from multiple initial times all

accurately predicted the location of the northward turn, the CP ensemble members predicted the TC to travel too far inland before turning north.

The rest of the thesis is organised as follows. Chapter 2 gives an overview of TCs with a focus on TC motion and interactions between TCs and their environments. Existing literature, in particular studies which address TCs associated with large track errors, is reviewed.

In Chapter 3 the methodology and data used in the thesis is outlined. This includes a detailed overview of the MetUM, a description of observational and analyses data, and a description of analysis methods used. The analysis methods include a TC tracking algorithm and a TC vortex removal technique. The TC vortex removal method is used throughout the thesis to calculate the TC's steering flow.

A synoptic overview of both storms is given in Chapter 4. This chapter also compares the track and intensity forecasts of Haiyan and Hagupit. Comparisons are made to observational data to demonstrate the TCs produced by the MetUM are realistic simulations of Haiyan and Hagupit.

Chapter 5 investigates in more detail the global ensemble forecasts of Haiyan and, in particular, Hagupit. The impact of Hagupit's position earlier in the forecast and the importance of different synoptic features on the uncertainty of Hagupit's track is explored. Statistical methods are used to highlight important differences between groups of ensemble members which predict the track of Hagupit to either make landfall or turn to the north. The global forecasts of Haiyan are also analysed to explain why the track of the storm was so predictable.

The CP forecasts of Hagupit are the subject of Chapter 6. In particular the chapter aims to understand why there are differences in the predicted motion of the storm in the CP forecasts compared to the global forecasts. Along with different resolutions, the global and CP forecasts also use different scientific configurations. That is, whilst both solve the governing equations using the same dynamical core, they use a slightly different set of physical and dynamical parameterisation schemes. A series of sensitivity tests explores whether the added resolution or the different science

configuration causes the difference in the CP tracks compared to the global. Two key differences between the global and CP forecasts are discussed. Firstly the storm environments in the CP and global forecasts are compared to explain the differences in the steering flow between the two forecast types. Secondly the different structures of the TC, how they react to vertical wind shear and the impact this has on the track is explored.

Using results from Chapter 6, Chapter 7 aims to understand why the tracks of both Haiyan and Florence differ in the CP forecasts compared to the global forecasts. The consequences of Haiyan's weak initialisation and thus differences in storm structure between the global and CP forecasts is discussed. For Florence, the differences in the depths of the optimum steering wind between global and CP forecasts is compared. Chapter 8 summarises the work and discusses possible avenues of future work.

Chapter 2

Tropical Cyclones

2.1 Introduction

A tropical cyclone is a large, powerful low pressure weather system that forms over tropical oceans and is driven primarily by heat transfer from the sea. Tropical cyclones produce powerful, destructive winds and torrential rain whilst also causing storm surges which can have a devastating impact on coastal areas.

This chapter provides a general overview of TCs and covers the relevant information for the rest of the thesis. The basic physics of mature TCs and how they move is outlined in Sections 2.2 and 2.3, respectively. The interactions between a TC and its environment is discussed in Section 2.4. Existing literature on predicting TCs and in particular TCs in which the motion is difficult to predict is reviewed in Section 2.5. A brief climatology of TCs in the western North Pacific is given in Section 2.6, and a summary is provided in Section 2.7.

2.2 Physics of Tropical Cyclones

2.2.1 Tropical Cyclone Structure

The main source of energy for TCs is the heat flux from the ocean (Emanuel, 2003). Without sea surface temperatures of at least 27°C (i.e. those found in the tropical

oceans), TCs are generally unable to develop (Gray, 1968). Along with warm oceans, other conditions that must be satisfied for TC genesis include lower level convergence of winds, which in turn causes ascent; a sufficient distance from the equator to allow for rotation; low vertical wind shear and an existing disturbance (Gray, 1975). Tropical cyclones dissipate when either they make landfall and thus no longer have the warm oceans as their energy source; move polewards and into cooler oceans, undergo extratropical transition; or when their structure is disrupted by other synoptic weather conditions such as large vertical wind shear.

Perhaps the most defining feature of a TC is the eye. The eye of a TC is the calm, often cloud-free centre of the storm with a typical radius of about 15-50 km (Weatherford and Gray, 1988), and is an area in which air descends slowly at approximately 5-10 cm s^{-1} (Emanuel, 2003). Around 60% of TCs feature an eye with it being common within the more intense storms (Vigh et al., 2012). Figure 1.1, a visible satellite image of Typhoon Haiyan (2013) close to peak intensity, shows the cloud free eye of the storm. The eye is also the region of the lowest pressure. The sea level pressure inside the eye is 10-30 hPa lower than area outside of the eye, and 50-100 hPa lower than the sea level pressure away from the TC (Willoughby, 1998). In the most intense storms, the minimum sea level pressure is under 900 hPa. Along with lower pressure, the TC eye also has higher temperatures than its surroundings at all altitudes. Therefore, a TC is said to be warm-cored, a key difference from mid-latitude cyclones which are cold-cored.

The TC eye is surrounded by the eyewall. The eyewall consists of deep convective clouds extending outwards for 20-50 km. The maximum wind speeds along with the highest rates of precipitation are found in the eyewall. In the eyewall, air ascends at approximately 5-10 m s^{-1}, reaching a maximum at mid-levels (Emanuel, 2003). The eyewall tends to slope outwards with height. This is due to a TC being warm-cored and the pressure gradient weakening with height (Shea and Gray, 1973).

Due to a canopy of high cirrus clouds surrounding the eye it is not clear where the eyewall ends in Figure 1.1. Microwave imagery is used to give a detailed view of the cloud structure of TCs by penetrating cirrus clouds. An example of an
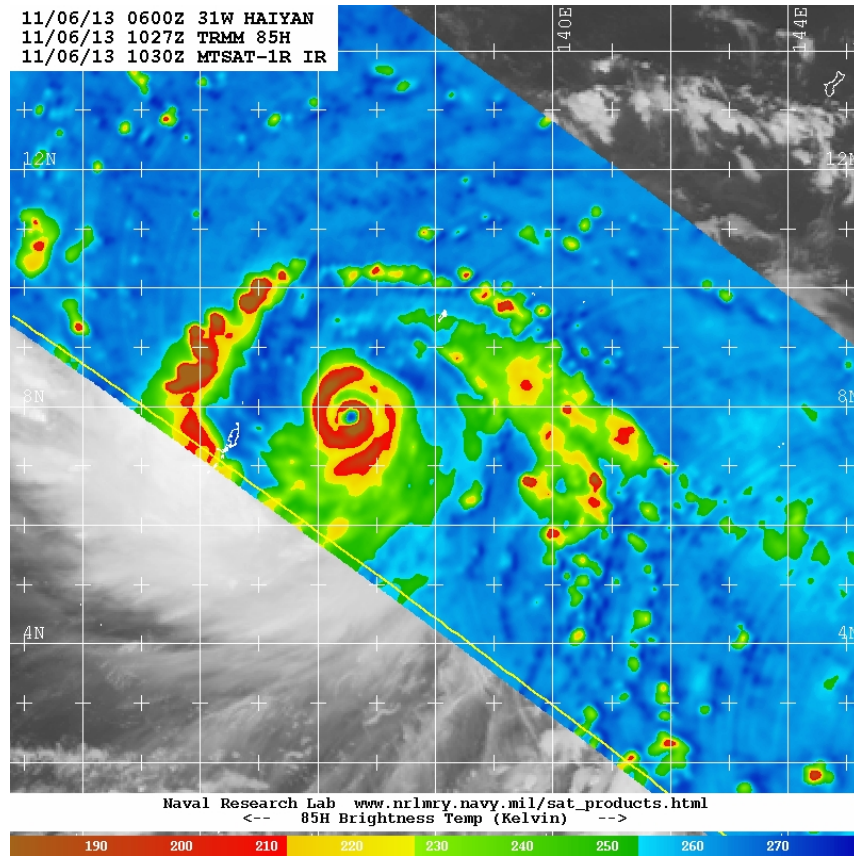
Figure 2.1: 85 GHz microwave image of Typhoon Haiyan at 1027 UTC 6 November 2013 from the SSM/I satellite. Image taken from NRL-MYR.

85 GHz image is shown in Figure 2.1, taken of Haiyan at 1027 UTC 6 November 2013. The cirrus canopy appears transparent, however, the 85 GHz channel is sensitive to precipitation and clouds at low- and medium-levels, meaning the eyewall can be identified, completely surrounding the eye. Figure 2.1 also highlights another important structural feature of TCs - spiralling rainbands. These are made of deep convective clouds which spiral out from the eyewall. These rainbands sometimes contract and form an outer eyewall. From here the storm may undergo an eyewall replacement cycle as the outer eyewall contracts during intensification (Emanuel, 2003). The rainbands, along with the eyewall, are the main source of the significant rainfall produced by TCs. This particular image (Figure 2.1) suggests that Haiyan has just one eyewall as no spiral rainband completely surrounds the eye.

After reaching a maximum at the radius of maximum wind, tangential winds decrease in strength gradually with distance from the TC centre. The TC winds become indistinguishable from the environmental winds at a typical radius between 100 and 1000 km from the TC centre. Away from the eyewall and the rainbands, there is

subsidence of air parcels (Emanuel, 2003).

2.2.2 Dynamics of a Mature Tropical Cyclone

The dynamics of a mature TC can be split into two key components: the primary circulation and the secondary circulation. The primary circulation describes the horizontal tangential winds rotating about the eye, whilst the secondary flow describes an air parcel's in-up-and-out motion in the radial and vertical direction. A mature TC refers to one which is at peak intensity, neither intensifying nor weakening.

The primary circulation of a mature TC is in approximate gradient wind balance above the boundary layer (Willoughby, 1990), which is a consequence of the radial momentum equation. Gradient wind balance is the balance between the pressure gradient force and the sum of the centrifugal and Coriolis forces:

$$\frac{v_{az}^2}{r} + f v_{az} = \frac{1}{\rho}\frac{\partial p}{\partial r}\,, \tag{2.1}$$

where v_{az} is the azimuthal velocity, p is the pressure, ρ is the density, r is the radial distance from the centre of the storm and f is the Coriolis parameter. Willoughby (1990) showed using aircraft observations that the gradient wind profile was a good approximation for TCs.

In the boundary layer the gradient wind balance approximation no longer holds. In this region friction acts on air parcels slowing the azimuthal velocity. As a result the centrifugal force is reduced and the pressure gradient force becomes dominant. This causes inflow in the boundary layer and a convergence of air parcels. As the air parcels spiral inwards they evaporate ocean water, supplying energy to the TC in the form of latent heat (e.g. Emanuel et al., 2005). Due to conservation of mass, the warm, moist air parcels are forced upwards out of the boundary layer. Convective instabilities cause the air parcels to rise through the eyewall which extends throughout the troposphere. As the moist air parcels rise, they expand and cool, releasing latent heat via condensation. This development of vigorous convection can eventually lead to large precipitation rates. The latent heat release in the eyewall ensures the TC

remains warm-cored. As the air ascends, it also slows, with the maximum winds usually occurring just above the boundary layer (Smith and Vogl, 2008). The angular momentum (M) of an air parcel is given as

$$M = v_{az}r + \frac{1}{2}fr^2 \,. \tag{2.2}$$

Above the boundary layer and thus in the absence of friction, M is conserved whilst following parcels of air. As the azimuthal winds decrease with height, Equation 2.2 suggests that r should increase. This causes the eyewall to slope outwards with height. At the top of the cyclone the flow becomes anticyclonic and asymmetric, often concentrated in outflow jets (Holland, 1984). Equation 2.2 also describes why an air parcel will speed up at smaller radii. As r decreases, v_{az} must increase to conserve angular momentum.

2.3 Tropical Cyclone Motion

To a first approximation, TCs move with the environmental flow in which they are embedded, averaged through the depth of the storm (George and Gray, 1976; Chan and Gray, 1982; Holland, 1983). The environmental flow is defined as the air flow that would exist in the absence of the TC. George and Gray (1976) found, for TCs in the western North Pacific, that there is a relationship between the movement of the storm and the winds averaged between $1° - 7°$ of the storm's centre at a height of 700 hPa. Chan and Gray (1982) expanded the study to include the west Atlantic and Australian-South Pacific basins. They showed that winds at an average distance of 5°-7° from the storm's centre and a pressure weighted average height of 500-700 hPa best correlated with the motion of a TC.

As there is no clear boundary between a TC and its environment, it is difficult to determine both the area and depth which should be averaged over to give the best representation of the environmental winds that are steering the storm. The depth of the environmental flow advecting the storm changes according to the storm intensity (Velden and Leslie, 1991; Dong and Neumann, 1986). Dong and Neumann (1986)

showed, based on 920 cases in the Atlantic, that the depth of the steering layer is greater for hurricanes than for tropical storms. Velden and Leslie (1991) suggested that the depth used to calculate the environmental flow should vary according to the intensity of the TC. They showed that weaker storms (defined as storms with a minimum sea level pressure $> 975\,\mathrm{hPa}$) had an optimum layer of 850-500 hPa, whilst stronger storms ($< 955\,\mathrm{hPa}$) had an optimum layer of 850-300 hPa (Velden and Leslie, 1991). The vertical average should not include the boundary level nor the outflow layer due to strong convergence and divergence in these regions (Holland, 1984), therefore, a bottom boundary of 850 hPa is considered for the majority of studies investigating the environmental flow of a TC. Similarly the radius of a TC can be different from storm to storm, and is not necessarily correlated to the intensity of the storm. Therefore, the radius used to calculate the environmental winds should be different dependent on the TC.

More recently a method developed by Galarneau and Davis (2013) for calculating the winds responsible for steering the storm has become popular. Using this method, the typical optimum vertical layer extends vertically from 850 hPa to an upper boundary between 300-200 hPa whilst the optimum radius is usually between 300-400 km (Galarneau and Davis, 2013; Fowler and Galarneau, 2017; Torn et al., 2018; Nystrom et al., 2018). However, allowing the radius and depth to change with time in the calculation of the environment flow results in a more accurate description of the steering flow (Galarneau and Davis, 2013). This method, with some modifications, is used in this study. The methodology is outlined in Section 3.5.2.

From the earlier studies of TC motion it was apparent that there is a systematic deviation of the storm's motion relative to the environmental winds. In the northern hemisphere this deviation meant that the TC would move slightly to the left of the environmental winds (e.g. Holland, 1983; Brand et al., 1981). The cause of this deviation is due to the $\beta-$effect (Chan and Gray, 1982; Holland, 1983; DeMaria, 1985; Chan and Williams, 1987). The general steering principle for TCs is that TC motion is controlled by the environmental winds plus a β-effect.

The basis for the TC steering principle is that a TC is an axisymmetric vortex

embedded in a barotropic atmosphere. A TC has particularly high relative vorticity, ζ, defined as

$$\zeta = \hat{\mathbf{k}} \cdot (\nabla \times \mathbf{u}) = \frac{\partial v}{\partial x} - \frac{\partial u}{\partial y}, \tag{2.3}$$

where $\hat{\mathbf{k}}$ is the vertical unit vector, $\mathbf{u}$ is the three-dimensional velocity vector and u and v are the zonal and meridional components of $\mathbf{u}$, respectively. A barotropic atmosphere is one in which the density is only a function of pressure, and the surfaces of constant pressure and density coincide. The barotropic vorticity equation,

$$\frac{\partial \zeta}{\partial t} = -u\frac{\partial(\zeta + f)}{\partial x} - v\frac{\partial(\zeta + f)}{\partial y}, \tag{2.4}$$

governs the motion of the flow. Considering the case in which a vortex is embedded in some environmental flow on an f-plane (i.e. one in which the Coriolis parameter does not have a meridional gradient), then Equation 2.4 reduces to a simple advection equation - the TC is advected by the environment in which it is embedded. However, if the β approximation is used such that $\frac{df}{dy} = \beta$, the advection of Earth's vorticity must also be considered. In this case the barotropic vorticity equation becomes,

$$\frac{\partial \zeta}{\partial t} = -u\frac{\partial \zeta}{\partial x} - v\frac{\partial \zeta}{\partial y} - \beta v. \tag{2.5}$$

It is useful to consider Equation 2.5 in the situation of no environmental flow. In this case, u and v are just the cyclonic winds associated with the TC. The streamlines of u and v are concentric with the contours of ζ and thus the advection of relative vorticity by the cyclonic winds is zero. Therefore, the only contribution to the relative vorticity tendency is due to the final term on the right hand side of Equation 2.5. In the northern hemisphere, β is positive. To the east of the TC centre, v is positive, whilst to the west of the TC centre v is negative. Therefore, in the absence of any environmental flow, the vorticity tendency, Equation 2.5 would produce a positive vorticity anomaly to the west of the TC and a negative anomaly to the east. This would have a consequence of shifting the TC slightly to the west, whilst also setting up a secondary circulation in the form of two gyres through the centre of the TC (Figure 2.2a).

(a)

(b)
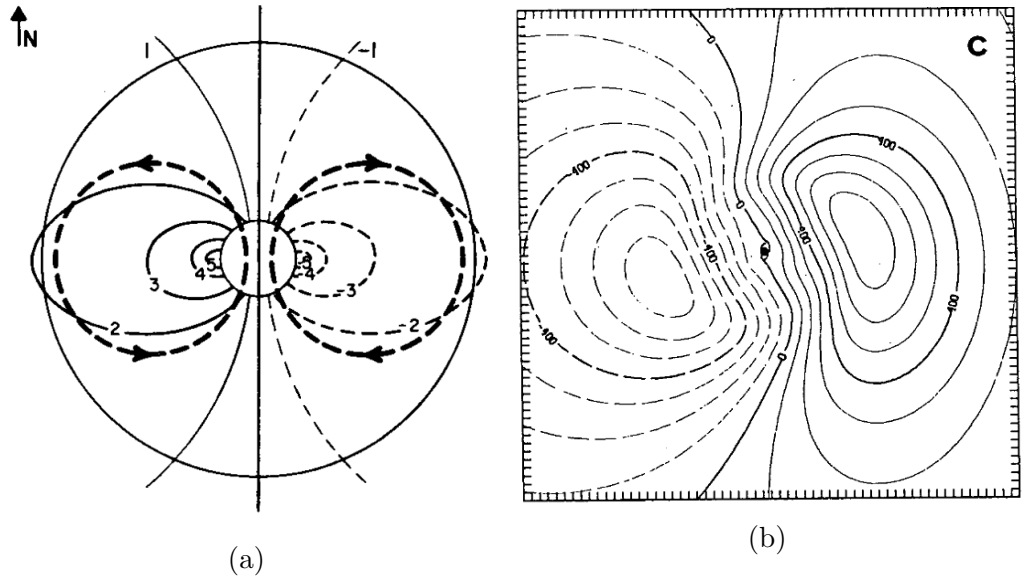
Figure 2.2: (a) Schematic showing the relative vorticity tendency in arbitrary units (thinner labelled contours) and the induced circulation by the vorticity changes (thicker dashed lines) centred on a cyclone on a β-plane in the Northern Hemisphere. Image taken from Holland (1983). ©American Meteorological Society. Used with permission. (b) The asymmetric streamfunction after integrating Equation 2.8 for 24 hours. Solid (dashed) lines show positive (negative) values of the streamfunction and indicate anticyclonic (cyclonic) flow. The TC symbol indicates the centre of the storm. Contours are every $10^5\,\mathrm{m^2\,s^{-1}}$. Image taken from Fiorino and Elsberry (1989).

The barotropic vorticity equation Equation 2.5 can be rewritten using the streamfunction, ψ, where

$$\nabla^2\psi = \zeta \tag{2.6}$$

and

$$u = -\frac{\partial\psi}{\partial y} \qquad \text{and} \qquad v = \frac{\partial\psi}{\partial x}\,. \tag{2.7}$$

Equation 2.5 then becomes

$$\frac{\partial}{\partial t}\left(\frac{\partial^2\psi}{\partial x^2} + \frac{\partial^2\psi}{\partial y^2}\right) = \frac{\partial\psi}{\partial y}\frac{\partial}{\partial x}\left(\frac{\partial^2\psi}{\partial x^2} + \frac{\partial^2\psi}{\partial y^2}\right) - \frac{\partial\psi}{\partial x}\frac{\partial}{\partial y}\left(\frac{\partial^2\psi}{\partial x^2} + \frac{\partial^2\psi}{\partial y^2}\right) - \beta\frac{\partial\psi}{\partial x}\,. \tag{2.8}$$

Chan and Williams (1987) solved both the linear (i.e. excluding all terms from the right hand side of Equation 2.8 except the β term) and nonlinear problem. The linear solution showed the vortex stretched in the westward direction, whilst the nonlinear effects caused the propagation of the vortex. The displacement direction and speed (initially $0.8\,\mathrm{m\,s^{-1}}$ in the first 12 hours and rising to $2.8\,\mathrm{m\,s^{-1}}$ by T+60)

in the nonlinear model were consistent with the observed TC deviation from the environmental winds.

Fiorino and Elsberry (1989) solved the same nonlinear problem (Equation 2.8), decomposing the flow into its symmetric and asymmetric components. They showed that the β drift is due to the asymmetric advection of symmetric vorticity. Further, they showed that the asymmetric flow has a strong dipole structure and that the flow through the centre of the TC (the ventilation flow) was consistent with the direction and speed of the TC. Figure 2.2b, from their study, shows a similar dipole structure to Figure 2.2a. However, this has been rotated approximately 45°. Fiorino and Elsberry (1989) attributes this rotation of the gyres to the symmetric advection of the asymmetric relative vorticity. Similar results were found by Smith and Weber (1993) who found an approximate analytical solution to describe the motion of a TC within a barotropic framework.

The theoretical studies of the β drift describe how the TC can deviate both westward and poleward from the environmental steering winds. In comparison, the earlier observational studies suggested a westward deviation of the TC compared to the environmental winds. The difference between the observational and theoretical studies is related to the definition of the steering winds (Holland, 1983). Observational studies calculated the steering winds by removing an azimuthally averaged wind field in the vicinity of the TC (e.g. George and Gray, 1976). Therefore, by definition, the asymmetric β-gyres are incorporated in the environmental steering flow (Holland, 1983) and only the westward part of the β effect remains. In comparison, the theoretical studies are able to prescribe a background flow, predict it's evolution and compare the TC location to where the TC would be if it had exactly followed the environmental flow. In this scenario the β-gyres are not part of the definition of the steering flow (e.g. Chan and Williams, 1987).

By changing the properties of the initial vortex in their model, Fiorino and Elsberry (1989) also demonstrated the sensitivity of the β-gyres to the strength of the flow between 300 and 1000 km from the vortex centre. If this flow is more cyclonic then the vortex will move further to the west in the Northern Hemisphere. On the other

hand, changing the winds close to the centre of the TC (i.e. making the storm more or less intense), whilst keeping the winds beyond 300 km from the centre the same, had little impact on the track.

These studies consider an axisymmetric vortex in zero background flow. Similar results are found when applying a uniform background flow. However, further complications arise when imposing a non-uniform background flow or when considering an asymmetric initial vortex. In reality a TC is asymmetric and is embedded in an environment which has a horizontal shear profile. The presence of horizontal shear due to non-uniform flow has been the subject to numerous studies (eg. Evans et al., 1991; Smith, 1991; Ulrich and Smith, 1991). Both the strength and orientation of the β-gyres is changed due to the environmental flow meaning the motion of the TC depends also on the characteristics of the environment.

2.4 Interactions Between Tropical Cyclones and their Environments

The previous section described how the environment of a TC steers the storm and thus is the main factor in determining the TC's track. It is also important to highlight that a TC can play an equally important role in changing its environment. A TC's interaction with its environment is two-way, and thus whilst the environment is steering the storm, the storm may also be changing the environment, which would then feedback onto its own motion. Failing to predict these interactions could lead to an error in the storm motion. Indeed, environmental errors are often cited as the cause for TCs which have been poorly predicted (Nystrom et al., 2018; Torn et al., 2018; Magnusson et al., 2019).

Potential vorticity (PV) combines the dynamical and thermodynamical properties of a flow into a single quantity. PV is defined as

$$PV = -g\left(\zeta + f\right)\frac{\partial\theta}{\partial p} \qquad (2.9)$$

where g is the gravitational constant, θ is the potential temperature and p is the pressure. In the mid-troposphere, the TC represents a strong positive PV anomaly, whilst at upper levels, in the region of strong outflow the PV anomaly is negative.

Interactions between a TC and its environment are often investigated within a PV framework (e.g. Keller et al., 2019, and references therein). Anticyclonic outflow from the TC enhances the downstream trough amplification through the advection of cyclonic PV and the implication of an enhanced anticyclonic component in the region of the downstream trough (Riemer and Jones, 2010; Keller et al., 2019). Meanwhile divergent outflow from the TC, associated with the latent heat release in the mid troposphere, contributes to ridge building and jet streak formation through the advection of low PV air which distorts the upper level PV field (Riemer and Jones, 2010; Grams et al., 2013; Keller et al., 2019). As a TC moves closer to the the midlatitudes, the cyclonic circulation of the TC advects anticyclonic PV towards the ridge and contributes to the ridge amplification. Each of these processes are summarised in Figure 2.3.

The interactions between a TC and midlatitude flow, particularly when a TC moves polewards and undergoes extratropical transition, can often have large impacts on the predictability of weather globally (Keller et al., 2019). Even if a TC does not turn polewards and interact directly with the midlatitudes, interactions between its outflow and the jet stream can influence the environment and thus the track of the TC. The location of a TC relative to an approaching trough is important to its future track (Riemer and Jones, 2014). This was the case in Typhoon Jangmi, where Grams et al. (2013) found that slight positional differences in the location of Jangmi changed whether or not the TC would turn to the north and undergo extratropical transition or not. The reason for this sensitivity to the position of the TC is the existence of a bifurcation point in the steering flow in a trough-relative frame (i.e. the full flow minus the trough phase speed). An example of this flow pattern is shown in Figure 2.4, taken from an idealised simulation in Riemer and Jones (2014).

In the case of Hurricane Sandy, track uncertainties were linked to differences in the
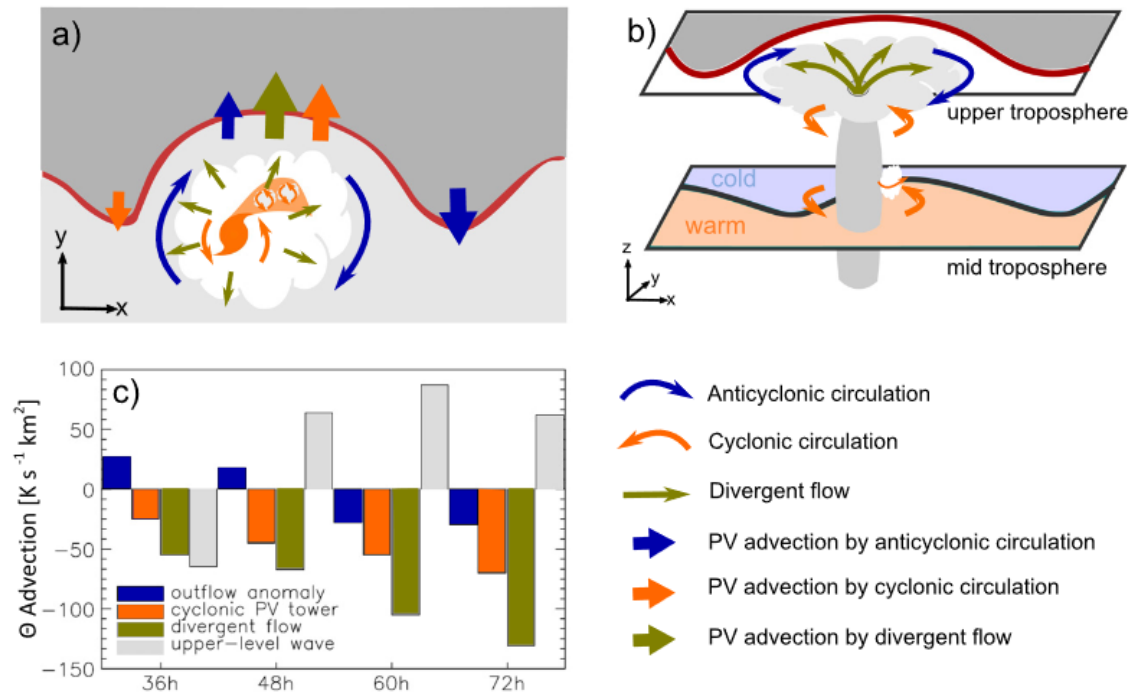
Figure 2.3: Contribution of different circulations associated with TCs to the modification of the environment. (a) Horizontal and (b) vertical schematic showing the cyclonic circulation (thin orange arrows), anticyclonic circulation (thin blue arrows) and irrotational outflow (thin green arrows) of the TC (orange symbol and grey clouds). The contribution of each of these circulations to the downstream ridge is shown by the thick arrows in (a). The red line shows the location of the jet stream with high-PV stratospheric air to the north and low-PV tropospheric air to the south. (c) The advection of potential temperature on the dynamical tropopause by the different circulations, integrated over a 72 hour idealised forecast. Figure taken from (Keller et al., 2019). ©American Meteorological Society. Used with permission.
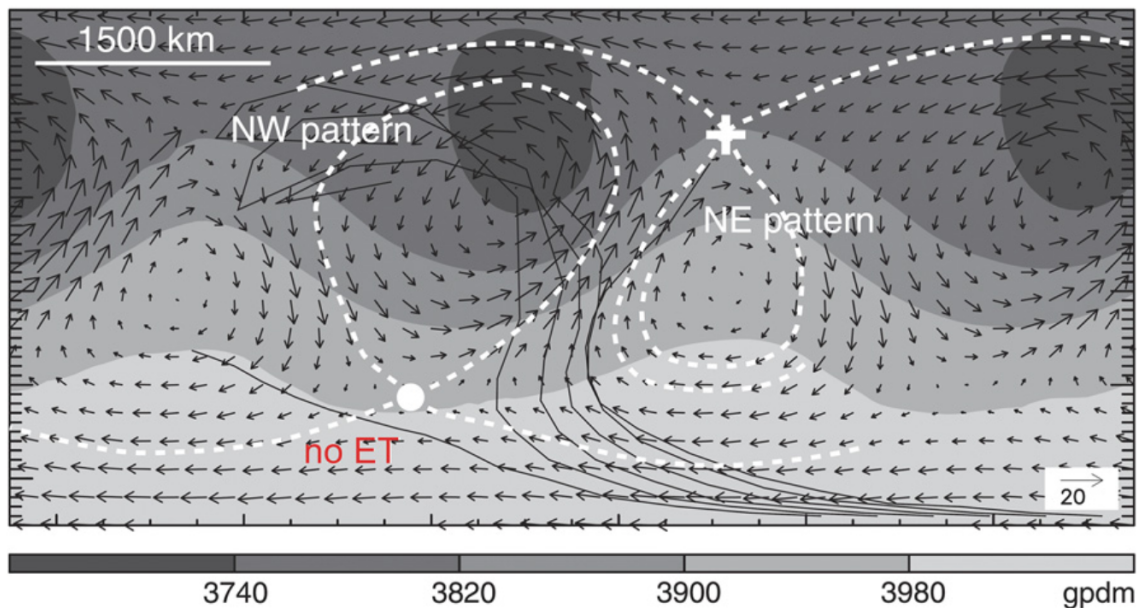
Figure 2.4: Example of TC tracks in an idealised midlatitude wave pattern. Geopotential height and winds in a frame of references which moves with the wave pattern at $620\,\mathrm{hPa}$ are shown by the shading and arrows, respectively. The thin black lines are examples of different TC tracks. "NW pattern" and "NE pattern" refers to two scenarios of extratropical transition described in (Riemer and Jones, 2014), "no ET" refers to a situation in which extratropical transition of the TC does not occur. The dashed contours depict the streamlines formed from the bifurcation points, which are marked by the dot and cross. Figure taken from Riemer and Jones (2014).

strength of the upper level ridge (Magnusson et al., 2014) and thus the steering winds (Munsell and Zhang, 2014). Torn et al. (2015) demonstrated that through PV advection by irrotational winds, Hurricane Sandy amplified the ridge controlling its motion, and differences in the irrotational outflow of the TC in different simulations caused the uncertainty in the track forecasts.

2.5 Predicting Tropical Cyclones

2.5.1 Overview of Track and Intensity Forecasts

The importance of accurately predicting the intensity and track of TCs is crucial to both save lives and limit the damage caused to infrastructure and livelihood. Track predictions have improved steadily for many years, mainly due to the improvements in NWP models[1], such as the increased frequency and density of satellite observations

---

[1]A more detailed summary of NWP models, and in particular the Met Office's Unified Model is provided in Section 3.2.

of the atmosphere and surface, increasingly accurate numerical models and the use of multi-model ensemble forecasts (Bauer et al., 2015; Alley et al., 2019). The mean error in TC track forecasts is approximately 75 km for a 24 hour forecast, compared to close to 250 km 25 years ago (Figure 1.2). However, there remain many outlying cases in which TCs are associated with large track errors (Yamaguchi et al., 2017).

Contrary to the track, numerical models fail to accurately predict the intensity of a TC (e.g. Ito, 2016; Hodges and Klingaman, 2019) and improvements to intensity forecasts have happened at a much slower rate than improvements to track forecasts (DeMaria et al., 2014). Intensity errors are particularly problematic during the first few days of a forecast and increase significantly in TCs which undergo rapid intensification - where a TC intensifies by 30 knots ($15.4\,\mathrm{m\,s^{-1}}$) in 24 hours - and where the initial intensity of a TC is underestimated in the model (Emanuel and Zhang, 2016). There are many factors which make TC intensity difficult to predict including the complex interactions across different scales which determine the TC intensity (e.g. Rotunno et al., 2009) and the importance of accurately predicting the response of the upper ocean to TCs (e.g. Yablonsky and Ginis, 2009), along with gaps in scientific knowledge of how a TC undergoes rapid intensification (Kaplan et al., 2010; Montgomery and Smith, 2017). Higher resolution, CP forecasts are able to better represent the structure and intensity of TCs, compared to global models (Jin et al., 2014; Short and Petch, 2018), however, there are still large errors associated with rapid intensification of TCs in CP models (e.g. Short and Petch, 2018).

The improvements in track forecasting are unsurprising. Section 2.3 explained that, although there are dynamical and thermodynamical considerations (e.g. the β-effect and diabatic heating), the main process controlling the motion of a TC is the environmental flow. Over the past decade NWP models have seen consistent improvements in forecast skill (Bauer et al., 2015) leading to a better representation of the synoptic circulations responsible for the TC motions. Unlike intensity forecasts, there is no evidence to suggest that CP forecasts perform better or worse, on average, at predicting the track compared to global models (Heming et al., 2019). However,

as demonstrated in Figure 1.6, there is evidence that there is a difference between the global and CP track forecasts. Short and Petch (2018) show that whilst the average the positional errors of global and CP MetUM TC forecasts are similar, there are significant differences between the forecasts. Therefore, in some cases the CP model must perform better at forecasting the track, whilst in other cases the global model must perform better.

As discussed in Section 2.3, the intensity of a TC impacts the vertical depth of the environmental winds which impact its track, with the stronger TCs being associated with a larger vertical depth. In addition, category 5 storms move, on average, $1\,\mathrm{m\,s^{-1}}$ faster than other tropical storms (Mei et al., 2012). The increased intensity is likely related to faster moving storms generating weaker sea surface cooling and thus are exposed to the cooling for a shorter time (Mei et al., 2012). Ngo-Duc et al. (2013) demonstrated that a reduction in track error - even for storms in which the track error was initially small - can lead to a reduction of intensity error. However, even with a perfect track forecast and a perfect model, there is a limit on the predictability of TC dynamics and thus our ability to reduce intensity errors beyond a certain threshold (Kieu et al., 2018).

To understand uncertainty in the atmosphere, ensemble forecasts are used. These consist of perturbing the initial conditions along with some model parameters to account for the uncertainty in observations and anaylses[2] (Bauer et al., 2015). Each of the major NWP centres run ensemble forecasts of different sizes (e.g. Toth and Kalnay, 1997; Buizza et al., 2005). For TCs, an ensemble forecast in which the TC track has large spread (i.e. one in which the storm is predicted to go in different directions in each of the ensemble members) demonstrates that the deterministic forecast may be associated with large track errors. This is critical to forecasters who can relay the information to decision makers (Titley et al., 2019). Both global and CP TC ensemble track forecasts tend to be under-dispersive at increasing forecast times, although using multi-model ensembles can lead to a significant improvement in the track and intensity spreads (Melhauser et al., 2017; Titley et al., 2020).

---

[2]A more detailed summary of ensemble forecasting is provided in Section 3.2.2.

Comparisons between models are useful for determining which models are performing better averaged over many cases. However, when comparing two models it is difficult to isolate the impact of one particular feature, such as the parameterisation of convection. This is due to the large amount of differences between different models. These differences include different dynamical cores (which involves the numerical methods, grid structures and prognostic variables used to solve the governing equations), different parameterisation schemes and different initial model analysis. For regional forecasts the differences will also include the boundary conditions provided at the edge of the domains. Melhauser et al. (2017) compared CP ensemble forecasts of Hurricanes Sandy (2014) and Edouard (2014) using three different models, initialised with the same initial conditions and perturbations. The spread for each individual forecast was less than that of the multi-model forecast, however, they were able to reproduce the multi-model spread through using varying parameterisations, stochastic physics algorithms and inflated initial perturbations, suggesting the differences in the dynamical core had less of an impact in the development of the TCs (Melhauser et al., 2017). There are currently no studies which specifically compare the track forecasts of global and CP ensembles using the same model. This comparison would highlight the impact of differences in resolution and parameterisations, without conflating the results with differences due to different dynamical cores.

Although there have been consistent improvements in track forecasts, there remain cases when a TC forecast has large errors (Yamaguchi et al., 2017). These cases are challenging for the forecaster, and thus identifying and understanding situations where the motion of a TC is difficult to predict is essential for preparing effective warnings and thus mitigating the potential impact of the storm. Further, identifying weaknesses in the model will help focus the future development of the model leading to the improvement of forecasts.

2.5.2 Some Examples of Difficult to Predict Tropical Cyclones

A number of difficult to predict TCs have been the subject of previous case studies into track forecast uncertainty. Section 2.4 described how TC-environment interactions impacted the predictability of Hurricane Sandy, and how the location of Typhoon Jangmi in relation to an upper level trough was critical to the future forecast. Hurricane Joaquin (2015) has also been the subject of multiple case studies, mainly due to its unusual looping track. Initially moving south-west towards the Bahamas, many forecasts predicted the storm would make landfall over the east coast of the U.S.. However, the storm actually slowed significantly before travelling back in a north-east direction into the North Atlantic Ocean. Nystrom et al. (2018) demonstrated that the uncertainty in the track was due to differences in the steering winds. In particular, small differences in the lower level (700 hPa) steering winds were found to be significant in deciding which side of a bifurcation in the steering flow the storm would travel. These differences were traced back to initial condition differences between 600 and 900 km of the storm's centre. Miller and Zhang (2019) attributed forecast errors of Hurricane Joaquin to both the near-storm winds and a shallow vortex depth meaning the storm was not impacted by the upper level winds. However, the results from Alaka Jr et al. (2019) suggest that the track of Joaquin was insensitive to the structure of the TC vortex and that the track uncertainties arose from the evolution of the environment and thus the steering flow, rather than the TC depth.

Using ensemble-based sensitivity analysis, Torn et al. (2018) showed that the forecast spread of three TCs [Joaquin, Debby (2012) and Lionrock (2016)] was associated with variability in the near-storm steering flow - in particular the steering flow within 500 km of the TC centre. Each of these TCs was characterised by being in a large-scale deformation flow, i.e. one in which a bifurcation point is present in the steering flow. Errors in the steering flow within 500 km of the centre of a TC can determine which side of the axis of contraction the TC will move to and thus the future position of the storm.

The size of a TC has also been related to errors in track forecasts. Tang et al. (2020) investigated three TCs which were all embedded in a split subtropical high position. They found that, using the Weather Research and Forecasting (WRF) model, differences in the initial TC size impacted which of the synoptic systems the TC would interact with and thus the steering flow. They also identified a link between the size of TCs in different NWP models and the track forecasts for these three particular storms. In their analysis of TC Lupit (2009) they found that NWP models which predicted Lupit to move westwards over-predicted the TC size, whilst the NWP models which predicted the TC to recurve under-predicted the TC size. However, in their WRF simulations the opposite was true with larger TCs moving to the north-east. Tang et al. (2020) showed this discrepancy was related to the strength of an anticyclone to the east of the storm in the different model. This example highlights that comparisons between different models are difficult. With so many different factors to consider (TC size, TC structure, the environment etc.), it is difficult to compare different models which will likely predict each of these things slightly differently. Despite this, their analysis using the WRF simulations did indeed show that it is important to consider TC size when investigating track uncertainty.

A number of diagnostic tools have been developed for analysing errors or uncertainty in TC track forecasts (Magnusson et al., 2019). Whilst some of these methods require the user to have access to the model (such as adjoint sensitivity and "bogussing" TCs in initial conditions), and may require complicated modifications to initial conditions or model physics, others (such as analysing the environmental flow and ensemble sensitivity analysis) can be applied to any forecast without the need to rerun it. In this study the latter two methods are used and are described in detail in Section 3.5. Other sensitivity tests which are unique to the MetUM and require forecasts to be rerun are also used in Chapter 6.

2.6   Tropical Cyclones in the Western North Pacific

This thesis will provide a detailed case study of two TCs which made landfall over the Philippines. In this section a general overview of the climatology of TCs in the western North Pacific is given.

The western North Pacific ocean basin has the highest number of TCs on average every year compared to the other tropical ocean basins (Peduzzi et al., 2012). Each year the region has approximately 25 named storms (Figure 2.5), less than five of which are categorised as category 3-5 on the Saffir-Simpson scale (i.e. having 1-minute maximum sustained winds greater than $50\,\mathrm{m\,s^{-1}}$). In the western North Pacific, TCs form all year around (Figure 1.3) with a maximum of approximately 5 in August.
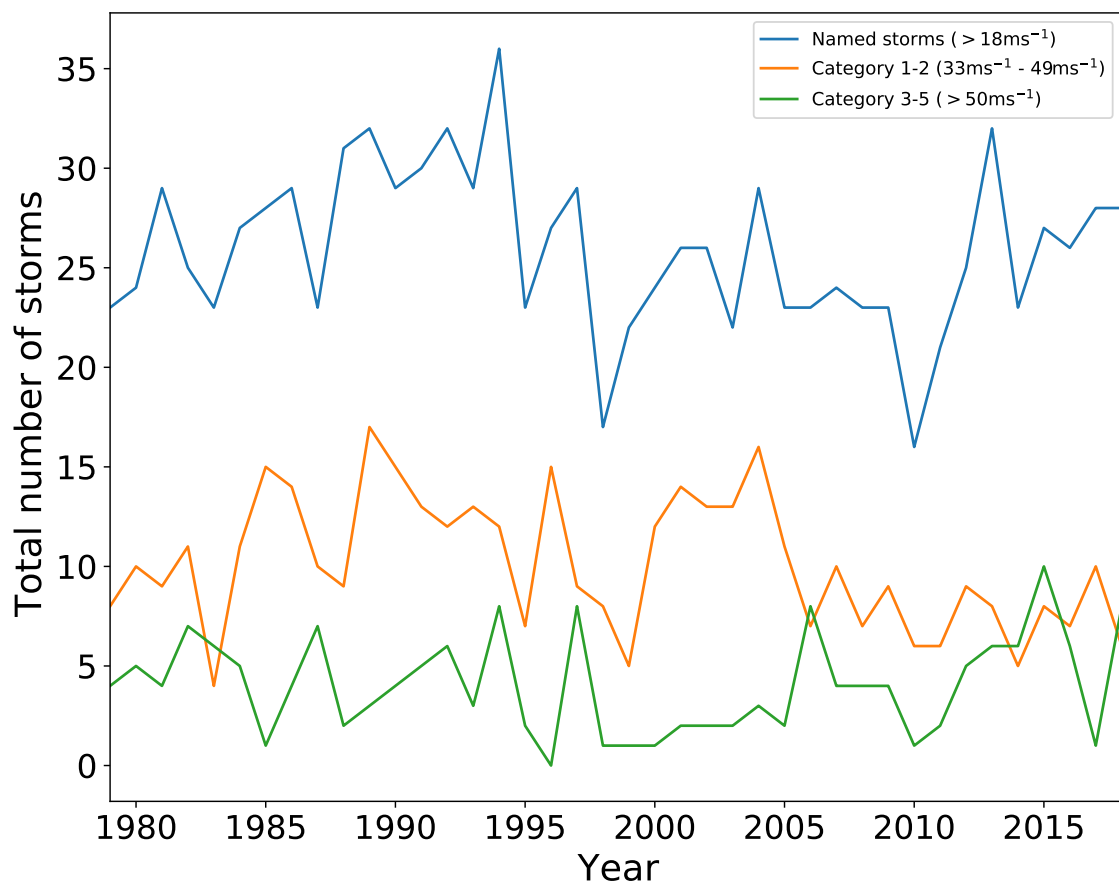
Figure 2.5: Number of Tropical Cyclones in the western North Pacific each year since 1977. Data taken from IBTrACS.

The tracks of all storms in the region since 1977 are shown in Figure 2.6. Many
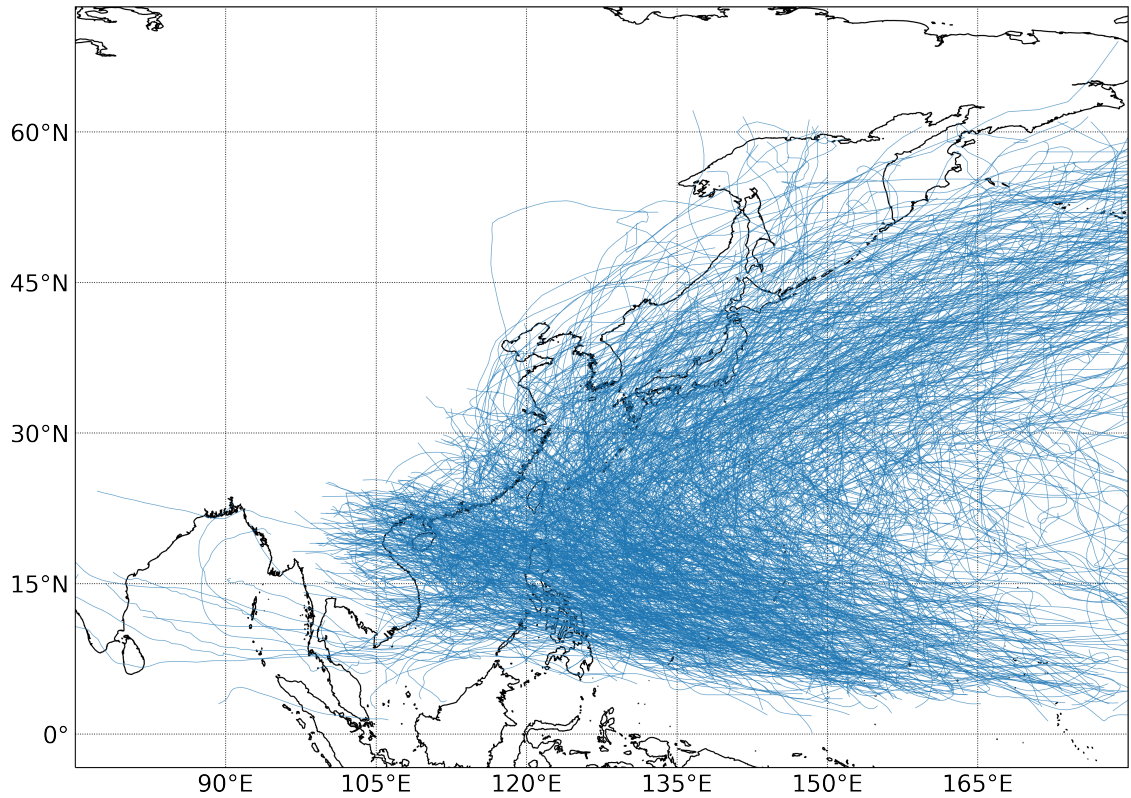
Figure 2.6: Tropical cyclone tracks in the western North Pacific between 1977-2019. Data taken from IBTrACS.

countries are affected by TCs in the area, including the Philippines, Vietnam and China. Annually the Philippines has on average 9 landfalling TCs (Cinco et al., 2016), and is the ninth most at-risk nation to natural disasters (Eckstein et al., 2019) due to the large numbers of people a TC could impact in the Philippines. Indeed, TCs contribute up to 54% of the annual rainfall in parts of the Philippines (Bagtasa, 2017).

As with other TC basins, the western North Pacific experience a number of TCs each year with large track errors. Peng et al. (2017) evaluated the typical steering flow for TCs associated with large track errors. They found that the most common synoptic set up which caused large errors was one in which the TC interacted with the subtropical ridge, a cyclonic circulation to the south and an upper-level trough to the north. The second and third most common synoptic set ups for TCs with large track errors were ones in which the TC was embedded in a weak background flow, usually between two anticyclones, and one in which the steering flow did not explain the TC motion. The situation in which TCs are embedded in weak steering

flow is likely to become more common over the western North Pacific in the future due to the changing climate (Chu et al., 2012; Kossin et al., 2016).

Short and Petch (2018) and Hodges and Klingaman (2019) summarise operational, global and CP, track and intensity MetUM TC forecasts in the western North Pacific. Following the global trend, track forecast errors have decreased in the west North Pacific for the global forecasts, although the global ensemble spread is underdispersive (Hodges and Klingaman, 2019). Compared to observations, there are generally large errors in intensity forecasts, although these are reduced with higher resolution, CP, regional forecasts (Short and Petch, 2018; Hodges and Klingaman, 2019). Short and Petch (2018) also shows the track errors for the CP forecasts are on average approximately the same as the global forecasts, however, there are clear positional differences between the two (Figure 1.6). This suggests that TC motion in CP and global forecasts behaves slightly differently.

2.7   Summary

Tropical cyclone motion is primarily controlled by the environmental flow, with other contributions from the β-effect and diabatic heating. The physics of TC motion is well understood, however, TC track errors can occur when a TC is in a sensitive environment, such as being embedded in a deformation flow. Case studies of these situations suggest that small differences in the steering flow or location of a TC between ensemble members can cause drastically different tracks. Further, the steering flow of a TC may be influenced by outflow from the storm. Studying high-impact TCs which are associated with large track uncertainty and track errors can provide insight into the potential causes of track uncertainty.

As available computer resources increase, CP forecasts will be more commonly used to operationally forecast TCs. Currently, there is evidence that the predicted motion of TCs in global and CP forecasts using the same model is different. The average errors remain approximately the same, but there are positional differences between the two types of forecast. This suggests that in some situations the global forecasts

perform better than the CP forecasts at predicting TC motion. The reasons for this have not yet been investigated and will be one of the problems this study seeks to gain knowledge on.

This chapter has summarised some important features of TCs and TC track prediction. Whilst track forecasts have continued to improve for the past few decades, there remain cases in which a TC's motion is difficult to forecast. These cases are problematic to decision makers and also of interest to model developers. This study will aim to improve our understanding of TC track forecasts associated with large uncertainty.

Chapter 3

Methodology and Data

3.1   Introduction

The aim of this chapter is to provide an overview of the model and analysis methods used throughout the thesis. Section 3.2 provides an overview NWP and ensemble forecasting. The MetUM, and the configurations of the MetUM used for this work is described in Section 3.3.1. Section 3.4 details the observational data and analyses used for model evaluation. A number of analysis methods used throughout the work are described in Section 3.5. A summary is given in Section 3.6.

3.2   Numerical Weather Prediction

3.2.1   Overview of Numerical Weather Prediction

Numerical weather prediction models are used to predict the future state of the atmosphere based on current weather conditions. The NWP models take current observational data and use numerical models along with powerful supercomputers to create short-, medium- and long-term weather forecasts.

The aim of NWP models is to solve the atmospheric governing equations, consisting of the conservation of mass, conservation of momentum, the conservation of energy and the ideal gas law.

The conservation of mass,

$$\frac{D\rho}{Dt} + \rho \nabla \cdot \mathbf{u} = 0\,, \tag{3.1}$$

where ρ is the density, $\mathbf{u} = (u, v, w)$ is the three-dimensional wind vector and

$$\frac{D}{Dt} = \frac{\partial}{\partial t} + \mathbf{u} \cdot \nabla \tag{3.2}$$

is the material derivative, states that the mass of the system must remain constant over time.

The conservation of momentum describes Newton's second law for a moving fluid. In vector form, the equations are;

$$\frac{D\mathbf{u}}{Dt} + 2\mathbf{\Omega} \times \mathbf{u} = -c_p \theta \nabla \pi + \mathbf{g} + \mathbf{F} \tag{3.3}$$

where $\mathbf{\Omega}$ is the Earth's rotation vector, c_p is the specific heat of dry air at constant pressure, θ is the potential temperature, $\pi = (p/p_0)^\kappa$ the Exner pressure with p denoting the pressure, p_0 a constant reference pressure (typically $1000\,\mathrm{hPa}$) and $\kappa = R/c_p$ where R is the gas constant of dry air per unit mass, $\mathbf{g}$ is the apparent gravitational vector (the sum of actual gravity and the centrifugal force) and $\mathbf{F}$ is the frictional force per unit mass.

The thermodynamic equation accounts for the conservation of energy. It is defined in terms of potential temperature,

$$\theta = T \left(\frac{p_0}{p} \right)^{\frac{R}{c_p}}\,, \tag{3.4}$$

where T is temperature. The potential temperature is the temperature that a parcel of dry air would attain if brought adiabatically to a reference pressure. The thermodynamic equation states

$$\frac{D\theta}{Dt} = \left(\frac{\theta}{T} \right) \frac{\dot{Q}}{c_p}\,, \tag{3.5}$$

where $\dot{Q}$ is the rate of heating per unit mass which a fluid element is subject to.

The ideal gas law, which is the equation of state relating p, ρ and T, states:

$$p = \rho R T \, . \tag{3.6}$$

Equivalently Equation 3.6 can be rewritten as

$$\pi^{(1-\kappa)/\kappa} = \left(\frac{R}{p_0} \right) \rho \theta \, . \tag{3.7}$$

Equations 3.1 to 3.7 considers a dry atmosphere. However, the atmosphere is not dry. An air parcel consists of both dry air and moisture. Moisture is important for computing quantities of interest, such as specific humidity and cloud cover, whilst it also impacts the development of the atmosphere through, for example, radiative feedback. Moisture can come in different forms. In the MetUM moisture is represented explicitly in three forms - water vapour, cloud liquid water and cloud frozen water. The following discusses how the dry dynamics above are modified to include moisture in the MetUM.

For each form of water substance, a NWP model should have a budget equation of the form

$$\frac{D m_\chi}{D t} = S^{m_\chi} \, , \tag{3.8}$$

where $m_\chi = \rho_\chi / \rho_d$ is the mixing ratio of water substance of type χ with respect to dry air, ρ_χ is the mass of water substance of type χ per unit volume of moist air, ρ_d is the mass of dry air per unit volume of moist air and S^{m_χ} is a source term for water substance of type χ. The three forms of water substance here - water vapour, cloud liquid water and cloud frozen water - are represented by va, cl and cf respectively. The total mass per unit volume of moist air is the sum of the mass per unit volume of each of the different components,

$$\rho = \rho_d + \rho_{va} + \rho_{cl} + \rho_{cf} \, . \tag{3.9}$$

The inclusion of moist dynamics impacts each of the governing equations. Only the dry part of an air parcel follows the continuity equation (Equation 3.1), as the moist

parts have source terms. Dry air contributes only a fraction of total air and thus ρ in Equation 3.1 is replaced with $\rho_d = 1/(\rho - m_v - m_{cl} - m_{cf})$.

The pressure is defined as the sum of pressures exerted by dry air and by water vapour (cloud liquid and cloud ice do not exert a pressure). Using the gas constant for dry air (R_d) and the gas constant for water vapour (R_v), the pressure becomes:

$$p = p_d + p_v = (\rho_d R_d + \rho_v R_v)T = \rho R_d T \left(\frac{\rho_d}{\rho} + \frac{\rho_v R_v}{\rho R_d} \right) . \tag{3.10}$$

This equation is simplified by making use of the virtual temperate (i.e. the temperature that dry air would have to have, at a given density, in order to exert the same pressure as the mixture of dry air and water substance at temperature T) to become

$$p = \rho R_d T_v , \tag{3.11}$$

where

$$T_v = T \left(\frac{1 + \frac{1}{\epsilon}m_v}{1 + m_v + m_{cl} + m_{cf}} \right) \tag{3.12}$$

and $\epsilon = \frac{R_d}{R_v} \approx 0.622$. The virtual potential temperature is defined in a similar way:

$$\theta_v = \theta \left(\frac{1 + \frac{1}{\epsilon}m_v}{1 + m_v + m_{cl} + m_{cf}} \right) . \tag{3.13}$$

For the conservation of momentum equation (Equation 3.3), the pressure gradient term becomes $-c_p \theta_v \nabla \pi$.

The moist-air formulation of the thermodynamic equation remains similar to Equation 3.5 providing a number of assumptions are made. The approximations are related to the specific heat capacities of dry air compared to moist air. For dry air, $\kappa = \frac{R_d}{c_p} \approx \frac{2}{7}$. However for moist air the specific heats of each substance differs. The ratio, κ, becomes

$$\kappa \approx \frac{2}{7} \left(1 - 0.23m_v - m_{cl}\frac{c_{p,cl}}{c_p - m_{cf}}\frac{c_{p,cf}}{c_p} \right) , \tag{3.14}$$

where $c_{p,cl}$ and $c_{p,cf}$ are the specific heat capacities for cloud liquid water and cloud frozen water, respectively. As m_{cl} and m_{cf} are so small, their contribution

is negligible. The mass of water vapour, m_v, is slightly greater, especially in the tropics, however the MetUM still neglects this in the formulation, thus using $\kappa = \frac{2}{7}$. The thermodynamic equation thus remains as in Equation 3.5. The MetUM uses the prognostic variable θ_v, rather than θ and so the thermodynamic equation is written as

$$\frac{D\theta_v}{Dt} = S^{\theta_v} \tag{3.15}$$

where S^{θ_v} is the source term of virtual potential temperature.

The equation of state for moist air is also modified and becomes,

$$\pi^{(1-\kappa)/\kappa} = \frac{R_d}{p_0}\theta_v\rho \,. \tag{3.16}$$

To summarise the full governing equations which the MetUM solves are:

$$\frac{D\mathbf{u}}{Dt} + 2\boldsymbol{\Omega} \times \mathbf{u} = -\frac{c_p\theta_v}{1 + m_v + m_{cl} + m_{ci}}\nabla\pi + \mathbf{g} + \mathbf{F} \,, \tag{3.17}$$

$$\frac{D\theta_v}{Dt} = S^{\theta_v} \,, \tag{3.18}$$

$$\frac{D\rho_d}{Dt} + \rho_d\nabla \cdot \mathbf{u} = 0 \,, \tag{3.19}$$

$$\frac{Dm_\chi}{Dt} = S^{m_\chi} \,, \quad \chi = v, cl, ci \,, \tag{3.20}$$

$$\pi^{(1-\kappa)/\kappa} = \frac{R_d}{p_0}\theta_v\rho \,. \tag{3.21}$$

To solve these equations, each term is discretised onto a three-dimensional spherical grid covering all, or part, of the globe. When choosing the resolution for the model there is a trade off between the benefit of added resolution, the number of ensemble members[1] and available computer power. Current operational global NWP models have a horizontal grid space of the order of $10\,\mathrm{km}$ (Bauer et al., 2015). This resolution is insufficient for some important processes which occur at smaller scales. For example, a typical cumulus cloud has a length scale of $100\,\mathrm{m}$. Hence, it is not possible to resolve every weather phenomenon on a global grid.

---

[1]A description of ensemble forecasting is given in Section 3.2.2

Parameterisations are used to account for sub-grid processes such as convection, gravity wave drag and boundary layer processes. Each parameterisation is formulated to implicitly include the impacts of the physical process in the model. Therefore, the parameterisations are limited by our understanding of the physical process, along with limitations of available computer resource.

Limited-area, high-resolution model domains, nested within a global model, are able to resolve explicitly some of the physical processes that need to be parameterised in the global model, e.g. by switching off the parameterisation of convection. The higher resolution domain takes boundary conditions from its driving global model and uses a different scientific configuration to produce forecasts which allow processes such as convection to develop freely in the model. As technological advances continue, these convection-permitting forecasts will eventually be run on a global domain (Bauer et al., 2015).

3.2.2   Ensemble Forecasting

Observations are irregularly spaced both spatially and in time, therefore, analyses are constructed by combining these observations with a background forecast via a complex assimilation process. The result is a 'best guess' for the state of the atmosphere, which is then used to initialise the model. Small errors in initial conditions, due to errors in the assimilation process, the background forecast and the observations themselves, can be amplified through time due to the chaotic nature of the atmosphere, until the forecasts are no longer reliable. Another source of errors comes from the numerical models used. Approximations made in the discretisation of the governing equations, and the parameterisation of physical processes lead to errors which may be amplified in the same way as errors in the initial conditions. As a result, no deterministic weather forecast is 100% accurate.

To capture some of the uncertainty inherent in NWP models, ensemble forecasts are used. An ensemble forecast involves creating many different forecasts through perturbations of the initial conditions and of the actual model. Ensemble systems are designed so that each member should be equally likely. In principle, in a situation

where each of the forecasts are similar there can be more confidence in the forecast; whereas when they differ the forecaster must take account of the uncertainty. The caveat is that ensembles are often under-spread (e.g. Hamill et al., 2011). This can lead to a false confidence in the forecast and potentially an incorrect forecast being communicated, with a degree of confidence, to the public.

Initial condition perturbations aim to account for potential errors in observations. Due to available computer power, only a relatively small number of ensemble members can be used. Therefore, the initial conditions of ensemble members should capture the fastest growing perturbations, i.e. the perturbations that will make a forecast diverge the most from the control forecast. Making random perturbations to the initial conditions is not useful as these perturbations may miss atmospheric states that could develop into extreme weather events. Instead methods are used to decide which perturbations are best to use within the model. Two common approaches are singular vectors and bred vectors.

Singular vectors consist of using a linearised version of the numerical model to identify the fastest growing perturbations over a short period (typically <48 hours). These perturbations are then scaled to ensure they match the error distribution from observations and analysis, before being used to initialise ensemble members. As singular vectors start out small and target fastest growing perturbations, they may not be suitable for short range forecasts (Bowler et al., 2008). Bred vectors follow an iterative process in which random perturbations are added to a models initial analysis (Toth and Kalnay, 1993). The perturbed forecast is then run out for a short amount of time (typically between 12 and 48 hours). The difference between the perturbed forecast and the control forecast is calculated and scaled to form new perturbations. After a number of iterations, the fastest growing perturbations become dominant. When creating ensemble members, perturbations are both added and subtracted to the control forecast which ensures the initial "best guess" of the atmosphere from the data assimilation process remains centred.

The ensemble transform Kalman filter (ETKF; Bishop et al., 2001), which is used to create initial perturbations in the Met Office global ensemble, is similar to the bred

vector method. The rescaling of evolved perturbations in the bred vector method is replaced with a linear transformation of evolved perturbations in the ETKF method. That is, each "new" set of perturbations consists of a linear combination of the evolved perturbations from the previous ETKF cycle.

In particular, the perturbations to the ensemble mean analysis ($\mathbf{X}^a$) are given by the equation,

$$\mathbf{X}^a = \mathbf{X}^f \mathbf{T} \mathbf{\Pi} \tag{3.22}$$

where $\mathbf{X}^f = \mathbf{x}^f - \bar{\mathbf{x}}^f$ are the forecast perturbations from the previous cycle with $\mathbf{x}^f$ the forecast ensemble members and $\bar{\mathbf{x}}^f$ the forecast ensemble mean, $\mathbf{T}$ is the transform matrix and $\mathbf{\Pi}$ is a scaling term to ensure the perturbations match the root mean square error of the ensemble mean forecast. The perturbations given in Equation 3.22 are added to the ensemble mean analysis ($\bar{\mathbf{x}}^a$), which is calculated using the ensemble Kalman filter (Evensen, 1994):

$$\bar{\mathbf{x}}^a = \bar{\mathbf{x}}^f + \mathbf{G} \left(\mathbf{Y} - \mathbf{H}(\bar{\mathbf{x}}^f) \right) \tag{3.23}$$

where $\mathbf{Y}$ are the observations, $\mathbf{H}$ is the observation operator, transforming analysis into the observation space and $\mathbf{G}$ is the Kalman gain which provides a weight between the previous forecast run and the new observations to create the new analysis. The full details of the configuration of the ETKF, including the structure of $\mathbf{T}$, which defines the linear combination of forecast perturbations to use, is provided in Bowler et al. (2008), with modifications in Bowler et al. (2009). The ETKF ensemble generation was found to better represent the errors in forecast observations and analysis, whilst the computational expense is only slightly greater than the bred vectors scheme (Wang and Bishop, 2003).

Stochastic physics are used to represent the model uncertainties. A random parameters scheme perturbs certain thresholds and parameters in parameterisation schemes which are often given arbitrary values (Bowler et al., 2008). For the MetUM the random parameters are perturbed in the large-scale precipitation, convection, boundary layer and gravity-wave drag schemes. Each of the values are bound by

minimum and maximum values to ensure they do not become unrealistic.

Another stochastic physics scheme used in the MetUM is the stochastic kinetic energy backscatter scheme (SKEB). The SKEB scheme addresses the fact that energy is lost in numerical models due to numerical advection errors, horizontal diffusion and parameterisation schemes (Shutts, 2005). The Met Office use a SKEB scheme to add vorticity perturbations to forecasts to address the dampening of small scale features (Bowler et al., 2009).

3.3 Met Office's Unified Model

3.3.1 Overview of the MetUM

The MetUM, a state-of-the-art operational NWP and climate model, is used in this study. The MetUM can be run at different horizontal resolutions. The current operational global configuration has a horizontal grid space of approximately 10 km, whilst regional configurations have grid lengths of the order of a km.

The MetUM solves the full, deep-atmosphere, non-hydrostatic equations of motion (i.e. those described in Section 3.2) using a semi-implicit, semi-Lagrangian numerical scheme (Wood et al., 2014). Prognostic variables are discretised on to a grid with Arakawa-C grid staggering (Arakawa and Lamb, 1977) in the horizontal and Charney-Phillips grid staggering (Charney and Phillips, 1953) in the vertical, with a hybrid-height, terrain-following vertical coordinate.

Two types of forecast are predominantly used in the thesis - global forecasts and CP forecasts.

The science configuration of the MetUM used in the global forecasts in this study is Global Atmosphere 6.1 (GA6.1; Walters et al., 2017), which includes the ENDGame (Even Newer Dynamics for General atmospheric modelling of the environment) dynamical core (Wood et al., 2014). The GA6.1 configuration contains a comprehensive set of physics parameterisations, outlined in Walters et al. (2017) and briefly summarised below.

- Shortwave radiation from the sun and longwave radiation from the planet interacts with the atmosphere, driving atmospheric circulations. Radiative processes are parametrised via the radiation scheme, which provides prognostic atmospheric temperature increments and surface fluxes. The radiation scheme of Edwards and Slingo (1996) is used with a configuration based on Cusack et al. (1999), with a number of significant updates (see Walters et al., 2017, for details).

- The formation and evolution of precipitation due to grid-scale processes is handled by a single-moment microphysics scheme, based on Wilson and Ballard (1999) with modifications described in Walters et al. (2017).

- The cloud parameterisation is used to determine the percentage of a grid box which is covered by cloud, along with the amount and phase of condensed water in these clouds. This information is used by the radiation and microphysics schemes to calculate the radiative effect of the clouds and to determine if any precipitation has formed, respectively. The parameterisation used in GA6.1 is the prognostic condensate (PC2) scheme (Wilson et al., 2008) along with modifications described in Walters et al. (2017).

- A sub-grid orographic drag scheme is used to account for the effect of features not resolved by the mean orography on the atmospheric flow. The smallest scales, where buoyancy effects are not important, are represented by an effective roughness parametrisation in which the roughness length for momentum used by the boundary layer scheme is increased over orography (Wood and Mason, 1993). The effects of the remainder of the sub-grid orography (on scales where buoyancy effects are important) are parametrised by a drag scheme, which represents the effects of low-level flow blocking and the drag associated with mountain waves. This is based on the scheme described by Lott and Miller (1997), but with some differences; see Walters et al. (2017).

- Gravity waves are also forced by other phenomena (e.g. convection, fronts and jets). These waves break in the upper stratosphere and mesosphere, depositing momentum. The contribution from waves on scales too small for the model to

sustain explicitly is provided by a spectral sub-grid parametrisation scheme (Scaife et al., 2002).

- Turbulent motions in the atmosphere are not resolved by global models, but are important to parameterise in order to give realistic vertical structure in the thermodynamic and wind profiles. The scheme used is that of Lock et al. (2000), with the modifications described in Lock (2001) and Brown et al. (2008). It is a first-order turbulence closure mixing adiabatically-conserved heat and moisture variables, momentum and tracers.

- Convection is parameterised by mass-flux scheme of Gregory and Rowntree (1990) with many extensions described in Walters et al. (2017). This parameterisation represents the sub-grid transport of heat, moisture and momentum associated with cumulus clouds within a grid box.

To include the exchange of surface fluxes in the MetUM, a land surface model - Global Land 6.0 is used (Walters et al., 2017). The Global Land configuration uses the Joint UK Land Simulator (JULES; Best et al., 2011; Clark et al., 2011) land surface model. JULES models the impact different types of land surface have on the atmosphere (Walters et al., 2017). The land surfaces modelled are types of vegetation (broadleaf trees, needle-leaved trees, temperate C3 grass, tropical C4 grass and shrubs) and types non-vegetated land (urban areas, inland water, bare soil and land ice). Each of these land types are important for determining the heating and moisture present in the boundary layer, the drag of surface winds and the impact the potential for disasters such as flooding and droughts. The land surface code also handles surface exchange over the sea, where SSTs are prescribed through ancillary files (Walters et al., 2017).

The science configuration used for the CP forecasts in this study is known as "Regional Atmosphere and Land" (RAL1). There are two sub-releases of this configuration - one for mid-latitudes (RA1-M) and one for the tropical regions (RA1-T). A full description and differences between the two sub-released is documented in Bush et al. (2019). The main differences between the RA1-T science configuration and the GA6.1 configuration, as detailed by Bush et al. (2019), are summarised below.

- The convection scheme that is used in GA6.1 is turned off in RA1-T.

- A "blended" boundary layer parametrisation scheme is used in RAL1 (Boutle et al., 2014). This scheme smoothly transitions from a 3D turbulent mixing scheme based on Smagorinsky (1963) when turbulent motions are well resolved, to the 1D vertical turbulent mixing scheme of Lock et al. (2000) used in GA6.1 when turbulent eddies are completely unresolved.

- Sub-grid parameterisation of either orographically or non-orographically forced gravity waves is not included in RAL1.

- Although not part of the RA1-T configuration, air-sea drag is limited at high wind speeds. In RAL1 the momentum roughness length over open ocean is given by a modified version of Charnock's formula (Smith, 1988) with a fixed Charnock coefficient of 0.011. The drag coefficient in the model thus increases almost linearly with increasing wind speed whereas observations suggest it levels off above approximately 64 knots, and may even decrease beyond this. In this study, the drag coefficient is capped at 0.0024, which corresponds to a constant – rather than increasing – drag at wind speeds above approximately 70 knots, consistent with observations. This has been found to improve wind-pressure relationships in TCs and will be included in the release of RA2-T (Bush et al., 2019).

- Frictional heating is where, due to turbulence, kinetic energy is broken down to smaller and smaller scales until the point it dissipates into thermal energy. Frictional heating is added to the temperature progonostic term in GA6.1 following Zhang and Altshuler (1999), however this is not used in RAL1.

In this study, the Met Office global ensemble prediction system, (MOGREPS-G; Bowler et al., 2008), is used. Initial conditions for each ensemble member are formed by adding perturbations to the Met Office global analysis, where perturbations are generated using an ETKF (Bishop et al., 2001). The effects of structural and subgrid-scale model uncertainties in the ensemble system are accounted for through two stochastic physics schemes: the random parameters scheme (Bowler et al., 2008)

and the SKEB scheme (Bowler et al., 2009).

Presently, MOGREPS-G cycles four times per day (at 00 Z, 06 Z, 12 Z and 18 Z). On each cycle there are 18 ensemble members run out to 7 days: 17 perturbed members plus one unperturbed control member which is run at the same resolution as the other members. In post-processing the two most recent cycles are combined to provide probability forecasts from an ensemble of 36 members (34 perturbed plus 2 control), known as a time-lagged ensemble. Different perturbed members are used depending on the cycle time: 00 Z and 12 Z uses perturbations 1,2,...,17, while 06 Z and 18 Z uses perturbations 18,19,...34 (and member 0 is the control). At the time when forecasts for this study were produced, the system was the same except there were only 12 members per cycle.

In the MOGREPS-G system, 44 perturbations are computed every forecast cycle by mixing and scaling evolved perturbations from the previous forecast cycle. A subset (in this study, 11) of these are used to initialise member forecasts, giving a 12 member ensemble in total (including 1 unperturbed member which is referred to as the control member). Due to available computer power, MOGREPS-G forecasts are run at a lower resolution (the current operational MOGREPS-G grid length is approximately 20 km at midlatitudes).

Convection permitting ensemble forecasts are produced by nesting down global ensemble members to a higher resolution grid. The nesting is one-way. Further, no stochastic physics schemes are employed in the CP ensemble and thus differences between the CP ensemble members are purely due to differences in the initial conditions and lateral boundary conditions inherited from the driving global model.

3.3.2 Model Set Up

In this study, two TCs are investigated in detail - Typhoon Haiyan (2013) and Typhoon Hagupit (2014). Global and limited-area, CP, 5-day, 12-member ensemble forecasts are produced for both storms from a sequence of initialisation times 12 hours apart.
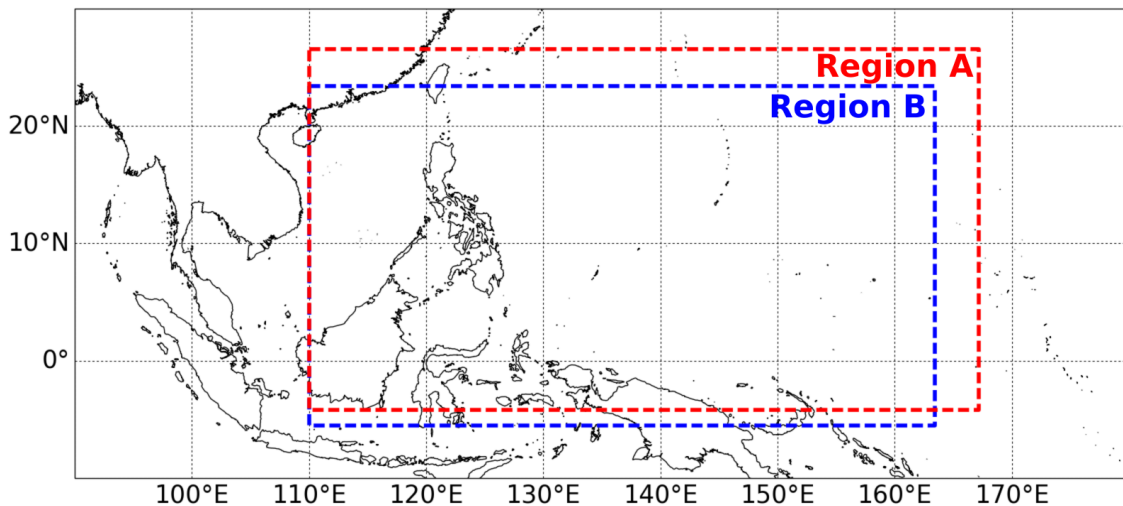
Figure 3.1: Map of the Philippines highlighting the three main island groups and the domain for the 4.4 km nesting suite. Region A is the domain used for forecasts of Haiyan and Region B is the domain used for forecasts of Hagupit.

The global model grid spacings are 0.45° and 0.3° in the zonal and meridional directions, respectively (approximately 50×33 km in the tropics). In the vertical there are 70 levels, the spacing of which increases quadratically with height, relaxing towards a horizontal lid 80 km above mean sea level. The model time-step is 12 minutes.

The limited-area domain for the CP forecasts is shown in Figure 3.1. The domains have been constructed so that the TCs are located well inside the boundary at the initialisation time of each forecast. In some forecasts the storm travels outside of the western boundary of the domain, however, the focus of this study is the predictability of the storms up until landfall over the Philippines. The domain was not extended further to the west to avoid including the Himalayas. The grid spacing of the limited area domain is 0.04° (approximately 4.4 km) in both directions. In the vertical there are 80 levels with the spacing increasing quadratically and relaxing towards a lid of 38.5 km above sea level. The timestep is 75 seconds.

For Haiyan 6 global and 6 CP forecasts were produced, initialised between 0000 UTC 4 November and 1200 UTC 6 November. For Hagupit 11 global and 11 CP ensemble forecasts were produced, initialised between 0000 UTC 2 December and 0000 UTC 7 December. Each forecast is run out to 120 hours.

For a single initialisation time (1200 UTC 3 December 2014) an experimental 45-

member ensemble forecast was created for Hagupit, using each of the 44 perturbations plus the control, rather than a subset of these perturbations. The results of this particular forecast are discussed in Section 5.6.

In Chapter 7 results from another storm, Hurricane Florence, are presented. A global and CP 4-day ensemble forecast for Florence was produced using the single initialisation time of 1200 UTC 13 September 2018. Due to using an updated version of MOGREPS, the forecasts of Florence contain 18 ensemble members as opposed to 12 (1 control plus 15 perturbations). The resolution of the MOGREPS global forecasts are also increased to $0.28°$ and $0.19°$ in the zonal and meridional directions, respectively (approximately 28×20 km). The CP forecasts use the RA1-T configuration and a regional domain with a south-west corner at $(21°N, 89°W)$ and a north-east corner at $(43°N, 59°W)$.

3.4   Reanalysis and Observation Data

The large-scale synoptic flow in the MetUM forecasts has been compared to ERA5 reanalysis data (Hersbach et al., 2020). The ERA5 dataset is provided by the European Centre of Medium-Range Weather Forecasts (ECMWF) and provides hourly estimates for a number of atmospheric, land and ocean diagnostics. The data is gridded globally with a grid spacing of 30 km. Vertically there are 137 levels from the surface up to a height of 80 km.

Satellite observations have been used to compare cloud structures and rainfall estimates to those in forecasts and provide synoptic overviews of the selected storms. The National Research Laboratory Montery Marine Division (NRL-MRY) provides an archive satellite imagery of tropical cyclones. Images of Haiyan and Hagupit have been collected from their website and include cloud images taken from a Special Sensor Microwave Imager (SSMI) 85 GHz satellite. At a frequency of 85 GHz, microwaves penetrate the cirrus canopy and identify rainband structures due to scattering by large precipitation particles.

Satellite rainfall estimates were retrieved from the 'AMSR/AMSR-E/AMSR2/TRMM

Tropical Cyclone Database (Ver. 1.2)' which was produced and distributed by the Earth Observation Research Center, Japan Aerospace Exploration Agency. For Hagupit, Global Precipitation Measurement (GPM) Microwave Imager (GMI; Draper et al., 2015) rainfall data was downloaded. The GMI data is able to give estimates of the instantaneous rainfall rates. For Haiyan, Advanced Microwave Scanning Radiometer 2 (AMSR2) rainfall data was downloaded. Note the difference is due to data availability for each storm.

In addition to the above, best track estimates for Haiyan, Hagupt and Florence are retrieved from the International Best-Track Archive for Climate Stewardship (IBTrACS) database (Knapp et al., 2010). IBTrACS provides 6-hourly estimates of storm track and intensity by merging TC information from a number of meteorological centres around the world.

3.5 Analysis Methods

In the following section various analysis methods used throughout the thesis are described. These methods are the pressure centroid TC tracking algorithm, a TC removal method for defining the steering flow of a TC, the Runge-Kutta 4th order method, used for calculating single layer trajectories, the method for calculating streamlines in both global and regional simulations and ensemble based sensitivity analysis which uses linear regression to highlight sensitive regions of a forecast.

3.5.1 Tropical Cyclone Tracking

To compute the track of a TC the first step is to identify the centre. There are many different methods of finding the TC centre including finding the minimum sea level pressure, the maximum 850 hPa relative vorticity, maximising the tangential inflow around a certain radius, maximising the circulation within a certain radius or finding the maximum potential vorticity, and a combination of these methods. Nguyen et al. (2014) compared five different methods of calculating the centre of a TC and recommended the pressure centroid method to locate the centre of the

storm. The pressure centroid method produces a smooth track, locates the TC in a region of weak storm-relative wind, and is insensitive to a change in the horizontal resolution of the model (Nguyen et al., 2014). Throughout this study the pressure centroid method is used to calculate the storm track.

The centre of the storm is calculated by determining a first guess of the storm centre as the grid point with the minimum sea level pressure. Then the pressure centroid is calculated within a defined radius R_{pc} around this initial guess:

$$\bar{x} = \frac{\sum_{r=0}^{r=R_{pc}} x_i P_i'}{\sum_{r=0}^{r=R_{pc}} P_i'} \quad \text{and} \quad \bar{y} = \frac{\sum_{r=0}^{r=R_{pc}} y_i P_i'}{\sum_{r=0}^{r=R_{pc}} P_i'}, \tag{3.24}$$

where $\bar{x}$ and $\bar{y}$ represent the longitude and latitude of the TC centre; x_i and y_i are the coordinates of the grid points inside the radius R_{pc}. The pressure term P_i' is defined as the pressure deficit from the environment, that is $P_i' = P_{\text{env}} - P_i$, where P_i is the sea level pressure on the grid point and P_{env} is the average sea level pressure around a radius $500\,\text{km}$ from the TC centre. The pressure centroid method is an iterative method. Using $\bar{x}$ and $\bar{y}$ as the "new guess" the calculation is repeated until the centre does not move further than a predefined distance, or a maximum number of iterations is reached. In this study a minimum distance of $0.01°$ or a maximum number of iterations of 1,000 is used. For most cases the centre of the storm is found in less than 20 iterations.

To calculate the radius R_{pc} (i.e. the radius of the pressure centroid) the same technique as in Nguyen et al. (2014) is used. The radius is defined as $R_{pc} = 2R_{80}$, where R_{80} is the distance from the storm centre where winds reach 80% of the maximum windspeed. This is chosen instead of the more obvious metric of the radius of maximum windspeed as, for a typical TC, R_{80} varies less in time than the radius of maximum windspeed. This is especially the case in weaker storms where the windspeed has a much flatter peak when plotted against distance from the storm centre (Nguyen et al., 2014).

In model configurations with a grid spacing of $4.4\,\text{km}$, the minimum sea level pressure

is defined by taking the minimum sea level pressure across all grid points within 100 km of the storm centre. For coarser resolutions, the minimum sea level pressure is found through extrapolation using a Taylor expansion about the minimum sea level pressure grid point.

In particular, defining the sea level pressure as a function $f(x, y)$ with a minimum grid point at (x_i, y_j), the Taylor expansion of $f(x, y)$ about (x_i, y_j) gives;

$$f(x, y) = f(x_i, y_j) + (x - x_i) \left.\frac{\partial f}{\partial x}\right|_{i,j} + (y - y_j) \left.\frac{\partial f}{\partial y}\right|_{i,j} + \frac{1}{2}(x - x_i)^2 \left.\frac{\partial^2 f}{\partial x^2}\right|_{i,j}$$
$$+ (x - x_i)(y - y_j) \left.\frac{\partial^2 f}{\partial x \partial y}\right|_{i,j} + \frac{1}{2}(y - y_j)^2 \left.\frac{\partial^2 f}{\partial y^2}\right|_{i,j}. \quad (3.25)$$

From here the following notation is adopted

$$f_x = \left.\frac{\partial f}{\partial x}\right|_{i,j}.$$

If (x_m, y_m) is the location of the minimum sea level pressure then it can be assumed that (x_m, y_m) is near the minimum grid point (x_i, y_i), and that

$$\frac{\partial f}{\partial x}(x_m, y_m) = 0 \quad \text{and} \quad \frac{\partial f}{\partial y}(x_m, y_m) = 0. \quad (3.26)$$

Thus Equation 3.25 gives the following

$$f_x + x_m f_{xx} - x_i f_{xx} + y_m f_{xy} - y_j f_{xy} = 0, \quad (3.27)$$

$$f_y + y_m f_{yy} - y_j f_{yy} + x_m f_{xy} - x_i f_{xy} = 0, \quad (3.28)$$

and (x_m, y_m) can be found via

$$x_m = x_i - \frac{f_x f_{yy} - f_y f_{xy}}{f_{xx} f_{yy} - f_{xy}^2} \quad (3.29)$$

and

$$y_m = y_j + \frac{f_x f_{xy} - f_y f_{xx}}{f_{xx} f_{yy} - f_{xy}^2}, \quad (3.30)$$

where the derivatives are calculated by central finite differencing. The minimum

sea level pressure, $f(x_m, y_m)$, is then found using Equation 3.25. Compared to the minimum sea level pressure taken on a grid point, this method only produced slightly smaller minimum sea level pressures ($<1\,\mathrm{hPa}$). Further, the values were checked by eye to ensure they were realistic, and to ensure no adverse pressure gradients between grid points lead to an unrealistically strong minima. This technique is similar to those used by operational centres. However, as noted by Heming (2016), the increased resolution of global models compared to previous decades means that it is perhaps unnecessary to continue to identify the TC centre to be between grid points. Historically, global forecast grids have been too coarse to accurately locate a TC to the accuracy required by forecasters, and thus extrapolation techniques were used to improve the TC forecast. As the differences between the grid point minimum and the extrapolated minimum SLP remain small in all cases, this study continues to use the method outlined in this section.

The maximum wind speed is defined as the maximum 10-m wind speed across all grid points within a circle of radius 3° of the storm centre (restricted to a grid point with no interpolation).

3.5.2   Tropical Cyclone Removal

Tropical cyclone motion is primarily controlled by the large scale environment (Holland, 1983; Velden and Leslie, 1991; Chan, 2005, e.g.) along with the beta effect caused by the Earth's Coriolis force (Holland, 1983; Fiorino and Elsberry, 1989; Smith et al., 1990). The steering flow of a TC is the environmental winds which are responsible for determining the motion of the storm. Recently the technique of removing the irrotational and nondivergent winds associated with a TCs vortex (Galarneau and Davis, 2013, hereafter GD13) has become popular. In GD13 the irrotational and nondivergent winds are removed from the total wind up to a certain radius from the storm to give the environmental winds. This is done throughout a vertically averaged depth which, along with the radius, has been optimised to ensure the environment winds accurately describe the storm's motion. The method allows for a calculation of the steering flow of a TC which can change in time dependent

on the size or depth of the storm. Typically the optimum depth is found to be a deep layer between a bottom boundary of 850 hPa to a top boundary between 300-200 hPa whilst the optimum radius ranges usually between 300-400 km (Fowler and Galarneau, 2017; Torn et al., 2018; Nystrom et al., 2018).

Using the relative vorticity (ζ) and divergence (δ) at a radius, r_0, from the centre of the storm, the streamfunction (ψ) and velocity potential (χ) are calculated by solving the associated Poisson equations;

$$\nabla^2 \psi = \begin{cases} \zeta, & \text{for } r \leq r_0 \\ 0, & \text{for } r > r_0 \end{cases} \quad \text{and} \quad \nabla^2 \chi = \begin{cases} \delta, & \text{for } r \leq r_0 \\ 0, & \text{for } r > r_0 \end{cases}. \tag{3.31}$$

The radius r_0 is determined through an optimisation process described below. The nondivergent ($\mathbf{u}_{\text{nd}}$) and irrotational ($\mathbf{u}_{\text{ir}}$) winds associated with the TC vortex can then be computed from the streamfunction and velocity potential respectively,

$$\mathbf{u}_{\text{nd}}(x, y, p) = \hat{\mathbf{k}} \times \nabla \psi \quad \text{and} \quad \mathbf{u}_{\text{ir}}(x, y, p) = \nabla \chi. \tag{3.32}$$

Finally the nondivergent and irrotational winds associated with the vorticity and divergence of the storm are removed from the wind field, $\mathbf{u}$, to leave the environmental winds $\mathbf{u}_{\text{env}}$:

$$\mathbf{u}_{\text{env}}(x, y, p) = \mathbf{u}(x, y, p) - \mathbf{u}_{\text{nd}} - \mathbf{u}_{\text{ir}}. \tag{3.33}$$

As the TC is steered by an average layer in the atmosphere, the environmental winds are averaged from a bottom pressure layer, p_b, to the top of the layer, p_t. To find the environmental steering vector $\mathbf{V}_{\text{env}}$, the environmental winds are also averaged spatially within a radius R. That is, after converting $\mathbf{u}_{\text{env}}$ to cylindrical coordinates centred on the storm centre:

$$\mathbf{V}_{\text{env}} = \frac{1}{p_b - p_t} \frac{1}{\pi R^2} \int_{p_t}^{p_b} \int_0^{2\pi} \int_0^R \mathbf{u}_{\text{env}}(r, \phi, p) r \, \mathrm{d}r \, \mathrm{d}\phi \, \mathrm{d}p. \tag{3.34}$$

A snapshot of $\mathbf{u}$, $\mathbf{u}_{\text{env}}$, $\mathbf{u}_{\text{nd}}$ and $\mathbf{u}_{\text{env}}$ is shown in Figure 3.2. The nondivergent winds which are associated with the relative vorticity are stronger than the irrotational

winds associated with the divergence. The removal of both of these leaves a weak environmental flow through the centre of the storm. The advantage of removing the storm-relative winds is the ability to identify the synoptic scale systems which are controlling the motion of the TC.

A number of variables must be chosen to calculate the environmental wind vector. In line with past studies the bottom pressure layer, p_b, was chosen to be $850\,\text{hPa}$ (e.g. Galarneau and Davis, 2013; Torn et al., 2018). This height is slightly above the boundary layer. To define the removal radius, r_0, and top pressure layer, p_t, a number of values were tested. The environmental wind should closely match the storm motion, therefore, the magnitude of the residual vector,

$$\mathbf{V}_{\text{res}} = \mathbf{V}_{\text{env}} - \mathbf{V}_{\text{fc}} \qquad (3.35)$$

should be minimised, where $\mathbf{V}_{\text{fc}}$ is the storm's forecasted motion vector. For r_0 values were tested between $250\,\text{km}$ and $650\,\text{km}$ at $50\,\text{km}$ intervals. For p_t values are tested between $700\,\text{hPa}$ and $200\,\text{hPa}$ at $100\,\text{hPa}$ intervals, with the additional height of $250\,\text{hPa}$ also tested.

The value of R was chosen to be $2R_{80}$, where R_{80} is the radius at which the winds are 80% of the maximum wind speed, as defined in Section 3.5.1. Using this method to define R was compared to using r_0, which has been used in past studies. Both using $2R_{80}$ and r_0 produced very similar results. Averaged across all times and ensemble members for an ensemble forecast of Typhoon Hagupit, the magnitude of the residual vector using $2R_{80}$ was $0.01\,\text{m}\,\text{s}^{-1}$ less than the average residual vector magnitude when using r_0. This study uses $2R_{80}$ as it allows for comparisons between different removal radii - that is, regardless of the value of r_0, environmental winds are averaged across the same area when calculating $\mathbf{V}_{\text{env}}$.

To reduce the impact of a sheared environmental vorticity, the zonal mean of the vertical component of relative vorticity ($\zeta_{\text{avg}}(\phi, z)$), averaged across a longitudinal range covering the western North Pacific was first removed from the total relative vorticity ($\zeta_{\text{tot}}(\phi, \lambda, z)$) at each grid point in the domain, where ϕ is the latitude and λ
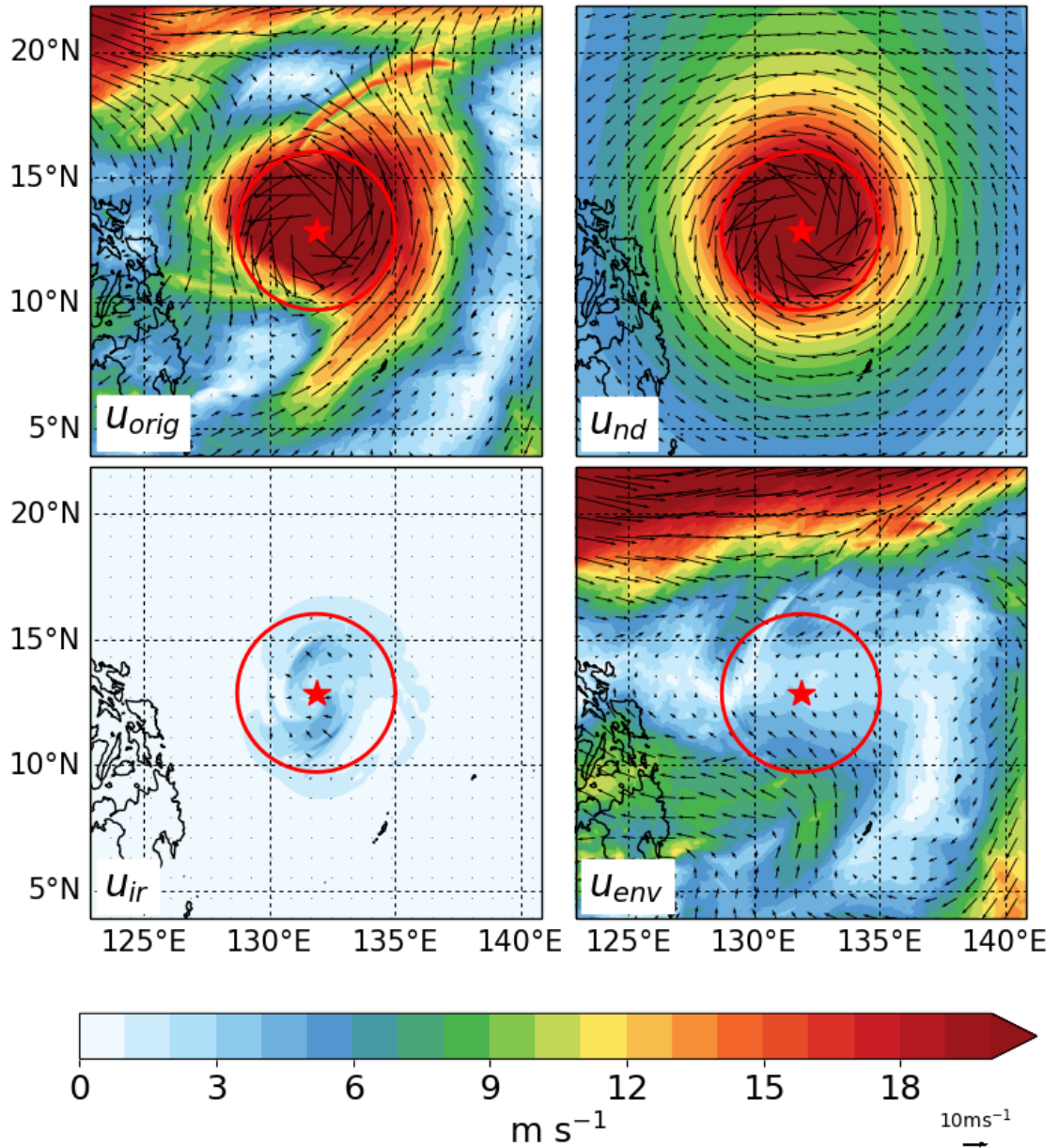
Figure 3.2: A snapshot of each of the quantities calculated in the TC removal method at $500\,\mathrm{hPa}$. From top left to bottom right the quantities are $\mathbf{u}$, $\mathbf{u}_{\mathrm{nd}}$, $\mathbf{u}_{\mathrm{ir}}$ and $\mathbf{u}_{\mathrm{env}}$. The arrows show the wind whilst the shading is the wind speed. The red circle shows a $300\,\mathrm{km}$ removal radius whilst the star indicates the TC centre. The fields are from the CP forecasts of Typhoon Hagupit.

the longitude. To avoid including the large values of relative vorticity associated with the TC, values where masked within a large $10° \times 10°$ area surrounding the storm before calculating the average. Therefore, the relative vorticity in Equation 3.31 has the averaged environmental vorticity removed (i.e. $\zeta(\phi, \lambda, z) = \zeta_{\text{tot}}(\phi, \lambda, z) - \zeta_{\text{avg}}(\phi, z)$. This is slightly different to past studies that have used this method.

It was found that the averaged environmental vorticity was at least an order of magnitude smaller than the relative vorticity in the vicinity of the storm, however, the removal of the environmental vorticity had an impact on the environmental steering vectors. In particular, on average, the directional range of $\mathbf{V}_{env}$ for different values of r_0 tended to decrease by approximately $6°$ after first removing the environmental vorticity.

The TC removal likely removes some of circulation associated with the β-effect, however the amount of this circulation removed is decreased at smaller radii (Galarneau and Davis, 2013). The asymmetric vorticity dipole caused by the advection of the Earth's vorticity is included in the calculation of $\mathbf{u}_{\text{nd}}$ (Equation 3.32). The maximum of this dipole structure (e.g. Figure 2.2) is located approximately 200-500 km from the centre of the storm (Smith et al., 1990; Chan, 2005). Therefore, with a larger r_0 more of the ventilation flow due to the β-effect is removed.

3.5.3 Trajectories

Single-layer trajectories are used in Chapters 5, 6 and 7. The trajectories are used to visualise airflow in proximity of a TC and to assess sensitivity of a TC position with respect to its location in the environment. A trajectory describes the motion of a single fluid particle in a fluid field. The path of a fluid particle follows the equation

$$\frac{\mathrm{d}\mathbf{x}}{\mathrm{d}t} = \mathbf{u}\left(\mathbf{x}, t\right) , \tag{3.36}$$

where $\mathbf{x}$ is the position of the trajectory and $\mathbf{u}$ is the velocity field.

To numerically solve Equation 3.36, a Runge-Kutta 4th order method is utilised. In particular, starting with some initial conditions of $\mathbf{x}(t_0) = \mathbf{x}_0$, the position of $\mathbf{x}$ at a

time $t_0 + h$ is given as

$$\mathbf{x}(t_0 + h) = \frac{k_1 + 2k_2 + 2k_3 + k_4}{6} h \, , \tag{3.37}$$

where k_1, k_2, k_3 and k_4 are slope estimates defined as:

$$k_1 = \mathbf{u}\left(\mathbf{x}_0, t_0\right) , \tag{3.38}$$

$$k_2 = \mathbf{u}\left(\mathbf{x}_0 + k_1 \frac{h}{2}, t_0 + \frac{h}{2}\right) , \tag{3.39}$$

$$k_3 = \mathbf{u}\left(\mathbf{x}_0 + k_2 \frac{h}{2}, t_0 + \frac{h}{2}\right) , \tag{3.40}$$

$$k_4 = \mathbf{u}\left(\mathbf{x}_0 + k_3 h, t_0 + h\right) . \tag{3.41}$$

The Runge-Kutta 4th order method is an iterative method meaning $\mathbf{x}_0 = \mathbf{x}(t_0)$ is replaced with $\mathbf{x}_0 = \mathbf{x}(t_0 + h)$ when computing $\mathbf{x}(t_0 + 2h)$. To calculate values of $\mathbf{x}$ and $\mathbf{u}$ in positions between grid points and between output timesteps, bilinear and linear interpolation is used respectively.

3.5.4 Streamlines

To visualise the fluid flow, two-dimensional streamlines are used throughout the study. Streamlines are instantaneously tangent to the velocity vector of a fluid parcel. To create streamlines, contours of the streamfunction, ψ, are used. The streamfunction is defined such that

$$u = -\frac{\partial \psi}{\partial y} \quad \text{and} \quad v = \frac{\partial \psi}{\partial x} \, , \tag{3.42}$$

or, equivalently by the Poisson equation

$$\psi = \nabla^2 \zeta \, , \tag{3.43}$$

where ζ is the relative vorticity.

For data gridded on a global domain, the streamfunction is calculated using the Windspharm python package (Dawson, 2016) which uses spherical harmonics. For regional data this is not possible. Instead the Poisson equation is discretised using

2nd-order finite differencing,

$$\frac{-4\psi_{i,j} + \psi_{i+1,j} + \psi_{i-1,j} + \psi_{i,j-1} + \psi_{i,j+1}}{s^2} = \zeta_{i,j} \,, \qquad (3.44)$$

where the subscripts i and j represent grid points in the east-west and north-south directions, respectively, and s is the distance between grid points. At the boundaries the streamfunction of the equivalent global ensemble member is linearly interpolated onto the 4.4 km boundary. As the global ensemble members provide lateral boundary conditions for the regional forecasts, this should not introduce errors into the calculation. The discretisation (Equation 3.44) represents a set of linear equations which can be put in the form of $\mathbf{A}\psi = \zeta$, where $\mathbf{A}$ is an $N \times N$ matrix describing the linear system in Equation 3.44, N is the number of grid points, ψ is the streamfunction at all grid points and ζ the relative vorticity at each grid point. The system is then solved using the NumPy linear algebra python package, to give the streamfunction.

3.5.5 Ensemble-based Sensitivity Analysis

In Section 5.6 ensemble sensitivity analysis will be performed on the larger 45 member ensemble. Ensemble sensitivity analysis can identify important features in a forecast which are critical to the predictability of high-impact weather events at a later forecast time.

Ensemble-based sensitivity analysis uses linear regression to highlight the sensitivity of a scalar forecast metric, J, to a state variable, $\mathbf{x}$, at a particular location and time earlier in the forecast (Ancell and Hakim, 2007; Torn and Hakim, 2008). For an ensemble of size N, the sensitivity of the forecast metric to a state variable at a particular grid point is defined as;

$$\frac{\partial J}{\partial x_i} = \frac{\mathrm{cov}(\mathbf{J}, \mathbf{x_i})}{\mathrm{var}(\mathbf{x_i})} \,, \qquad (3.45)$$

where $\mathrm{cov}(\mathbf{J}, \mathbf{x}_i)$ is the covariance of the forecast metric and state variable at grid point i, and $\mathrm{var}(\mathbf{x}_i)$ is the variance of the state variable at grid point i. A full

derivation of this equation is found in Ancell and Hakim (2007). Both $\mathbf{x_i}$ and $\mathbf{J}$ are $1 \times N$ vectors of the state variable and forecast metric respectively with each normalised by the ensemble standard deviation to eliminate the impact of different magnitudes and units. Thus the sensitivity $(\partial J/\partial X_i)$ demonstrates the impact on the forecast metric of increasing the state variable by one standard deviation. High sensitivity indicates that correctly forecasting the state variable at an earlier lead time is crucial to correctly forecasting the forecast metric later on.

3.6   Summary and Conclusion

This chapter provides an overview of the NWP, and in particular the MetUM which will be used in this work. The set up of the MetUM and the various different forecasts in this study is described. The source of observations which will be used to compare to model output is outlined. In the final section of this chapter a number of analysis methods have been described. These methods are used throughout the thesis in each of the following results chapters.

Chapter 4

Typhoon Haiyan and Typhoon Hagupit

4.1 Introduction

Two major TCs made landfall over the Philippines approximately 13 months apart. Typhoon Haiyan, which made landfall at 2000 UTC 7 November 2013, devastated the country with over 6,200 people losing their lives, a further 4 million displaced from their homes and over US $ 775 million of damage caused (Food and Agriculture Organization, 2014; Lum and Margesson, 2014). Typhoon Hagupit made landfall over the Philippines at 1300 UTC 6 December 2014. Initial fears that Hagupit would cause a similar amount of damage to Haiyan were subsided as the TC weakened before landfall. However, Hagupit was still a high-impact storm with a total of 18 deaths, over 4 million people affected and approximately US $ 100 million of damage to infrastructure (OCHA, 2014).

Haiyan was the most intense storm to have ever made landfall when it struck the Philippines (Choy et al., 2015), so, it is unsurprising that Haiyan has been the subject of numerous studies. The majority of these studies focus on the intensity (e.g. Lin et al., 2014; Wada et al., 2018), the associated large storm surge (e.g. Mori et al., 2014; Lagmay et al., 2015), and the social impact of the TC (e.g. Lum and Margesson, 2014). Two key causes of the exceptionally high intensity of Haiyan

upon landfall were high SSTs and a quick translation speed (Lin et al., 2014). The quick translation speed, strong wind gusts and low central pressure upon landfall were also the factors in causing a huge storm surge, which in some places reached an inundation height of 7 m (Takagi et al., 2017). The return period for a storm to make landfall over the Philippines with similar intensity to Haiyan is estimated to be 200 years (Takagi and Esteban, 2016), although this is calculated using data between 1945 and 2013. Climate models suggests there will be an increasing number of high-intensity TCs in the future (e.g. Bhatia et al., 2018), and this may impact the return period of Haiyan. The rarity and speed of approach of Haiyan contributed to the devastating damage it caused. A survey by Esteban et al. (2015) revealed that a number of local residents under estimated the TC, could not conceptualise the storm surge and misunderstood the urgency at which evacuation needed to happen.

Despite being a high-impact storm with an uncertain track forecast, Hagupit has received little attention in literature. Kure et al. (2016) found that, in Leyte, the evacuation in anticipation of Hagupit was much more successful than that of Haiyan. This is due to lessons learnt from Haiyan 13 months prior to Hagupit. Residents were provided with more training and a greater awareness of the potential impact of the TC (Kure et al., 2016). On 4-5 December, there was a broad region of high rainfall rates to the south of Hagupit. This lead to the flooding of Biak, a small island in Indonesia (Ismail and Siadari, 2017). Whilst Hagupit was not the direct cause of the flooding over Biak, the TC likely interacted with the broad region of enhanced convection over Biak.

Lee et al. (2017) compared both Haiyan and Hagupit using satellite data. Motivated by the similarities in the storms they discussed the interactions between the TCs and a nearby cold front. In particular they highlight that both storms strengthened and slightly changed their track at the time when the cold front was closest to the TC. However, their study does not consider other influences which may have changed the intensity or track. For example, other studies show that high SSTs are one of the main causes of the rapid intensification of Haiyan, yet this is not considered in Lee et al. (2017). Further, an observational study of two TCs is not a large enough sample

to draw conclusions about the impact of the interactions of the TC and the cold front. Many more TCs would need to be studied, or numerical models and ensembles of forecasts would need to be used to produce statistically significant results. Lee et al. (2017) also highlighted limitations of this study which uses remote sensing imagery and image processing techniques, and recommended numerical modelling for further investigation of the two TCs.

The aim of this chapter is to provide a thorough overview of Typhoons Haiyan and Hagupit along with their respective track and intensity forecasts. In Section 4.2, a synoptic overview of each storm is provided with focus on the atmospheric conditions affecting the storms' tracks, using ERA-5 reanalysis. Track and intensity forecast results from the ensembles described in Section 3.3.2 are presented in Sections 4.3 and 4.4, respectively. In Section 4.5, satellite imagery of both storms is used to make a number of comparisons. In particular, using microwave satellite imagery, the size and general structure of Haiyan is compared to that of Hagupit at a time when each storm is close to peak intensity. For each of the storms satellite precipitation rate estimates are compared to MetUM output of precipitation and areas of ascent to ensure the forecasts produce realistic simulations of both Haiyan and Hagupit. A summary is provided in Section 4.6.

4.2   Synoptic Overview

There are many similarities in the track and intensity of Haiyan and Hagupit, as shown in Figure 4.1. Both storms originated in similar locations, had a similar path through the Pacific towards the Philippines and reached peak intensity in similar locations. In this section a synoptic overview of each TC is given.

4.2.1   Typhoon Haiyan

Haiyan developed from a westward moving tropical disturbance in a mixed Rossby-gravity wave train on 2 November 2013 (Shu and Zhang, 2015). A favourable environment, including exceptionally high sea surface temperatures (SSTs) and
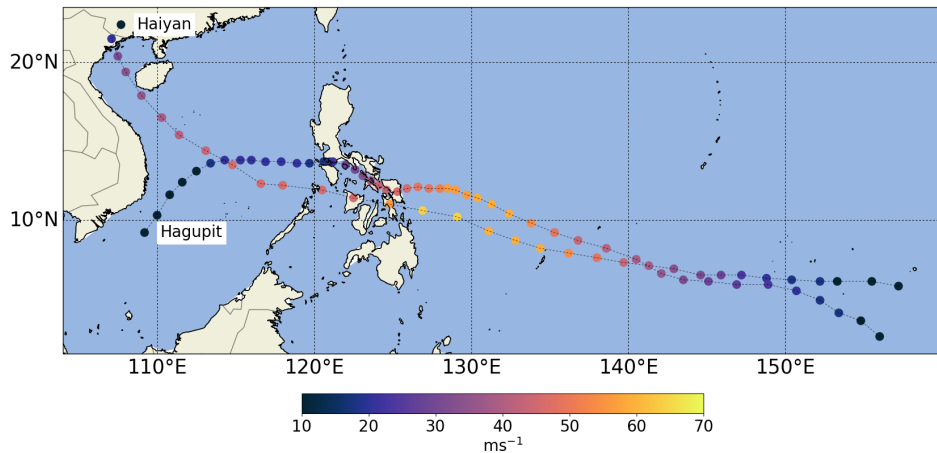
Figure 4.1: Best track of Haiyan (2013) and Hagupit (2014). Each marker is six hours apart and colours indicate the intensity of the storm (maximum 10-minute sustained winds). Best track data retrieved from IBTrACS.

weak vertical wind shear, led to rapid intensification and the storm becoming a category-5-equivalent (on the Saffir-Simpson scale) super typhoon at 0000 UTC 5 November. Rapid intensification continued and the storm reached a peak intensity of $85 \, \mathrm{m \, s^{-1}}$ (1-minute sustained winds) and a minimum sea level pressure of $895 \, \mathrm{hPa}$ at 0000 UTC 7 November. Haiyan remained at this intensity as it approached the Philippines and made landfall approximately 20 hours later with an intensity of $83 \, \mathrm{m \, s^{-1}}$.

The high intensity of Haiyan at landfall is partly due to the storm's fast propagation speed across the Pacific Ocean (Lin et al., 2014). Slow moving TCs mix the ocean surface water, cooling the SSTs and thus suppressing the intensification of the storm, a process known as "SST feedback" (Schade and Emanuel, 1999). However, Haiyan was a particularly quick moving storm, with a translation speed of $8\text{-}11 \, \mathrm{m \, s^{-1}}$ prior to landfall (Figure 4.2). This quick, direct motion was due to Haiyan's position on the southern periphery of the subtropical high (Figures 4.3a and 4.3b). The subtropical high, shown by the $500 \, \mathrm{hPa}$ geopotential height contours and labelled 'H' in Figure 4.3, was elongated across the north-west Pacific inducing an easterly geostrophic flow, consistent with the motion of Haiyan. This synoptic set up is common for TCs which make landfall over the Philippines (Peng et al., 2017). After landfall
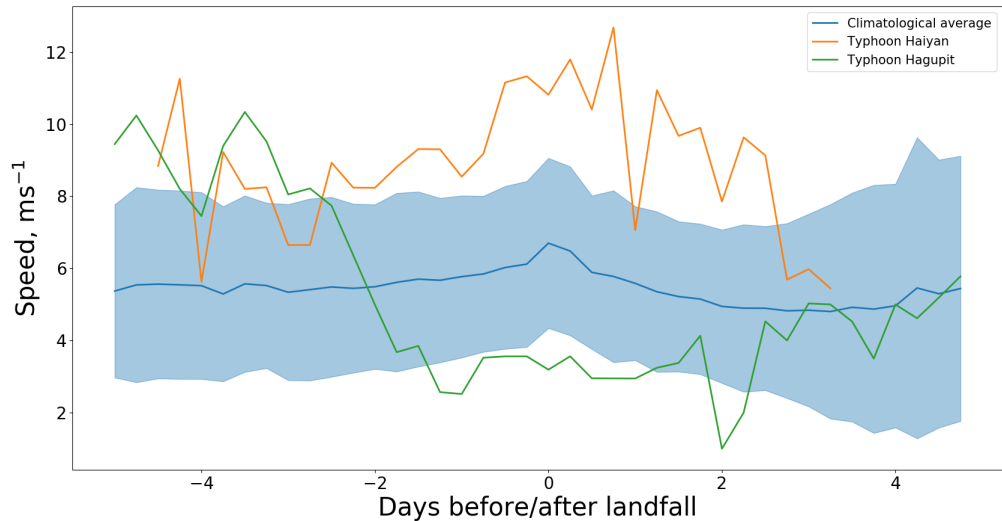
Figure 4.2: The translation speed of Haiyan and Hagupit compared to the climatological mean for TCs making landfall over the Philippines. The shading shows the region within one standard deviation of the climatological mean.

Haiyan is located towards the western edge of the anticyclone, which lead to a strong northward component to the induced geostrophic flow. After Haiyan crossed the Philippines and moved into the South China Sea, the storm travelled in a north-west direction compared to its earlier west-north-west motion, interacting with Vietnam and making landfall over China at 0000 UTC 11 November with a much weaker intensity of 990 hPa and $20\,\mathrm{m\,s^{-1}}$. Haiyan dissipated over China at 1200 UTC 11 November.

4.2.2 Typhoon Hagupit

As a tropical storm on 1 December 2014 Hagupit was initially located in a similar position to Haiyan, and moved in a west-north-west direction. The storm underwent rapid intensification on 3 December, reaching peak intensity of $83\,\mathrm{m\,s^{-1}}$ (1-minute sustained winds) at 0600 UTC 4 December. However, on the 5 December Hagupit slowed and took a more westerly direction, making landfall approximately 36 hours later. At the point at which the storm slowed it also weakened due to large vertical wind shear, quelling concerns that the storm would make landfall with similar intensities to Haiyan 13 months earlier.

As with Haiyan, Hagupit was initially positioned on the southern periphery of the subtropical anticyclone, albeit further to the west (Figure 4.3c, labelled 'H'). As
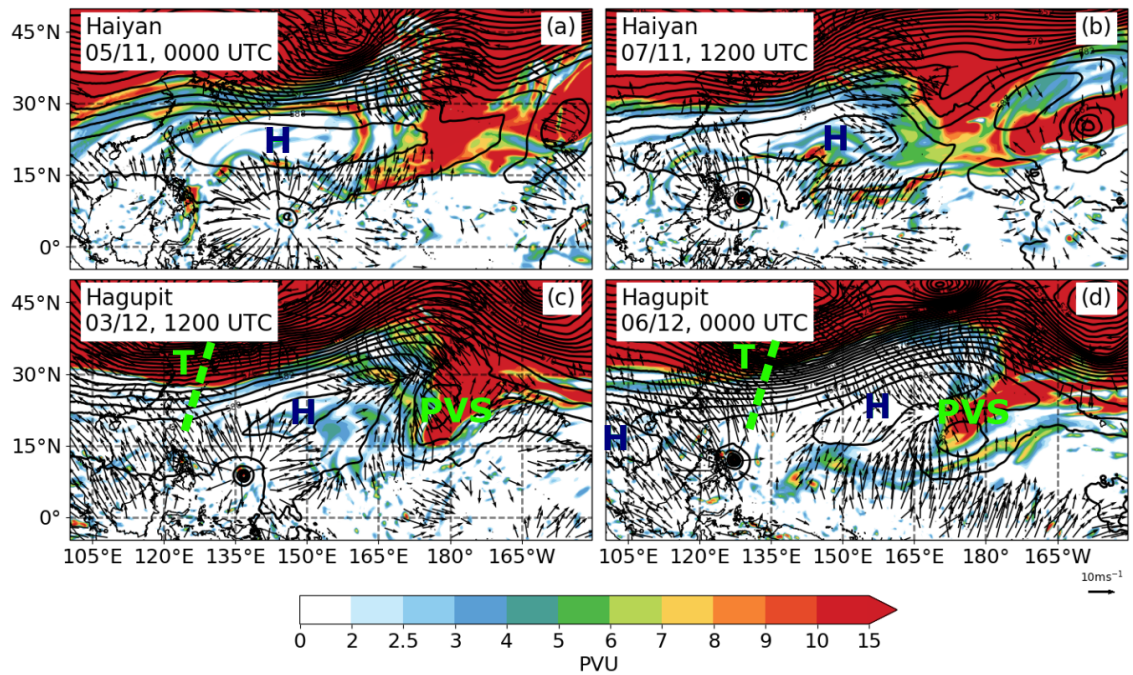
Figure 4.3: ERA-5 reanalysis of Typhoon Haiyan (2013) and Typhoon Hagupit (2014). Shading is PV (PVU) at 200 hPa, contours are geopotential height at 500 hPa (contoured every 3 dam), and arrows are of irrotational winds greater than $5 \, \mathrm{m \, s^{-1}}$ at 200 hPa. (a) and (b) are plots of Haiyan at 0000 UTC 5 November 2013 and 1200 UTC 7 November 2013, and (c) and (d) are of Hagupit at 1200 UTC 3 December 2014 and 0000 UTC 6 December 2014. Labels are used to identify features discussed in the text. 'H' indicates the position of the subtropical high, 'PVS' is the position of the PV streamer for Hagupit and 'T' along with the dashed line is the approximate position of the upper level trough.

the storm moved across the Pacific, the elongated anticyclone split, forming two anticyclones either side of the storm and an upper level trough directly to the north (Figure 4.3d, the anticyclones and the trough are labelled 'H' and 'T', respectively). From 1200 UTC 4 December to 1200 UTC 7 December Hagupit's propagation speed slowed to approximately $3 \, \text{m} \, \text{s}^{-1}$ (Figure 4.2). During this period the trough also remained almost stationary. The outflow of the storm led to ridge-building and the subsequent detachment of a PV streamer downstream of the trough (Figure 4.3d labelled 'PVS'). The PV streamer interacted with the upper level high and became positioned to the south of the anticyclone.

4.2.3 Storm Tracks

Despite similar tracks the speed of Haiyan and Hagupit is distinctly different, particularly prior to making landfall. Figure 4.2 compares the propagation speeds of the two storms to the climatological average of all storms making landfall over the Philippines. From five days to two days before landfall, both storms move quicker than the climatological average speed, at approximately $7\text{-}10 \, \text{m} \, \text{s}^{-1}$. Two days prior to landfall Hagupit slows significantly, whilst Haiyan speeds up slightly. Hagupit makes landfall whilst travelling well below the climatological average, at approximately $2 \, \text{m} \, \text{s}^{-1}$. Meanwhile, Haiyan travels at a speed of $10\text{-}12 \, \text{m} \, \text{s}^{-1}$. This difference in translation speed is seen in Figure 4.1 by the distance between the circles. Each circle represents a 6 hr period. Hagupit is over land for approximately 60 hours, compared to just 12 hours for Haiyan.

Figure 4.4 shows the pressure-weighted, depth-averaged streamlines of Haiyan and Hagupit using ERA-5 reanalysis. The features identified in Figure 4.3 can also be identified in Figure 4.4. In particular the subtropical anticyclone contributes to a strong easterly flow in which Haiyan is embedded throughout its path across the Pacific and as it makes landfall over the Philippines (Figures 4.4a and 4.4b). At 1200 UTC 3 December, Hagupit is also embedded in an easterly flow associated with the subtropical anticyclone, but the anticyclone is positioned to the north-east as opposed to directly to the north. Later, at 0000 UTC 6 December, when Hagupit is
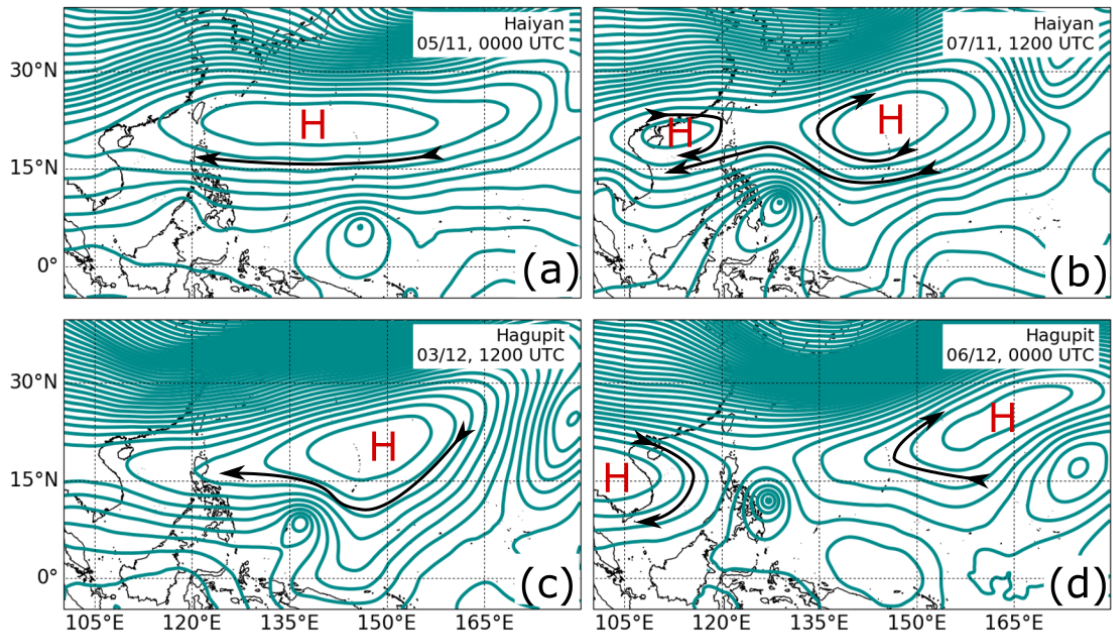
Figure 4.4: Streamlines of Haiyan (2013) and Hagupit (2014) calculated using ERA-5 reanalysis at a pressure-weighted, depth-averaged height between 850 and 200 hPa. The 'H' symbols show the location of the anticyclones. The TC is located in the region of dense circular contours (i.e. to the south of the anticyclone in the first three figures, and between the anticyclones in the last figure), the arrows are for visual purposes only to illustrate the direction of the circulations.

positioned between the two anticyclones (e.g. Figure 4.4d) it is unclear which of the anticyclones is dominant in steering the TC. Unlike Haiyan, Hagupit is not embedded in strong environmental flow but is located in an area of weak environmental steering. The time in which Hagupit becomes positioned between the two anticyclones is also the time when the storm slows down. Comparing the environments of Haiyan and Hagupit suggests that the differences in the tracks and the storm speeds are related to differences in the large-scale environment.

4.3 Track Forecasts

Global and CP ensemble forecasts have been produced for both Haiyan and Hagupit, as described in Section 3.3.2. Forecasts were initialised 12 hours apart between 0000 UTC 4 November 2013 and 1200 UTC 6 November 2013 for Haiyan and between 0000 UTC 2 December 2014 and 0000 UTC 7 December 2014 for Hagupit. Each ensemble has 12 members, thus, there were 72 global and 72 CP simulations for Haiyan and 132 global and 132 CP simulations for Hagupit, totalling 408 individual

simulations. Figures 4.5 to 4.8 show ensemble forecasts from 3 initialisation times for each model configuration and each storm compared to the best track. The forecasts chosen are initialised between 0000 UTC 4 November and 0000 UTC 5 November 2013 for Haiyan; and between 0000 UTC 3 December and 0000 UTC 4 December 2014 for Hagupit. These forecasts are chosen as they cover the period 3-4 days before the storms made landfall and also include the period of rapid intensification and peak intensity of the storms. Due to differences in storm translation speeds, the track plots in Figures 4.5 to 4.8 are on different horizontal scales to allow for better visualisation.

The fairly straight east to west motion of Haiyan was well predicted by the Met Office global ensemble. Figure 4.5 shows the global track forecasts for three initialisation times 12 hours apart for Haiyan, coloured by each 24 hour forecast period. The forecast for the earliest initialisation time, 0000 UTC 4 November, exhibits the greatest spread in the track. Two ensemble members predict the storm to make landfall significantly to the north of the best track. Overall, there is a lot of certainty in the forecast - all of the ensemble members predict the storm to be moving westwards directly towards the Philippines. Subsequent forecasts (Figures 4.5b and 4.5c) show even less spread, with the exception of one ensemble member in the forecast initialised at 0000 UTC 5 November which moves slightly further north earlier on in the forecast. In each case the best track lies within the ensemble spread and the translation speed is accurately predicted, suggesting a small track error.

Whilst the direction of the storm is still well predicted in the CP forecast, the timing is not (Figure 4.6). After just 24 hours of the forecast a significant number of ensemble members lag 12 hours or more behind the best track line - an error that does not occur in the global forecasts. The error remains for the whole forecast. After five days the TC in each of the ensemble members are located where Haiyan was located 18 hours earlier. This is an example of a large along track error as opposed to a cross track error - the path of the storm is well predicted but the speed of the storm is not.

Global track forecasts for Hagupit (Figure 4.7), in contrast to those of Haiyan, exhibit

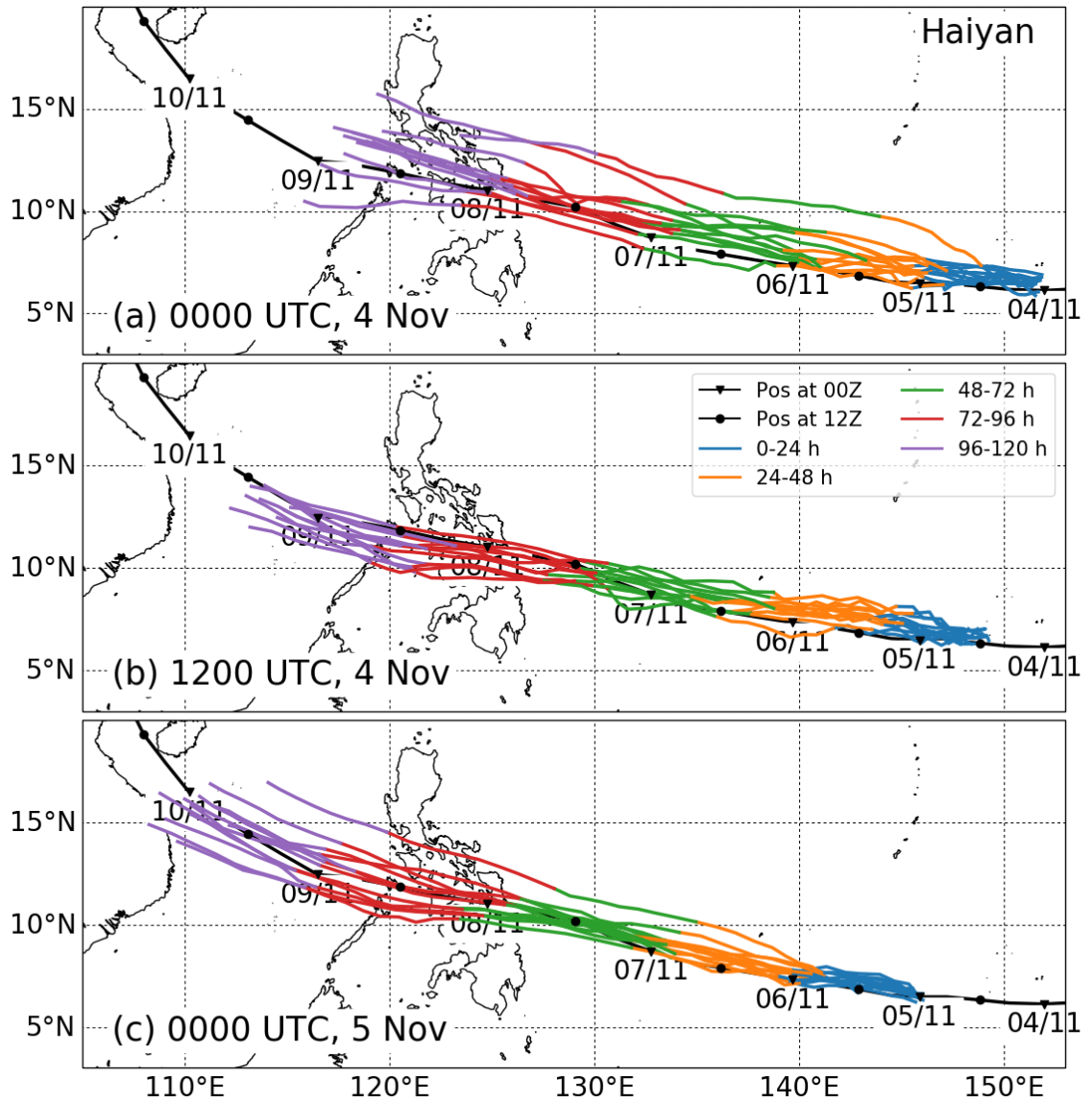Figure 4.5: Global MetUM ensemble 5-day track forecasts for Typhoon Haiyan initialised at (a) 0000 UTC 4 November 2013, (b) 1200 UTC 4 November 2013, and (c) 0000 UTC 5 November 2013. The black line is the best track according to IBTrACS, with the position of the storm at 0000 UTC (1200 UTC) denoted by a triangle (dot). Each colour represents 24 hours of the forecast.
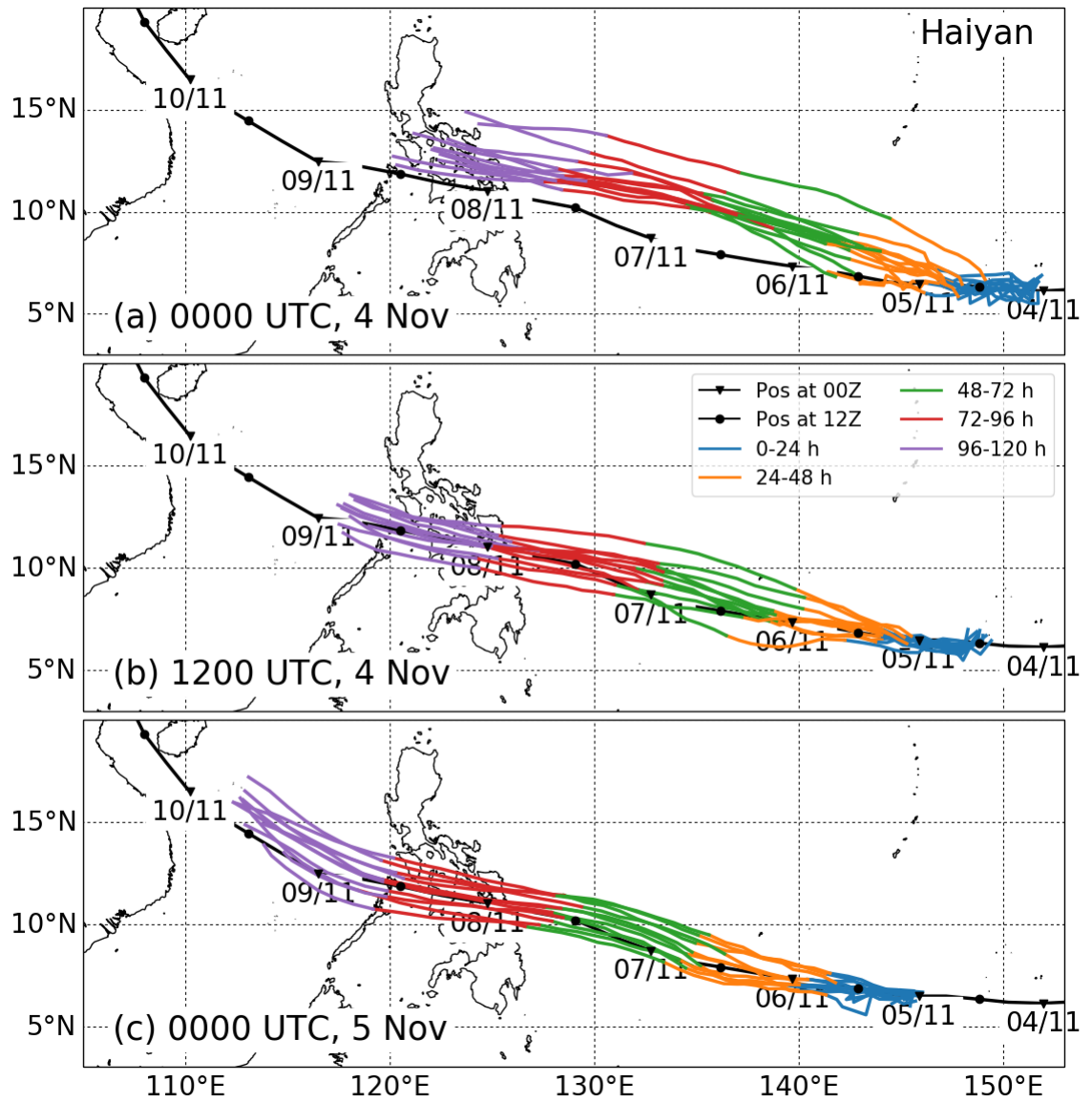
Figure 4.6: As in Figure 4.5 but for the CP forecasts.

a large amount of variability. Although some members of the forecast initialised at 0000 UTC 3 December (Figure 4.7a) predict Hagupit to veer toward the south, most ensemble members from all three forecasts predict that Hagupit will either make landfall over the central Philippines or turn to the north prior to making landfall. In each of the forecasts the storm slows considerably for approximately 48 hours from 0000 UTC 5 December. Following this period, at approximately 0000 UTC 7 December, the storm's speed increases and the tracks begin to diverge. The forecast initialised at 0000 UTC 4 December (Figure 4.7c), less than 3 days before landfall, are still unable to predict with certainty whether or not the storm will make landfall. This uncertainty in whether or not Hagupit would make landfall remained present in the forecast initialised at 0000 UTC 5 December, which still included some ensemble members predicting the TC to turn to the north (not shown).

The behaviour of the CP ensembles for Hagupit is markedly different to the global ensembles (Figure 4.8). Initially each of the ensemble members are predicted to move too far northwards. Just before 0000 UTC 5 December, each ensemble member turns towards the south-west. This south-west turn occurs in each of the ensembles and become more pronounced in the later initialisation time of 0000 UTC 4 December (Figure 4.8c). The best track shows that as the ensemble members turn to the south-west, Hagupit's motion changes to a westwards direction (turning from the initial north-west direction). The error due to the south-west turn in each of the ensemble members is particularly problematic for a forecaster as it occurs before Hagupit makes landfall. The south-west turn represents a forecast bust.

The spread, S, of the tracks at any given time is calculated by taking the unbiased estimator for the variance of the ensemble members (Fortin et al., 2014). That is,

$$S = \sqrt{\left(\frac{n+1}{n}\right)} \sqrt{\frac{1}{n-1} \sum_{i=1}^{n} \left(\bar{\boldsymbol{x}} - \boldsymbol{x_i}\right)^2}, \tag{4.1}$$

where n is the number of ensemble members, x_i is the position of ensemble member i and $\bar{\mathbf{x}}$ the ensemble average position. The $[(n+1)\, n^{-1}]^{1/2}$ term is a correction factor used with a small ensemble. A forecast with large spread in tracks suggests there
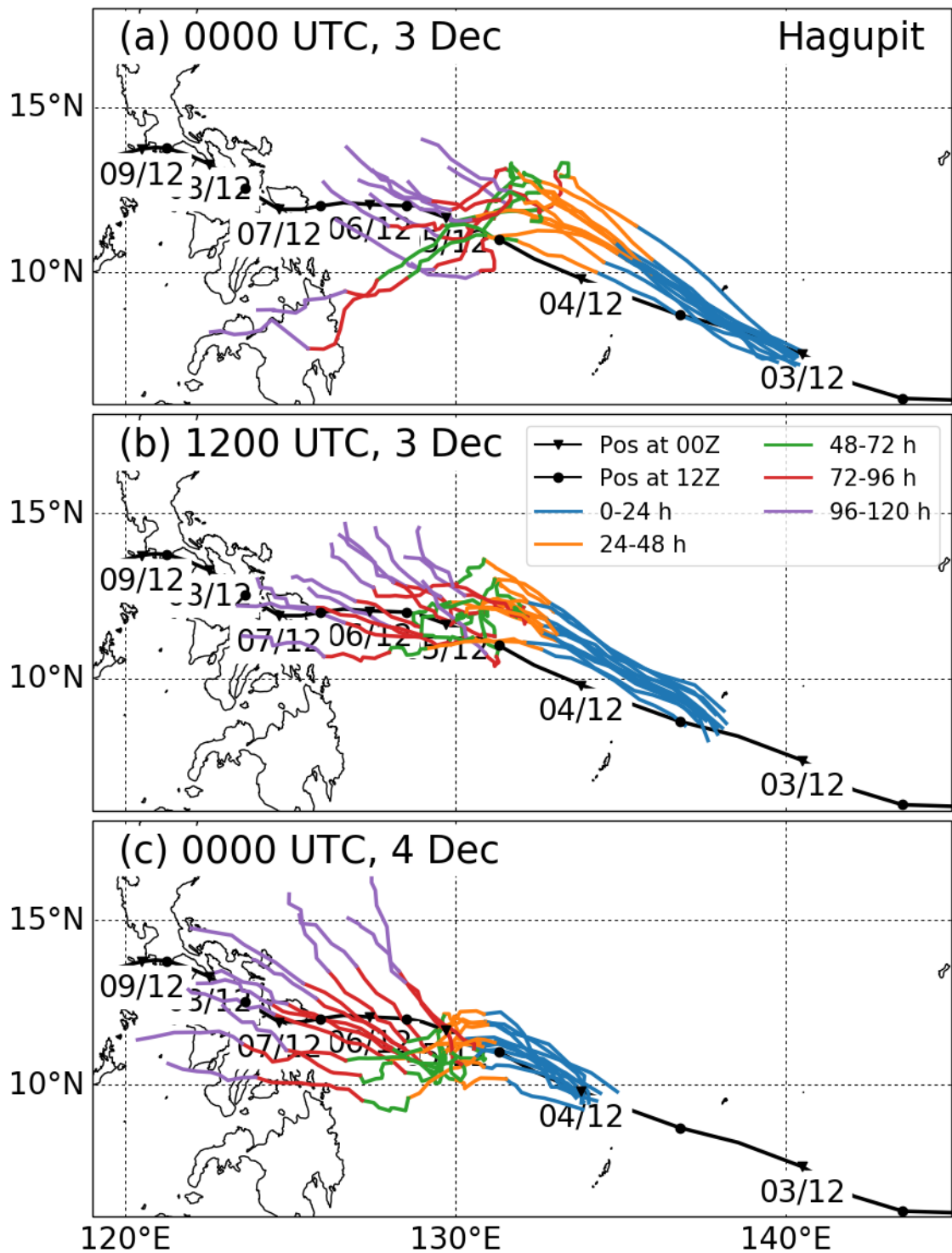
Figure 4.7: As in Figure 4.5 except for Typhoon Hagupit. Global forecasts initialised at (a) 0000 UTC 3 December 2014, (b) 1200 UTC 3 December 2014, and (c) 0000 UTC 4 December 2014.
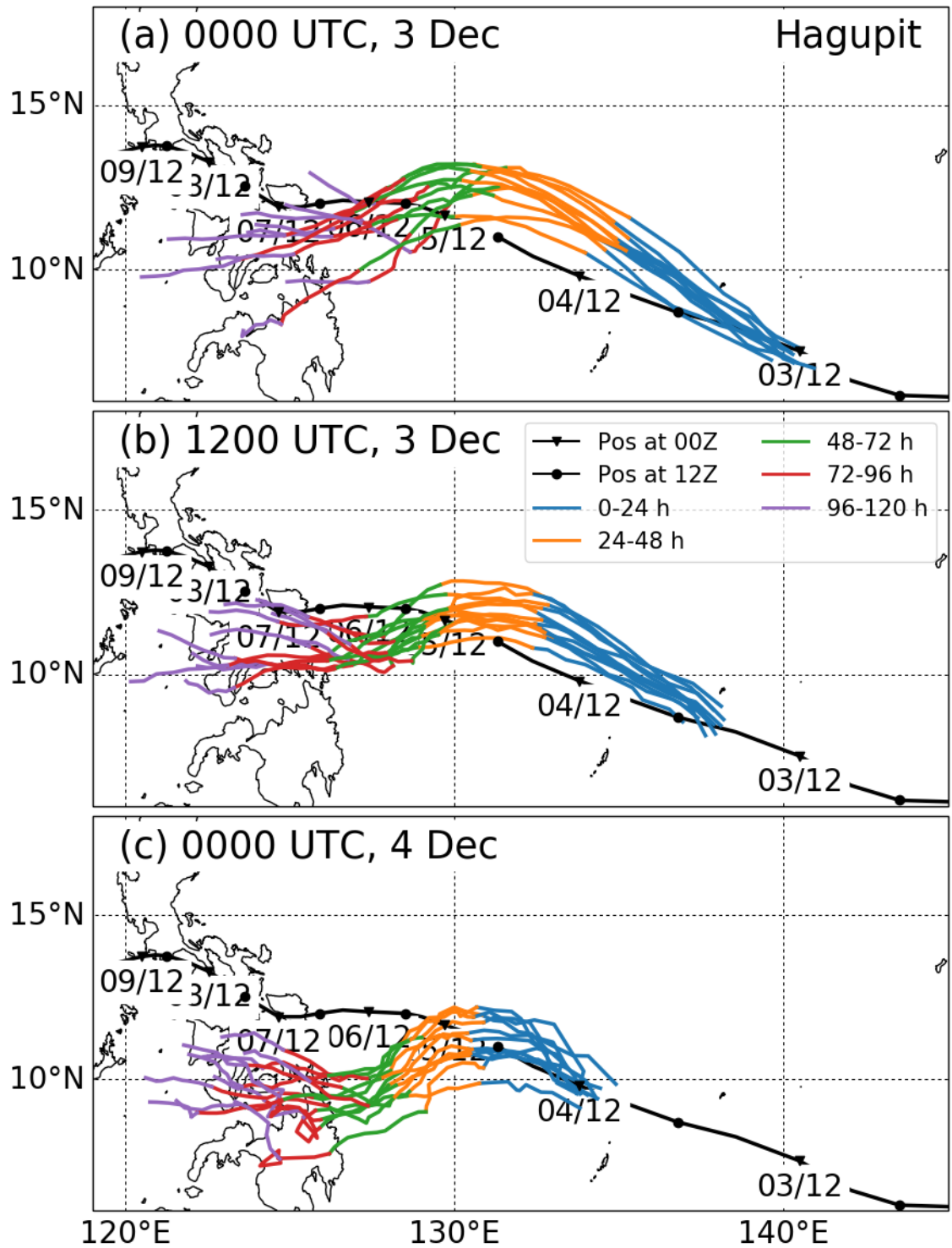
Figure 4.8: As in Figure 4.7 but for the CP forecasts.

is a large amount of uncertainty surrounding the location of the TC. Over many forecasts there should be good correlation between the error in the forecast mean and the ensemble spread.

Figure 4.9 compares the spread and direct positional error of the ensemble mean against lead time for each of the forecasts. For each storm and model configuration the error and spread is averaged across the three forecasts shown in Figures 4.5 to 4.8. The positional error of the global forecasts for Hagupit and the CP forecasts for Haiyan (both over 400 km after 5 days) are significantly greater than the CP forecasts for Hagupit (approximately 300 km after 5 days) and the global forecasts for Haiyan (50 km after 5 days). The global forecasts of Hagupit also exhibit the greatest spread of approximately 275 km after the 5 day forecast. For Hagupit the spread in both the global and CP forecasts continues to increase with time. In comparison the spread of the forecasts for Haiyan increases up to a lead time of 36 hours (at this point Haiyan's global track spread is almost double that of the Hagupit forecasts). After 36 hours, Haiyan's global track spread plateaus for the remainder of the forecasts. This suggests that whilst there is some early variation in the position of the storms in the Haiyan forecasts, after approximately 36 hours each of the forecasts are predicting the TC to move in the same direction (i.e. to the west) and thus the spread does not increase further. However, for Hagupit, particularly in the global forecasts, each of the ensemble members is moving in a different direction and the spread continues to increase throughout the forecast. The spread in the CP forecasts of Hagupit is substantially less than the spread in the global forecasts for Hagupit.

In general, Figure 4.9 demonstrates that the track of Haiyan is better predicted than that of Hagupit. The spread and positional error in the forecasts are smaller than the global forecasts for Hagupit. Although there is a large along track error in the CP forecast for Haiyan, the spread remains small. The speed of Haiyan is much higher than that of Hagupit. Had the distances in Figure 4.9 been normalised by the distance each of the storms had travelled then the differences would be even more striking.
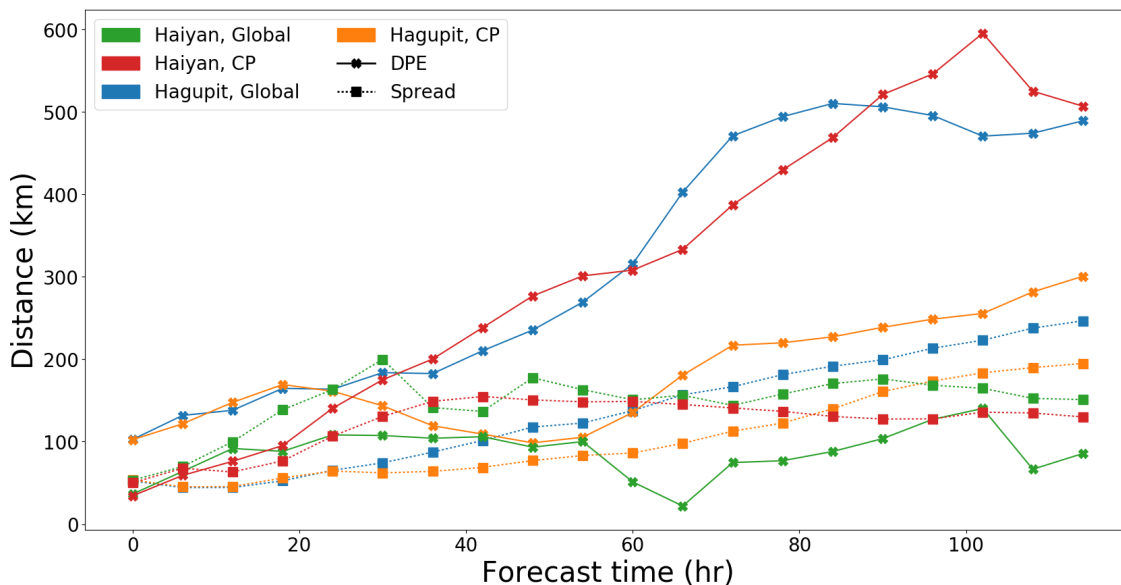
Figure 4.9: Direct positional error (DPE) of the ensemble mean (crosses) and ensemble spread (squares) of each of the forecasts outlined in Figures 4.5 to 4.8. For each storm and model configuration the DPE and spread is averaged across the three initialisation times.

4.4   Intensity Forecasts

The initial intensity of both Haiyan and Hagupit was too weak in the forecasts (Figures 4.10 and 4.11). This is attributed to problems initialising the storm caused by rapid intensification of the TC and high sea level pressure gradients (Heming, 2016). In particular, the intensity of the storm is input into the data assimilation process as the minimum sea level pressure value. However, during periods of rapid intensification, the quality control check of observations can flag up these observed intensities. This is because the background model is unable to predict rapid intensification, and thus when the observation is compared to the background forecast there are large discrepancies.

The global ensembles are unable to intensify the storm at the correct intensification rates. For Haiyan (Figure 4.10) the minimum sea level pressure in the global model does not decrease for the first 36 hours of the forecast initialised at 1200 UTC 4 November. After this, at 0000 UTC 6 November, the forecasts predict the TC start intensifying. During the final 36 hours of the forecasts the average minimum sea level pressure decreases from 990 hPa to 970 hPa, however, this is still some way off the minimum sea level pressure of 895 hPa according to the best track. When analysing

the maximum wind speed in the different forecasts (the bottom figure of Figure 4.10), intensification occurs from the start of the forecast. The rate of intensification is initially slow, but increases after 36 hours.

The global forecasts of Hagupit predict a slow decrease in minimum sea level pressure throughout the forecasts. The storm is initialised slightly stronger than Haiyan with an initial average sea level pressure of 990 hPa for Hagupit, compared to over 1000 hPa for Haiyan, and an initial maximum wind speed of $25\,\mathrm{m\,s^{-1}}$ for Hagupit compared to less than $15\,\mathrm{m\,s^{-1}}$ for Haiyan. During the 5-day forecast the ensemble average minimum sea level pressure decreases to 980 hPa, although there is little change in the maximum wind speed. Whilst global forecasts of Haiyan predict a greater intensification rate of the storm, for much of the 5-day global forecasts Hagupit is predicted as a stronger TC than Haiyan at equivalent lead times, due to the stronger initialisation.

The CP forecasts of both storms produce much stronger TCs than the global forecasts, as would be expected due to their increased resolution. For Haiyan the CP forecasts predict a large increase in intensity earlier on, although there is large spread in the intensities of the ensemble members - particularly when considering the minimum sea level pressure. The ensemble average sea level pressure reaches less than 950 hPa in CP forecasts of Haiyan, whilst the maximum wind speed increases to approximately $45\,\mathrm{m\,s^{-1}}$. Convection permitting forecasts for Hagupit also intensify the storm to under 950 hPa and increases the maximum speed to approximately $50\,\mathrm{m\,s^{-1}}$. In both cases this increase in intensification represents only approximately 60% of the intensification of the actual TCs.

In Figures 4.10 and 4.11 only one initialisation time is shown for simplicity. However, in other forecasts initialised within 24 hours of these forecasts the storm is still initialised too weak and thus produce similar intensity predictions. Compared to the best track the intensity forecasts are poor. Even without the weak initialisation, the intensification of the storms does not match reality. Both storms undergo a period of rapid intensification (defined as an increase in intensity of $15.4\,\mathrm{m\,s^{-1}}$ in 24 hours), however, the only time this criteria is met is during the first 24 hours

of the CP forecasts of Haiyan, as the storm is spinning up in the simulations. The timing of peak intensity is off in both CP forecasts (a "peak intensity" cannot be identified in the global forecasts as they do not weaken). This is likely related to the track errors which cause the forecasts to inaccurately predict when the TC will make landfall.

The analysis here considers ensemble averaged intensity with the spread shown by errorbars in Figure 4.10 and 4.11. Whilst there was some spread in the different ensemble members, there were no links found between the intensity of the storms and the track. That is, for Hagupit, there was no link between the TC intensity and whether or not the track would turn to the north or make landfall.

4.5   Storm Size and Structure

For both Haiyan and Hagupit observational data was limited to satellite data. In this section comparisons are made between some model diagnostics and satellite imagery. The aim is to demonstrate that the forecasts produce realistic simulations of Haiyan and Hagupit, by comparing the size of the two storms along with features such as their eye, eyewall and rain bands. The aim is not to produce a detailed comparison of the inner core structure of the storms or to diagnose forecast errors relating to the structure, but to get an idea of how well the simulations capture the basic structural features of Haiyan and Hagupit.

Microwave remote sensing is capable of penetrating the cirrus canopy of TCs which is often seen in visible satellite images. The convective clouds associated with the internal structure of a TC can be identified as large water droplets and ice particles cause a scattering of microwaves and a loss of energy. The 85 GHz images are able to identify deep convective clouds, but they do not identify low level precipitating clouds.

Here, 85 GHz satellite images from the special sensor microwave/imager (SSM/I) are used to compare the structure of both Haiyan and Hagupit close to peak intensity (the top right figures of Figures 4.12 and 4.13). Both storms feature a clear cloud-free

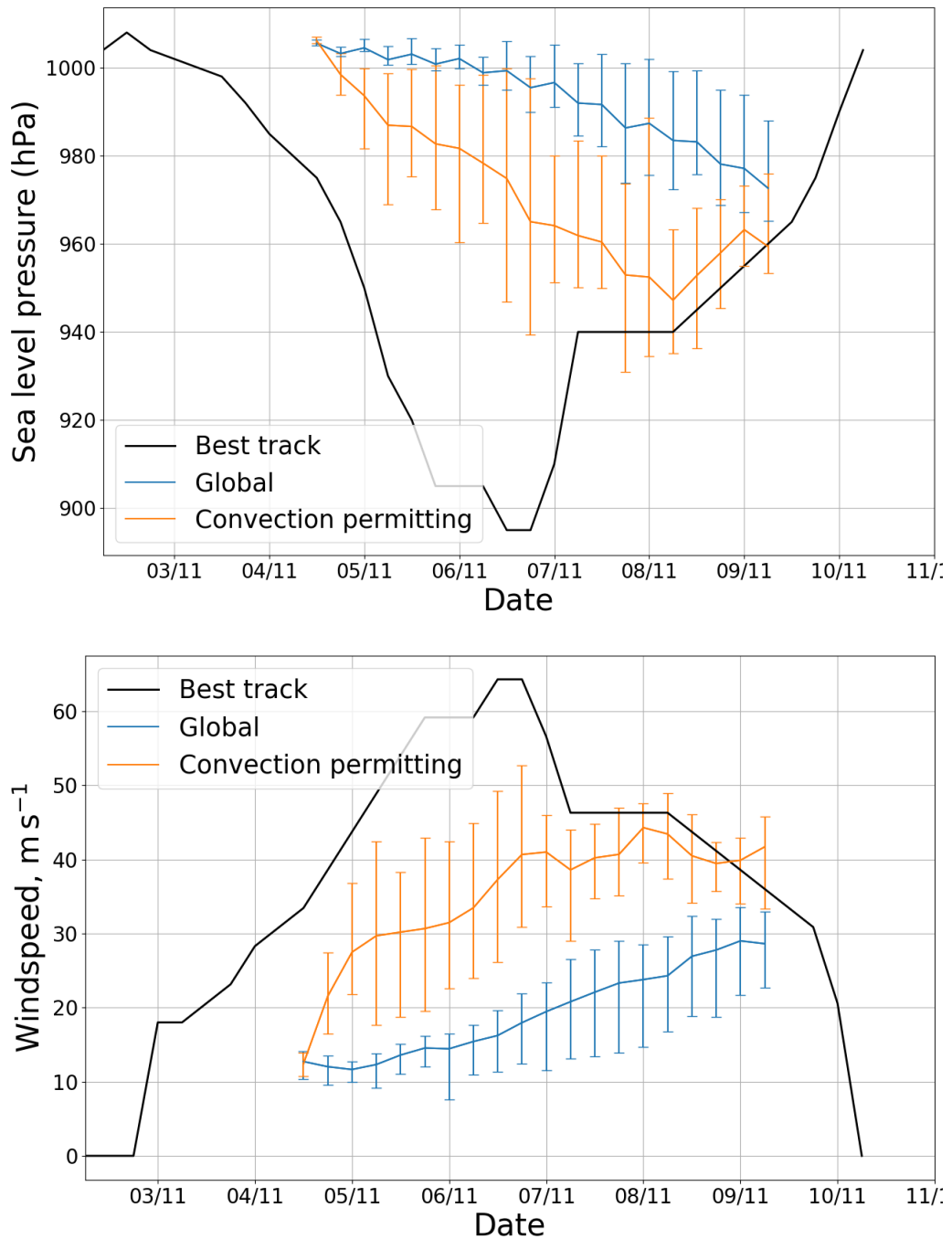Figure 4.10: Intensity forecasts of Haiyan according to (top) minimum sea level pressure and (bottom) maximum 10 m windspeed. Lines are the ensemble average with the error bars showing the minimum and maximum intensities from all of the ensemble members at those times. The forecasts are initialised at 1200 UTC 4 November 2013.
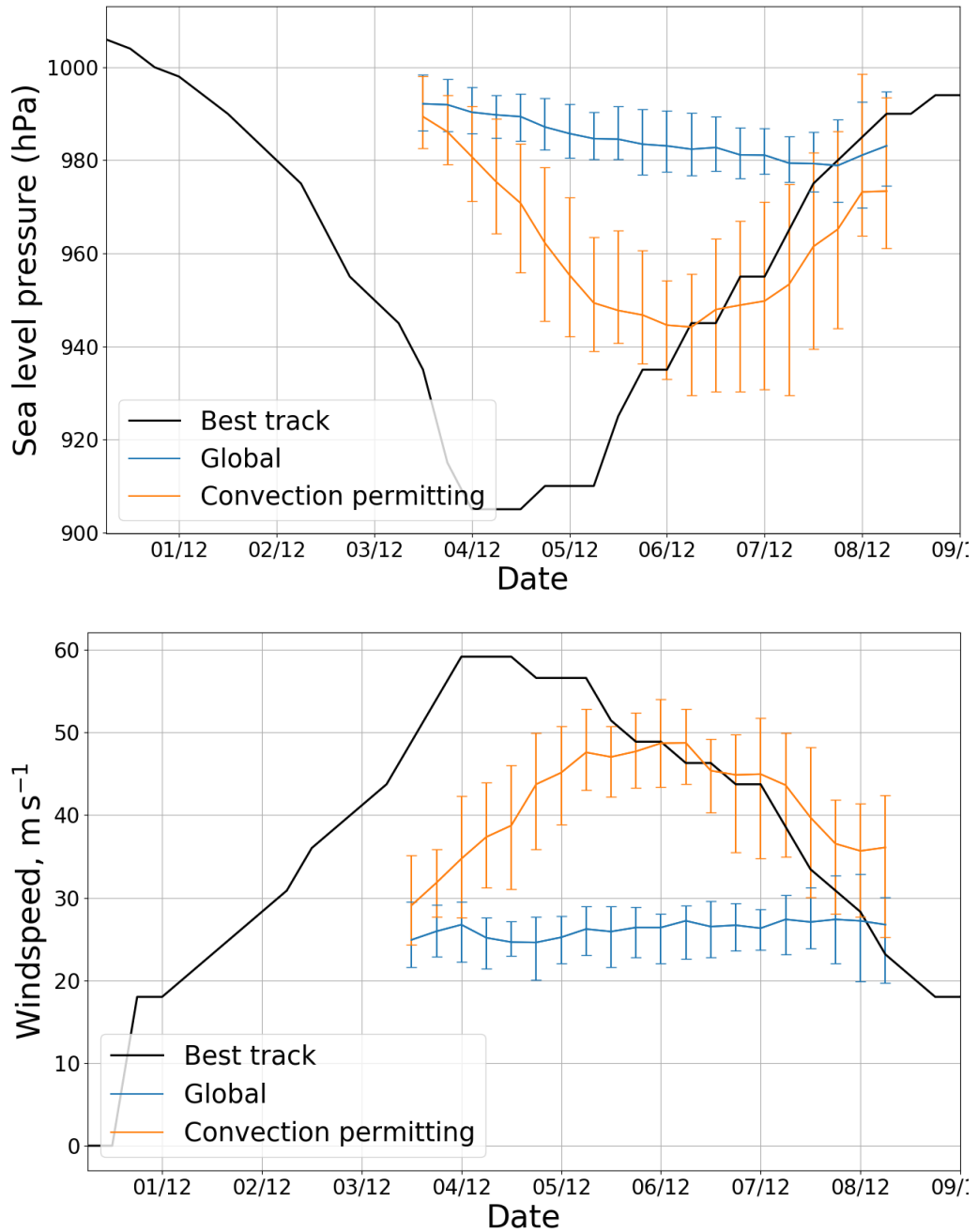
Figure 4.11: As in Figure 4.10 but for forecasts of Hagupit initialised at 1200 UTC 3 December 2014.

eye and cover approximately the same area. For Hagupit (Figure 4.12) there is enhanced convection to the west of the storm centre, whilst for Haiyan (Figure 4.13) deep convective clouds surround the eye. Rainbands spiral out towards the north in both storms.

The plots in the top left of Figures 4.12 and 4.13 are rainfall rate estimates for the TCs from different satellites. Note that the time of these satellite images is different to the plots in the top right of the figures. For Hagupit, Global Precipitation Measurement (GPM) Microwave Imager (GMI) precipitation rates are used. The GMI observes energy from 13 different microwave frequencies and combines this data to produce quantitative maps of precipitation. It provides a continuation of measurements made from the Tropical Rainfall Measuring Mission. For Haiyan, rainfall estimates from Advanced Microwave Scanning Radiometer 2 (AMSR2) sensor, on board the Global Change Observation Mission satellite is used. The AMSR2 uses 6 different microwave frequencies to estimate rainfall. The difference in satellite imagery used for Haiyan and Hagupit is due to data availability.

The estimated rainfall distribution can be compared to the rainfall distribution from the Met UM forecasts. For Hagupit (Figure 4.12) the rainfall is predicted well in the MetUM. For the CP forecasts (bottom right of Figure 4.12), there is no rain at the centre of the storm. Stronger precipitation rates are to the west of the TC with an area of enhanced rainfall also occurring to the north-east of the TC centre. Each of these features matches the satellite derived rainfall estimates (top left of Figure 4.12). The CP forecasts show lots of small scale structures (shown by the pink contours, representing areas of relatively high ascent), highlighting the convective detail of CP forecasts. On the other hand, the global forecasts produce a much lower rainfall rate. Ascent is limited to the north-west of the TC and the finer structure of the spiralling rainbands cannot be seen in the rainfall. However, the general region of rainfall is still well predicted.

For Haiyan the CP forecasts again capture some of the small scale features of the TC (Figure 4.13, bottom right). There is lower precipitation in the TC eye whilst there are also spiralling rainbands to the east. The rainband which spirals from the
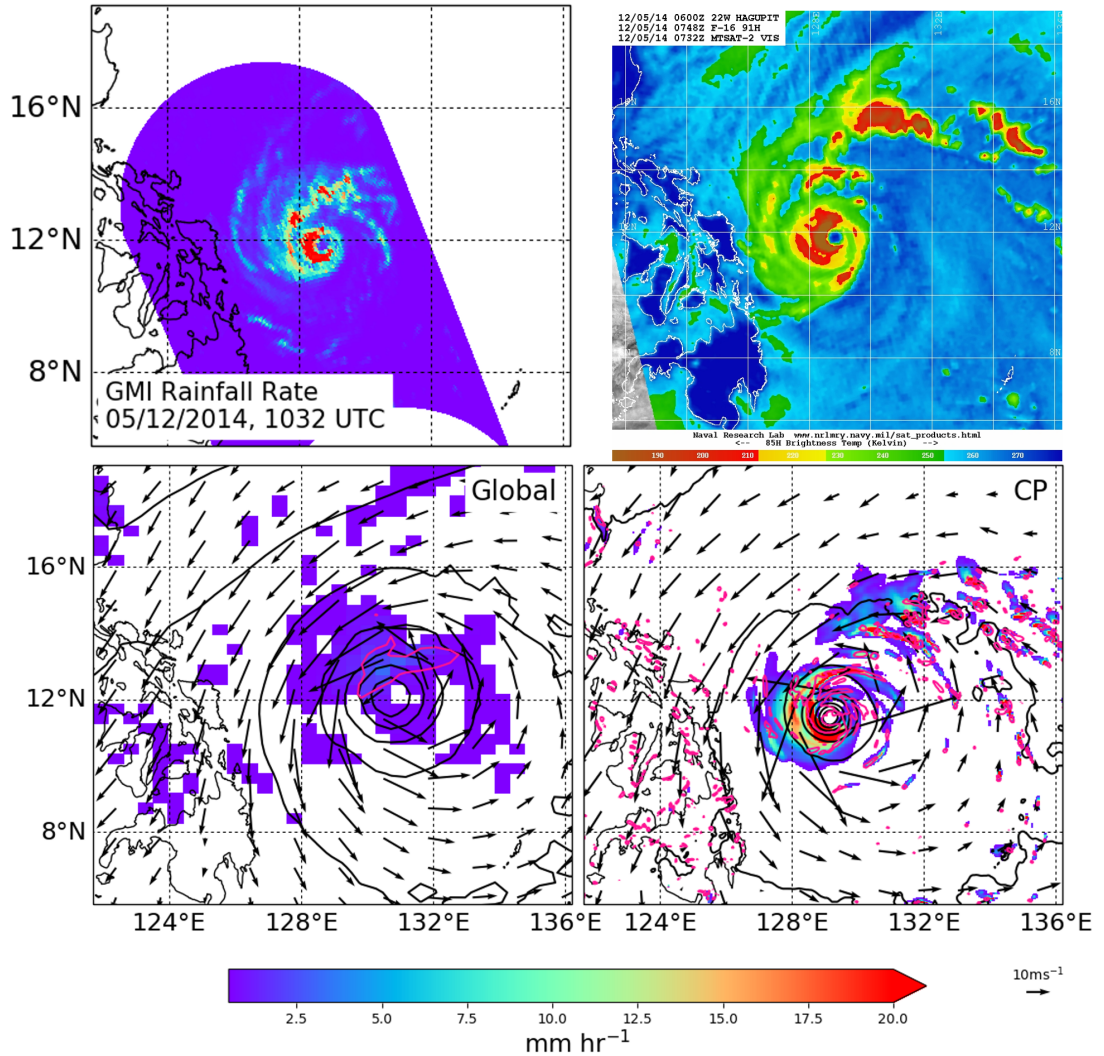
Figure 4.12: GMI rainfall rate estimate of Hagupit at 1032 UTC 5 December (top left). 85 GHz microwave satellite image of Hagupit at 0732 UTC 5 December 2014 (top right). MetUM forecasts of mean rainfall rate using ensemble member 0 of the global (bottom left) and CP (bottom right) forecasts. For the model output shading is of the mean precipitation, arrows show the 850 hPa winds, pink contours are areas of relatively high ascent at 500 hPa and contours are of sea level pressure, contoured every 8 hPa. The Figures in the bottom panels are at a valid time of 1100 UTC 5 December 2014. The forecasts were initialised at 1200 UTC 3 December. The satellite image in the top right is taken from the National Research Laboratory, Marine Meteorology Division.

south of the TC to the north of the TC in the satellite image is not seen in the CP forecasts. However, for these forecasts the time of the simulated TC and the satellite image is different. This is due to the errors in the TC motion meaning that a like for like comparison (i.e. same location and at the same time) is not possible. As with Hagupit, the detail in the global forecasts is much less. Higher relative ascent is seen in a broad region around the eyewall of the TC. However the finer structure cannot be identified.

Comparing satellite imagery at a couple of times to MetUM forecast data at a single time is inadequate to diagnose errors in the storm structure. Despite this, some features of Haiyan and Hagupit which are present in the satellite images can be identified in the MetUM forecasts, particularly in the CP forecasts. For Hagupit the area of enhanced convection on the west side of the eyewall is seen in the CP forecasts along with the satellite images. The spiralling raindbands of Hagupit, particularly to the north-east of the TC centre are also present in the CP simulations. The comparisons suggest that the MetUM is producing realistic simulations of both Haiyan and Hagupit. Further comparisons between TC structure and observations are not made as the aim of this work is to consider the predictability of TC motion, and the influence of the larger scale steering flow, not to diagnose errors in the storm structure.

4.6   Summary and Conclusion

This chapter introduces Typhoons Haiyan and Hagupit, gives a synoptic overview of each storm, presents the track and intensity forecasts from global and CP ensembles, and briefly discusses the structure of the storms in comparisons between model output and observations.

There are a number of similarities between Haiyan and Hagupit. Both storms were category-5 TCs, both made landfall over the Philippines having followed similar paths, and both were high-impact TCs. Each storm was initially steered by the sub-tropical anticyclone. Haiyan was steered by the anticyclone up until landfall.
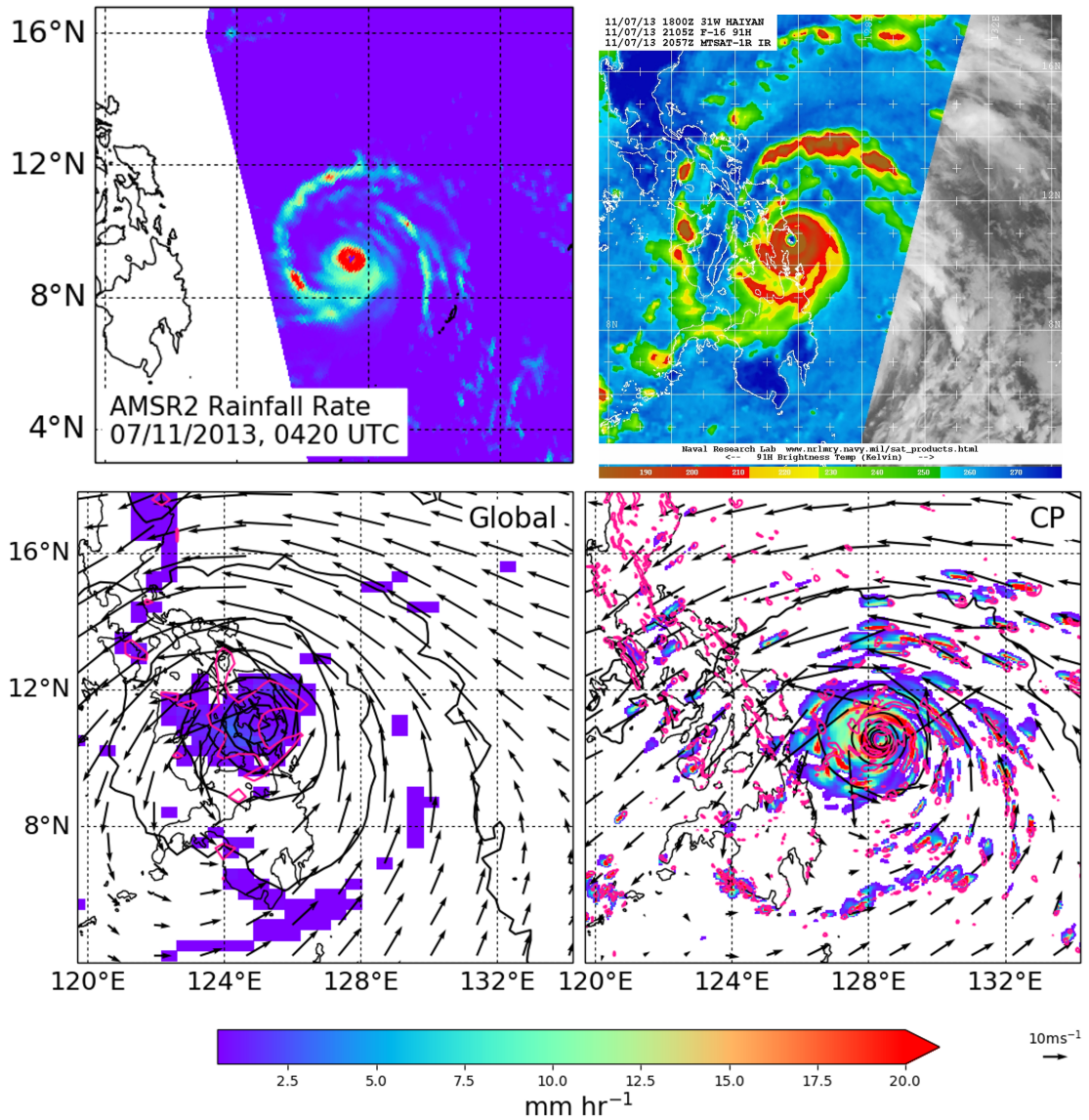
Figure 4.13: As in Figure 4.12 but for Haiyan. The rainfall estimate in the top left is from the AMSR2 sensor taken at 0420 UTC 7 November 2013. The microwave image on the top right is at 2057 UTC 7 November 2013. The MetUM rainfall forecasts are at 2100 UTC 7 November, using the forecasts initialised at 1200 UTC 4 November. The satellite image in the top right is taken from the National Research Laboratory, Marine Meteorology Division.

However, Hagupit became positioned between two anticyclones, one to the east and one to the west of the storm. Upon entering this position the storm slowed significantly. Chapters 5 and 6 will investigate this position in Hagupit's lifetime in more detail.

The track forecasts are a key motivation in studying these storms further. Ensemble forecasts of Haiyan predicted the storm's motion with a large degree of certainty. An error in timing in the CP forecasts meant that they induced a large positional error, however the path of the storm was still well predicted. The global model predicted both the location and the speed of Haiyan accurately. On the other hand, the global forecasts of Hagupit were associated with a large amount of uncertainty. At the same time that the motion of Hagupit slowed, global track forecasts diverged. Some ensemble members predicted the storm to turn north, completely missing the Philippines, whilst others predicted the TC to continue west and move across the Philippines. This behaviour was the same in forecasts initialised at 0000 UTC 5 December, just 18 hours before landfall. Comparing the environments of the two storms it seems likely that the position of Haiyan and Hagupit with respect to the anticyclone steering the TCs is key in the predictability of both storms.

Section 4.5 compared the structure of the storms to some satellite imagery. The MetUM forecasts were able to identify some of the structural features in Haiyan and Hagupit which were present in the satellites. These included realistic estimates of rainfall and the locations, relative to the TC centre, where there was increased rainfall. As expected, the CP forecasts demonstrated these structural features in finer detail. The comparisons were used as a 'sanity check' to demonstrate that the MetUM was producing realistic simulations of both Haiyan and Hagupit.

Throughout the chapter comparisons have been made between the CP and global forecasts. This has brought up a number of questions, for instance: Why do the CP forecasts behave differently to the global forecasts? What causes the systematic turn to the south-west in the CP forecasts of Hagupit? What causes the unpredictability in the global forecasts of Hagupit compared to those of Haiyan? Chapter 5 addresses the latter question and focuses on the global ensemble forecasts. Chapter 6 and

Chapter 7 focus on understanding the CP forecasts.

Chapter 5

Interaction of Hagupit and Haiyan with their environments

5.1 Introduction

Despite the substantial improvements in TC track errors in general, there are still TCs such as Hagupit for which the track is difficult to predict. Each season there are examples of storms which are associated with large track errors and large uncertainties in the ensembles (Magnusson et al., 2019). Case studies are often conducted to understand the sources of errors and uncertainties and to allow for better preparedness for future cases. Two storms which have been the subject of numerous case studies are Hurricane Sandy (2012) and Hurricane Joaquin (2015).

Hurricane Sandy exhibited large uncertainty in track forecasts prior to making landfall over the U.S. (Magnusson et al., 2014). The uncertainties were attributed to uncertainty in the steering flow of the TC (Munsell and Zhang, 2014) and differences in the amplitude of the anticyclone to the north of the storm (Torn et al., 2015). Torn et al. (2015) also demonstrated that Sandy contributed to the amplification of the ridge to the north through the storm's irrotational outflow. Additionally, differences in SSTs between ensemble members caused differences in the depth of Sandy but these differences did not impact the track forecasts (Magnusson et al., 2014).

Hurricane Joaquin produced a very unusual TC track. Initially the storm moved south-westwards towards the Bahamas before making a 180° turn and moving back out to sea. Track forecasts failed to predict the unusual looping track of Joaquin, and many operational forecasts were predicting the TC to make landfall over the U.S. east coast. Nystrom et al. (2018) used perturbations of the TC structure and steering flow in CP forecasts to demonstrate that the TC was sensitive to steering winds between 600-900 km from the centre. The impact of these different steering winds influenced which side of a bifurcation point in the steering the TC would move to. Using the National Centers for Environmental Prediction Global Forecast System, Miller and Zhang (2019) highlighted the impact of a shallow vortex in some ensemble members causing the TC not to interact with the steering flow at upper-levels. On the other hand, Alaka Jr et al. (2019) found the structure of Joaquin did not impact the TC track in the Hurricane Weather Research and Forecasting Model but rather the motion of Jaoquin was sensitive to differences in the steering flow of ensemble members, which originated from the initial perturbations. These contradicting conclusions highlight the importance of understanding difficult-to-predict TCs.

Using ensemble-based sensitivity analysis, Torn et al. (2018) showed that the forecast spreads of three TCs [Joaquin, Debby (2012) and Lionrock (2016)] were all associated with variability in the near-storm steering flow - in particular the steering flow within 500 km of the TC centre. Each of these TCs was characterised by being in a large-scale deformation flow. This steering flow can be responsible for determining which side of the axis of contraction the TC will move to and thus the future position of the storm. In reviewing available diagnostic tools for difficult to predict TCs, Magnusson et al. (2019) highlighted ensemble sensitivity analysis as particularly useful. Unlike other methods, ensemble sensitivity analysis, which uses linear regression to imply the impact of a state variable on a forecast metric, can be used on an existing ensemble without the need to rerun forecasts.

From each of the studies described above, along with other case studies of difficult to predict storms (e.g. Huang et al., 2020), it is obvious the steering flow of a TC plays a big role in the predictability of its track. A TC's interaction with its environment

is two-way, meaning that whilst the environment steers the storm, the TC can also impact the development of synoptic scale environmental features. One key interaction is when the outflow of a TC interacts with the midlatitude flow (Jones et al., 2003; Keller et al., 2019). These interactions are often investigated within a PV framework. Anticyclonic outflow from the TC enhances the downstream trough amplification through the advection of cyclonic PV and the implication of an enhanced anticyclonic component in the region of the downstream trough (Riemer and Jones, 2010; Keller et al., 2019). Meanwhile divergent outflow from the TC, associated with the latent heat release in the mid troposphere, contributes to ridge building and jet streak formation through the advection of low PV air which distorts the upper level PV field (Riemer and Jones, 2010; Grams et al., 2013; Keller et al., 2019). In the case where the TC is in a sensitive region of steering flow, these interactions can impact the storm's environment enough to change its track (Grams et al., 2013).

In this chapter the causes of the uncertainty in the global track forecasts of Hagupit are explored and compared to the more predictable case of Haiyan. In Section 5.2 the large-scale flow in which Haiyan and Hagupit are embedded is compared. In Section 5.3 the TC removal technique, outlined in Section 3.5.2, is utilised to investigate the steering flows of each of the TCs. Using this steering flow, Section 5.4 explores the sensitivity of Hagupit's position earlier in the forecast to its future track. Section 5.5 looks in more detail at the environment of Hagupit. Using composite groups of ensemble members, differences in the storms environments between members which move to the west and make landfall and members which turn to the north are highlighted. The contribution of the TC's outflow in regulating its environment is also investigated. Section 5.6 uses the 45-member ensemble and ensemble sensitivity analysis to add robustness to the results from previous sections. Ensemble sensitivity analysis uses linear regression to relate features of Hagupit's environment earlier in the forecast to the motion of the storm in the final 24 hours. A discussion and conclusion is given in Section 5.7.

5.2 The Environments of Haiyan and Hagupit

In Chapter 4 the environments of Haiyan and Hagupit were identified as possible causes for the differences in track predictability (Figure 4.4). In this section the large-scale environments of Haiyan and Hagupit in the global forecasts are investigated and compared to Figure 4.4.

Figure 5.1 shows the ensemble averaged streamlines for the 850-250 hPa pressure-weighted depth-averaged flow, for both Haiyan and Hagupit at two different times - the same times as shown in Figures 4.3 and 4.4. This depth represents a typical steering flow layer for intense TCs (Velden and Leslie, 1991; Wang and Holland, 1996). At 1200 UTC 5 November Haiyan is on the southern periphery of the sub-tropical anticyclone. The anticyclonic flow associated with the anticyclone creates an easterly flow which steers Haiyan towards the Philippines. The anticyclone is elongated throughout the whole of the western North Pacific basin and the storm is located on the southern periphery of the anticyclone throughout the forecasts (Figure 5.1b).

At 0000 UTC 4 December (Figure 5.1c) Hagupit is located to the south-west of the sub-tropical anticyclone. As such the motion of the storm is in a north-west direction. By 1800 UTC 5 December (Figure 5.1d) Hagupit has moved into a position between two anticyclones, one to the east and one west, with the subtropical jet to the north. The two anticyclones are separated by both the storm and an upper level trough, whose axis is in line with the storm. This synoptic set up shows a sensitive position in the environment with the anticyclone to the east steering the storm to the north towards the subtropical jet and the anticyclone to the west steering the storm south and across the Philippines. Upon reaching this position the storm's speed slows; over the next 36 hours the storm moves slowly, at approximately $2\,\mathrm{m\,s^{-1}}$, in a westwards direction up until it makes landfall.

The shading in Figure 5.1 shows the standard deviation of depth-averaged windspeeds in the ensemble. The magnitude of the standard deviation in the environment in each storm is similar, despite the differences in track forecasts. For Haiyan the regions

of greatest variance are close to the TC and on the periphery of the subtropical anticyclone (Figure 5.1a and 5.1b). For Hagupit, Figure 5.1c shows that, earlier on, there is some variance close to the storm along with variance to the east of the sub tropical anticyclone (approximately 25°N and 175°E). When the TC becomes positioned between the two anticyclones (Figure 5.1d), the largest variance is in the region of the storm, in the location of the PV streamer (approximately 20°N and 175°E) and to the south of the storm (approximately 5°N and 130°E). There is little variance on the sides of the anticyclones which are closest to the TC.

The mean 850-200 hPa flow is well represented in the forecasts for each storm. When compared to the ERA-5 reanalysis (Figure 4.4), the main differences occur as Hagupit makes landfall. In the MetUM the storm moves too slowly prior to landfall, meaning that the ensemble members that predict the storm to hit the Philippines do so slightly too late. During landfall there are also some differences in the development of the downstream ridge (located to the north-east of Hagupit), with each ensemble member having a stronger downstream ridge than ERA-5 in the final 24 hours of the forecasts. Other than these differences the ERA-5 analysis lies within the ensemble spread of throughout the forecasts.

5.3 Analysis of the Steering Flow

The large track spread of Hagupit suggests that the steering flow of the storm may be important in determining its predictability. The steering flow of a TC is the environmental flow which best matches the storm's movement. To investigate the steering flow of a storm, it is necessary to partition the winds associated with the storm from those of the environment which are responsible for the steering of the storm. This is done using the TC removal method described in section 3.5.2. Due to the associated computational costs, the TC removal technique was carried out on a single 12-member ensemble forecast for each storm. The forecasts used were initialised at 1200 UTC 4 November 2013 for Haiyan and 1200 UTC 3 December 2014 for Hagupit. Figure 5.2 shows, for both Haiyan and Hagupit, a contour plot of the residual vector magnitude for different pressure levels and radii. This plot is created

Figure 5.1: Streamlines of the pressure-weighted vertically averaged wind between 850 hPa and 250 hPa. All streamlines are of the global MetUM ensemble mean (using time-lagged ensembles initialised at 1200 UTC 4 November and 0000 UTC 5 November for Haiyan, and 1200 UTC 3 December and 0000 UTC 4 December for Hagupit). The shading shows the ensemble standard deviation of the depth-averaged wind speeds. Centres of anticyclones are denoted by a 'H', centres of cyclones with an 'L', the position of the storm is shown with a TC symbol. The black arrows are for illustrative purposes to indicate the direction of flow. Figures (a) and (b) are for Haiyan at times 0000 UTC 5 November and 1200 UTC 7 November. Figures (c) and (d) are of Hagupit at times 1800 UTC 3 December and 0000 UTC 6 December.

using every ensemble member at every 3-hourly output time. The figures produced are very similar to previous studies using the same technique (Galarneau and Davis, 2013; Fowler and Galarneau, 2017; Torn et al., 2018), with the optimum radius on average being approximately 300-400 km, and the optimal top layer of 300 hPa for Hagupit and 200 hPa for Haiyan. Figure 5.2 suggests optimum height for Haiyan may be higher than 200 hPa, however, a top layer of 200 hPa still produced a small average residual vector when compared to the speed of the storm.

Averaged across all times and ensemble members, the magnitude of the residual vector when using an optimum radius as a function of time as opposed to a constant radius is approximately $0.6 \, \mathrm{m \, s^{-1}}$. This residual is significantly less than the average
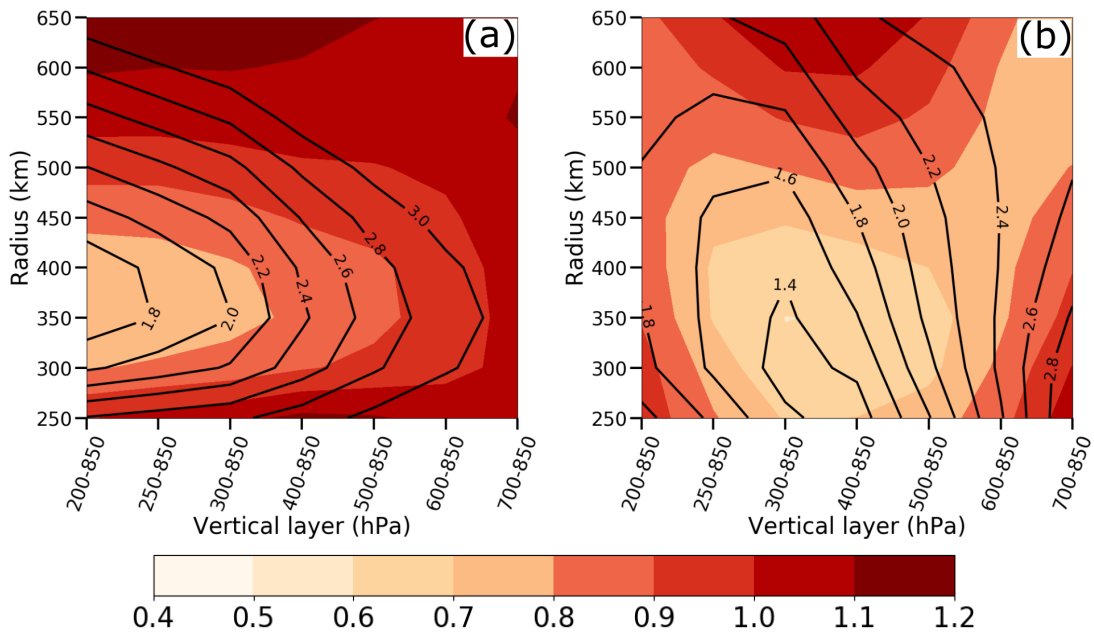
Figure 5.2: The average magnitude of the residual vector, $\mathbf{V}_{res}$, defined as absolute difference between the storm motion vector and storm-removed environmental wind vector (contours, $\mathrm{m\,s}^{-1}$) as a function of vertical layer and removal radius, r_0. The shading denotes the standard deviation across all times and ensemble members. The two plots are of (a) Haiyan ensemble forecasts initialised at 1200 UTC 4 November 2013 and (b) Hagupit ensemble forecasts initialised at 1200 UTC 3 December 2014. The averages are computed across all 120 hours of the forecast.

minimum residual of slightly under $1.0\,\mathrm{m\,s}^{-1}$, produced when using a constant radius (over a 5-day forecast this difference in error would equate to approximately $175\,\mathrm{km}$). Therefore, the analysis in this section uses a radius which has been optimised at every time step.

Figure 5.3 shows the ensemble averaged streamlines for the 850-250 hPa pressure-weighted depth-averaged storm removed winds, for both Haiyan and Hagupit at two different times. In the case of Haiyan the streamlines show the storm is embedded in the easterly flow which is associated with the anticyclone to the north (Figure 5.3a). This flow strengthens as the forecast continues and Haiyan approaches the Philippines (Figure 5.3b). In comparison Figure 5.3c shows Hagupit is located to the south-west of the subtropical anticyclone. As such the motion of the storm is in a north-west direction. By 1800 UTC 5 December (Figure 5.3d) Hagupit has moved into a position of weak steering flow between two anticyclones. To the west of the storm the anticyclone steers the storm towards the Philippines, whilst to the east of the storm the anticyclone creates a northward steering flow.
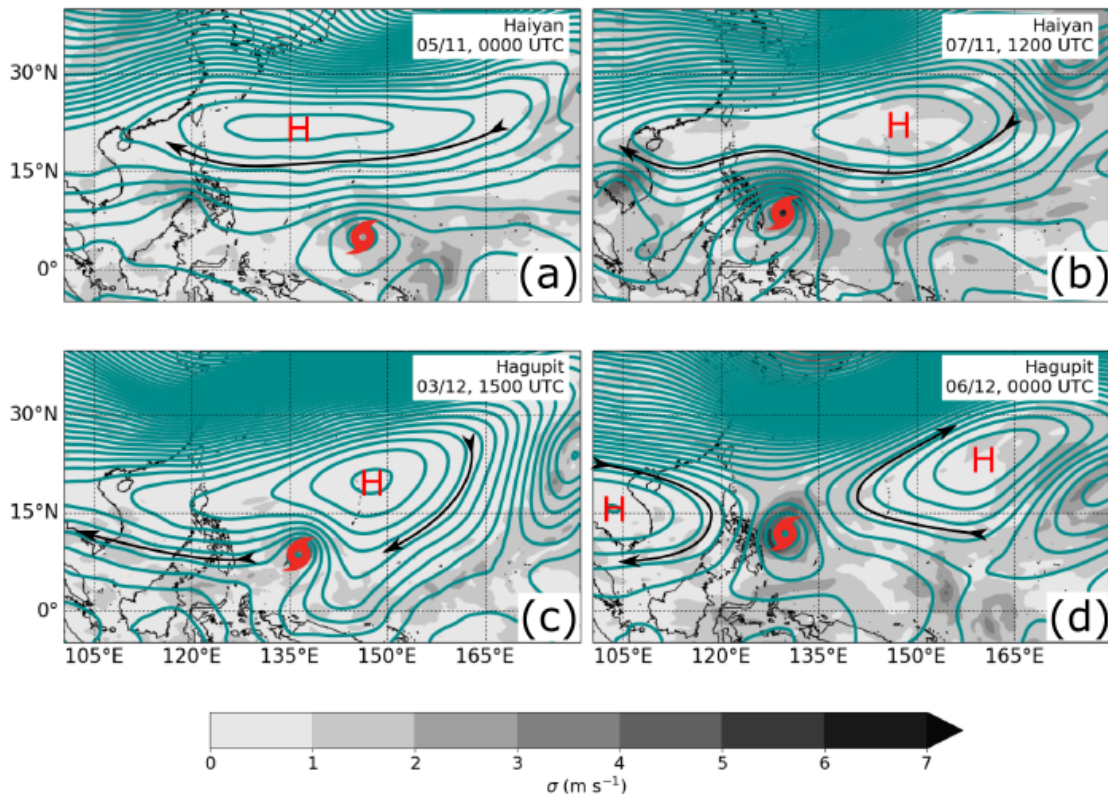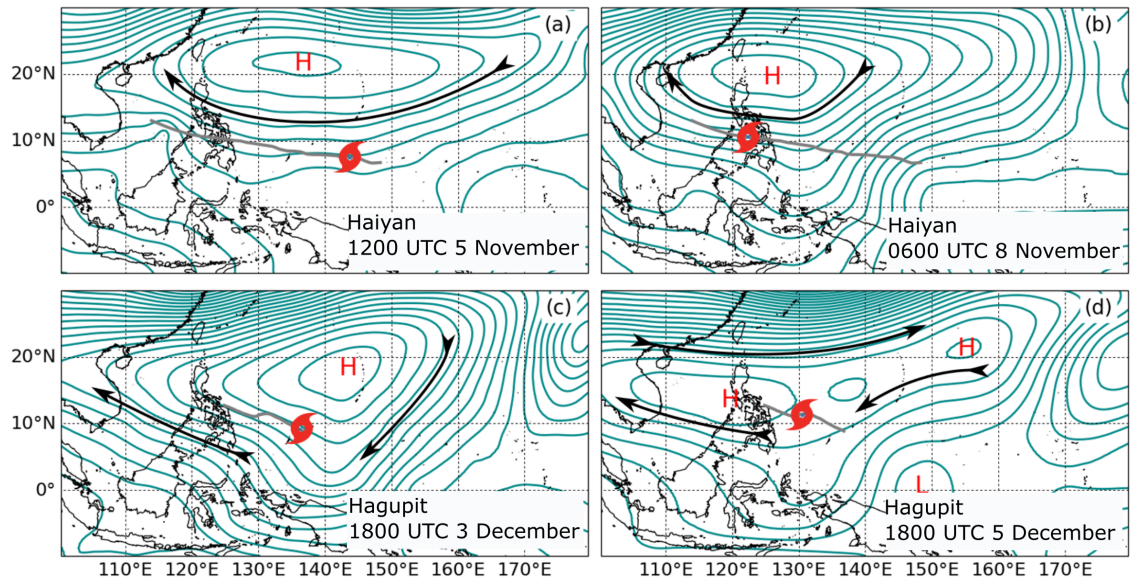
Figure 5.3: Streamlines of the pressure-weighted vertically averaged storm-removed wind between 850 hPa and 250 hPa. All streamlines are of the MetUM ensemble mean (using the ensemble initialised at 1200 UTC 4 November for Haiyan, and 1200 UTC 3 December for Hagupit), with the grey line indicating the ensemble average track. Centres of anticyclones are denoted by a 'H', centres of cyclones with an 'L', the position of the storm is shown with a TC symbol. The black arrows are for illustrative purposes to indicate the direction of flow. Figures (a) and (b) are for Haiyan at times 1200 UTC 5 November and 0600 UTC 8 November. Figures (c) and (d) are of Hagupit at times 1800 UTC 3 December and 1800 UTC 5 December.

5.4 Storm Sensitivity to Initial Position

To investigate the sensitivity of the storm's location to its predicted track, trajectories are initialised at T+24 in a $1.6° \times 1.6°$ box around the centre of the forecasted storm. The box dimensions were chosen such that the maximum displacement between the initial location of a trajectory and the forecasted position of the storm, at T+24, was slightly larger than the average error of NWP models T+24 TC track forecasts (approximately 75 km, Short and Petch, 2018). This means that trajectories starting in the box represent what would be considered to be within the bounds of a normal track error. Trajectories are calculated up to T+120 with a Runge-Kutta 4th order scheme using the 3-hourly storm-removed environmental winds.

Figure 5.4 shows the trajectories computed for ensemble member 6 of Hagupit. Ensemble member 6 was chosen as its track was similar to the ensemble average and it predicted Hagupit would make landfall close to the observed location. The trajectories exhibit a similar behaviour to the original ensemble (Figure 4.7b). The
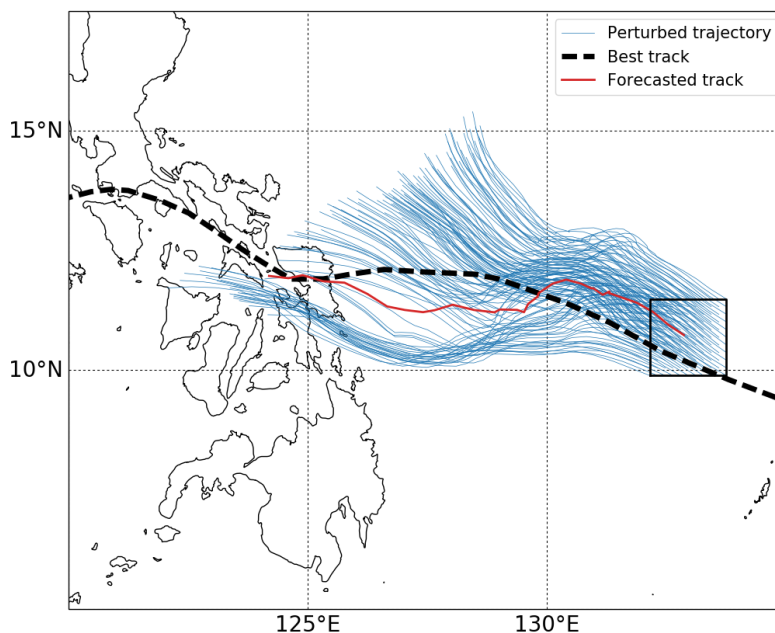
Figure 5.4: Trajectories (blue lines) calculated using the storm-removed environmental winds of ensemble member 6 of the forecast for Hagupit initialised at 1200 UTC 3 December 2014. The trajectories are initialised at 1200 UTC 4 December (T+24) in a $1.6° \times 1.6°$ box (indicated by the black box) around the forecasted position of the storm. The forecasted track is shown by the red line, whilst the black dashed line is the best track according to IBTrACS.

trajectories show that had the storm been located in a slightly different position at T+24 it may have recurved and missed the Philippines, or alternatively it may have propagated too far south. This highlights that in a single ensemble member the track of the storm is sensitive to its position earlier in the forecast. It could be expected that, if the environment in each of the global ensemble members was the same as that in ensemble member 6, then small differences in the position of the storm in different ensemble members could lead to a large track spread. Note, this analysis is an approximation as it ignores any feedbacks of the TC on the environment.

Trajectories were computed using the storm-removed environmental winds for each of the 12 ensemble members for both storms. As with the original ensemble of tracks, the spread of the trajectories is calculated using Equation 4.1. The ensemble average of these trajectory spreads is shown in Figure 5.5. In calculating the ensemble average of trajectory spreads for Hagupit, ensemble members 5 and 10 were omitted. These ensemble members were the most southerly and northerly ensemble members, respectively, and their perturbed trajectories remained very close to the forecasted
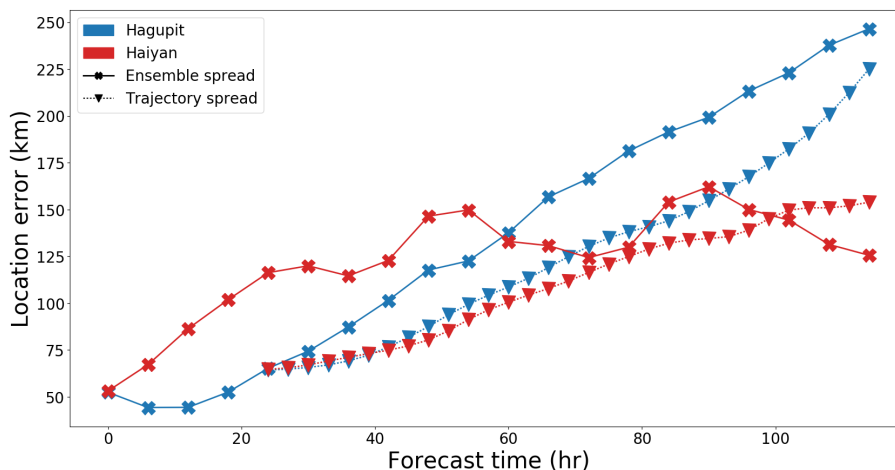
Figure 5.5: Spread comparison of the global ensembles for Typhoons Haiyan (red) and Hagupit (blue) initialised at 12000 UTC 4 November 2013 and 1200 UTC 3 December 2014, respectively. The ensemble spread is shown by the solid lines and crosses whilst the spread of trajectories initialised at T+24 and calculated using the storm-removed environmental winds are shown by the dotted line and triangles.

position of the storm. Thus the spread in these two cases was very small. The spread of the trajectories for Hagupit is very similar to the spread of the 12-member ensemble forecast, further illustrating that the uncertainty in the forecasts of Hagupit is caused by the environment in which the storm is embedded.

Unlike those of Hagupit, the storm removed trajectories for ensemble member 1 of Haiyan show a much more predictable environment (Figure 5.6). Trajectories remain close to the forecasted track (and indeed, the best track) and move westwards directly towards the Philippines. Thus even if there was a small positional error at T+24, this error would not develop into a large error and the storm location would still be predicted with a high degree of certainty. As with Hagupit, the ensemble average of trajectory spreads is plotted in Figure 5.5. Unlike the ensemble track spread, the trajectory spread does increase with lead time. However at T+120 the spread is approximately 50% of the trajectory spread of Hagupit, and only slightly higher than the global track spread of Haiyan. Therefore, the same uncertainty that was seen in Hagupit is not seen in the environment of Haiyan.

Whilst not a perfect technique (it does not account for different environmental winds in the ensemble members), this method provides a computationally cheap way to illustrate the uncertainty in a deterministic forecast of a TC. It has the potential
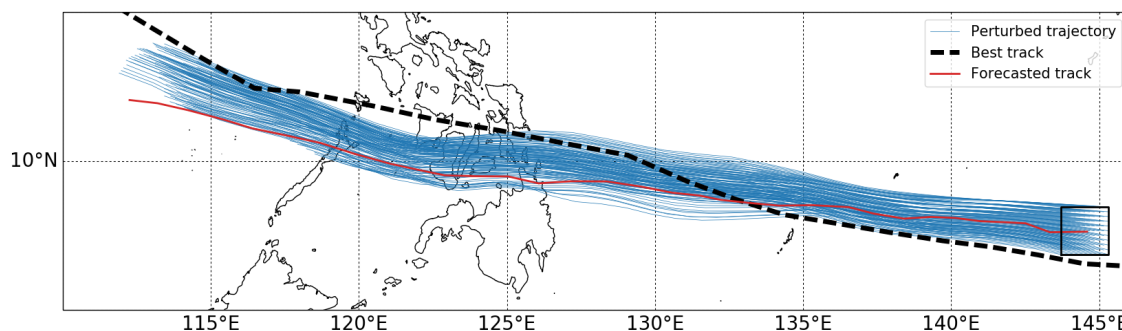
Figure 5.6: Same as Figure 5.4 but for ensemble member 1 of Haiyan with trajectories initialised at 1200 UTC 5 November (T+24).

to be used operationally to determine how uncertain a TC forecast is likely to be without the need for a full ensemble.

5.5 Impact of the Storms' Environment on the Steering Flow

The remainder of this chapter focuses on the forecasts of Hagupit to further understand the reasons for the low predictability of the storm. This section investigates how Hagupit interacts with its environment and how subtle differences in the environment of different ensemble members are related to differences in the track forecasts. This section uses two forecasts that are time-lagged to create a 24-member ensemble. Forecasts initialised at 1200 UTC 3 December and 0000 UTC 4 December 2014 are used. These forecasts show similar characteristics with some ensemble members turning north and others making landfall over the Philippines. They are initialised approximately 81 and 69 hours before the storm made landfall. Ensemble members are split into two groups depending on whether the forecasted storm turns to the north (NORTH members) or makes landfall (WEST members). These two groups, based on the time-lagged ensemble, are shown in Figure 5.7. Each group consists of 8 members, four from the earlier forecast initialised at 1200 UTC 3 December, and four from the later forecast initialised at 0000 UTC 4 December. The remaining ensemble members were omitted for various reasons (shown in green in Figure 5.7). Two ensemble members in the later forecast went considerably further south than other members and one in the earlier forecast turned considerably further north.
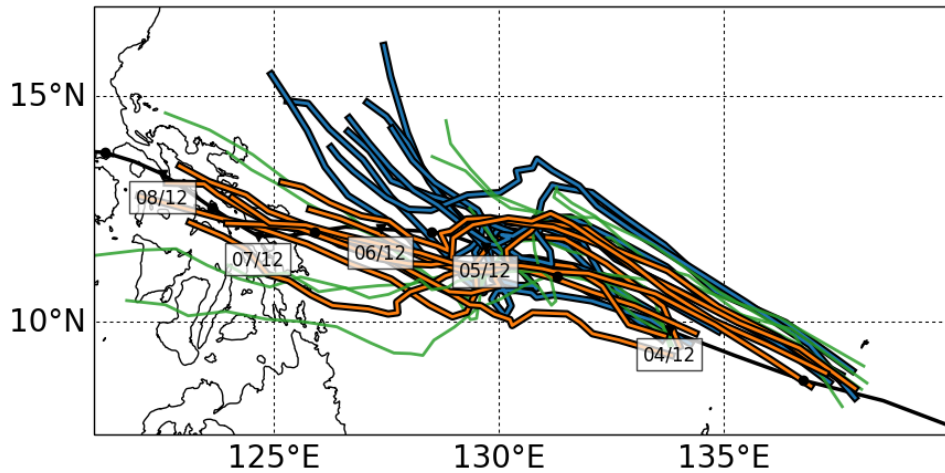
Figure 5.7: Track forecasts for Hagupit split into two groups depending on if the storm is forecast to make landfall close to the correct location ("WEST", orange) if it is forecast to turn to the north ("NORTH", blue), or if the ensemble member is omitted from both groups (green). Two 12-member forecasts, initialised at 1200 UTC 3 December and 0000 UTC 4 December are time-lagged.

These extreme members were omitted to ensure they did not skew the group averages. Other members were omitted to ensure equal size groups, they were chosen as ensemble members which were borderline between two groups (i.e. members which made landfall over north Philippines).

Figure 5.8 shows the depth-averaged and ensemble-averaged steering flow for both the WEST group and the NORTH group at 0000 UTC 7 December. The steering flow has been calculated using a constant removal radius (r_0) of 350 km to allow for a comparison between the ensemble members. To calculate the average steering flow, the steering flow for each ensemble member in the WEST and NORTH groups is centred on the average forecasted location of the storm in that group, following this the steering winds are averaged across all ensemble members. The solid red circle in Figure 5.8 is the removal radius whilst the dashed circle shows the position of the removal radius of the other group. Comparing the two groups shows there is a distinct difference in the steering flow. The NORTH group has a stronger northward component to the steering flow compared to the WEST group which is being steered towards the Philippines. In both cases there is a deformation field with very weak steering flow to the north-west of the storm. Compared to the NORTH group, the WEST group has an average position further to the south-west and thus is embedded
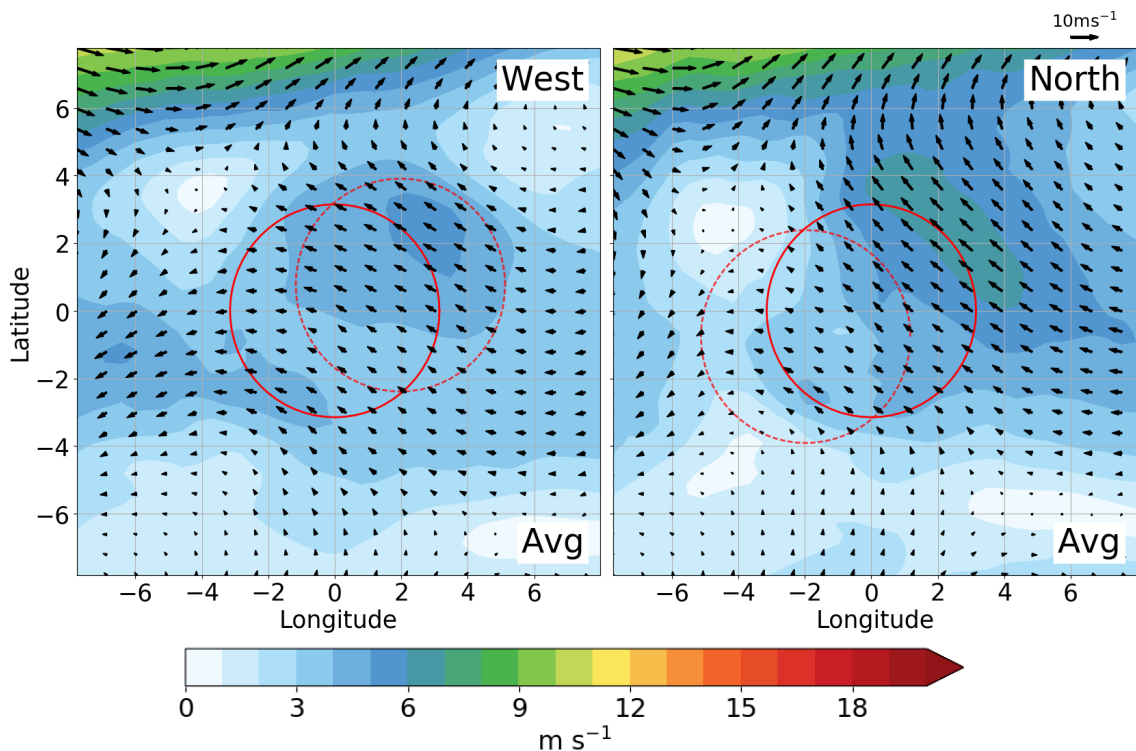
Figure 5.8: Average 850-200 hPa steering flow of the WEST and NORTH groups (shown in Figure 5.7) at 1200 UTC 7 December. Solid red circle shows the removal radius of 350 km and is centred on the position of the group, whilst the dashed red circle is the relative position of the other group. Arrows are the winds and the shading is the wind speed ($m s^{-1}$).

in a stronger easterly flow.

Whilst the depth-averaged steering flow accurately matches the motion of the ensemble members, it does not highlight what levels of the atmosphere are most important in steering Hagupit. Figure 5.9 splits the depth-averaged steering flow into different levels. The biggest influence to the depth-averaged steering flow occurs at the upper levels. At 850 hPa the steering flow in both the WEST and NORTH groups is very similar and weak. At 500 hPa there are differences in the direction of the environmental winds, however the windspeeds are still relatively weak. At 300 hPa there is a much larger contribution to the average steering as well as a stronger southerly flow in the NORTH group. Thus, it can be concluded that the main contribution to the differences in steering winds between the two groups is due to the upper level winds.

The differences in the upper level steering between the two groups suggest there are differences in the upper level environments. Figure 5.10 shows the differences
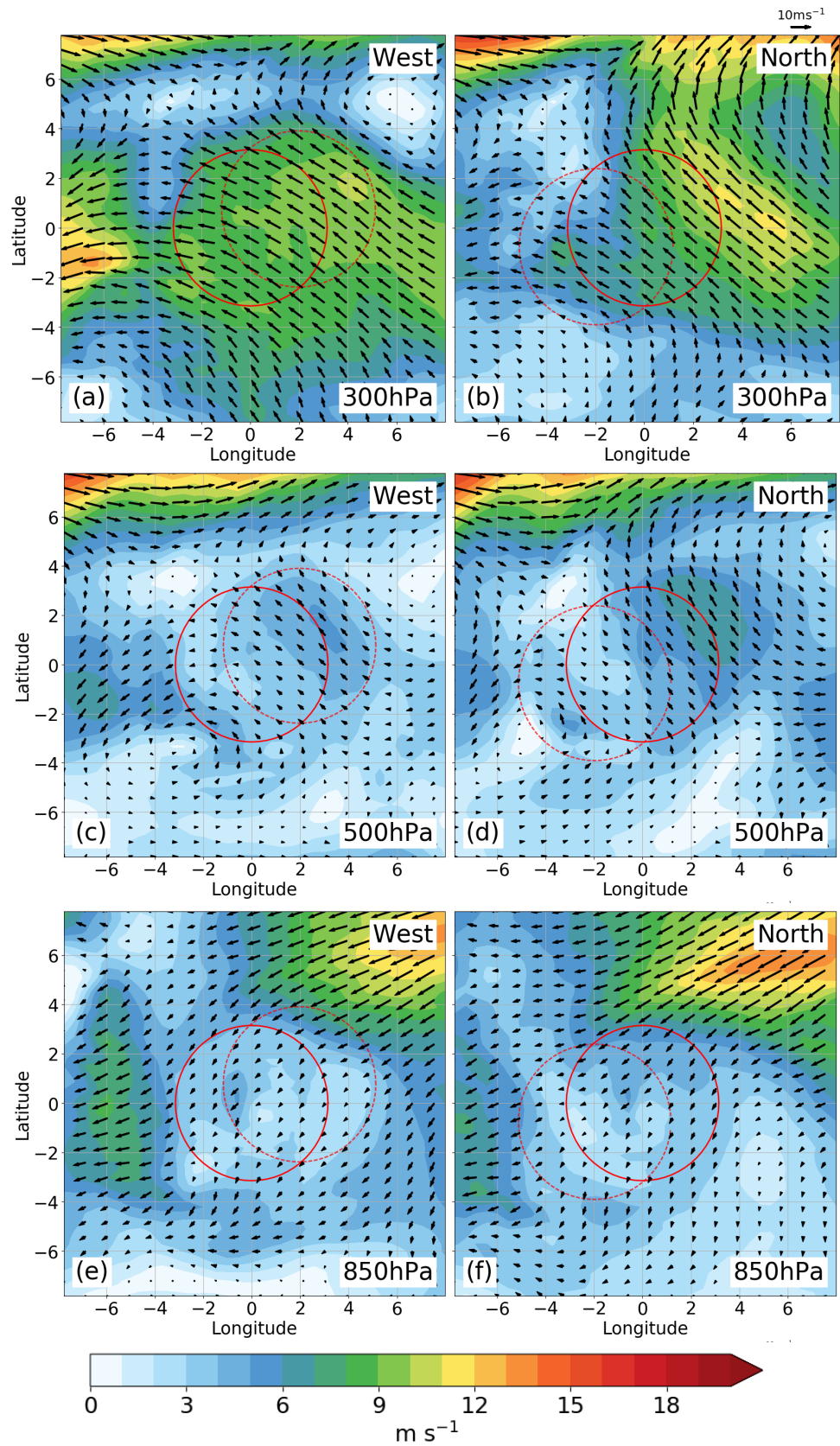
Figure 5.9: Same as Figure 5.8 but at a pressure level of 300 hPa (a-b), 500 hPa (c-d) and 850 hPa (e-f).
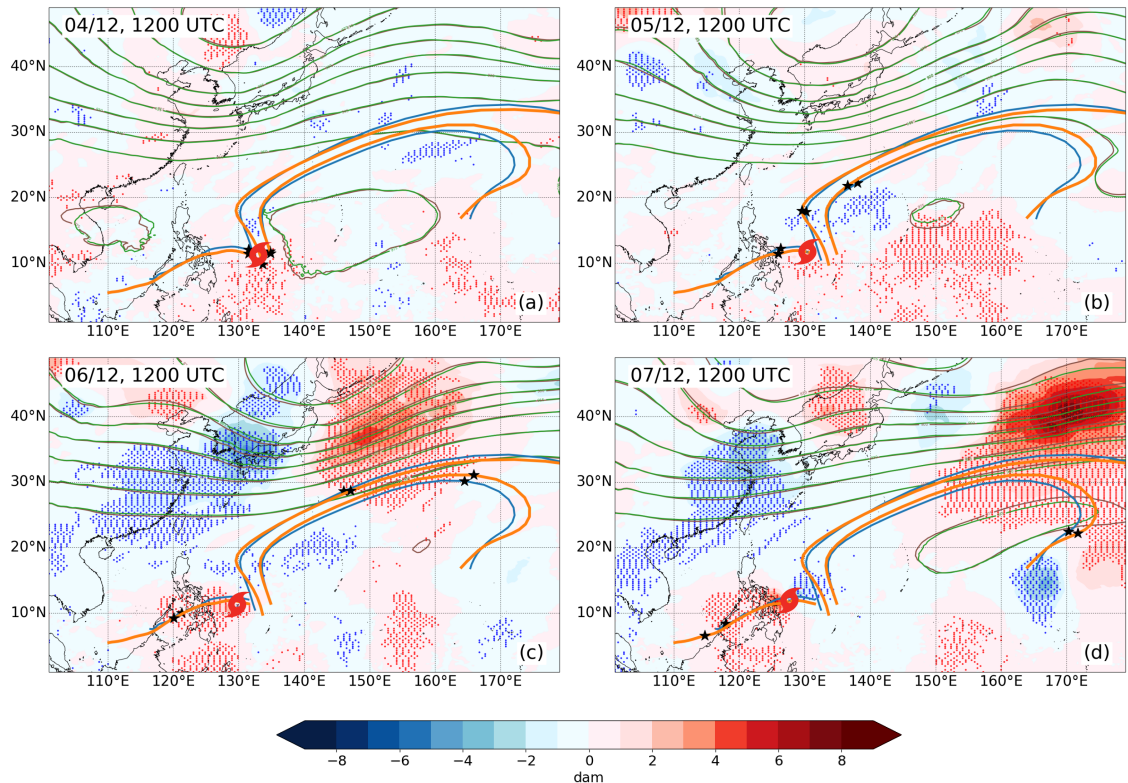
Figure 5.10: Geopotential height differences (dam) at 300 hPa between NORTH and WEST groups (NORTH−WEST). Contours are the average geopotential heights at 300 hPa for NORTH (brown) and WEST (green) groups. Stippled regions signify that the differences are statistically significant at the 95% confidence level. The blue (NORTH) and orange (WEST) lines are average trajectories of the TC outflow calculated from trajectories which are initialised over a $2.5° \times 2.5°$ box centred on the location of the storm at 1200 UTC 4 December. The trajectories are calculated using the wind fields at 300 hPa. During averaging they are split into three groups depending on if they head west, north towards the downstream ridge or become wrapped in the upper-level anticyclone. The stars indicate the position of the trajectory at the particular time shown in the plot. The TC symbol is the time-lagged ensemble mean TC position at the time shown in the plot. The times shown are (a) 1200 UTC 4 December, (b) 1200 UTC 5 December, (c) 1200 UTC 6 December and (d) 1200 UTC 7 December.

between the average 300 hPa geopotential heights of the NORTH and WEST groups. Statistical significance, shown by the stippled regions, is determined using a bootstrap resampling method. Two groups of ensemble members of equal size to those of the WEST and NORTH groups are chosen at random without replacement. The difference between these two groups is calculated. This process is repeated 300 times. A 95% confidence interval is then calculated from the 300 samples for the difference between the two groups. Regions where the difference between the NORTH and WEST groups are outside of this confidence interval are statistically significant.

Prior to 1200 UTC 5 December only small and subtle differences are seen between the two groups. In particular the NORTH members are associated with a slightly stronger upper-level anticyclone to the east of the storm (Figures 5.10a and 5.10b). Although the differences are only small they become statistically significant by 1200 UTC 5 December. By 1200 UTC 6 December more significant differences begin to develop between the two groups. The NORTH members are associated with stronger downstream ridge building (Figure 5.10c, approximately 35° N and 150° E) which ultimately leads to differences in the position of the detached PV streamer shown in Figure 4.3d, and shown here by the differences in geopotential height (Figure 5.10d, 15°N and 165°E). The PV streamer in the NORTH members has propagated further to the west than in the WEST members, also impacting the southern periphery of the anticyclone. Finally a dipole can be seen close to the location of the storm in Figure 5.10d, approximately (12°N,128°E). This indicates that by 1200 UTC 7 December there are statistically significant differences in the location of the storm in each of the groups, with the WEST members already further to the west at this point.

The trajectories in Figure 5.10 represent the outflow of the storm. They are calculated on a single pressure level using the winds at 300 hPa (i.e. they do not account for vertical motion) from the location of the storm at 1200 UTC 4 December, the time when the motion of the storm slows. In each ensemble member trajectories are initialised 0.25° apart in a 2.5° × 2.5° box centred on the group average location of the storm. Therefore, from the 8 members of each group 968 trajectories are calculated. These trajectories are then split into three groups depending on whether they go to the west, interact with the downstream ridge or interact with the upper-level anticyclone (Figure 5.11). Each group consists of approximately 33 % of the trajectories. A small number of trajectories are omitted from the averaging if they do not fulfil any of the criteria, which occurs when the trajectories become wrapped in the storm's circulation. Once split into the groups the trajectories are averaged to form one trajectory per group. The criteria for splitting the trajectories and averaging over each group is somewhat arbitrary, however, the three resulting average
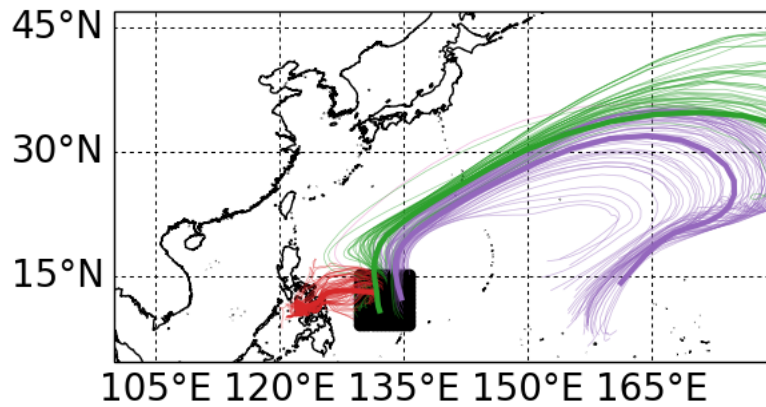
Figure 5.11: Example of how the trajectories in Figure 5.10 are calculated. The different colours show the three different groups whilst the thick line is the average trajectory which has been calculated from the thinner trajectories. The black box is made up of small black dots at each of the trajectory initialisation locations.

trajectories for each group demonstrate the general paths of the TC outflow. Whilst the trajectories shown are initialised at 1200 UTC 4 December and are calculated at 300 hPa, a number of other initial times and heights were used to explore the outflow channels of Hagupit. It was found that the outflow of Hagupit to the north-east remained stationary during the three days prior to landfall when the motion of Hagupit had stalled, and was always present at heights above 400 hPa. The fact that the outflow pattern was similar at all heights above 400 hPa suggests that outflow of the TC is well captured by these trajectories despite them not including vertical motion.

The outflow from both the NORTH and WEST groups interacts with the upper level trough and the downstream ridge (Figure 5.10). Figure 5.10d shows that in both groups the position of the trajectories by 1200 UTC 7 December is close to the location of the PV streamer (located at approximately 15°N and 165°E). This suggests that the anticyclonic outflow of Hagupit helps promote the Rossby wavebreaking event by increasing the anticylonic wind component in the downstream trough. This is similar to other observed processes often seen in TCs which undergo extratropical transition (e.g. Riemer and Jones, 2010; Keller et al., 2019). Associated with the outflow channel shown by the trajectories is Figure 5.10 is strong upper level irrotational flow from the storm (Figure 5.12). Although no significant differences were found between the NORTH and WEST groups, this irrotational outflow plays
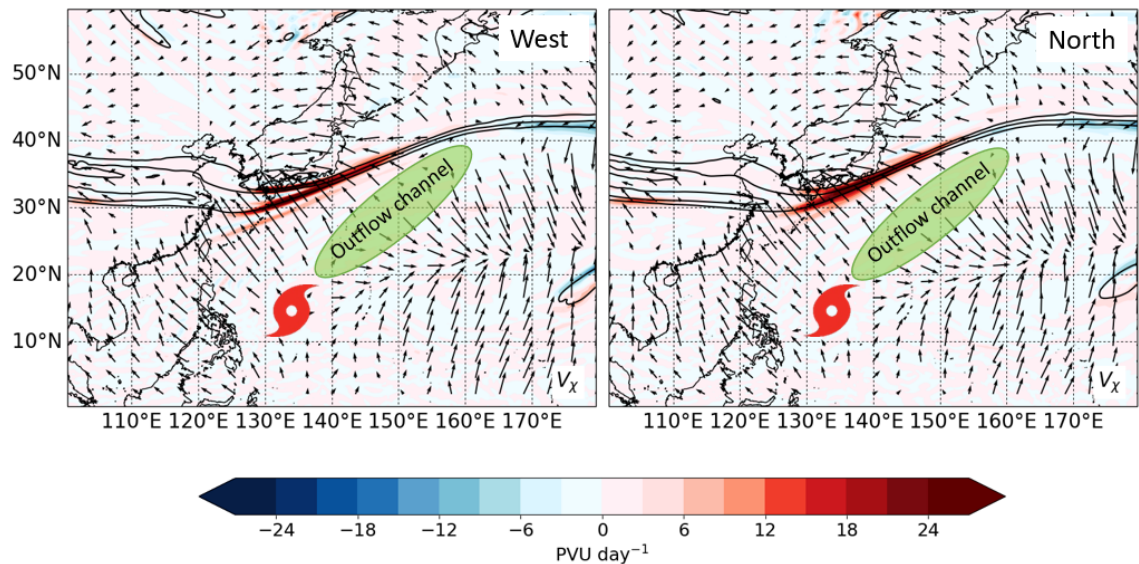
Figure 5.12: Anticyclonic PV advection by irrotational winds at 250 hPa (shading) for the WEST and NORTH groups at 1200 UTC 6 December. Arrows are the irrotational winds greater than $2\,\mathrm{m\,s}^{-1}$, PV at 250 hPa is contoured at 2, 4 and 6 PVU. The TC symbol is the average location of the storm and the green oval is the approximate location of the outflow channel.

a crucial role in regulating the environment. The upper level trough is located at the boundary between low upper-level PV to the south and high upper-level PV to the north, whilst the jet is associated with the PV gradient at this boundary. The irrotational winds aid the ridge amplification and formation of the jet streak through the poleward advection of anticyclonic PV, enhancing the PV gradient and deflecting the jet stream (Archambault et al., 2013; Keller et al., 2019). At the same time anticyclonic PV advection, associated with the PV outflow, on the eastern side of the upper level trough opposes the eastward propagation of the wave (Riemer et al., 2008; Keller et al., 2019). These processes, similar to those shown in Figure 2.3, ensure that Hagupit remains in the weak environmental flow for a number of days before making landfall.

Differences in the average outflow of the storm between the NORTH and WEST groups (shown by the trajectories in Figure 5.10) are very small and subtle. The complexity of the interactions between the TC and its environment and the feedback of these interactions onto the steering flow make it difficult to distinguish which of the subtle differences between the two groups are significant to the future forecast of the storm. However, the small differences do show the complex interplay between

the storm and the environment in which it is embedded. Comparisons between the NORTH and WEST groups show that differences in the depth-averaged steering flows of the ensemble members are dominated by differences in the upper level winds. A number of differences in the upper level environments are highlighted. The next section looks more closely at the impact of these differences using a larger 45 member ensemble. In particular ensemble sensitivity analysis is used to determine the impact these features have on the steering of the storm.

5.6 Ensemble-Based Sensitivity Analysis

The 45-member ensemble is produced for the forecast initialisation time of 1200 UTC 3 December. The track forecasts for the 45-member ensemble are shown in Figure 5.13. The ellipses are the contours of the 95% bivariate normal distribution at each 24 hr time in the forecast (and T+3, the first output time). The forecast of the larger ensemble shows similar characteristics to that of the smaller ensemble from the same initial time (Figure 4.7b). In particular, the storm is predicted to stall before landfall in each of the members. The ellipses do not include the best track position (shown by the stars in Figure 5.13) from as early as T+24, showing the large error associated with the forecasts. After the storm has stalled, from approximately T+48 to T+96, forecasts predict the storm to either move towards the Philippines before making landfall or turn to the north.

The orientation of the ellipses in Figure 5.13 demonstrates the direction in which there is greatest spread in the track forecasts at that time. The orientation changes between T+72 and T+120 from west to east to south-west to north-east. The major axis is defined in the same way as in Hamill et al. (2011) and is the direction in which the track forecasts vary the most at any particular time. Figure 5.14 shows the correlation of ensemble members along the major axis line at each time to the position of the ensemble members along the major axis at T+120. Statistically significant (> 0.294) correlations are seen after 24 hours of the forecast, however, it should be noted that at this time the ellipse is almost circular, i.e. there was not a clear major axis. By T+48 the correlation has exceeded 0.5 highlighting the importance of the
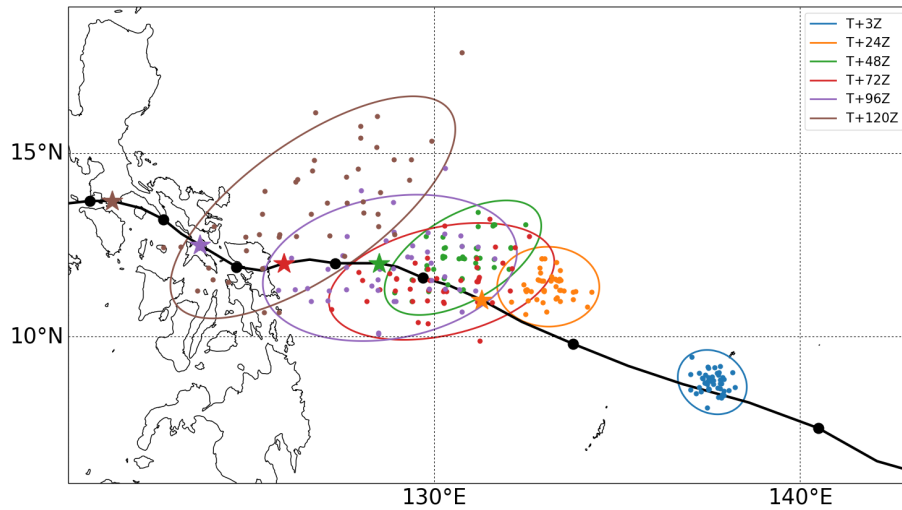
Figure 5.13: Track forecasts using the 45 member ensemble initialised at 1200 UTC 3 December 2014. The ellipses denote the 95% bivariate normal distribution whilst the dots show the position of the storm every 24 hours. The thick black line is the best track according to IBTrACS. The coloured stars show the best track position of the storm at the same times are the forecasted ellipses.

storm's location earlier in the forecast to whether it turns to the north or heads straight towards the Philippines. For example, ensemble members which predict the TC to be further to the east at T+72 are correlated to the ensemble members which predict the TC to be further towards the north-east by T+120. This is consistent with the results of the previous section where statistically significant differences in the storm's position were seen in the NORTH and WEST groups at 1200 UTC 6 December and 1200 UTC 7 December (Figures 5.10c and d).

Sensitivity tests are carried out to investigate the impact the environment has on the final position of the storm. Using ensemble sensitivity analysis, described in Section 5.6, the sensitivity of the average meridional steering wind component for the final 24 hours of the forecast is compared to the geopotential height at 300 hPa. The quantities in Equation 3.45 are normalised by the ensemble standard deviation, therefore, the ensemble sensitivity analysis shows the likely impact on the steering flow should there be a perturbation of one standard deviation to the ensemble average geopotential height. To calculate the meridional steering wind component the TC was removed with a removal radius of 350 km in each of the ensemble members. This constant radius was chosen due to the additional computational cost of finding the optimum radius in each of the ensemble members. The environmental steering vector
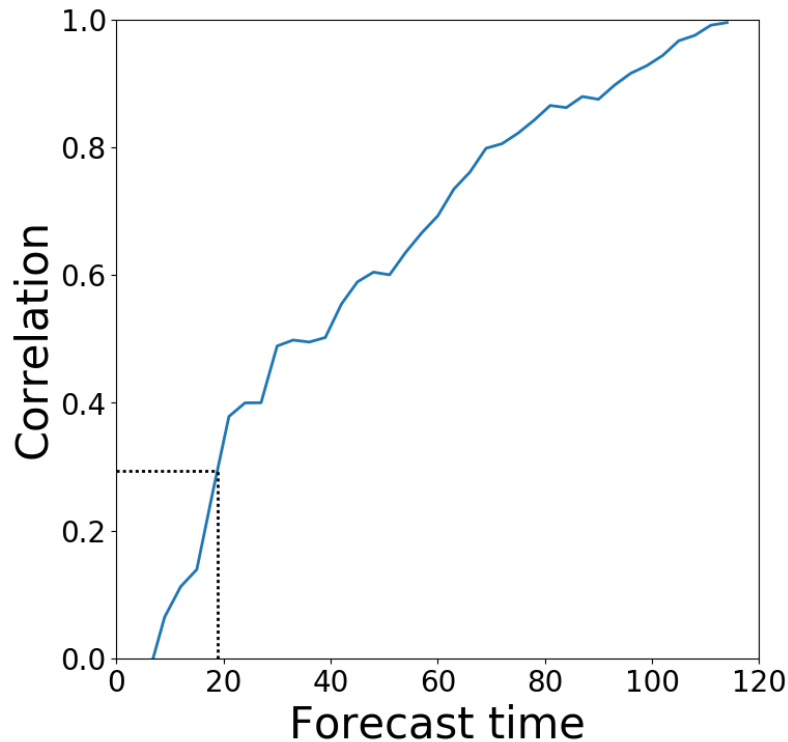
Figure 5.14: Correlation between Hagupit's T+120 position along the major axis to the position along the major axis at earlier lead times. The dashed black line highlights the point at which the correlation becomes statistically significant (i.e. a correlation of 0.294 and above). Correlation for the 45 member ensemble forecast initialised at 1200 UTC 3 December 2014.

is then calculated as described in Section 3.5.2 and the northward component of the vector is averaged across the final 24 hours of the forecast.

Figure 5.15a shows that increasing the geopotential height by one standard deviation at T+6 (1800 UTC 3 December) in the region to the east of the storm would lead to an increased meridional wind component of approximately $0.9\,\mathrm{m\,s^{-1}}$. This would correspond to the storm being steered approximately 80 km further north of the ensemble mean position over the last 24 hours of the forecast. On 3 December, Hagupit is still positioned on the south-west periphery of the subtropical anticyclone which is elongated across the western North Pacific (Figure 4.3c). Increasing the strength of the anticyclone over the area highlighted by the large sensitivity in Figure 5.15a would lead to a stronger northward geostrophic wind component to the upper level winds steering the storm. To the north in Figure 5.15b there is a region of strong negative sensitivity (approximately 40°N and 150°E) indicating differences in the strength of the downstream ridge are important to the steering flow later on in the

forecast. The magnitude of this sensitivity weakens over the next 24 hours (Figure 5.15c), however, the differences in the strength of the downstream ridge likely impact the differences seen in the location of the PV streamer (e.g. Figure 5.10d). In Figure 5.15c the broad region of sensitivity over the upper-level anticyclone to the east has decreased. Instead there is high sensitivity to the geopotential height to the south of the storm. Increasing the geopotential at this point would induce an anticyclonic geostrophic flow to the south of the storm which opposes the westward motion of the TC. The sensitivities suggest that the storms with an increased geopotential to the south will be subject to a greater northward steering flow of up to $1.5\,\mathrm{m\,s^{-1}}$ during the final 24 hrs of the forecast, leading the TC to be positioned approximately 130 km further north than the ensemble average. This result is consistent with Figures 5.10, 5.13 and 5.14 which suggested that differences in the west to east position of the storm earlier in the forecast lead to differences in the north-east to south-west position of the storm at the end of the forecast. Figure 5.15c also shows a large sensitivity in the upper level environment to the north of the storm. This again agrees with Figure 5.10 where NORTH members were associated with stronger ridge building.

Figure 5.15d shows further sensitivities to the Hagupit's steering flow over the final 24 hours of the forecast to the 300 hPa geopotential height at T+72 (1200 UTC 6 December). At this time the position of the storm is strongly correlated to the final location of the storm (Figure 5.14). This is seen in the figure due to the area of red surrounding the location of the storm, suggesting storms further to the east will be steered further north during the final 24 hours. The sensitivities again show differences in the downstream development of the upper level environment. Storms steered to the north have a stronger ridge, a stronger area of upper level high pressure directly to the south of the storm and a difference in location of the upper level trough, shown by the area of negative sensitivity in Figure 5.15 d at approximately (25°N, 105°E). However, these differences could be due to the difference in location of the storm. As at this time the location of the storms in both groups is significantly different, it can be expected that the storm itself is impacting its environment
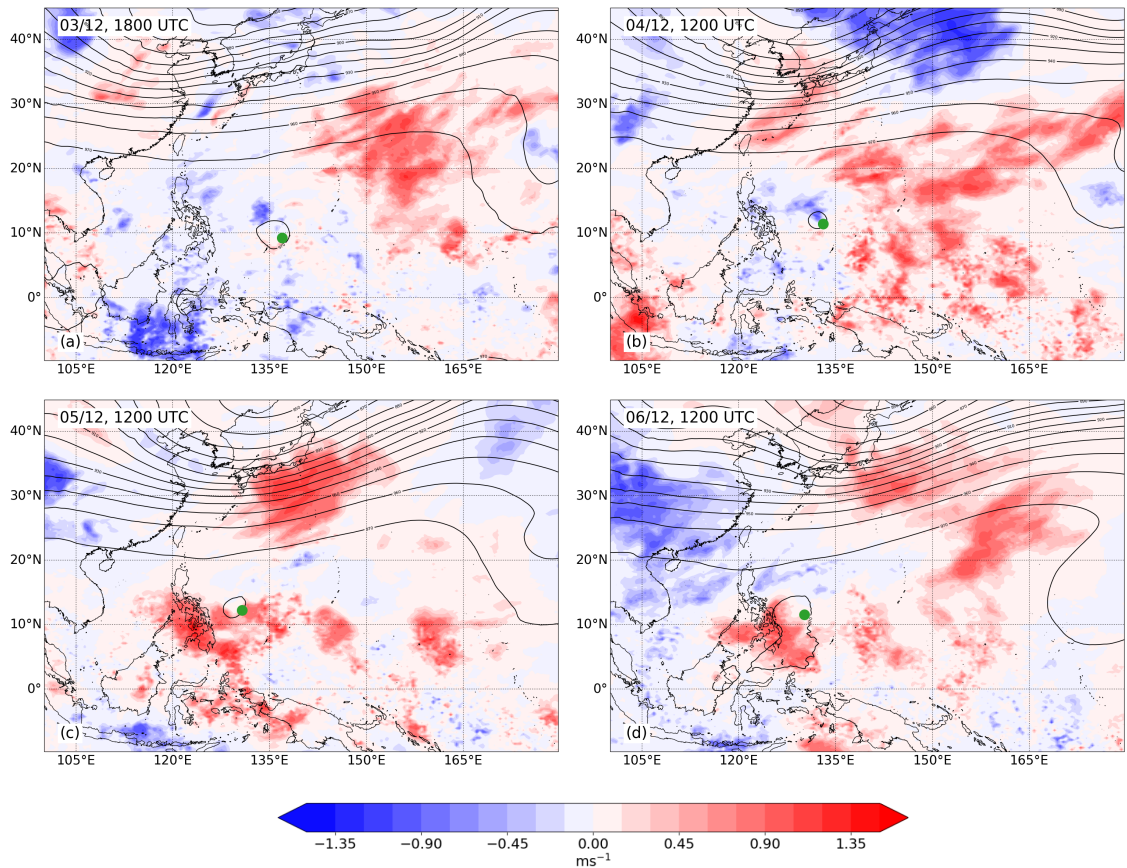
Figure 5.15: Ensemble sensitivity of Hagupit's mean northward steering flow during the final 24 hours of the forecast to the geopotential height at 300 hPa (shading) at (a) 1800 UTC 3 December (T+6), (b) 1200 UTC 4 December (T+24), (c) 1200 UTC 5 December (T+48) and (d) 1200 UTC 6 December (T+72). The sensitivities show the expected response to the mean northward steering should the 300 hPa geopotential height be increased by one standard deviation at that point. The contours are of the ensemble mean 300 hPa geopotential height, contoured every 10 dam. The green dot is the ensemble average position of the TC at that particular time.

differently in each of the ensemble members. Further to this, the forecast metric used - the steering flow in the final 24 hours - is sensitive to the location of the storm as has been seen in section 5.4. Therefore, as the forecast lead time increases the assumption that the forecast metric is independent of the state variable no longer holds. Indeed sensitivities at longer lead times are dominated by a strong dipole structure close to the location of the TC (not shown). At later times the sensitivities also continue to highlight the differences in ridge building and the differences in the location of the detached PV streamer.

The above analysis calculates sensitivities of the TC motion in the final 24 hours of the forecast to geopotential height at 300 hPa earlier on. At other heights the sensitivity between the geopotential height and the northward motion of the TC
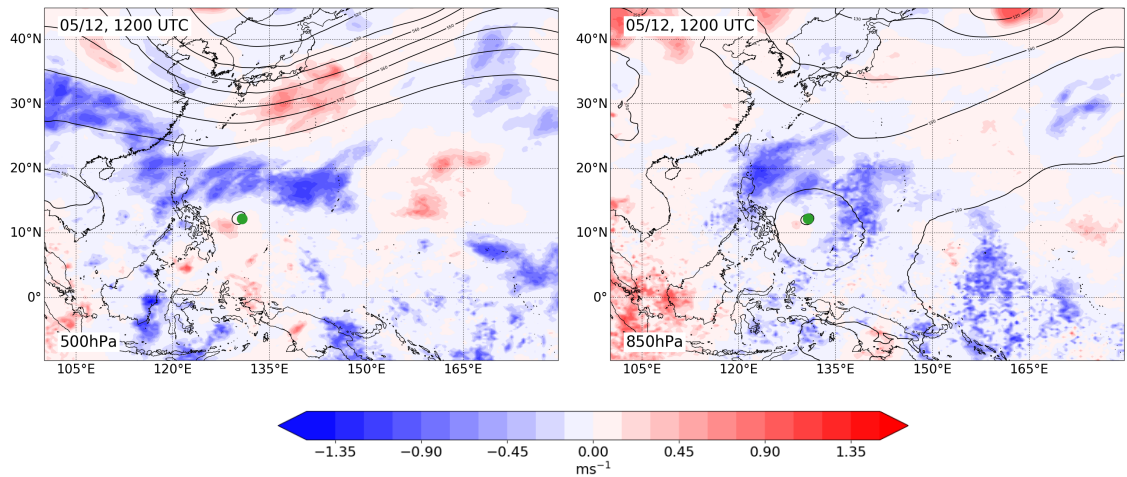
Figure 5.16: As in Figure 5.15 but at heights of (a) 500 hPa and (b) 850 hPa at a time of 1200 UTC 5 December.

in the final 24 hours is significantly less. However, at mid and lower levels there is a region of negative sensitivity to the north of the storm. Figure 5.16 shows the sensitivities between the geopotential height at 500 hPa and 850 hPa at a time of 1200 UTC 5 December. To the north of the storm (approximately 17°N and 130°E) there is a region of negative ensemble sensitivity. This negative sensitivity first develops at 0000 UTC 5 December and remains throughout the forecast. Therefore, increasing the geopotential at this location by one standard deviation will likely lead to decrease in meridional steering velocity of approximately $1\,\mathrm{m\,s^{-1}}$ during the final 24 hours. This again agrees with Figures 5.10, 5.13 and 5.14 as changing the geopotential at this point would impact magnitude of the easterly steering flow and thus create a west-east positional difference in the ensemble. The fact that the region of negative sensitivity is directly to the south of the trough to the north of Hagupit suggests that the depth and position of the trough is important to the future motion of the storm.

5.7   Summary and Conclusion

This chapter has explored the influence of Hagupit's environment compared to that of Haiyan in determining the predictability of the track forecasts. Hagupit's uncertain track was linked to the weak environmental flow in which the storm was embedded. Whilst Haiyan was steered by a strong subtropical ridge, Hagupit was embedded in

a much weaker steering flow and became positioned between two anticyclones. To the east an anticyclone pulled the storm to the north, and to the west an anticyclone steered the storm towards the Philippines. The storm removed environmental steering flow showed that in each ensemble member the exact location of Hagupit during the first 24 hours of the forecast initialised at 1200 UTC 3 December was critical to its position later in the forecast.

The most significant contributions to the depth-averaged steering flow for Hagupit came from the upper levels. North turning ensemble members were associated with a slightly stronger upper-level anticyclone to the east of the storm earlier in the forecasts. As the storm slowed on approach to the Philippines there were significant differences in the downstream ridge building and the position of a detached PV streamer. At approximately 0000 UTC 7 December there was a statistically significant east-west positional difference of the TC between NORTH and WEST groups of ensemble members, with the NORTH members being positioned further to the east. A global 45-member MetUM ensemble showed there was indeed a statistically significant correlation between, for example, ensemble members predicting the TC to be positioned further to the east at T+72 (1200 UTC 6 December) to ensemble members predicting the storm to be positioned further to the north-east at T+120 (1200 UTC 8 December). Further to this, ensemble sensitivity analysis showed that this positional difference earlier on in the forecast is linked to the upper-level geopotential height directly south of the storm and lower-to-mid-level geopotential height to the north of the storm. Increasing the 300 hPa geopotential height by one standard deviation directly south of the storm at T+48 (1200 UTC 5 December) will lead to an increase in the northward component of the steering flow over the final 24 hours of the forecast. The same increase of geopotential height at 500 hPa and 850 hPa to the north of the storm will lead to a less northward component of the steering flow over the final 24 hours of the forecast. These slight differences in pressure directly north and south of the storm can explain the east-west positional differences in the NORTH and WEST ensemble members. Hagupit is located on the south-west periphery of the subtropical high and thus increasing the pressure

south of the storm centre will decrease the eastward geostrophic component of the steering flow. As a result the westward TC motion will be reduced and the TC slows down. Ensemble sensitivity analysis also highlighted sensitivities to the strength of the upper-level anticyclone earlier in the forecast and the development of the downstream ridge and subsequent detached PV streamer.

This chapter shows some of the complexities of forecasting TCs embedded in weak environmental flow. In a case where the TC steering flow is weak, subtle differences between the environment, the position of the TC or the interactions between the TC and the environment can lead to significantly different storm tracks. This was indeed the case with Typhoon Hagupit.

Chapter 6

Convection Permitting Forecasts of Hagupit

6.1 Introduction

Convection permitting simulations at a resolution of the order of 1 km are the future of global weather forecasting (Bauer et al., 2015). Currently the resolution of a global weather forecast is of the order of 10 km, however, technological advances will allow weather centres to produce global operational forecasts at a much higher resolution in the future. One of the key advantages of a higher resolution model is the ability to produce forecasts without needing some of the physical parameterisation schemes currently used. In particular, for forecasts of the order of 1 km, convection can develop freely rather than implicitly estimating the impact of convective processes through use of a parameterisation scheme.

Currently, CP forecasts are carried out over various limited-area domains. For example, a limited-area, CP configuration is used over the western North Pacific by the Met Office, with the aim of providing improved TC forecasts for the Philippines (Short and Petch, 2018). The intensity of and precipitation associated with TCs is better represented in CP forecasts than in global forecasts (Jin et al., 2014; Short and Petch, 2018). However, there are a number of cases in which track predictions in CP forecasts include large, systematic errors. Whilst CP forecasts have the potential

to significantly improve TC intensity forecasts, it is not desirable to reduce the skill of track forecasting.

The causes of the uncertainty in the global forecasts for Typhoon Hagupit were explored in Chapter 5. However, the results do not explain why the CP forecasts (shown in Figure 4.8) behaved so differently. Rather than a large track spread demonstrating the large uncertainty in the storm motion, CP ensemble track forecasts systematically turned to the south-west in each of the ensemble members from forecasts initialised prior to 0000 UTC 5 December. In this situation an inaccurate track forecast is worse than no track forecast. By introducing systematic errors into the ensemble there is a false confidence in where the storm is likely to move.

The aim of this chapter is to understand what causes the large track differences between the global and CP simulations. As Hagupit was an intense, high-impact storm with large levels of precipitation, strong pressure gradients and intense winds, it can be expected that the higher resolution, CP forecasts produce storms that vary significantly in structure to those produced by the global simulations. This is implied through the intensity forecasts (Figure 4.11), and through comparisons of precipitation rates and ascent (Section 4.5). Therefore, unlike Chapter 5 where the ensemble members produced similarly structured storms, focussing discussion on differences in the environment and position of the TC, both the storm structure and the environment steering flow will be considered in this chapter.

The structure of a TC can have a large impact on the future position of the storm. Miller and Zhang (2019) showed that the depth of Hurricane Joaquin caused differences in track forecasts due to the interactions of the TC with strong upper level-winds. Asymmetric TC structure, i.e. situations when convection is enhanced on one side of the eyewall, can lead to asymmetric diabatic heating distributions (Wu and Wang, 2000). Diabatic heating asymmetries are often the cause of TCs deviating from steering flow over mountainous regions (e.g. Hsu et al., 2013) and over areas with large variation in SSTs (e.g. Wu et al., 2005).

The remainder of this chapter is structured as follows. In Section 6.2, a number of sensitivity tests are carried out to determine if the science configuration or the

resolution is the cause of the systematic differences in the forecasts for Hagupit. In Section 6.3 the contribution of the steering flow in the CP and global forecasts to the track deviations is calculated. The differences in the environments of the two different simulations which lead to differences in the steering flow are explored in Section 6.4. The other cause of track deviations between the global and CP forecasts is related to how the storm responds to the steering flow, and in particular the large vertical wind shear. In Section 6.5 the structure of the storms in the two scientific configurations is compared to investigate how the storm structure is impacted by vertical wind shear. In Section 6.6, the forecasts from Section 6.2 which use global physics at 4.4 km is investigated in more detail. A summary is given in Section 6.7.

6.2   Sensitivity Tests

The global and CP forecast set ups differ in several ways, as detailed in Section 3.3.2. The resolution of the global configuration is approximately 50×33 km in the tropics with 70 vertical levels up to 80 km above mean sea level. The CP forecasts have a horizontal resolution of 4.4×4.4 km and have 80 vertical levels up to 38.5 km above mean sea level. The increased resolution in the CP forecasts allows for a difference in science configurations. In the global simulations the Global Atmosphere 6.1 (GA6.1, Walters et al., 2017) configuration is used, whilst in the CP forecasts the Regional Atmosphere 1 Tropical (RA1-T, Bush et al., 2019) configuration is used with reduced air-sea drag at high wind speeds, which improves wind-pressure relations in TCs and will be used in the release of RA2-T (Bush et al., 2019).

The formation of the ensembles also differ between the global and CP ensembles. Initial conditions for the MOGREPS-G forecast are formed by adding perturbations to the Met Office global analysis, where perturbations are generated using an ensemble transform Kalman filter (ETKF; Bishop et al., 2001). The effects of structural and subgrid-scale model uncertainties are accounted for through two stochastic physics schemes: the random parameters scheme (Bowler et al., 2008) and the stochastic kinetic energy backscatter scheme (SKEB; Bowler et al., 2009). For the CP forecasts

the initial conditions are formed by nesting each of the global ensemble members down to the 4.4 km grid. Lateral boundary conditions are provided to the CP simulations from the global ensemble members every 3 hours. Thus, the initial conditions and boundary conditions are inherited from the global model. No further perturbations are made to the model physics in the CP forecasts.

A series of experiments (summarised in Table 6.1) are carried out to determine which of the differences in the model configurations cause the differences in the forecasts. These experiments consist of reproducing the forecasts for Hagupit initialised at 1200 UTC 3 December 2014 using slightly different configurations of the model. The aim is to step from the global forecasts to the CP forecasts and identify which of the differences in configurations are the cause for the forecast differences, and hence which physical processes are important in determining the track of Hagupit.

The forecast properties which are investigated as a potential cause for these differences are:

- the use of stochastic physics in the global model (both the random parameters and the SKEB scheme);
- the difference in model resolutions;
- the different model configurations.

Stochastic physics are only used in the global simulations, thus turning the scheme off (*NoSto*) will only impact the boundary conditions of the higher resolution, regional configurations. The two model resolutions tested are a nested, regional, 4.4 km domain (*Hi*), and the global ($\sim 50\,\mathrm{km} \times 33\,\mathrm{km}$) domain (*Lo*). The different model configurations refer to the GA6.1 configuration (*Par*) or the RA1-T configuration (*Exp*). Each of the experiments is summarised in Table 6.1. Note that the experiments named Par-Lo and Exp-Hi are identical to the global and CP forecasts that have been discussed throughout this thesis. The names in Table 6.1 are adopted for this section only.

The forecast differences which are to be investigated are:

- the systematic turn to the south-west in the CP model, causing an increase in

Table 6.1: Summary of the different experimental set ups used in this section. The two rows in bold are the main global and CP configurations which are used throughout this thesis. The other rows are the additional sensitivity tests discussed in this chapter.

Name	Science Configuration	Resolution	Sto. Phys.
Par-Lo	**GA6.1**	$\sim \mathbf{50 \times 33\,km}$	**Yes**
Par-Lo-NoSto	GA6.1	$\sim 50 \times 33\,\mathrm{km}$	No
Par-Hi	GA6.1	$4.4 \times 4.4\,\mathrm{km}$	Yes
Par-Hi-NoSto	GA6.1	$4.4 \times 4.4\,\mathrm{km}$	No
Exp-Hi	**RA1-T**	$\mathbf{4.4 \times 4.4\,km}$	**Yes**
Exp-Hi-NoSto	RA1-T	$4.4 \times 4.4\,\mathrm{km}$	No

positional error in each of the ensemble members;

- the large track spread in the global forecasts compared to the small spread in the CP forecasts.

Figure 6.1 shows the track forecasts for each of the experiments. In each of the global forecasts the spread is very similar with some ensemble members turning to the north and some ensemble members making landfall over the Philippines (Figures 6.1 a and b), suggesting stochastic physics has a very small impact on the global ensemble spread and characteristics. Figure 6.2 compares the Par-Lo-NoSto, Par-Hi and Exp-Hi track positions to the Par-Lo track positions. Every 6 hours the direct positional distance between equivalent ensemble members (i.e. ensemble members in which the initial conditions are the same) is calculated. This distance is then averaged over all 12 ensemble members to produce the average deviation line, and the shading showing the ensemble spread. The deviation between the global ensemble members with and without stochastic physics remains below 100 km for almost all ensemble members throughout the forecast (the blue line in Figure 6.2). When comparing the Par-Hi forecast to the Par-Lo, i.e. comparing the impact of changing the resolution, the average deviation exceeds 100 km after 48 hours of the forecast, and remains above 100 km for the remainder of the forecast with some Par-Hi members ending up over 250 km away from the equivalent Par-Lo ensemble member (orange line in Figure 6.2). In the Exp-Hi forecast the average deviation exceeds 100 km after 30 hours and quickly rises to above 300 km after 72 hours (green line of Figure 6.2). By
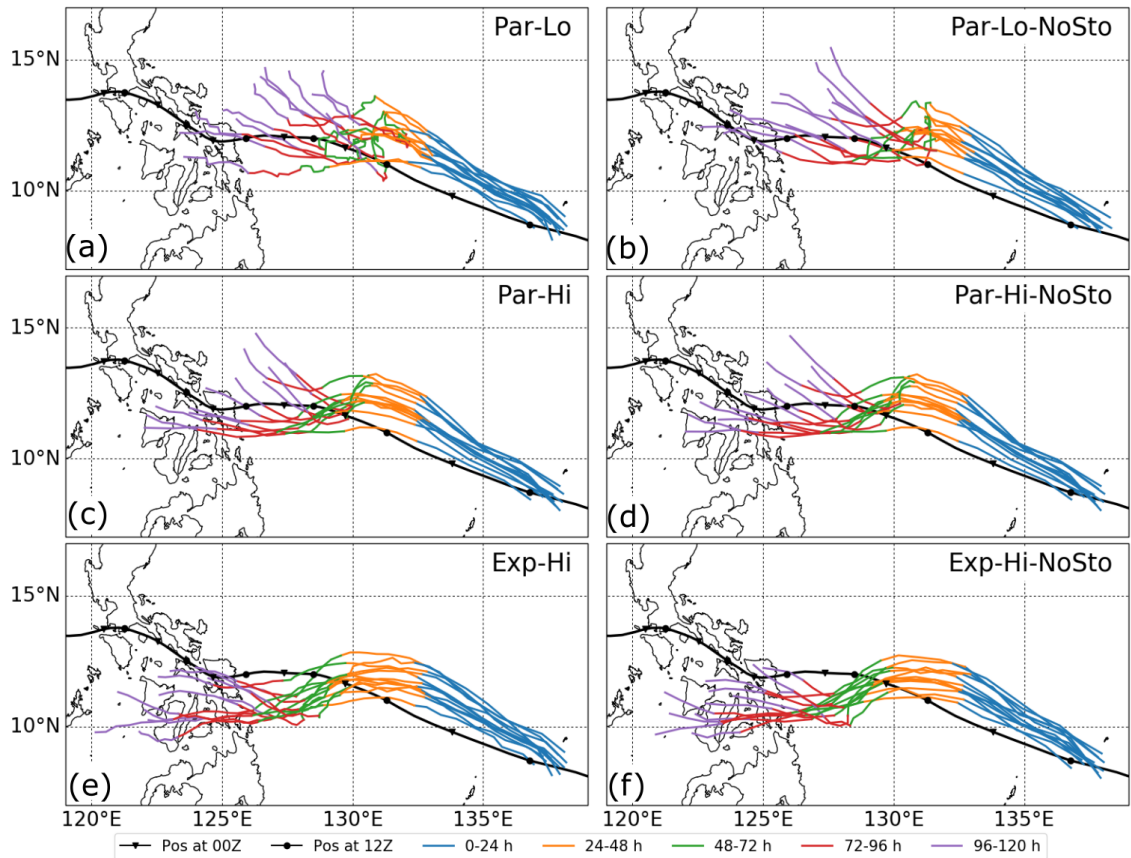
Figure 6.1: Track forecasts of the sensitivity tests. Each forecast is for Typhoon Hagupit, initialised at 1200 UTC 3 December 2014.

the end of the forecast the average deviation is 440 km and even the closest Exp-Hi member is over 280 km away from its Par-Lo equivalent. These results suggest that the cause of the differences between the Par-Lo and Exp-Hi forecasts is a combination of the resolution and science configuration.

The small impact of stochastic physics on the global forecasts leads to only small differences in the nested, limited-area forecasts which are being driven by the global ensemble with and without stochastic physics (i.e. comparing Figure 6.1c to 6.1d and Figure 6.1e to 6.1f). Figure 6.3 demonstrates this by showing the tracks of two ensemble members (ensemble member 2 in which the Par-Lo forecast predicts the storm to turn north and ensemble member 8 in which the Par-Lo forecast predicts the storm to make landfall) in each of the experiments. In each case turning stochastic physics on/off has little impact on the track. The greatest impact is between the Par-Lo and Par-Lo-NoSto forecasts in ensemble member 2, where differences arise from the region where Hagupit becomes positioned in the weak steering flow between
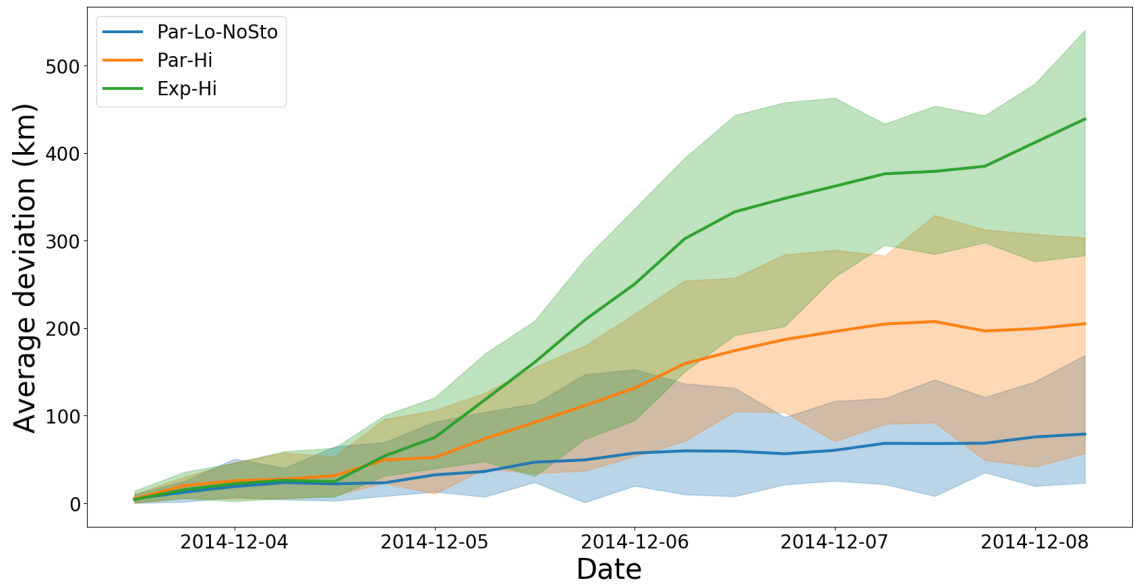
Figure 6.2: Average track deviation from the global model (with stochastic physics) for the global model without stochastic physics, Par-Hi and Exp-Hi forecasts. At every 6 hourly time the distance between the equivalent ensemble members in the forecasts is calculated. These distances are then averaged across all ensemble members. The shading shows the full range of distances.

two anticyclones (i.e. the sensitive region discussed in Chapter 5). The Par-Hi and Par-Hi-NoSto forecasts predict the storm track to lie between where the Par-Lo and Exp-Hi forecast tracks. As the stochastic physics has only a very small impact, the rest of the section only considers the forecasts with stochastic physics turned on (i.e. the Par-Lo, Par-Hi and Exp-Hi forecasts).

The Par-Hi forecast (Figure 6.1c) exhibits a similar track spread to the Par-Lo forecast. Some members are predicted to turn north and miss the Philippines whilst others make landfall. The members which hit the Philippines tend to make a southwest turn beforehand, much like the Exp-Hi forecasts. The direct positional error (DPE) for the ensemble average of the Par-Hi forecast is less than for the Par-Lo forecast and somewhat similar to the Exp-Hi forecast (Figure 6.4). It could be argued that the GA6, 4.4 km forecast is the best forecast - the DPE is less than for the global model, yet the spread is still significant and demonstrates the uncertainty in the motion of Hagupit. Whilst some members take the south west turn seen in the Exp-Hi forecasts, not every member does and thus there is not a systematic error in the forecast. For this reason the forecast will be studied in more detail in Section 6.6. However, the GA6.1 configuration has not been designed to be run on a limited
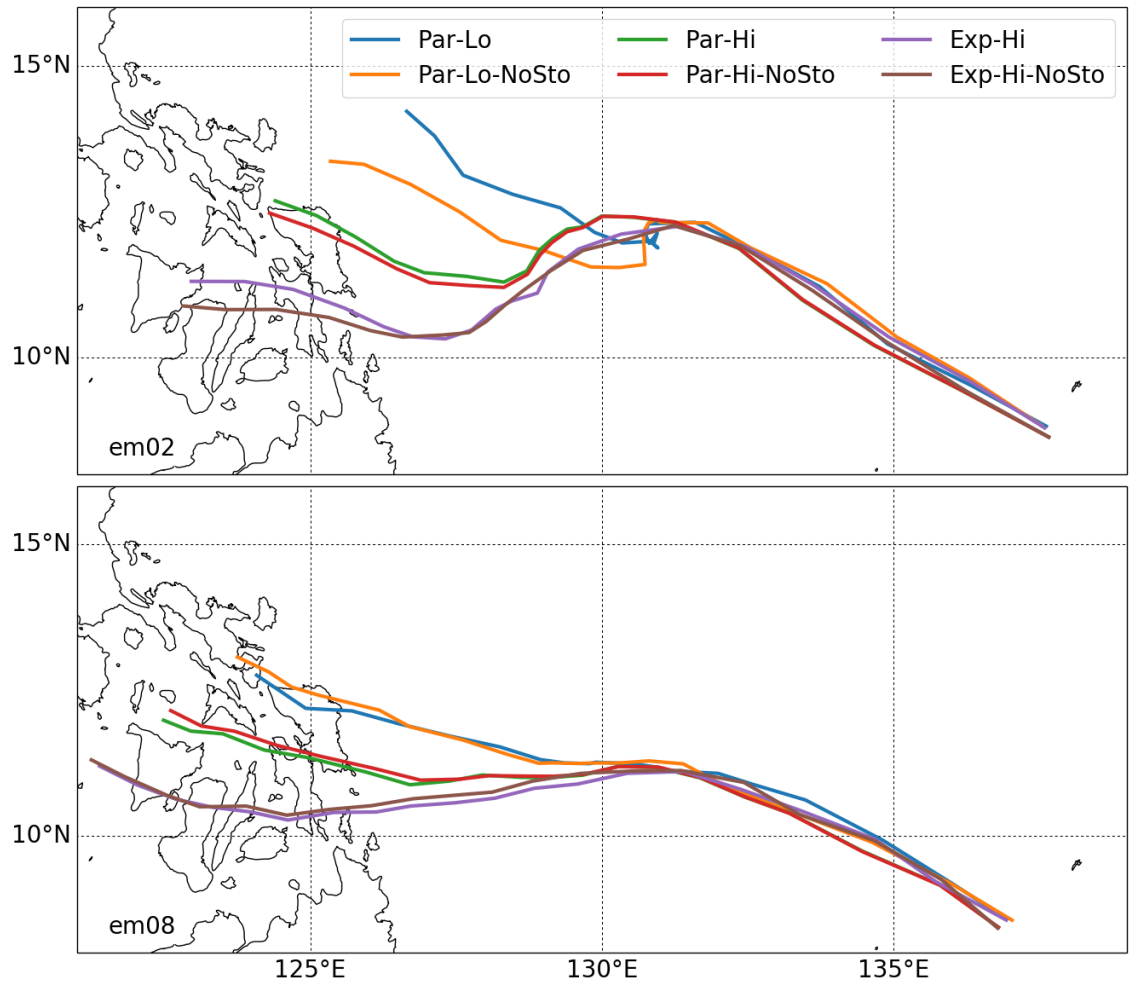
Figure 6.3: Comparison of track forecasts of ensemble member 2 and 8 in each of the experiments.
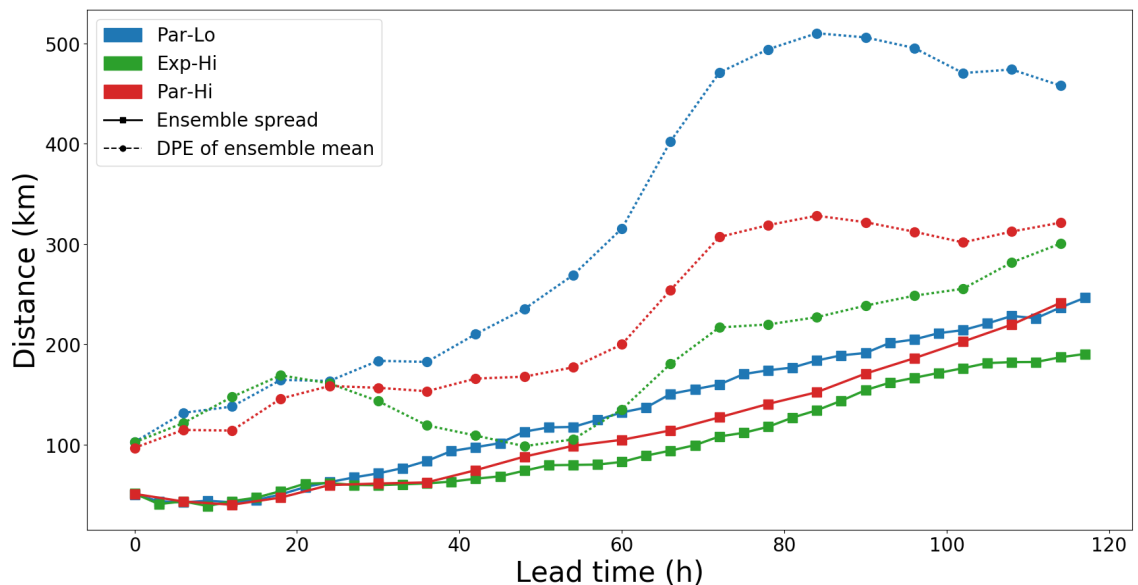
Figure 6.4: Comparison between the direct positional error (DPE) of the ensemble average and the ensemble spread for each of the experiments which had stochastic physics turned on.

area 4.4 km grid in the tropics. Whilst the forecasts for Hagupit in this case seem better, it is unlikely the configuration would regularly produce more accurate weather forecasts than the configurations used in the Par-Lo and Exp-Hi experiments.

From these tests we can conclude three things about the track forecasts: (a) stochastic physics in the global ensemble does not cause the large spread in comparison to the CP forecasts; (b) increasing the resolution whilst using the global physics decreases the spread and the DPE of the ensemble, but does not cause the systematic error seen in the CP forecasts; (c) increasing the resolution and using the RA1-T science configuration together causes the south-west turn in the CP forecasts.

Changing the resolution has a significant impact on the intensity of the storm (Figures 6.5 and 6.6). Although the maximum wind speed forecasts of the Exp-Hi and Par-Hi forecasts are similar (Figure 6.6), there are some differences in the minimum sea level pressure forecasts (Figure 6.5) particular after approximately 0000 UTC 5 December. The Par-Hi forecast continues to intensify Hagupit whilst the intensity in the Exp-Hi forecasts plateaus. It is not immediately obvious why this is the case. However, compared to the Par-Lo forecasts, the differences between the Exp-Hi and Par-Hi intensity forecasts are small up until around the time Hagupit makes landfall. At later times, when the differences are greater, all of the Exp-Hi ensemble member have
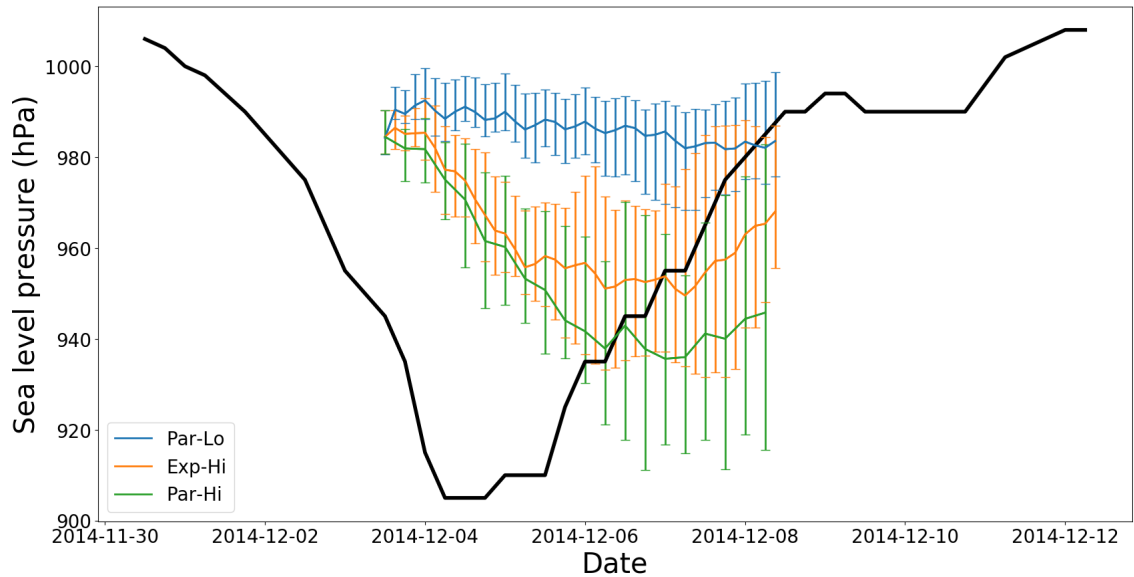
Figure 6.5: Comparison of the minimum sea level pressure for each of the experiments in which stochastic physics was turned on. Error bars show the full range of all ensemble members. The black line is the minimum sea level pressure of Hagupit according to IBTrACS.

made landfall and thus are weakening, whereas only a subset of Par-Hi members have made landfall and are weakening.

A further test was carried out to assess the impact of the limited area domain size. The CP forecasts were rerun using a larger domain which includes the anticyclones which control Hagupit's motion (shown in Figure 6.7). The result was an almost identical forecast to the Exp-Hi forecast with very little deviation in the tracks or intensities between equivalent ensemble members using the original and large domain (not shown). Therefore, In the case of Hagupit, increasing the domain size does not impact the CP track forecasts.

6.3 Contribution of the Storm's Steering Winds to Track Deviations

Section 6.2 demonstrated that the differences in track forecasts for Hagupit in the global and CP simulations is caused by both the difference in resolution and the difference in scientific configurations. In Chapter 5 it was shown that Hagupit's environment is critical to the track uncertainty in the global forecasts. In this section
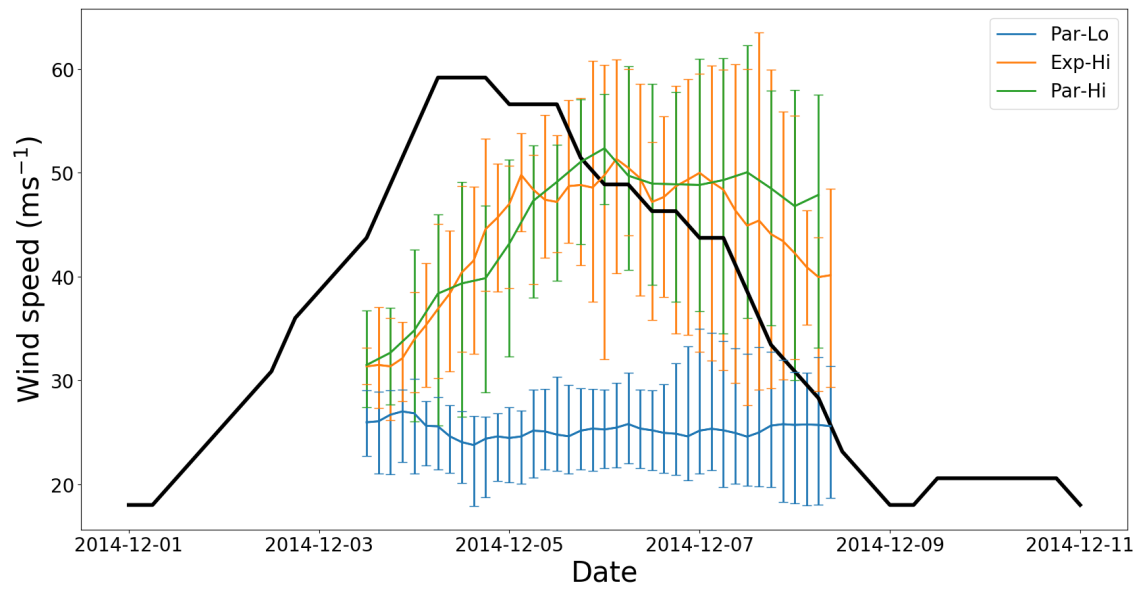
Figure 6.6: As in Figure 6.5 but for maximum 10-m wind speed.
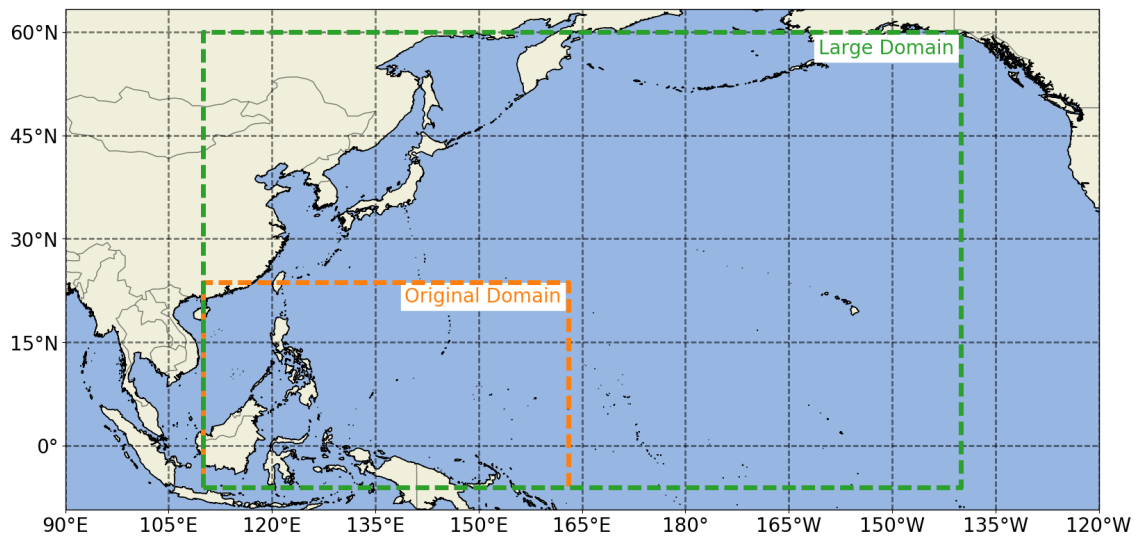
Figure 6.7: Map showing the original and large CP domain.
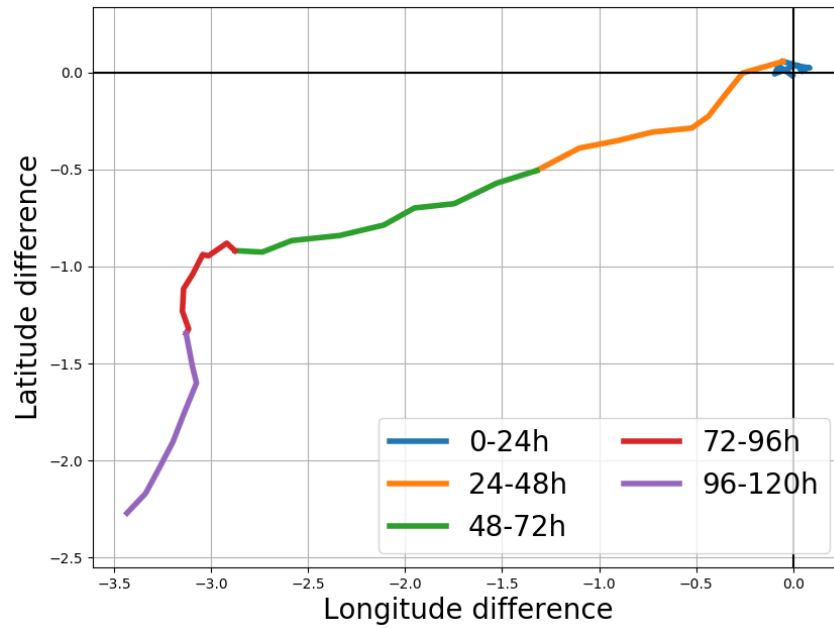
Figure 6.8: The ensemble average of the CP Hagupit forecast compared to the global Hagupit forecast. Forecasts initialised at 1200 UTC 3 December 2014

the contribution of Hagupit's steering flow in the CP ensemble is compared to that of the global ensemble. The aim is to investigate to what extent the differences in the track forecasts can be explained by differences in the steering flow.

Figure 6.8 shows the ensemble mean position of Hagupit in the CP forecast compared to the ensemble mean position in the global forecast. The figure shows that for the first 24 hours of the forecast the location of the CP and global ensembles are similar. However, at T+30, the position of the CP ensemble is to the south of the global ensemble. From here the position of the CP ensemble mean compared to that of the global increases quickly in the south-west direction. Comparing this plot to the track plot (Figure 6.3) shows that, just after T+24, when the global and CP forecasts begin to deviate, the CP ensemble members turn to the west whilst the global forecasts continue to move to the north-west. Note that at this point the ensemble spreads of both the CP and global ensembles are approximately 50 km (Figure 6.4) and therefore the ensemble mean is representative of the different ensemble members. Later on the spread of the global ensemble increases substantially, however it remains the case that each of the CP forecasts move south-west of the global forecasts.

In order to investigate the storm environment, the TC was removed from each of the ensemble members using the same storm removal method as in Section 5.3 and
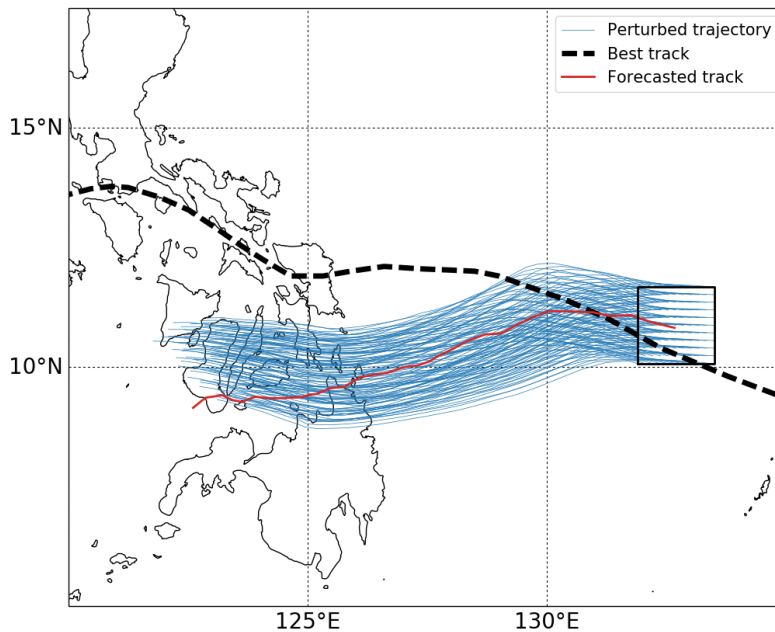
Figure 6.9: Trajectories (blue lines) calculated using the storm removed winds of ensemble member 0 in the CP forecast. The trajectories are initialised 24 hours into the forecast at 1200 UTC 4 December in a $1.6° \times 1.6°$ box around the forecast position of the storm. The forecasted track is shown by the red line whilst the IBTrACS best track is shown by the black dashed line.

outlined in Section 3.5.2. The top pressure height, p_t, is chosen as $300 \, \text{hPa}$ whilst the removal radius, r_0, is optimised at every timestep. Trajectories are calculated using this optimum steering flow. The trajectories are initialised $0.16°$ apart in a $1.6° \times 1.6°$ centred on the forecasted location of the storm to represent the typical 24 hr TC track error. The trajectories demonstrate that the CP model is insensitive to the exact location of the TC earlier in the forecasts (Figure 6.9). The spread of the trajectories remains small and each trajectory turns to the south-west away from the best track line. Ensemble member 0 is shown in Figure 6.9, however the same behaviour was seen in each of the ensemble members. This suggests that the steering winds are responsible for both the lack of spread in the CP forecasts and the turn to the south-west.

On average (across all times and all ensemble members) the optimum r_0 and p_t for the CP forecasts is $300 \, \text{km}$ and $300 \, \text{hPa}$, respectively (Figure 6.10). Using these values gives an average residual vector of magnitude $0.8 \, \text{m s}^{-1}$. The optimum depth and radius is similar to that of the global forecasts (Figure 5.2), however the magnitude of the residual vector is less in the CP forecasts. To allow for comparisons of the
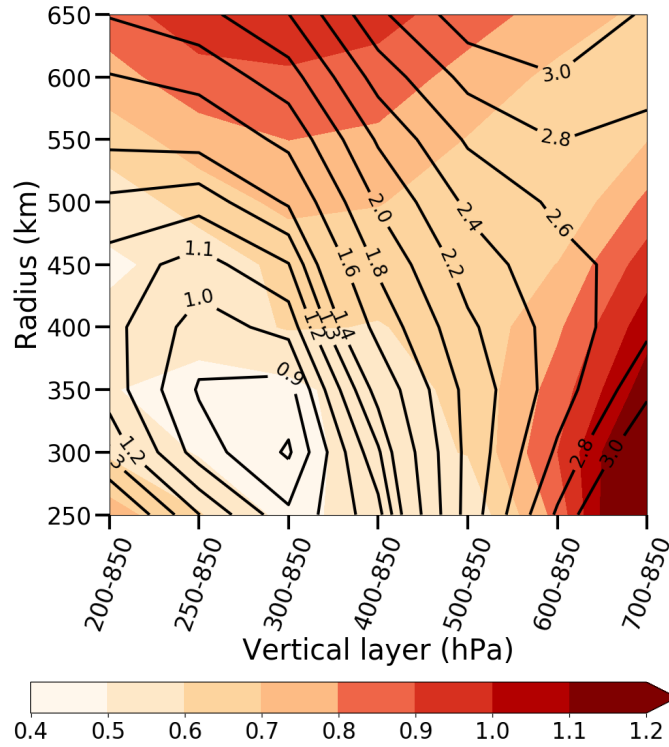
Figure 6.10: Average magnitude of the residual vector $\mathbf{V}_{res}$, defined as the difference between the storm motion vector and the environmental wind vector (contours, $\mathrm{m\,s^{-1}}$) as a function of storm depth and removal radius. The shading denotes the standard deviation across all times and ensembles. The CP forecast initialised at 1200 UTC 3 December is used.

environmental winds in the global and CP forecasts, a constant r_0 of 300 km and a constant p_t of 300 hPa is used. The winds are averaged over r_0 to compute the environmental vectors $\mathbf{V}_{env}$. This is different to previous calculations which used $2R_{80}$ (i.e. $R = r_0$ in Equation 3.34). The reason for this is that the difference in intensities of the storms in the different forecasts cause large differences in R_{80}. By using the value of r_0 (300 km), the same horizontal area is averaged over in both cases. As outlined in Section 3.5.2, the difference between using $R = 2R_{80}$ and $R = r_0$ in calculating $\mathbf{V}_{env}$ is small.

Figure 6.11 compares the average distance between the equivalent ensemble members in the CP and global ensembles to the distance between the ensemble members if the storm would be exactly steered by the steering wind (i.e. if, using the values of r_0 and p_t defined above, $\mathbf{V}_{fc} = \mathbf{V}_{env}$). If the steering flow accounted for all of the differences in the storm's track then the blue and red lines in Figure 6.11 would overlap. The figure shows that the forecasted storm positions deviate significantly
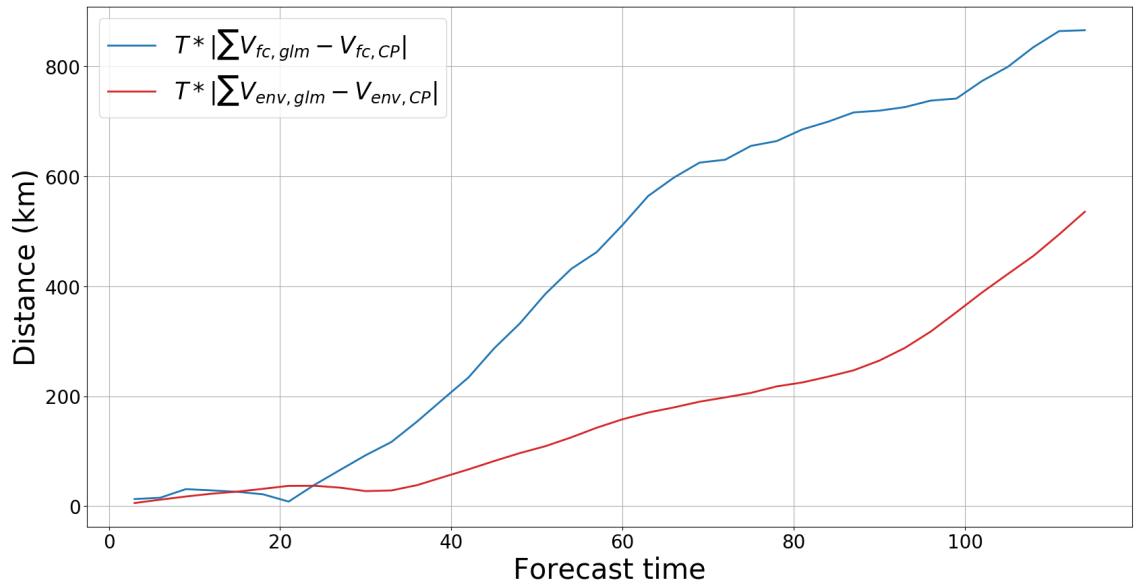
Figure 6.11: The distance between the forecasted locations of the global ensemble mean and the CP ensemble mean (blue line) compared to the distance between the locations of the storms if they were controlled exactly by the steering flow (red line). Forecasts initialised at 1200 UTC 3 December 2014.

from approximately T+21, whilst the steering winds deviate significantly from approximately T+36. Further to this, between T+36 to T+90, the gradient of the deviation due to the environmental winds is less than that of the forecasted position. This suggests that some of the differences between the ensemble member positions in the global and CP forecasts can be explained by different environmental winds, but not all of the differences. By the end of the forecast the gradient of both lines in Figure 6.11 is similar and hence the environmental winds explain most of the positional differences occurring. This is expected as by this point, due to differences in the location of the storm in the CP and global forecasts, the environments steering the TC are very different.

Figures 6.12a (global) and 6.12b (CP) compare the track of each of the ensemble members to the would-be track if the storm followed exactly the storm-removed environmental winds. The environmental wind trajectories differ from the trajectories in Figure 6.9 in two important ways. First, the next three hours of the trajectory is always calculated using the storm-removed environmental winds at the forecasted TC position according to the original ensemble, rather than the position in which TC would be if the storm-removed environmental winds exactly predicted its motion.

Second, the trajectory is calculated using the vector $\mathbf{V}_{env}$ (defined in Equation 3.34) and thus includes an average over an area of r_0 (300 km) rather than just a single point. The first 12 hours of the forecast are omitted for this comparison due to the fact the storm is spinning up and intensifying during this time.

For almost all ensemble members in the global model, the trajectories calculated using $\mathbf{V}_{env}$ travel further than the forecasted tracks (Figure 6.12a). From T+24 to T+72 there is significant deviation between the forecasted tracks and the environmental winds tracks. To highlight this Figure 6.13a shows just three ensemble members from Figure 6.12a. The ensemble members (0, 4 and 6) are chosen as they are representative of the global ensemble (one turns north, one makes landfall and one stops just before landfall). At T+24 (the first triangle) the environmental track and the actual track closely match in all three members. However, at T+72 (the third triangle), the actual track position is close to the environmental track position at a much earlier time. In the case of ensemble member 0 (the blue line), the actual position at T+72 is between the environmental track positions at T+48 and T+60. For ensemble member 4 (orange) the T+72 actual position is close to the T+48 environment position. For ensemble member 6 (green) the T+72 actual position is near the T+60 environmental position. In each case the forecasted storm stalls and travels slower than the steering environmental winds.

Differences also occur in the actual and environmental tracks of the CP forecast (Figures 6.12b and 6.13b, which highlight the same three ensemble members as in Figure 6.13a). However, unlike the global forecasts these differences are more systematic. There is some difference between the two sets of tracks as early as T+24 and this difference increases during every 12 hour period. Between T+24 and T+72 the differences between the actual and environmental tracks continue to increase but the rate of increase is no different to earlier or later times.

The above discussion, and Figures 6.11 to 6.13, demonstrates that there is one period between T+24 and T+72 in the global forecasts in which the storms are not directly steered by the steering flow, whilst the CP forecasts tend to travel faster than the steering flow. This contributes to the differences in the track forecasts
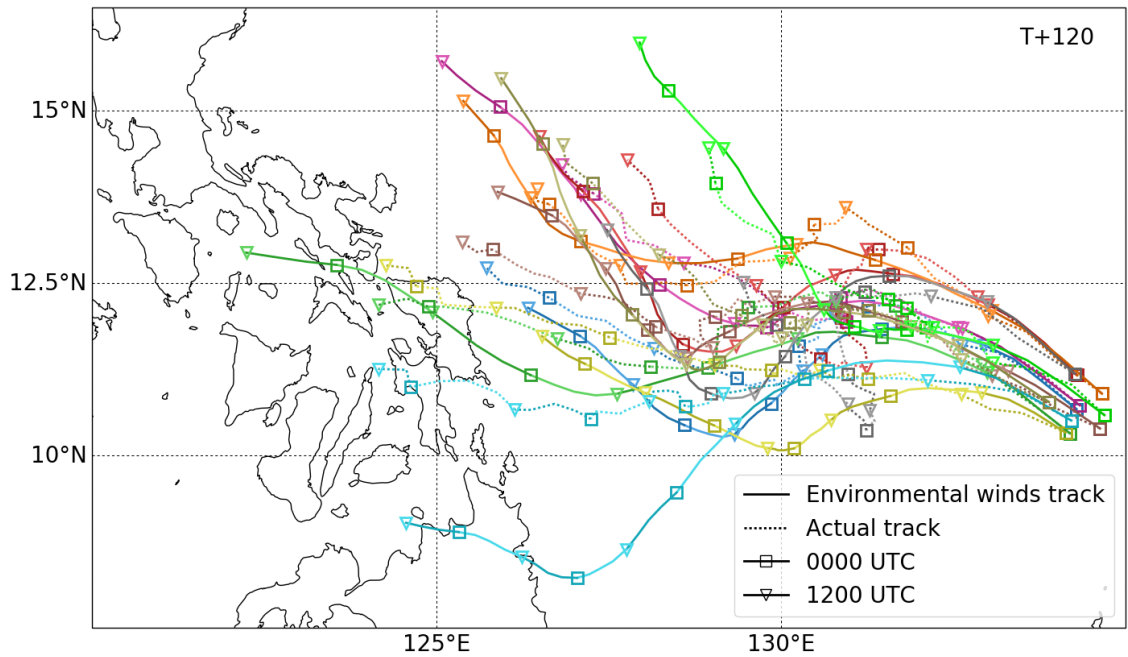
(a)
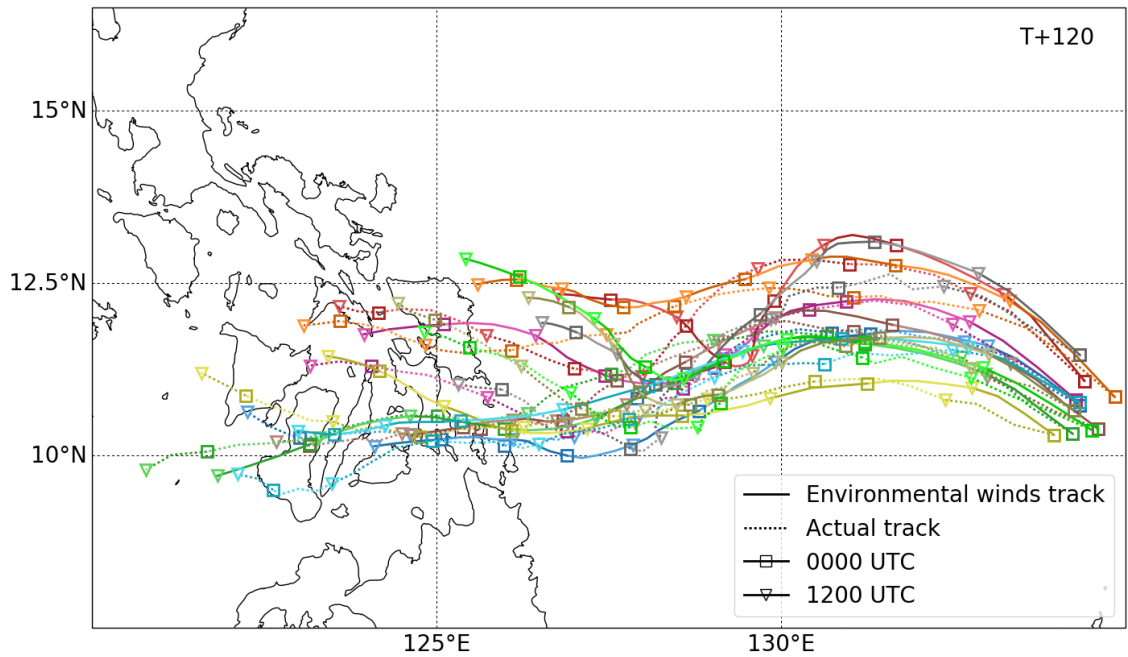
(b)

Figure 6.12: Comparison of the (a) global and (b) CP ensemble storm tracks and to the trajectories calculated using the storm-removed environmental winds at the TC centres. The storm-removed environmental winds use a removal radius, r_0, of 350 km and a top pressure layer, p_t of 300 hPa. Squares are the position of the storm at 0000 UTC, whilst triangles are the position of the storm at 1200 UTC. Each colour represents a different ensemble member. The forecast used is initialised at 1200 UTC 3 December, comparisons made from T+12 to T+120 (i.e. the first square is 0000 UTC 4 December).
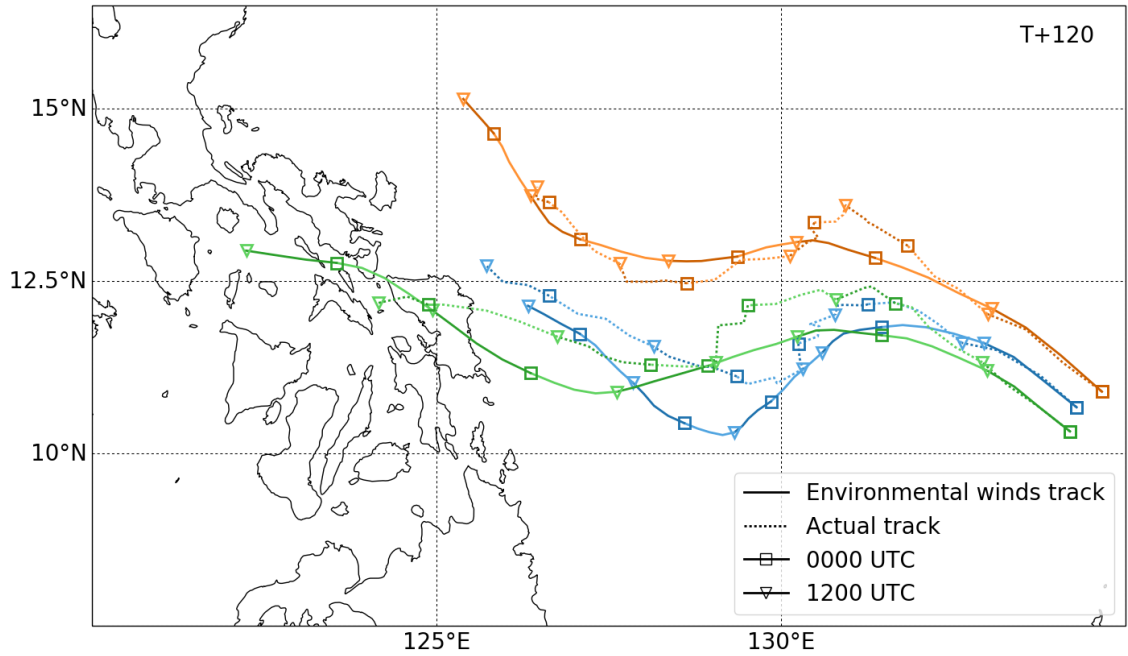
(a)
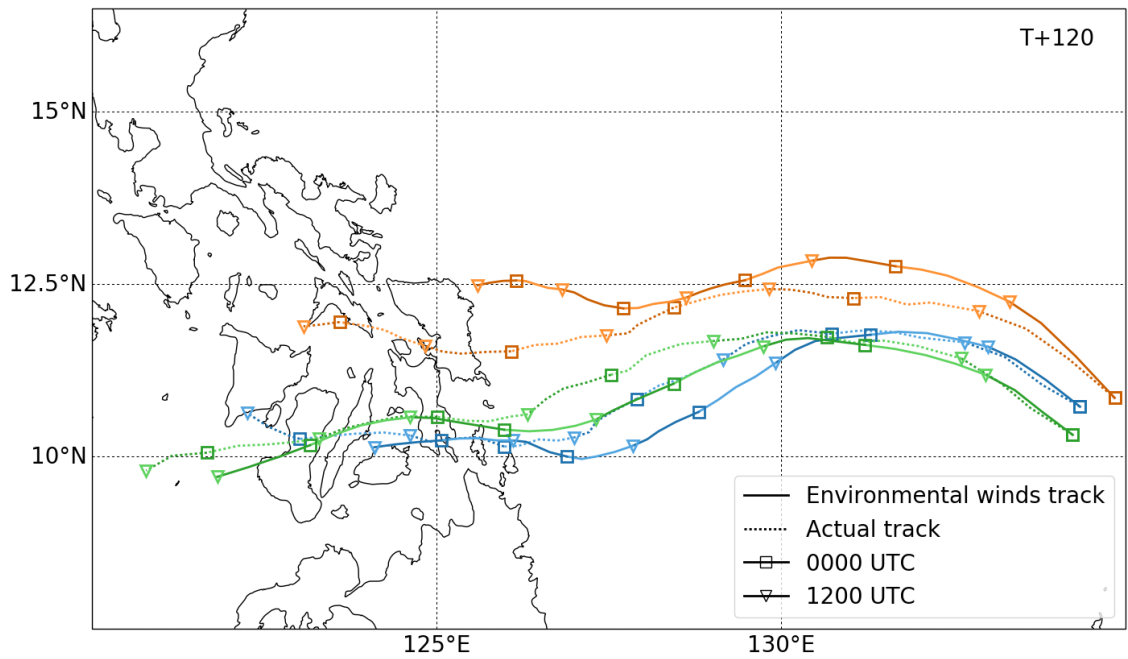
(b)

Figure 6.13: Same as Figure 6.12 but only showing ensemble members 0, 4 and 6.

and will be investigated in Section 6.5. As shown by Figure 6.11, there is also a significant contribution to the track differences from the steering flow. Section 6.4 will investigate how the environment contributes to the differences in the steering flow.

6.4   Global and CP Environmental Differences

In this section the environment of Hagupit in the global and CP forecasts is compared to highlight why the differences in the steering flow occurs.

Between T+36 and T+84 the environmental trajectories in equivalent ensemble members of the global and CP forecasts move on average from $50\,\mathrm{km}$ apart to $250\,\mathrm{km}$ apart (Figure 6.11). Thus, there is an average steering flow speed difference of approximately $1\,\mathrm{m\,s^{-1}}$. The trajectories in Figure 6.9 show that earlier in the forecast the track is not too sensitive to the position of the storm in the CP forecasts. This suggests that small positional differences earlier in the forecast will not impact the track of Hagupit in the CP simulations, and differences in the storm's environment causes the systematic differences between the steering flow of the CP and global forecasts. Figure 6.14 compares the depth-averaged steering winds at T+36, showing differences of approximately $1\,\mathrm{m\,s^{-1}}$ through the centre of the storm. This depth average is then split into three levels in Figure 6.15. The steering winds at upper levels are stronger than those at lower- and mid-levels. However, the average differences between the global and CP forecasts are of approximately the same magnitude regardless of vertical level.

Figure 6.16 shows the geopotential height differences of the global and CP ensemble means at four different times and three different heights. Gradients in the geopotential induce a geostrophic wind ($\mathbf{u}_g$) via the geostrophic wind balance,

$$\mathbf{u}_g = \frac{g}{f}\hat{\mathbf{k}} \times \nabla Z \, , \tag{6.1}$$

where g is gravity, f is the Coriolis parameter, $\hat{\mathbf{k}}$ is the unit vector in the vertical and Z is the geopotential height. Equation 6.1 implies that, over an area of $100\,\mathrm{km}$,
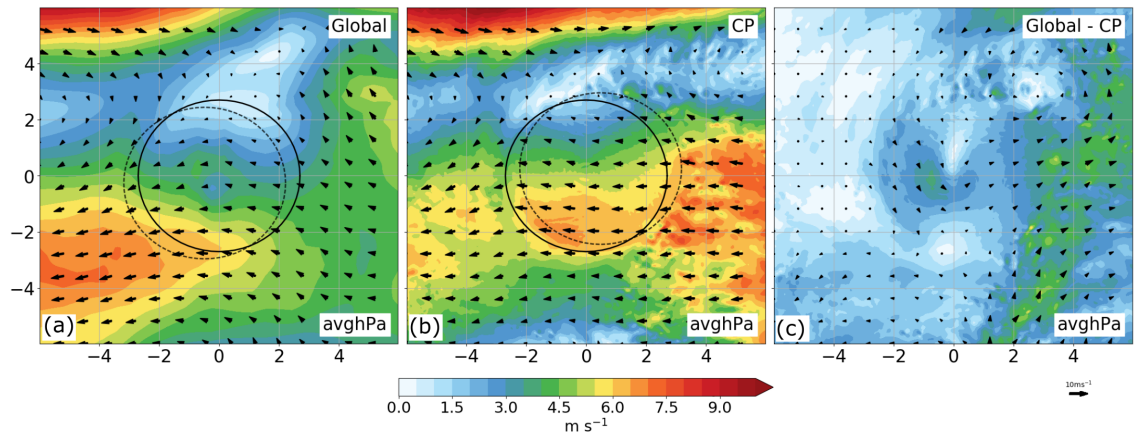
Figure 6.14: Comparison of the ensemble-averaged, depth-averaged (between 850 and 300 hPa) steering flow for Hagupit in the global and CP forecasts at 0000 UTC 5 December (T+36). Each ensemble member is centred on the forecasted storm location before averaging. In (a) and (b) shading shows wind speeds, arrows are the wind vectors, the solid red circle is the 300 km storm removal location whilst the dashed red circle is the relative location of the storm in the other model. In (c) shading and arrows show the difference in steering winds between the global and CP averages.

a geopotential height difference of 0.04 dam would be required to induce a wind of $1\,\mathrm{m\,s^{-1}}$. Therefore, when comparing the geopotential heights in Figure 6.16, values of this magnitude are significant.

Earlier on, at T+12, the main difference in the ensemble mean geopotential heights occurs at approximately 5°N and 145°E. At this location the geopotential is greater in the CP forecasts than the global forecasts at 300 hPa, whilst at 850 hPa the opposite is true with the geopotential to the south-east of the storm being weaker in the CP forecasts than in the global forecasts. The steering winds in both types of simulation are similar at this point. However, it is not clear if the differences in geopotential height have no impact on the steering flow because they are relatively far away from the storm, or if the upper level and lower level differences cancel each other out when computing the depth averaged steering flow.

Later in the forecast, at T+24 and T+36, geopotential height differences between the ensemble averages become greater at all levels. To the south of the storm there is a region of lower pressure in the CP forecasts (i.e. approximately 10°N and 130°E at 500 hPa and 850 hPa), whilst elsewhere the geopotential height is generally similar in both the global and CP forecasts (i.e. regions to the north and level with
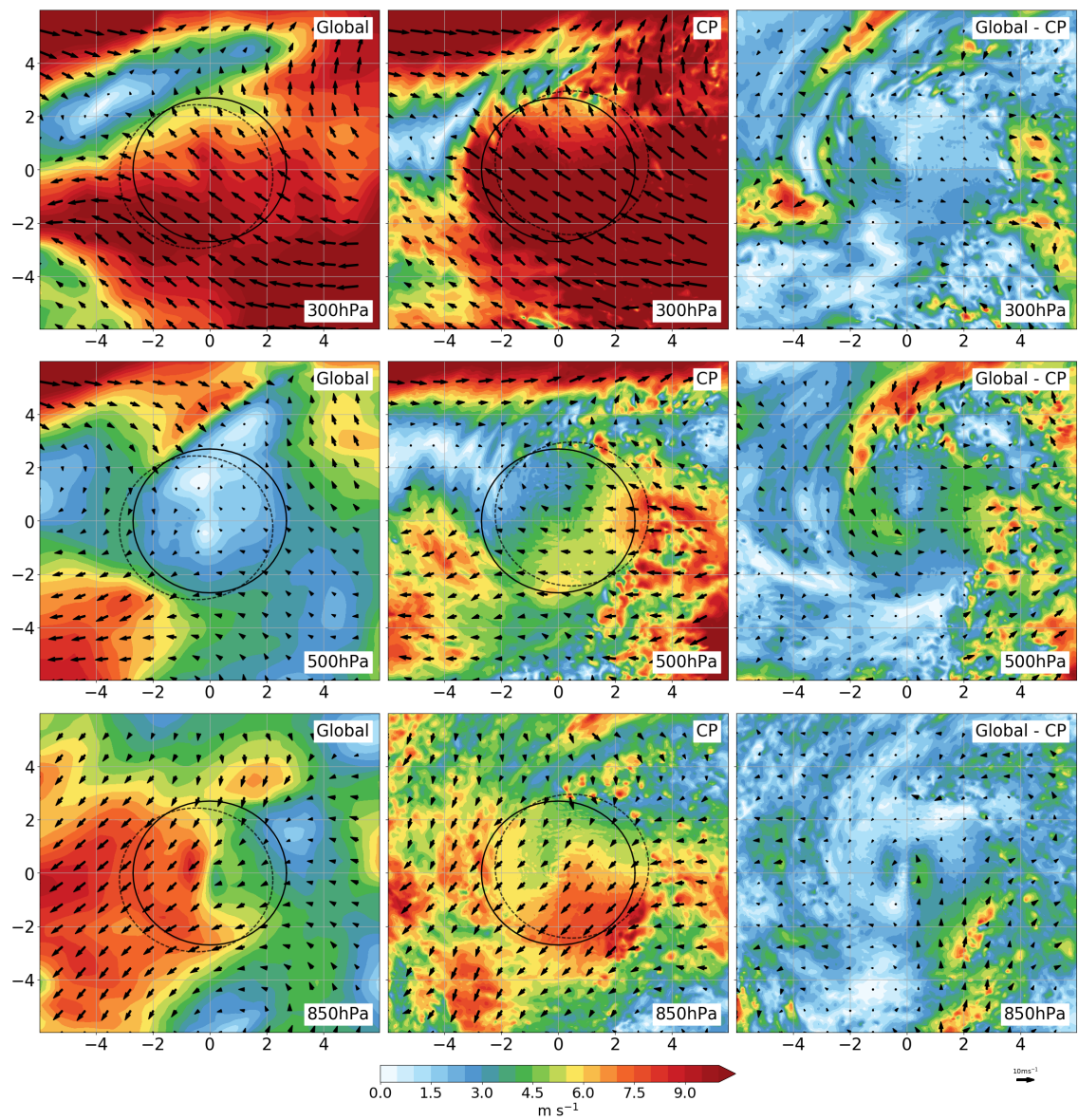
Figure 6.15: As in Figure 6.14 but for different pressure levels.
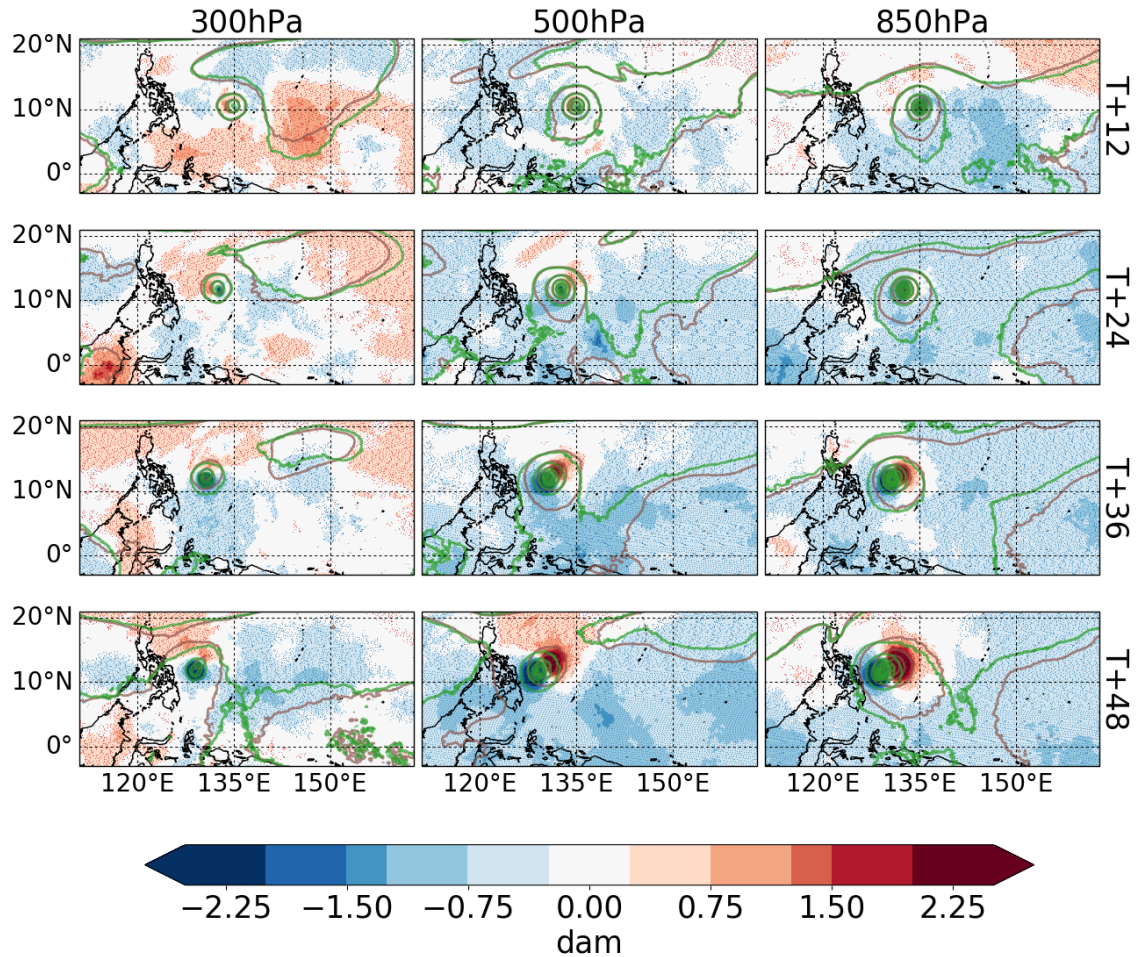
Figure 6.16: Geopotential height differences between the global and convection permitting ensemble averages, for the ensembles initialised at 1200 UTC 3 December. Shading is of the geopotential height difference (Convection permitting - global). The brown contours are of the global ensemble average geopotential and the green contours of the CP ensemble average geopotential (contoured every 3 dam). The plots on the left are at a height of 300 hPa, in the middle at 500 hPa and on the right at 850 hPa. Time increases each row by 12 hours from T+12 at the top. Stippling indicates differences are statistically significant in the 95% confidence interval.

the TC). These differences are consistent with the steering wind differences. For example, at T+24 and 500 hPa, there is a geopotential height difference of 1.5 dam between the global and CP ensemble averages at approximately 10°N and 130°E (with the global forecasts having the greater geopotential height). In the region of the storm (approximately 12°N and 132°E) there is a small dipole due to slight positional differences, however elsewhere the differences are close to zero. Thus, the geopotential height gradient gradient is greater in the CP forecasts, inducing a more easterly steering flow for Hagupit compared to the global forecasts.

Stippling in Figure 6.16 shows areas in which the geopotential difference is statistically significant in a 95% confidence interval. The statistical significance is calculated using a bootstrapping method. Random groups of 12 ensemble members from both the global and CP forecasts are chosen, without replacement. This is repeated 300 times with the difference between the two groups calculated each time. Using the sample of 300 differences a 95% confidence interval is calculated. Differences in the global and CP ensemble average comparison which are outside of this 95% confidence interval are statistically significant. Note that almost all differences in Figure 6.16 are statistically significant. This indicates that the differences between the model configurations are much greater than differences between ensemble members in the same configuration.

Once the position of the TCs in the global and CP forecasts deviate, positional differences along with environmental differences become important. Figure 6.17 shows the ensemble averaged, depth averaged streamlines of the CP forecasts. The shading shows differences between the global and CP steering winds, with positive differences indicating stronger steering winds in the CP forecasts. At T+12 both the position and the steering winds between the ensemble averages are similar. However at T+36 there is stronger steering winds in the CP forecast, caused by differences in geopotential height to the south, which leads to positional differences by T+60. At T+60 and T+84, whilst there are still some differences between the environments in the CP and global forecasts, as shown by the shading, the positional differences are also important. For example, if the CP forecast predicted Hagupit to be where the
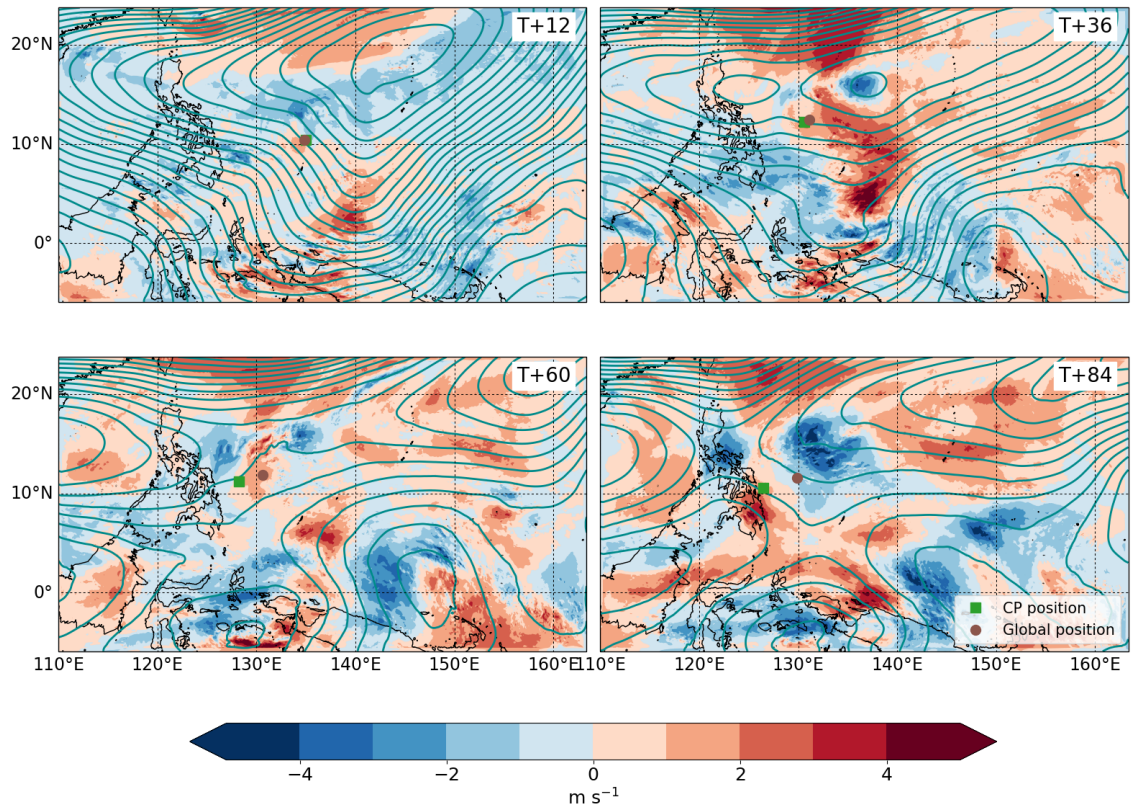
Figure 6.17: Depth averaged (850-300 hPa) TC removed streamlines averaged across all CP ensemble members (contours). Shading shows the differences between the ensemble averaged CP and global storm-removed environmental winds (CP - global). The green square and red circle are the positions of the ensemble average CP and global forecasts, respectively, at the relevant lead time. Forecast initialised at 1200 UTC 3 December 2014.

global forecasts predicted Hagupit to be at T+84, then the steering flow would have a more northerly component. Figure 6.17 also shows the steering flow causes the south-west turn in the CP forecast. At T+60 the storm is embedded in a south-west flow, to the south of the bifurcation point which was discussed in Chapter 5.

As the global model provides lateral boundary conditions for the CP model, the cause of the environmental differences to the south of the storm must be caused by processes within the CP domain. One possible cause of the geopotential differences is the enhanced convection to the south of Hagupit. During the time of Hagupit, there was significant flooding due to heavy precipitation in Indonesia (Ismail and Siadari, 2017). Such large scale precipitation events can interact with the environment in similar ways to a TC - through outflow of the storm and release of latent heat. It seems plausible that the different representations of convection in the CP and global forecasts cause differences in the region to the south of the storm which ultimately

has a significant impact on the TC track.

This section compared the differences in the environments of the storms between the global and CP ensemble forecasts and showed that these differences are able to explain the steering flow differences found in Section 6.3. The steering flow differences are only half of the story and the next section will investigate how differences in the structure of the storms can lead to different tracks.

6.5   Impact of Vertical Wind Shear on Hagupit

Section 6.3 demonstrated how differences in the global and CP tracks are partly due to differences in the steering winds and partly due to differences in how the TC responds to the steering winds in the global and CP simulations. The former was investigated in Section 6.4. In this section, Hagupit's response to strong vertical wind shear in the CP and global forecasts is investigated. Prior to landfall Hagupit weakened due to strong shear. This is shown in the steering winds (e.g. Figure 6.15) where there are much stronger winds at upper levels than at lower levels. It was shown in Section 6.3 that the TCs in the global simulations stall, moving slower than the storm-removed environmental winds, whereas the TCs in the CP forecasts move slightly quicker than the steering flow. In this section the structure of the storms is compared to understand why the storm in the global forecasts stalls whilst the storm in the CP forecasts does not.

The vertical wind profiles are shown at three different times in Figure 6.18. The shear is calculated by averaging environmental winds over a large $6° \times 6°$ box centred on the location of the storm. To ensure the definition of the shear was suitable both the size of the box and location of the box was perturbed but the conclusions remained the same and only the results using the $6° \times 6°$ box are shown. The shear is similar in both the global and CP forecasts. From T+24 up to T+48 the shear increases substantially. At upper-levels the winds remain strong and in a north west direction, however at lower levels the winds weaken and change from easterly to mainly northerly. The increase in shear is caused by changes in winds at lower levels
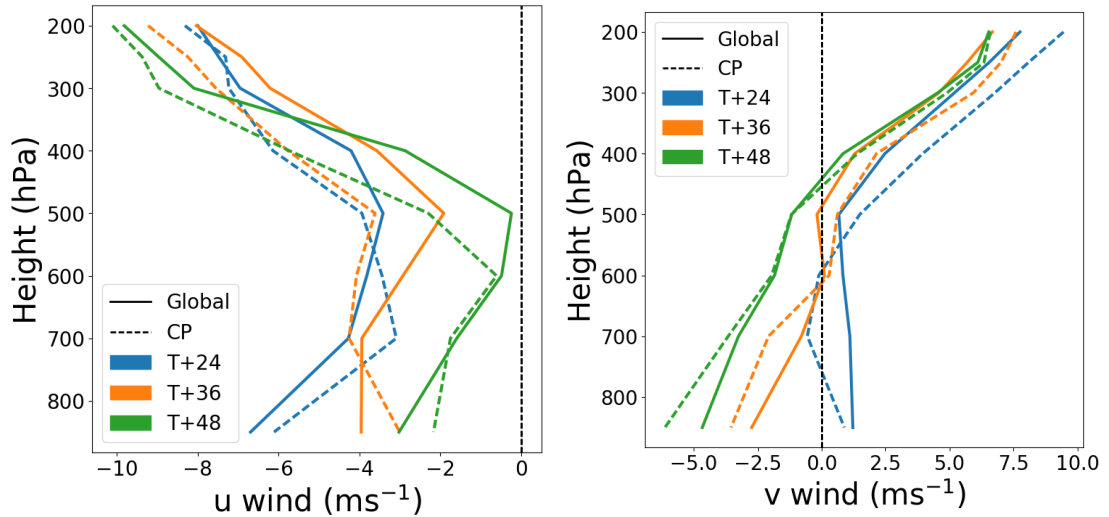
Figure 6.18: Comparison between the ensemble averaged vertical wind shear in the global and CP forecasts. Shear is calculated using storm removed winds averaged over a 6° box centred on the storm. The profiles on the left are of the zonal wind (u) and on the right of the meridional wind (v). Forecast initialised at 1200 UTC 3 December 2014.

(changing from a westward direction at T+24 to a southward direction at T+48), however the strongest winds occur at the upper levels.

In the global forecasts the storm does not travel as far west as the steering wind predicts it to. This suggests that the storm is not interacting with the upper level winds. Comparing the azimuthal and radial velocities in the storms suggest that this may indeed be the case. Figure 6.19 shows the azimuthal winds in a cross section of Hagupit orientated in the direction of the shear vector. Here, the shear vector is $\hat{\mathbf{u}}_{200} - \hat{\mathbf{u}}_{850}$ where $\hat{\mathbf{u}}_{200}$ and $\hat{\mathbf{u}}_{850}$ are the environmental winds averaged in a $6° \times 6°$ box centred on the storm location at 200 hPa and 850 hPa, respectively. The orientation of the vector is shown by the number in the top right, measured in degrees from north (i.e. $-45°$ is in the north-west direction). In the global model (Figure 6.19) the storm tilts under large vertical wind shear. Initially a tall symmetric vortex, by T+48 the eye is tilted significantly down shear, with anticyclonic winds appearing at 200 hPa on the upshear side. This tilting continues further at T+60, when the shear is at a maximum. As the storm tilts the depth decreases. Therefore, the storm is no longer being steered by the upper level winds. Instead these winds simply act to shear away the vortex at upper levels.

In comparison, the CP forecast is much more resilient to vertical wind shear (Figure

(a) T+24

(b) T+36

(c) T+48

(d) T+60
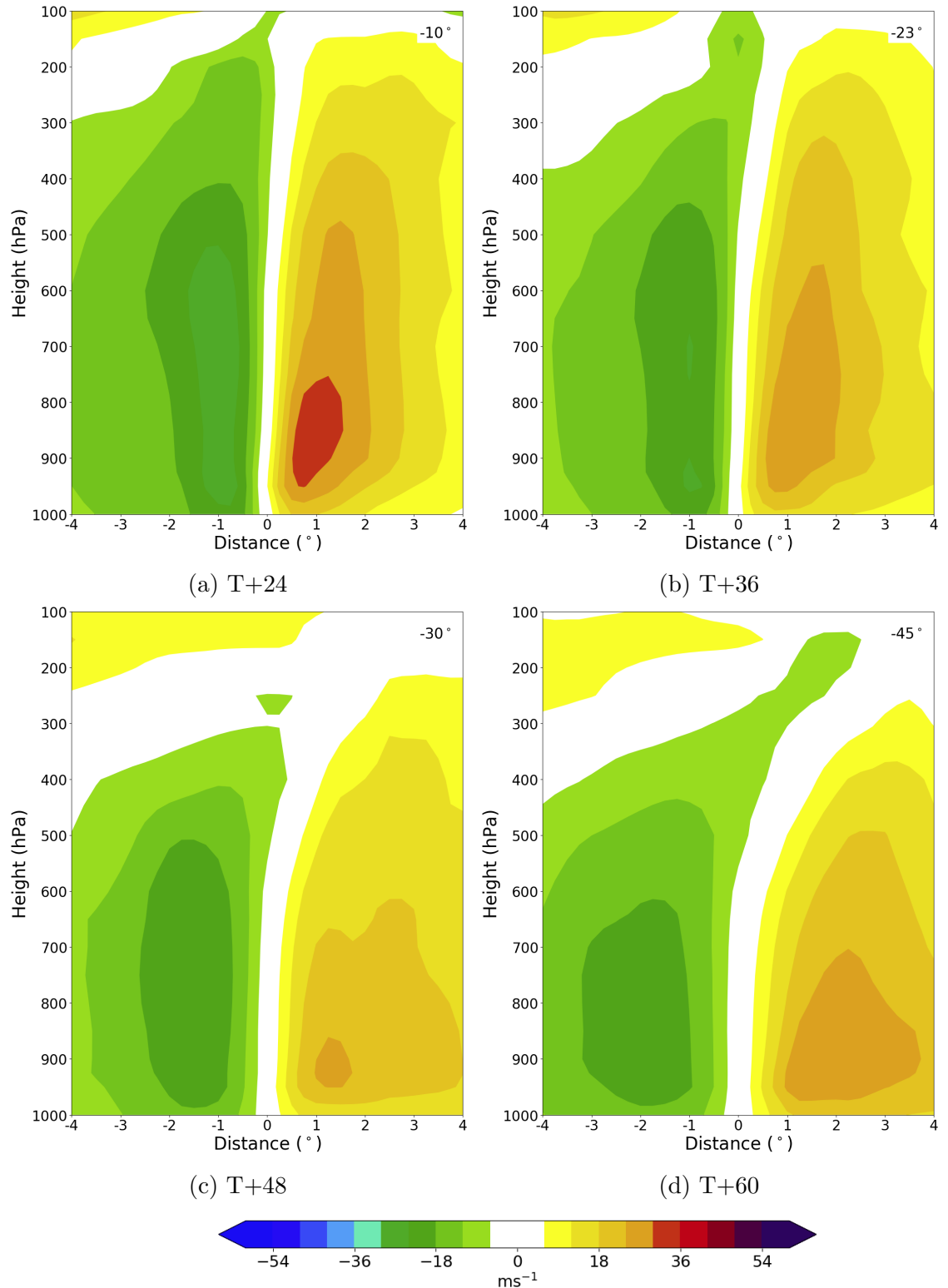
Figure 6.19: Azimuthal wind (shaded) cross section through the centre of the storm in the direction of the shear vector (shown by the number in the top right) using ensemble member 0 from the global forecast initialised at 1200 UTC 3 December 2014. The downshear region is to the right. The storm motion vector is subtracted from the winds before calculating the azimuthal wind. Numbers on the x-axis are approximate distances in degrees.

6.20). The storm in the CP forecasts remain upright and the vortex remains strong at upper levels. Therefore, the storm continues to be influenced by the steering flow at 300 hPa and above. This explains why there is a deviation of the actual tracks compared to the environmental wind tracks (Figure 6.11). The global model stalls as the strong upper level winds just shear the storm away, whilst the CP model travels further than the mean steering flow between 850-300 hPa as it is also likely influenced by steering winds above 300 hPa.

To summarise the above for each ensemble member across all times, the top of the storm is compared to the vertical wind shear for each ensemble member. Calculating the depth of the storm is non-trivial as there is no clear boundary of what is a TC and what is part of a TC's environment. Here, the depth of the storm is defined as the vertical layer from the surface up to the top height of the storm. The top height of the storm is defined as follows. The relative vorticity is first azimuthally averaged about the centre of the TC. The maximum relative vorticity of the whole storm is found. This is usually at a height of approximately 850 hPa. Starting at the top the maximum relative vorticity at each height is then calculated. The top height of the storm is defined as the height at which the maximum relative vorticity at a particular height first exceeds 10% of the maximum relative vorticity of the whole storm. This definition allows for a comparison between the global and CP forecasts. It is preferable to defining an arbitrary value of relative vorticity as it accounts for the differences in intensities of the storms between the two configurations.

Figure 6.21 compares the ensemble averaged storm top height to the ensemble averaged shear. It demonstrates that as the shear increases in both models, the storms react in very different ways. In the CP forecasts the depth does not significantly change. However, in the global forecast the storm's top height decreases towards 500 hPa. As the shear decreases the storm recovers and the top height of the TC increases back up towards 200 hPa. Recall from Figure 6.11 that at the later times in the forecast the differences in motion can be explained completely by the differences in the storm-removed environmental winds, thus the fact that the storm depth increases as the shear decreases supports the idea that the wind shear and subsequent

T+24

T+36

T+48

T+60
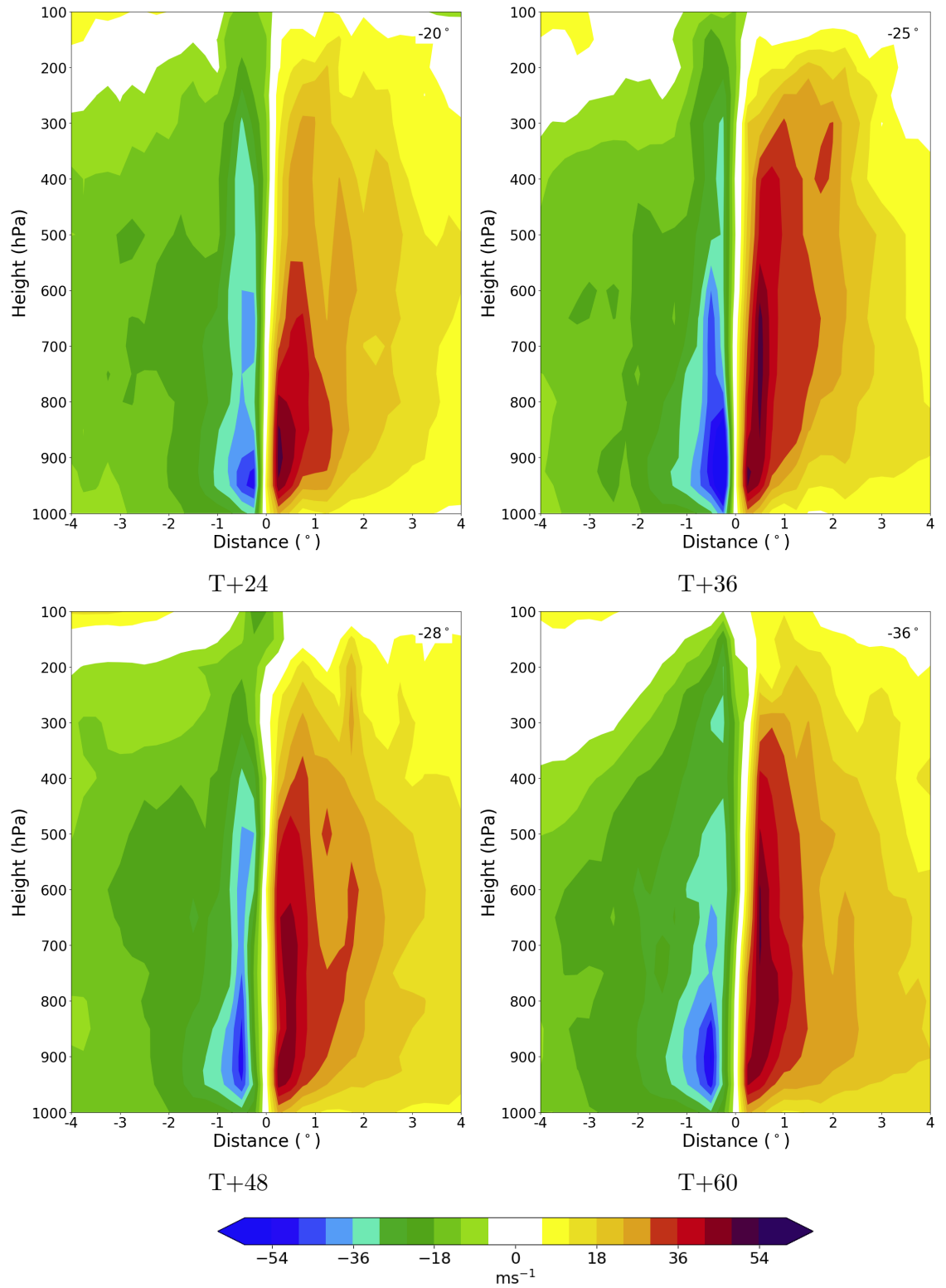
Figure 6.20: As in Figure 6.19 but for ensemble member 0 of the CP forecast initialised at 1200 UTC 3 December 2014.
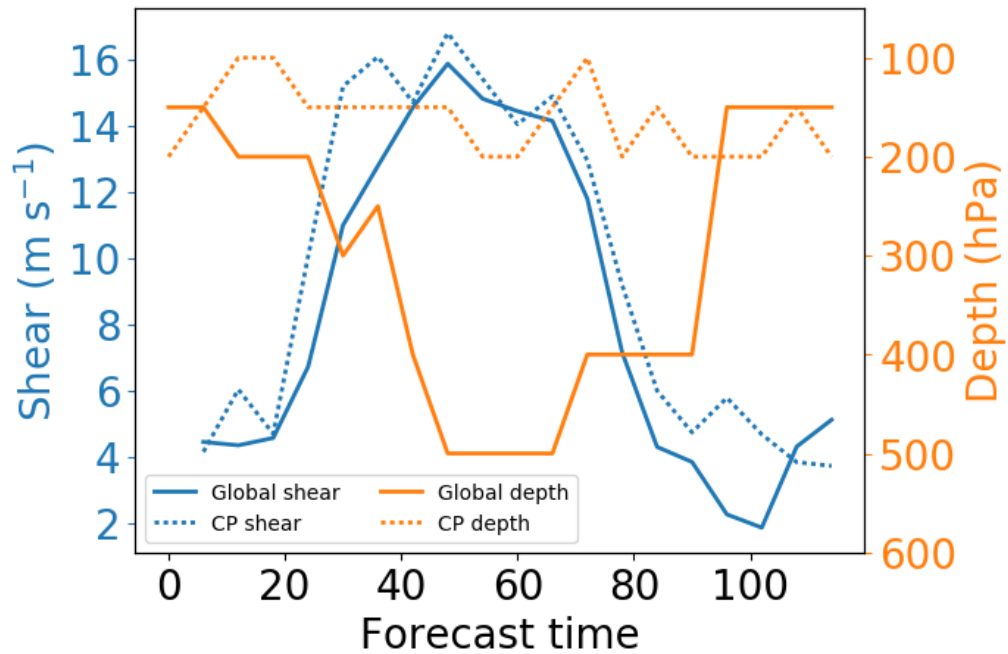
Figure 6.21: Comparison between of the environmental shear and the TC top height (indicated here by depth) in the global and CP forecasts initialised at 1200 UTC 3 December 2014.

decrease in storm depth is the cause of the global TCs stalling.

A TC tilting under vertical wind shear is not a new concept and has been the focus of research for many years (e.g. Jones, 1995). Typically the shear causes the storm to tilt downshear and to the left, causing convective asymmetries. This often leads to a weakening of the storm, although procession and subsequent realignment can often trigger a period of rapid intensification, a scenario which NWP models often struggle to predict.

The reasons why the TCs in the CP forecast do not tilt and shear away whilst the TCs in the global forecasts do likely relates to the intensity of the TCs in the different simulations. The TC is much stronger in the CP forecasts and thus has higher inertial stability at all vertical levels. This will make it more resilient to the strong upper levels winds. Another potential cause is due to differences in the outflow of the storm. Ryglicki et al. (2019) used Bernoulli's equation to describe how the outflow of the storm can cause a boundary to oppose the upper level winds and thus impact of shear on the TC. They showed that this situation sometimes occurs before rapid intensification.

Along with the environmental differences discussed in Section 6.4, structural differences between the global and CP configurations can ultimately cause differences in the TC tracks due to the differences in the storm's interactions with upper level winds. Understanding why the CP forecast was resilient to the wind shear when the global forecast was not may be important future work to limit the track and intensity errors of storms in the future, especially as CP ensemble become more common.

6.6   The GA6, 4.4 km forecast

The Par-Hi ensemble in section 6.2 is intriguing as the spread was similar to the global model yet some ensemble members took a south-west turn similar to that of the CP ensemble. In this section we explore the environment of the Par-Hi ensemble along with how the storm responds to vertical wind shear in this model configuration.

The Par-Hi ensemble can conveniently be split into two groups of six according to their tracks (Figure 6.22) - the west group and the north group. Broadly the west group behaves like the CP forecasts as each ensemble member takes a south-west turn and the storm is predicted to travel further across the Philippines than it is in the landfalling members of the global ensemble. The north group behaves more like the global model. Each of the ensemble members predicts the storm to slow and later turn to the north. Whilst not every global ensemble member turns to the north, the stalling of the storm earlier on does occur in each of the ensemble members.

As with the global and CP comparisons, the contribution of the storm-removed environmental winds to the differences in the motion of the storm between the global and CP groups is shown in Figure 6.23. Here, the environmental winds contribute much more to the positional differences than in the global and CP comparison (Figure 6.11).

The environments of the two groups are compared using geopotential height in Figure 6.24. The differences are smaller than in the global/CP comparison in Figure 6.16. Earlier in the forecast there is little difference between the group means, and there
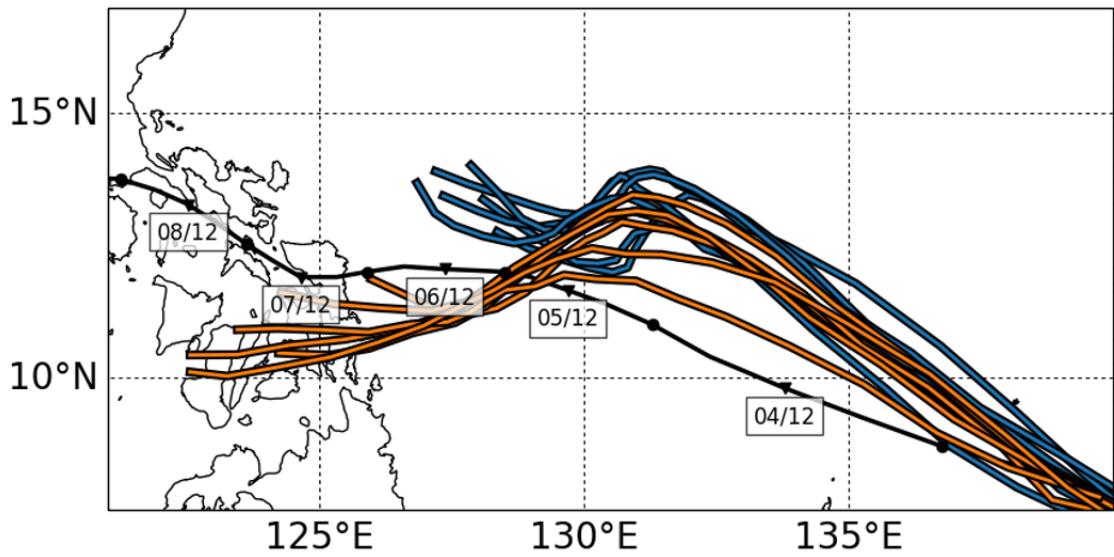
Figure 6.22: Track forecast of the Par-Hi forecast split into two groups according to location. Blue tracks are the storms which turn north and orange tracks are the storms which go west.
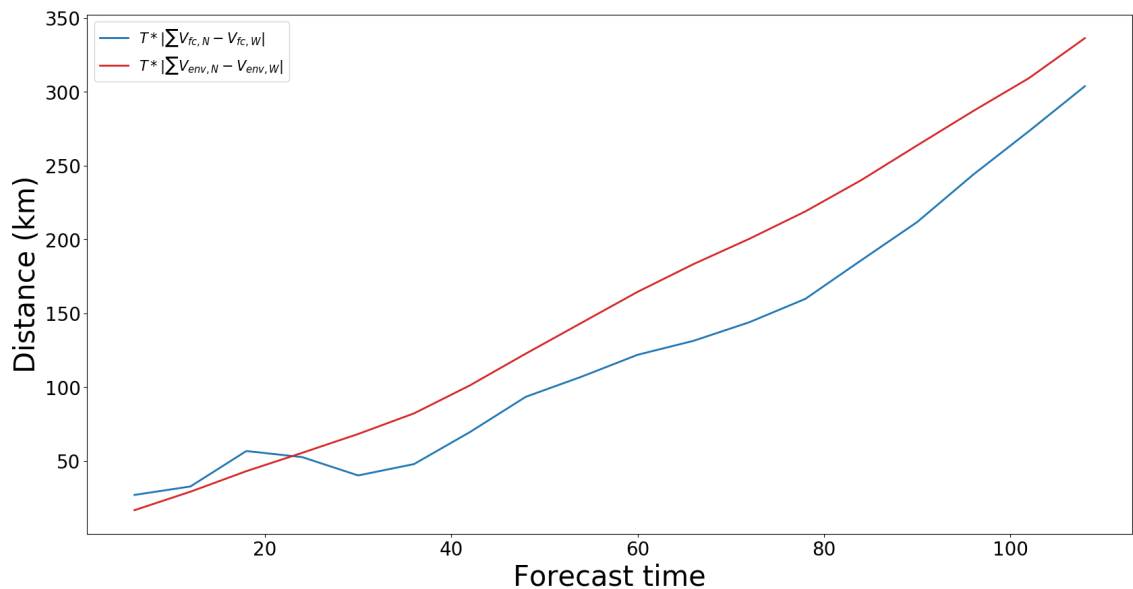
Figure 6.23: Comparison between the average distance between the forecasted positions of the north and west group to the average distances between the groups if they were exactly steered by the steering flow.
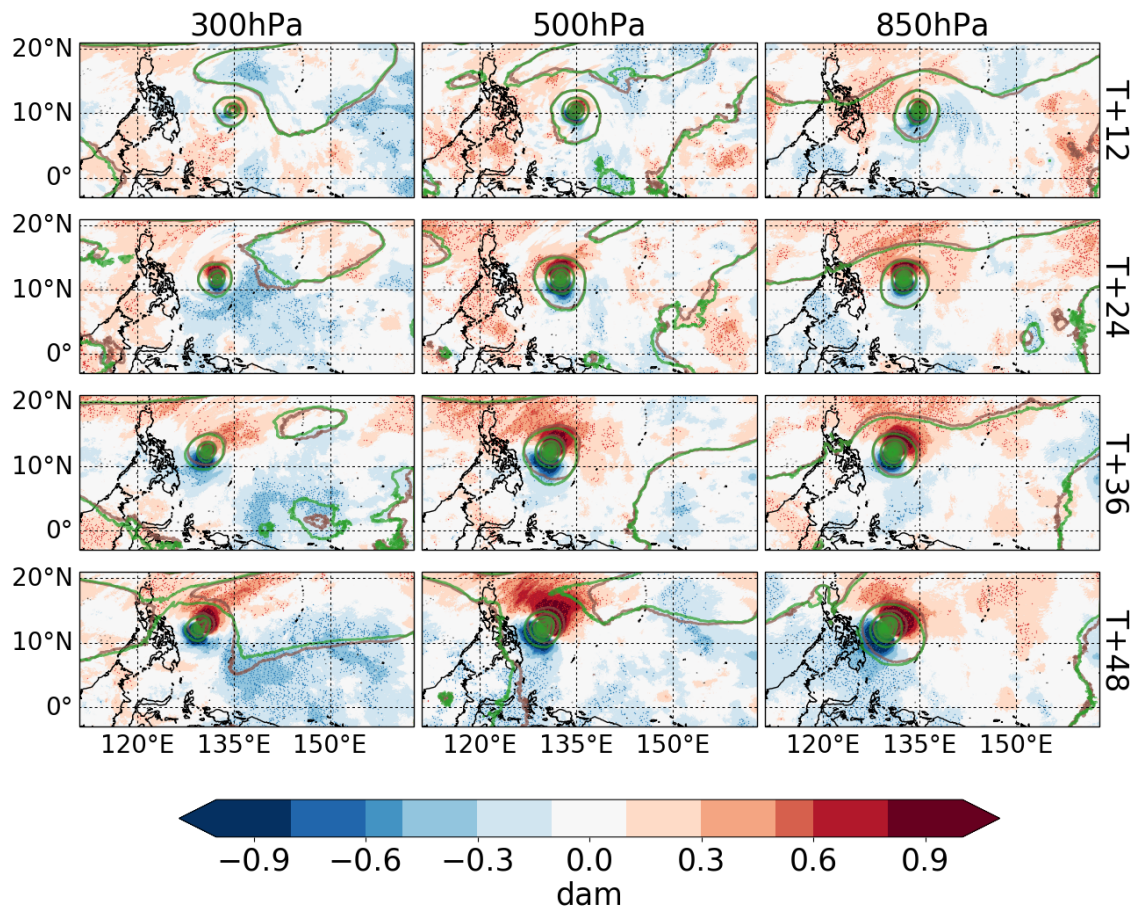
Figure 6.24: As in Figure 6.16 but for comparisons between the west and north (west-north) groups of the Par-Hi ensemble.

is also little separation between the forecasted TC positions in the two groups of ensemble members. After T+24 there are larger difference between the strength of the anticyclone to the east of the storm and the geopotential height to the north. In particular, the group that moves to the north is associated with a stronger anticyclone. This stronger anticyclone induces a geostrophic wind component to the north which matches the motion of the storm in that group. To the north of the storm, the west group are associated with stronger geopotential heights. The induced flow from these differences would lead to a stronger westward propagation of the TC. Again the statistically significant differences are highlighted by stippling in Figure 6.24 and calculated using the same method as outlined above.

When comparing ensemble averages it was found the environment of the Par-Hi ensemble closely matches the global environment as opposed to the CP environment. The maximum absolute difference in geopotential height on any level at any location between the global and Par-Hi ensemble averages was less than 1 dam, compared to

over 2 dam for the comparison to the CP model. In general the difference between the Par-Hi simulations was close to zero at all locations whereas comparing the CP to the Par-Hi ensembles gave a similar result as Figure 6.16 (not shown). Unlike the comparisons between the global and CP forecasts in Section 6.4 which used the full ensemble, comparisons in this section involve ensemble members which have different initial conditions and boundary conditions (supplied by the global forecast). In Section 5.5 two groups (NORTH and WEST) of global ensemble members were compared using geopotential height (Figure 5.10). Each group contained four ensemble members from the global forecast initialised at 1200 UTC 3 December along with four ensemble members from the forecast initialised at 0000 UTC 4 December. Each of the ensemble members in the NORTH global group from Section 5.5 are also in the north Par-Hi group in Figure 6.22, whilst each of the global WEST group are in the Par-Hi west group. This demonstrates that the results of Chapter 5 are relevant here. The global forecasts provide boundary conditions for the Par-Hi forecasts and thus the differences between the WEST and NORTH groups which develop in the global forecasts influence the Par-Hi forecasts.

In Section 6.4, it was suggested that the difference in the environments between the CP and global forecasts may be caused by the representation of convection to the south of the storm in the two configurations. Whilst this hypothesis is not investigated in detail, the analysis here supports the hypothesis. The Par-Hi ensemble, which has the same science configuration as the global forecasts, matches the environment of the global forecasts more so than the CP forecasts. Further, the differences between the north and west groups, which broadly behave like the global and CP ensembles respectively, are mainly in the strength of the anticyclone to the east of the storm, not in the geopotential strength to the south of the storm. The only time when the geopotential to the south of the storm changes is when the CP science configuration is used.

Aside from the environment itself, the second thing to investigate between the two groups of ensemble members is the storm's reaction to the vertical wind shear. As the environment of the Par-Hi simulations is similar to the global model, yet the

Par-Hi ensemble shows characteristics similar to both the global and CP forecasts, it is unsurprising that the structure of the storm is much more similar to the CP forecast. Under the strong vertical wind shear, the storm does not tilt or shear away in either group. Instead the structure remains strong at all levels (Figure 6.25). This explains why the storms do not stall as much as in the global model and why some ensemble members turn to the south west, without reaching the area of weak steering. Figure 6.25 shows the vertical structure of ensemble member 0 in the Par-Hi forecast, however, ensemble members from both groups show the same results.

The Par-Hi ensemble was interesting because it has characteristics of both the global and CP ensembles. The spread of the Par-Hi ensemble was significant and similar to the global model as the environment was more like the global model. However, the ensemble members which made landfall generally behaved like the CP ensemble - making a systematic turn to the south-west and travelling further across the Philippines than those which made landfall in the global forecasts. The reason for this is because the structure of the storm did not change under large vertical wind shear. The strong upper level winds did not impact the structure of the TC, but rather contributed to the steering of the TC. Therefore the ensemble members in the Par-Hi ensemble which made landfall (and which were also the same ensemble members making landfall in the global forecasts) experienced stronger depth-averaged steering flow than those in the global forecast.

6.7   Summary and Conclusion

The CP track forecasts for Hagupit behaved markedly different to the global forecasts. Each of the CP ensemble members turned to the south-west before landfall, away from the best track line. In comparison the global forecasts predicted Hagupit to slow significantly before landfall, with some ensemble members predicting the storm to subsequently turn to the north and miss the Philippines altogether. The spread in the CP forecasts remained small, whilst the spread in the global forecasts was large. The aim of this chapter has been to understand these discrepancies between the two sets of simulations.
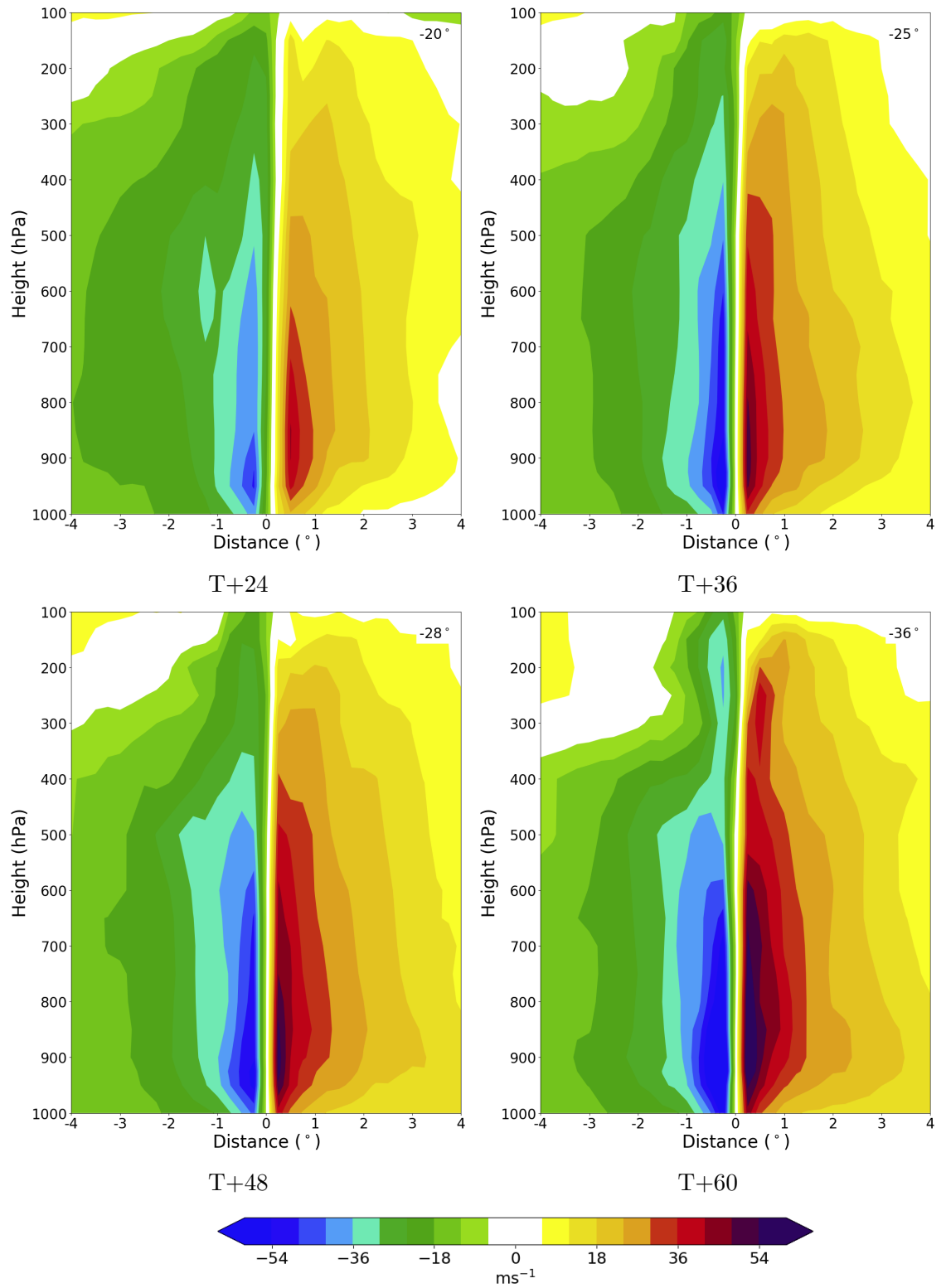
Figure 6.25: As in Figure 6.20, but for ensemble member 0 of the Par-Hi ensemble.

A series of experiments in Section 6.2 showed that changing the resolution of the global model to 4.4 km, but not changing the physics (i.e. the Par-Hi ensemble) leads to a reduced, but still significant track spread with some ensemble members behaving like the CP members by turning to the south-west and passing over the Philippines. The fact that some ensemble members of the Par-Hi forecast were still predicted to turn to the north shows the importance of the change in physics in causing the systematic turn to the south-west in the CP forecast.

Section 6.3 compared the tracks to the storm-removed steering winds of the different ensembles. In particularly it was shown that the difference in tracks was due to a combination of the steering winds and how the TC reacted to the steering winds in the simulations.

The main differences in the environments between the CP and global forecasts, which lead to the differences in the steering winds, were due to lower pressure to the south of the storm in the CP forecasts compared to the global forecasts (Section 6.4). This caused a stronger geoptential gradient and thus a stronger easterly geostrophic flow through the TC. As such, the TC in the CP forecasts moves further to the west than the global simulations after 24 hours of the forecast. During the time in which CP forecasts experienced lower geopotential heights to the south of the TC, there was a broad region of enhanced convection. It is speculated that this difference in geopotential height is related to the representation of the convective systems to the south by the different science configurations.

The other key component in determining the track of the storms in the ensemble is vertical wind shear. A link was found between the shear magnitude and the height of the storm in the global model, however, the height remained unchanged under large vertical wind shear in the CP and Par-Hi forecasts. Rather than steering the storm, the strong upper level winds in the global forecast act to shear away the TC core. The upper level winds are the strongest winds and thus the global model stalls whilst the stronger CP forecasts continue to propagate the storm.

The Par-Hi forecasts can provide insight into the impact of both the environmental differences and the structural differences between the global and CP forecasts. The

forecasts of Hagupit in the Par-Hi ensemble all had similar structures and intensities to the CP forecasts. However, the environment was much more similar to the global forecasts. In the Par-Hi forecasts, the TCs do not shear away and stall. Further, the forecasts that predict the TC to move to the north are the same ensemble members as those in the global forecast which predict the storm to move to the north, demonstrating that the increased spread in the global forecasts compared to the CP forecasts is mainly due to the environmental differences rather than the storm structure differences. The fact that the environment, particularly to the south of Hagupit, is similar to the global forecasts rather than the CP forecasts supports the hypothesis that the region of enhanced convection to the south of the TC is represented differently and causes environmental differences in each of the simulations.

The Par-Hi forecast was produced as a series of experiments and was not analysed in great detail. It would be interesting to compare the results of the Par-Hi forecast to the CP forecast to gain an understanding of the impact of parameterised convection in TCs. For instance, it would be of interest to compare the resolved updrafts and rainfall rates in the Par-Hi and CP models. Similarly, it would be interesting to understand the impact of increased resolution on the CP forecasts. At a higher resolution more convective processes would be fully resolved, it would be of interest to see if this impacts Hagupit's track, and if so if there is a threshold at which increased resolution no longer impacts the track.

Whilst differences between the TC environments and the vertical structure of Hagupit in global and CP forecasts have been highlighted as the causes of deviations in the track forecasts, it is not clear which type of simulation performs best at predicting the evolution of Hagupit. The Par-Hi forecast implies that the structure of the TC was more accurate in the CP forecasts, and it was the environmental differences which caused the CP forecasts to turn to the south-west. The spread of the global forecasts was greater than the CP forecasts, and this was related to the storm's environment in the global forecasts along with the position Hagupit is in when it stalls due to the large vertical wind shear. However, it is plausible that this is a

case of getting the right result for the wrong reason. Hagupit was a category-5 TC, and the global forecasts predict the storm to shear away whilst it was in reality close to peak intensity. Indeed, the Par-Hi ensemble suggests that had the TC been more resilient to the vertical shear then there would have been an improvement in the average direct positional error and only a small decrease in spread. The sparse observations of Hagupit make further comparisons difficult and motivate a more systematic study of TCs in global and CP forecasts.

In conclusion there are two key processes which cause the differences between the global and CP ensemble forecasts. The first is differences in the steering winds (of approximately $1\,\mathrm{m\,s^{-1}}$) early in the forecast (from approximately 1200 UTC 4 December to 1200 UTC 5 December), caused by slight differences in the environments. The second is the storm in the CP forecasts is more resilient to the large vertical wind shear. Whilst the global forecasts stall as the shear disrupts the structure of the vortex at upper levels, the storm in the CP forecast continues to be steered by the strong upper level winds.

Chapter 7

Convection Permitting Forecasts of Haiyan and Florence

7.1 Introduction

Chapter 6 investigated the differences between global and CP forecasts of Typhoon Hagupit, highlighting the impact on the storm track of small environmental and structural differences between different simulations. Hagupit is not the only TC which features large differences between the global and CP MetUM forecasts. As shown in Chapter 4, the CP forecasts of Typhoon Haiyan contained large track errors. Whilst these errors were limited to along-track errors, i.e. the path of the storm was well predicted but the timing was not, there is still a clear difference between the global and CP forecasts.

Another TC to contain systematic differences in the global and CP forecasts is Hurricane Florence (2018). For multiple forecast lead times, CP MetUM forecasts failed to predict the location of an inland turn to the north in the forecasts of Florence. This puzzled model developers at the Met Office as global forecasts accurately predicted the location of this northward turn. Florence was a high-impact TC, causing 53 deaths and $ 24 billion of damage. As Florence formed over the North Atlantic ocean and due to the fact that differences in the global and CP tracks occurred as the TC was weakening, it provides a good case study to test results from

the analysis of CP forecasts of Hagupit on a TC which is significantly different to that of Hagupit.

The fact that Hagupit was not the only high impact TC in which track differences between global and CP forecasts occurred demonstrates the important need to understand why there are differences and to reduce the risk of forecast busts in the future, particularly as operational CP TC forecasts become more common. Comparing the causes of track deviations between global and CP simulations of different storms can highlight some important processes which may impact the accuracy of track forecasts in the CP simulations.

In this chapter forecasts for both Haiyan and Florence are analysed, using results from the previous chapter as motivation. For Hagupit differences in the vertical structure of the TC in the global and CP simulations lead to differences in how the storm interacted with upper level steering winds. These structural differences were linked to the intensity of the storm. The stronger CP forecasts were more resilient to the strong vertical wind shear, whilst the global forecasts were sheared away at upper levels. Another difference was found in the environment of the storm in the CP and global forecasts. To the south of Hagupit there was a region of higher pressure in the global forecasts. This influenced the steering flow compared to that of the CP forecast by inducing an westerly steering current through the global forecasts of Hagupit, opposing the westwards motion. One possible cause of this difference is how the different forecasts represented the large area of enhanced convection to the south of Hagupit, and thus how this area of convection interacted with the TC's environment.

In Section 7.2 the forecast for Haiyan initialised at 1200 UTC 4 November 2013 is analysed, whilst in Section 7.3 the forecast for Florence initialised at 1200 UTC 13 September 2018 is analysed. In both cases differences in the TC structures and the steering flow will be investigated. Similarities and differences between Haiyan, Hagupit and Florence in the global and CP forecast behaviour will be summarised in Section 7.4.

7.2 Typhoon Haiyan

The CP forecasts for Typhoon Haiyan (Figure 4.6) lagged behind their global equivalents (Figure 4.5). For the forecasts initialised at 0000 UTC and 1200 UTC 4 November, this means that the CP forecast predicted Haiyan to make landfall approximately 18 hours later than the global forecasts and the best track. For the forecast initialised at 0000 UTC 5 November, much of this error in the speed of the storm was rectified, although the CP forecasts did still lag slightly behind the global forecasts.

In this section the CP forecast initialised at 1200 UTC 4 November is compared to the global forecast initialised at the same time. This initial time is chosen as despite the error in translation speed, the path of the storm is still well predicted in the CP forecast. The location of landfall is predicted to a high degree of certainty, but the timing was incorrect. For the global forecasts both the location and timing of landfall were forecast accurately (to within a few hours).

Figure 7.1 compares the paths of the CP ensemble average relative to the global ensemble average. The CP forecasts initially move slightly further south than the global forecasts. After approximately 12 hours the CP forecasts begin to lag behind the global forecasts (shown by the increase in longitude difference in Figure 7.1 as the TC moves to the west). The TC in the CP forecasts continues to move slower than the global forecasts up until T+96. At this point the storm moves at a similar speed in both forecasts. The initial southward motion of the CP forecasts relative to the global forecasts is gradually decreased up until T+96. Here, the CP ensemble average is slightly to the north of the global ensemble average. Between 72-96 hours, when the TC makes landfall in both types of simulations, the latitude difference is small. Unlike Hagupit (Figure 6.8), the deviation between global and CP forecasts for Haiyan occurs from the very start of the forecast (the forecasts for Hagupit remained similar for the first 24 hours, before diverging).

To calculate the steering winds in both the global and CP forecast the TC is removed using the method outlined in Section 3.5.2 with $r_0 = 300\,\mathrm{km}$ and $p_t = 250\,\mathrm{hPa}$
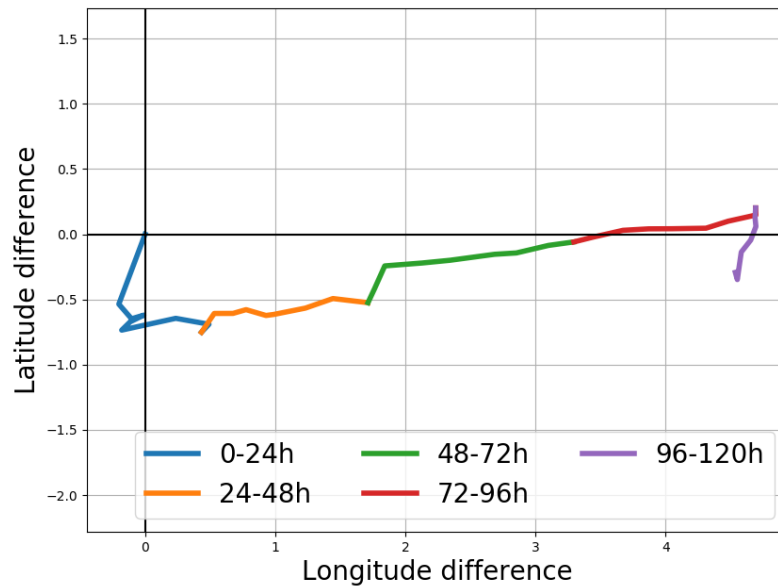
Figure 7.1: The ensemble average position of the CP forecasts of Haiyan relative to the global ensemble average position. Forecasts initialised at 1200 UTC 4 November 2013.

(the values found to give, on average, the lowest residual vector). Figure 7.2 shows that almost all of the differences between the global and CP forecast tracks can be accounted for by the steering winds which the TCs experience. Figure 7.2 also shows that these differences in steering winds differ from the start of the forecast. The positional differences not accounted for by the difference in steering winds is small (approximately 80 km after 100 hours, compared to approximately 420 km difference due to the steering winds).

The differences in steering flow indicated by Figure 7.2 may not be down to differences in the environments of the TC, but rather slight differences in the position of the storm due to the initial southwards motion of the TC in the CP forecasts relative to the global forecasts. This is demonstrated in Figure 7.3 which shows the depth-averaged steering flow of the global and CP ensemble average at T+6. Haiyan is located on the periphery of the anticyclone in a region of large horizontal wind shear. The easterly flow steering the storm is much stronger to the north than it is to the south. Differences between the environments are small, but there is a northward residual wind when comparing the global to CP forecast (i.e. the right panel of Figure 7.3). This contributes to the relative southwards motion of the CP forecasts, and thus the steering flow in which the CP forecast becomes embedded is weaker than
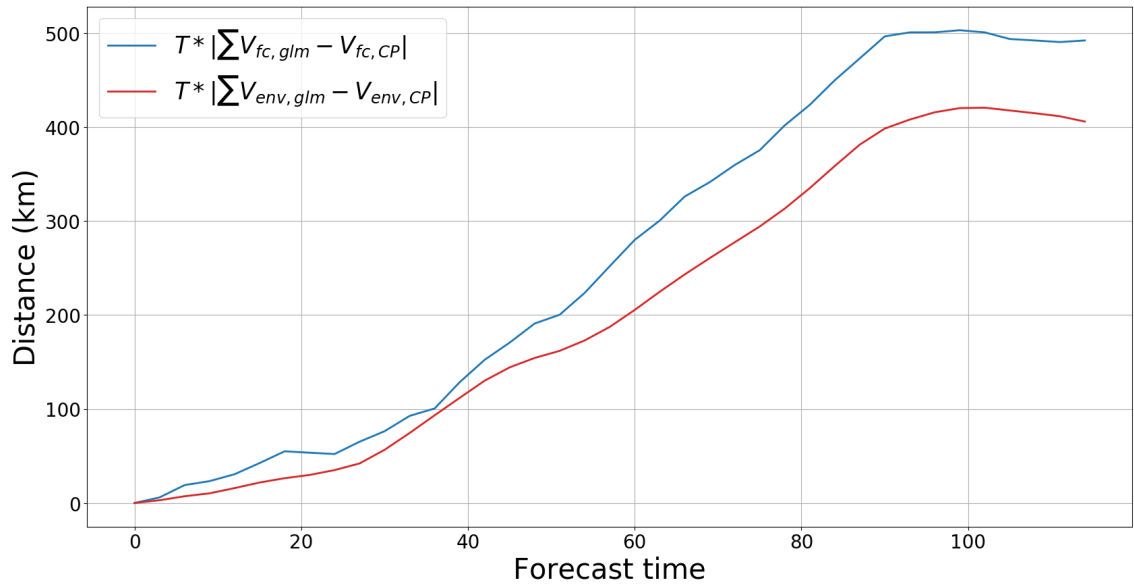
Figure 7.2: As in Figure 6.11 but for forecasts of Haiyan initialised at 1200 UTC 4 November 2013.

the steering flow the global forecast is embedded in, even at the short lead time of just 6 hours. Note that to calculate the residual in the third panel of Figure 7.3, each of the ensemble averaged winds are centred on the ensemble averaged positions. Therefore, the environment could be exactly the same but a difference in position of the storm could still cause there to be a residual in the steering, due to the fields being centred on a different location.

Later in the forecast, at T+ 48, there are east-to-west differences between the average position of global and CP ensembles (Figure 7.4). The global forecasts, which are located to the west and slightly to the north, are embedded in easterly flow that is approximately $1.5\,\mathrm{m\,s}^{-1}$ stronger than the CP forecasts. The figure also suggests that had the CP forecast been located where the average position of the global forecasts is at this point, then the CP forecasts would experience stronger steering flow.

Figure 7.5 shows the vertical wind shear profiles in a $6° \times 6°$ centred on the TC in the global and CP forecasts. A southward component of steering flow occurs at upper levels in both the global and CP forecasts. At T+12 and T+18 these upper level (i.e. above $500\,\mathrm{hPa}$) northerly winds are stronger in the CP forecasts than the global forecasts. Although the meridional component of the wind is much less than the zonal component of the wind (approximately $2\,\mathrm{m\,s}^{-1}$ compared to $10\,\mathrm{m\,s}^{-1}$), the
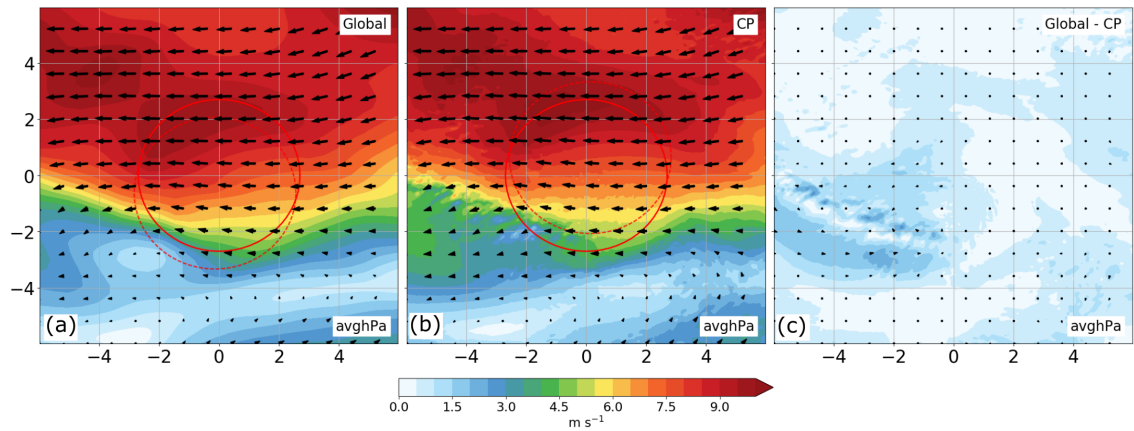
Figure 7.3: Ensemble averaged storm removed winds of Haiyan at 1800 UTC 4 November (T+6) in (a) the global and (b) the CP forecasts. The difference between the winds is shown in (c). Shading shows the wind speeds, the arrows show the wind directions. The solid red circle is the 300 km removal radius whilst the dashed red circle shows the relative position of the other forecasts. Environmental winds are centred on the storm's forecast position before averaging through the ensemble.
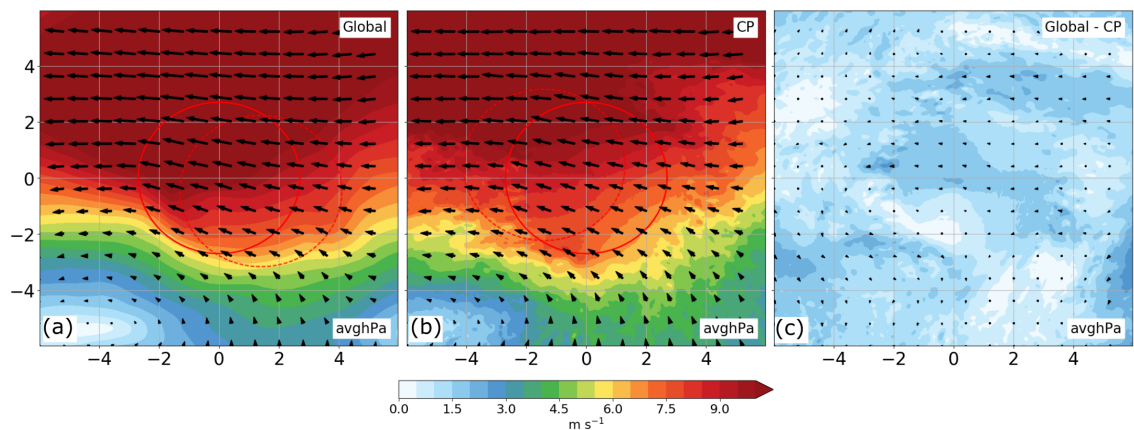
Figure 7.4: As in Figure 7.3 but at 1200 UTC 6 November (T+48).
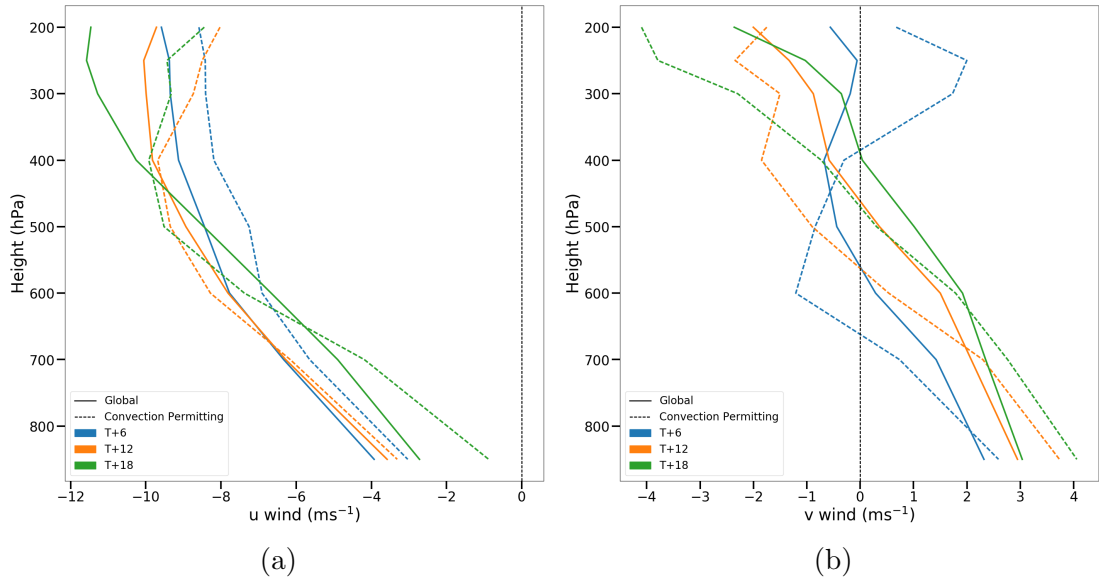
Figure 7.5: Wind profiles in the global and CP forecasts at 1800 UTC 4 November, 0000 UTC 5 November and 0600 UTC 5 November (T+6, 12, 18, respectively). Winds are calculated by averaging the (a) u storm-removed environmental wind component and (b) v storm-removed environmental wind component in a $6° \times 6°$ box centred on the forecasted location of the storm. Shear profiles are then averaged through the whole ensemble.

difference in the upper level winds is enough to push the CP towards the south relative to the global forecasts.

The comparison between the global and CP forecasts is further complicated by the large differences in intensity and structure of the storms. The global forecasts do not spin up the storm for the first 48 hours of the forecast (Figure 4.10). Therefore, as shown by Figure 7.6, the TC in the global forecasts of Haiyan remains a weak tropical disturbance for the first 48 hours, whilst the CP forecasts contract the TC as it intensifies. This has a number of impacts. The first is that there is not a clear centre of the storm, due to weak sea level pressure gradients making identifying the centre difficult. This is the reason for the "chinks" early in the global track forecasts for Haiyan. As a result comparisons of the steering flow, and in particular the third panel of Figure 7.3, may be inaccurate as the centre of the storm is not well-defined. At T+12 in Figure 7.6, the global forecast shows a minimum of sea level pressure covering a region slightly to the north of where the maximum relative vorticity is. In comparison, the CP forecast at the same time shows a clearer location of minimum sea level pressure which is at the same location as the maximum relative

vorticity.

The second impact of the weak initialisation is that, for the first 24 hours, the global forecasts for Haiyan predict the TC vortex to remain weak and to cover a broad area. Figure 7.6 shows Haiyan in the CP forecasts contracting as the storm spins up. Whilst the vorticity at the centre of the storm increases, the contour showing vorticity greater than $10^{-5}\,\mathrm{s}^{-1}$ decreases in area. In comparison the vorticity in the global forecast only slightly increases, and the $10^{-5}\,\mathrm{s}^{-1}$ contour covers approximately the same size region throughout the first 12 hours. This means that the TCs in the two simulations are likely steered by winds covering a different horizontal area. Comparing to Figure 7.3, this means that the TC in the global forecasts will interact with the stronger winds to the north, yet the CP forecasts will not. This is somewhat similar to the discussions of Tang et al. (2020), in which the size of a TC was significant in determining to what extent it is steered by nearby synoptic weather features.

The initial cause of the southwards motion in the CP forecasts is not clear. Although the steering winds comparison suggest that there is a more northerly component in the winds in the CP forecasts at T+6 (Figure 7.3), positional differences may have already caused this southward residual when comparing the steering flows. One possible cause of the southward motion is that the CP forecast spins up in an area of weaker vertical wind shear. One requirement for a TC to develop is that it must be in an area of weak vertical wind shear (Gray, 1968). As shown by Figure 7.3, the steering flow to the north is much stronger than the steering flow to the south. The main contributor to this depth-averaged steering flow is from up the upper levels (Figure 7.5). Therefore, from the region of higher relative vorticity at T+0 in Figure 7.6, it is more favourable for the TC to develop towards the south. At later times the vertical wind shear in the proximity of the storm decreases (Figure 7.7). At T+36, as the global forecast begins to intensify and develop into a TC, the shear has decreased significantly with strong easterly winds at every level.

To summarise, the differences between global and CP forecasts of Haiyan is related to movement to the south in the CP forecasts relative to the global forecasts. Due
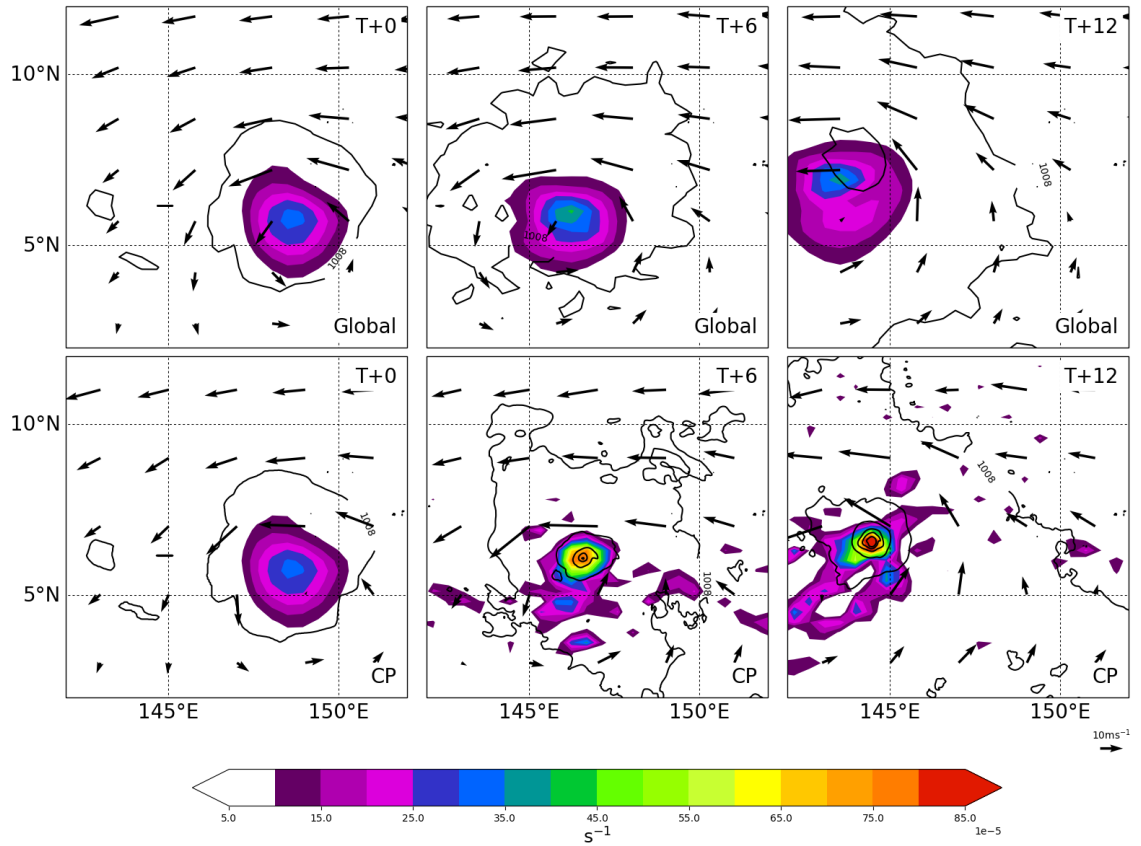
Figure 7.6: Relative vorticity at 850 hPa (shading), winds at 850 hPa (arrows) and sea level pressure (contours, every 8 hPa) of (top) the global ensemble member 0 and (bottom) the CP ensemble member 0. Forecasts are initialised at 1200 UTC 4 November 2013 with valid times of (left) 1200 UTC 4 November, (middle) 1800 UTC 4 November and (right) 0000 UTC 5 November.
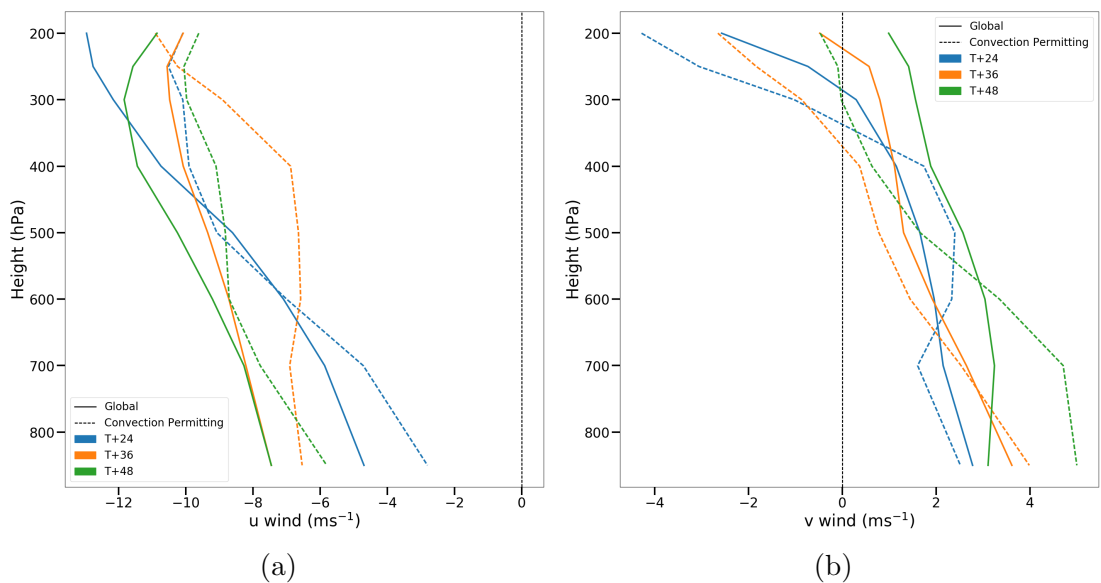
Figure 7.7: As in Figure 7.5 at times 1200 UTC 5 November, 0000 UTC 6 November and 1200 UTC 6 November.

to large horizontal wind shear, the TC initially moving to the south in the CP forecasts immediately places it in an area of weaker easterly flow. In comparison the global forecasts do not intensify the storm and instead it remains as a large tropical disturbance. This disturbance is propagated faster across the Pacific as the strong winds to the north help steer it. The cause of the relative southwards motion of the CP forecasts is unclear. Differences in the steering flow suggests that the environment causes a more southward steering of the storm. However, these comparisons are sensitive to the location of the storm, which due to the very weak TC vortex is uncertain in the global model. One plausible explanation is that the CP forecast moves to the south as that is the region most favourable for spinning the storm up. The southwards motion happens immediately, thus rather than an existing storm being steered there, it is the case that Haiyan developed towards the south in the CP forecasts as it was a more favourable region. Large horizontal shear meant that to the north, where the global forecasts are, there is also large vertical wind shear. This large wind shear is not conducive to the development of TCs.

This explanation also agrees with behaviour seen in other forecasts of other initialisation times. The forecasts initialised 12 hours earlier, at 0000 UTC 4 November, exhibited similar behaviour to the forecast investigated here. However, the difference between global and CP forecasts was reduced at 0000 UTC 5 November and there were no differences at 1200 UTC 5 November. Further, the intensity in the global and CP forecasts were similar in all initialisation times. This suggests that at later initialisation times, when the vertical wind shear near to the storm has decreased, the CP forecast develops Haiyan at a location closer to the global forecast and closer to the best track, eliminating the initial southwards deviation and thus embedding the TC in the correct steering flow.

The weak initialisation of the storm in this case has implications not just on future intensity forecasts, but also on future track forecasts.

7.3 Hurricane Florence

Hurricane Florence made landfall over North Carolina at 1100 UTC 14 September 2018. Having formed on the 31 August, Florence was a long-lived Atlantic storm. Florence reached peak intensity at 1800 UTC 11 September, with winds of $67\,\mathrm{m\,s^{-1}}$, making it a category-4 storm. Upon making landfall with winds of $40\,\mathrm{m\,s^{-1}}$, Florence weakened towards a tropical depression on 16 September. Despite the weakening, slow storm motion lead to record-breaking rainfall and catastrophic flooding over the Carolinas. This flooding resulted in 53 deaths and over $\$\,24$ billion of damage (Paul et al., 2019).

Having made landfall over North Carolina, Florence travelled inland and then turned to the north (Figure 7.8 at approximately 34°N and 82°W). Whilst the global MetUM ensemble members predict this turn to the north reasonably well (albeit the forecasts do predict the storm to travel slightly too far to the west after turning), the CP ensemble members predict the storm to travel too far inland, significantly overshooting the location of the northward turn (Figure 7.8). As with Hagupit, this is an example of a forecast bust - the CP track forecasts deviate significantly from both the best track line and from the global forecasts. Here the forecast initialised at 1200 UTC 13 September is used. However, the overshoot in the CP forecasts was observed in forecasts initialised 24 hours either side of this.

Unlike the forecasts of Haiyan and Hagupit, the intensity of Florence is similar in both the global and CP forecasts (Figure 7.9), and is also predicted with greater accuracy when compared to the best track. The forecasts for Florence were initialised as the storm was weakening and dissipating unlike the forecasts for Haiyan and Hagupit which were initialised as the storm was strengthening. After the initial time the storm is predicted to be slightly too weak. As the forecast continues, the global forecasts predict Florence to be weaker until 0000 UTC 16 September (T+72), after which the TC is weaker in the CP forecasts. However, the difference in intensity between the global and CP forecasts is small, with the errorbars in Figure 7.9 overlapping. Figure 7.9 shows the intensity of Florence in terms of sea level pressure, however the same conclusions apply when considering maximum 10 m wind speeds.
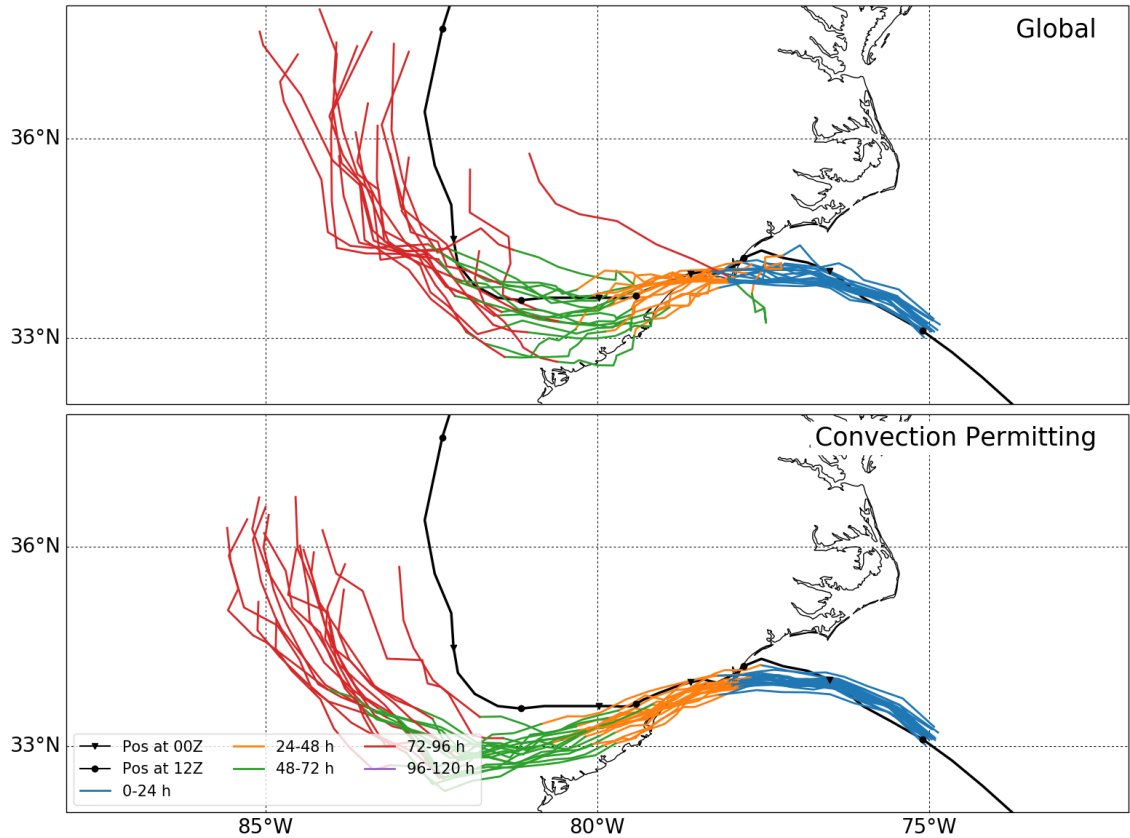
Figure 7.8: Global (top) and CP (bottom) track forecasts of Hurricane Florence initialised at 1200 UTC 13 September 2018. The black line shows the best track according to IBTrACS.
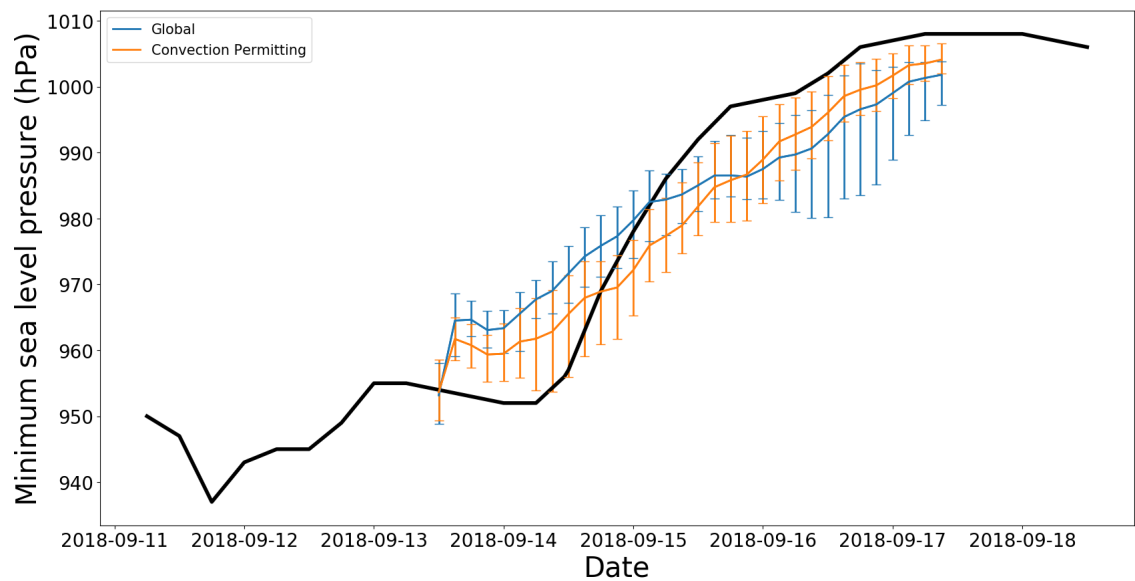
Figure 7.9: Global and CP minimum sea level pressure forecasts of Hurricane Florence initialised at 1200 UTC 13 September 2018. The error bars show the ensemble range whilst the black line is of the best track data according to IBTrACS.
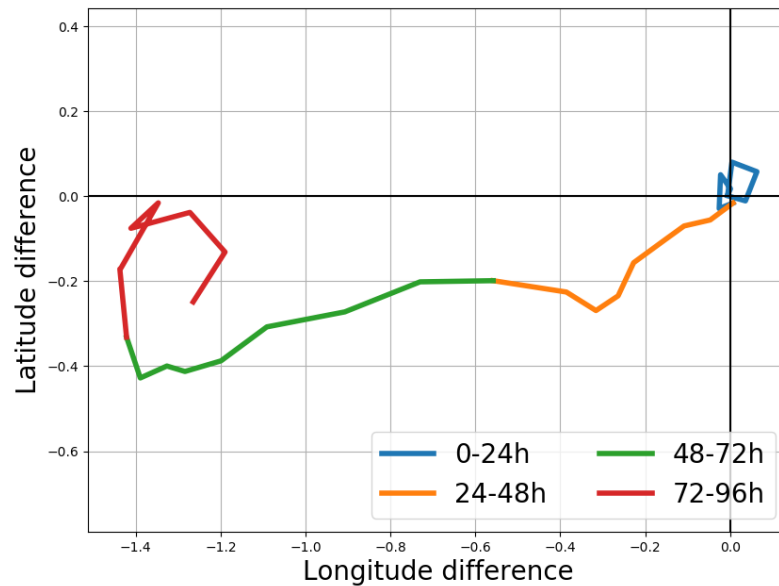
Figure 7.10: Difference between the global ensemble average position and the CP ensemble average position. Each colour is 24 hours of the forecast. The forecasts were initialised at 1200 UTC 13 September 2018.

As with Hagupit, the initial track deviation between the CP and global forecasts of Florence occurred before the differences became obvious to the eye. Florence turned to the north at approximately T+72 (Figure 7.8). This was the case in both the global and CP forecasts. However, in the CP ensemble Florence had travelled too far inland, to the west, before turning. Figure 7.10 demonstrates that these differences occur between T+24 and T+72. Initially the average location of the TC in the global and CP ensembles are similar. After 24 hours the positional difference indicates that the CP forecasts have travelled further to the west and slightly further south. At approximately T+66, the CP forecasts turn north. Here, the latitude difference between the two forecasts decreases, but the longitude difference of 1.4° remains due to the overshoot before the CP forecasts turned.

To understand why the TC moved in the way that it did, Figure 7.11 shows the synoptic set up of Florence. The storm is steered by an upper level anticyclone. Earlier on, this anticyclone is located to the north of the storm (approximately 42°N and 85°W) leading to Florence moving to the west. As the TC travels inland the anticyclone moves to the east. Eventually Florence becomes located on the western edge of the anticyclone, which results in the turn to the north. Both the movement of the anticyclone and the movement of the TC are responsible for Florence
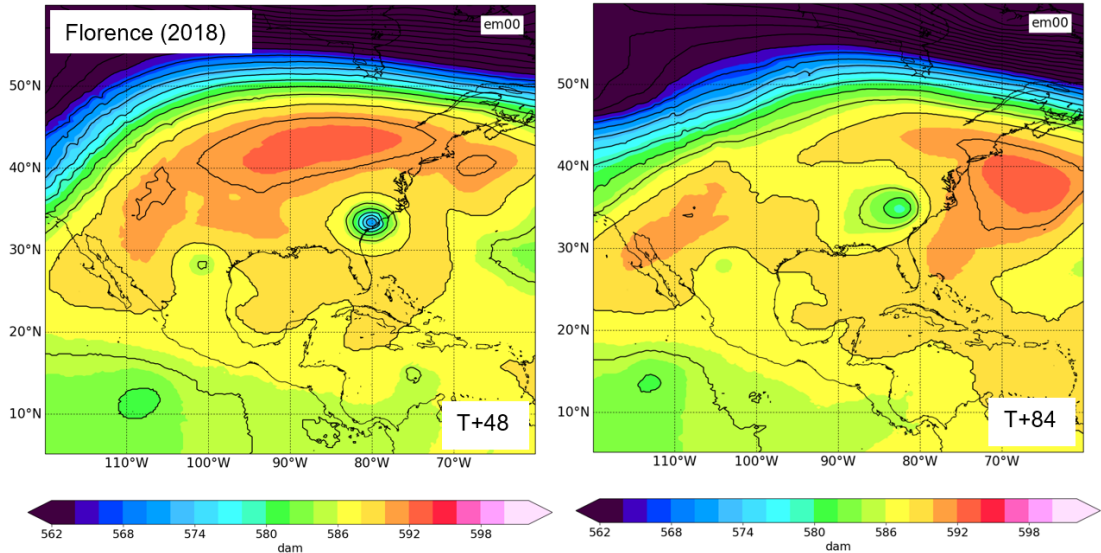
Figure 7.11: Geopotential height at $500\,\text{hPa}$ for Hurricane Florence using ensemble member 0 of the global ensemble initialised at $1200\,\text{UTC}$ 13 September 2018. Shading and contours are both of the geopotential height.

becoming positioned on the western edge of the anticyclone. Figure 7.11 shows the environment of the global ensemble member 0, however comparisons between all ensemble members of the global and CP ensemble forecasts showed there were no large differences in the synoptic scale environment of the storm.

To further investigate the cause of the differences in the global and CP forecasts, the TC is removed using the method outlined in Section 3.5.2. Of particular interest is the period between T+24 and T+48, when the global and CP ensemble average positions first begin to deviate. As was the case with Hagupit, it can be assumed that once there is an initial deviation between the global and CP forecasts, then the storms are in different positions and thus experience different steering flows. The optimum top pressure level and radius of the steering flow for Florence between T+24 and T+48 is shown in Figure 7.12 for both the global and CP ensemble. For both sets of simulations there are well defined optimum depths. For the CP forecasts the optimum depth is between 850 and $500\,\text{hPa}$, whilst the optimum depth of the global forecasts is between 850 and $400\,\text{hPa}$. For the global forecasts this optimum depth gives an average residual of $1.2\,\text{m s}^{-1}$, whilst for the CP forecasts the average residual vector magnitude is $1.4\,\text{m s}^{-1}$. For Florence the optimum depth was very sensitive to the time period in which it was investigated. For example, between 0-24 hours the optimum top pressure level in both the global and CP forecasts was $300\,\text{hPa}$,
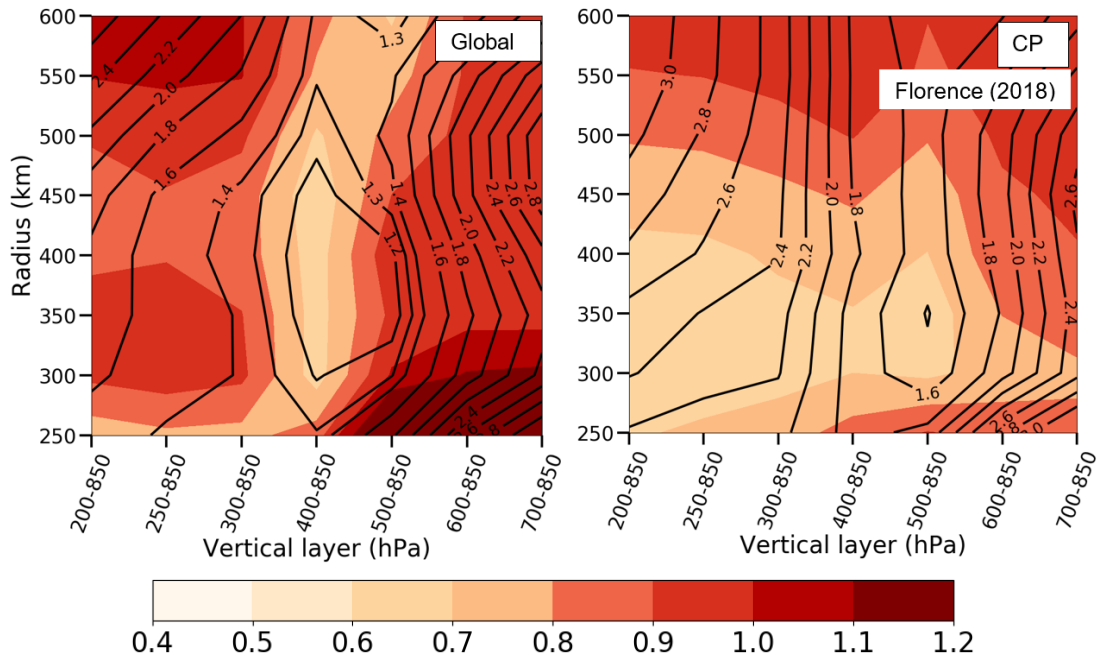
Figure 7.12: Contour plot showing the residual vector when comparing the environmental steering vector to the storm global (left) and CP (right) forecast vector using different values of r_0 and p_t for Hurricane Florence between T+24 and T+48. The residual magnitude is shown by the contours and the standard deviation shown by the shading. Forecasts initialised at 1200 UTC 13 September 2018.

whilst between 72-96 hours an optimum p_t was 600 hPa was calculated. This in unsurprising as the forecasts cover the time period in which the TC dissipates.

Figure 7.13 shows the shear profiles for the global and CP forecasts between T+24 and T+48. The shear is very similar across all times, particularly below 400 hPa. The winds between 500 hPa and 400 hPa, i.e. the winds in which the global simulations are being steered by but the CP are not, are westerly. This is expected as westward motion of the storm in the global forecasts is slower than that in the CP forecasts. Defining a steering depth of 850-400 hPa in the CP forecast between the times of T+24 and T+72 gives an average easterly wind component of $1.98\,\mathrm{m\,s}^{-1}$. In comparison, a depth of 850-500 hPa gives an easterly wind component of $2.94\,\mathrm{m\,s}^{-1}$. This difference of $0.96\,\mathrm{m\,s}^{-1}$ over the 48 hours would translate to a positional distance of 166 km. This is the approximate track deviation of the CP forecasts to the global forecasts during this time. The fact that the global model is influenced by winds in the 500-400 hPa height range but the CP is not accounts for all of the track deviations between the two types of simulations.
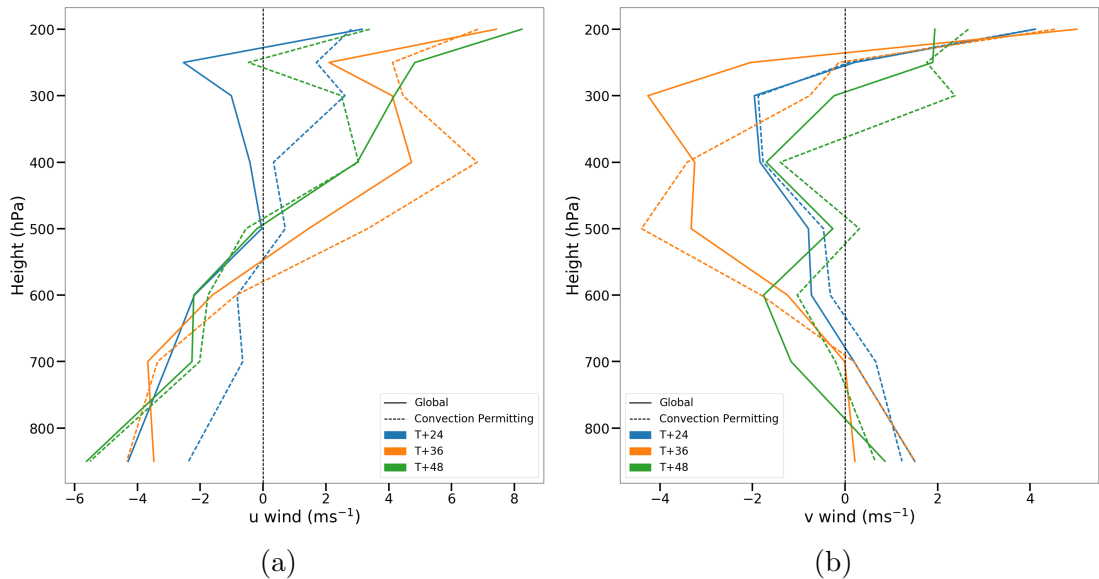
Figure 7.13: Vertical (a) u and (b) v wind profiles for Hurricane Florence in the global and CP forecasts. Profiles are calculated using the environmental winds in each ensemble member averaged in a $6° \times 6°$ box centred on the location of the storm. All ensemble members are averaged over to create a wind profile for each forecast type. Forecasts initialised at 1200 UTC 13 September 2018.

Despite the storms responding to different depths of steering flow, there are surprisingly no clear differences between the vertical structure of the storm in global and CP simulations (Figures 7.14 and 7.15). The cross section plots in Figures 7.14 and 7.15 show the azimuthal winds in a slice taken in the direction of the vertical wind shear vector. Unlike the forecasts of Hagupit there is no tilting under vertical wind shear in the global or CP forecasts. The wind speeds are similar at all levels and the TC extends towards 200 hPa in both simulations.

The deviations in Florence's tracks occur when the storm has made landfall. At this point the storm becomes asymmetric. Figure 7.16 shows a comparison between the steering flow and original winds in ensemble member 0 of Florence just after landfall at the 500-400 hPa layer. A single ensemble member is shown to highlight the finer detail which is averaged out when considering the ensemble average. The eastwards flow which steers the global forecast but not the CP forecast is similar in both cases (bottom panels of Figure 7.16). Rather than the storm being embedded in this eastwards flow, the flow is slightly to the north of the storm's central location. The structure of the storm in both the global and CP forecasts between 500 and 400 hPa differs and is asymmetric. Florence is no longer a strong symmetric vortex embedded
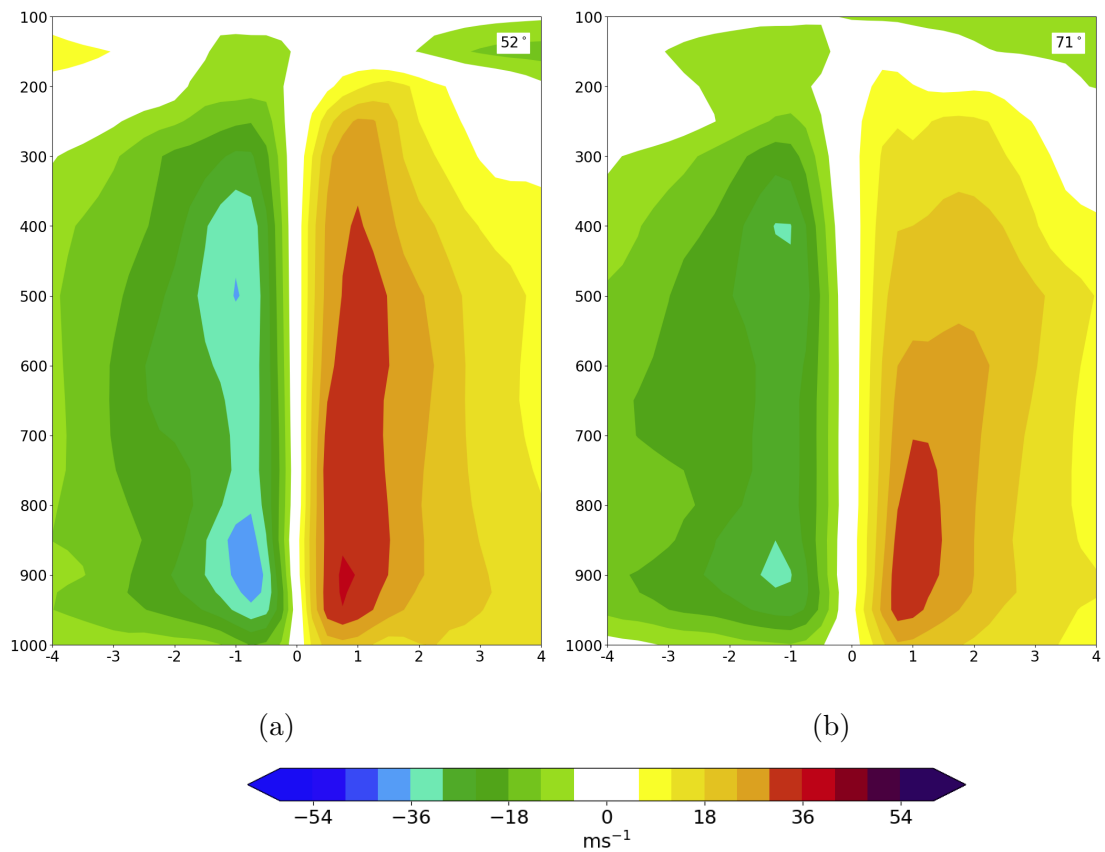
Figure 7.14: Cross sections of azimuthal velocities of Florence in the global forecasts. The cross section is taken in the direction of the vertical wind shear vector between 200 hPa and 850 hPa (indicated by the number in the top right). The times are (a) 1200 UTC 14 September (T+24) and (b) 1200 UTC 15 September (T+48).
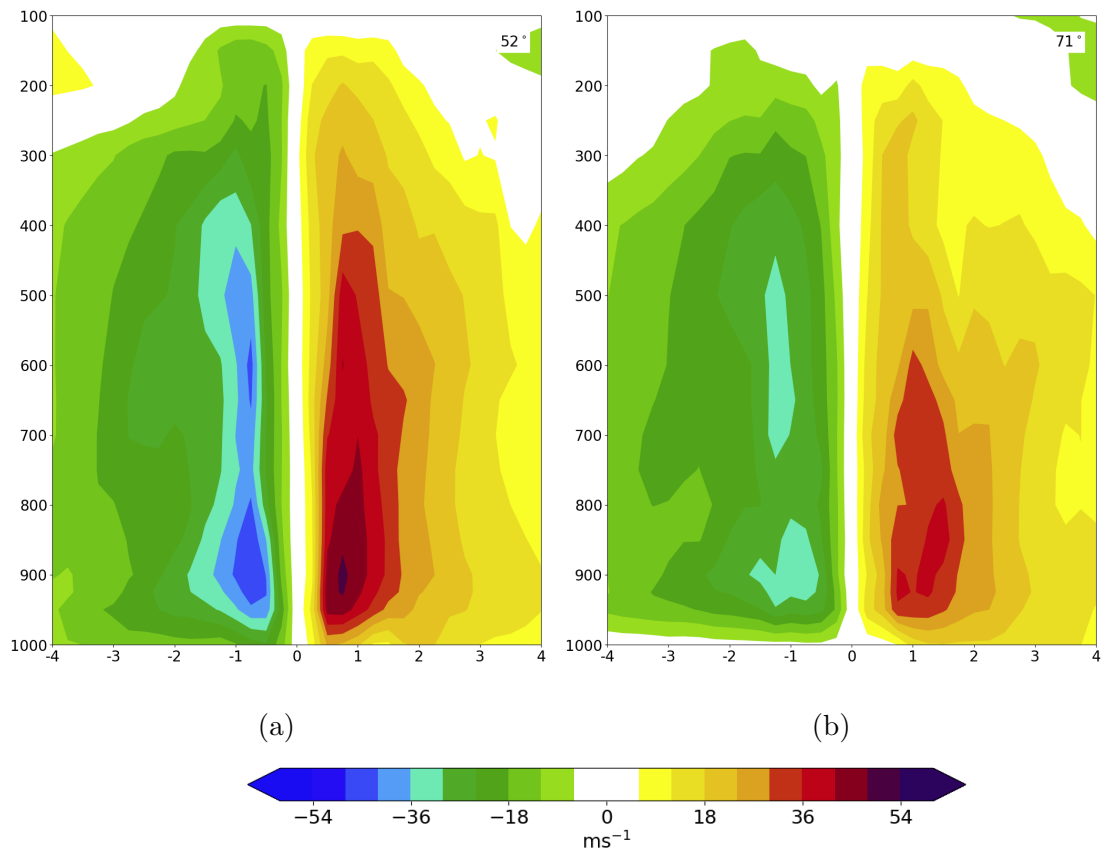
Figure 7.15: As in Figure 7.14 but for the CP forecasts.

in a strong steering flow. The optimum steering flow for the CP simulations was shallower than that for the global, this may be a reflection of the fact that the stronger steering flow in Figure 7.16 does not interact with the stronger parts of the TC vortex at upper-levels. This demonstrates the need to accurately forecast the structure of the storm as well as the large scale environment when a storm is embedded in a weak and non-uniform steering flow.

The asymmetries in the structure of Florence and weak steering flow may impact the contribution of diabatic heating to the TC motion, meaning the steering flow may not accurately describe the motion of the storm. Florence was a slow moving storm, in the forecasts between T+24 and T+48 the TC travelled at a speed of approximately $3\,\mathrm{m\,s}^{-1}$. The residual of the optimum storm-removed environmental wind has an average magnitude of $1.4\,\mathrm{m\,s}^{-1}$ for the CP forecast during this time period (Figure 7.12). This is a significant magnitude for a period of time when the TC is moving so slowly. This suggests that other factors may be influencing the TC motion other than just the environmental winds. Both the topography impact
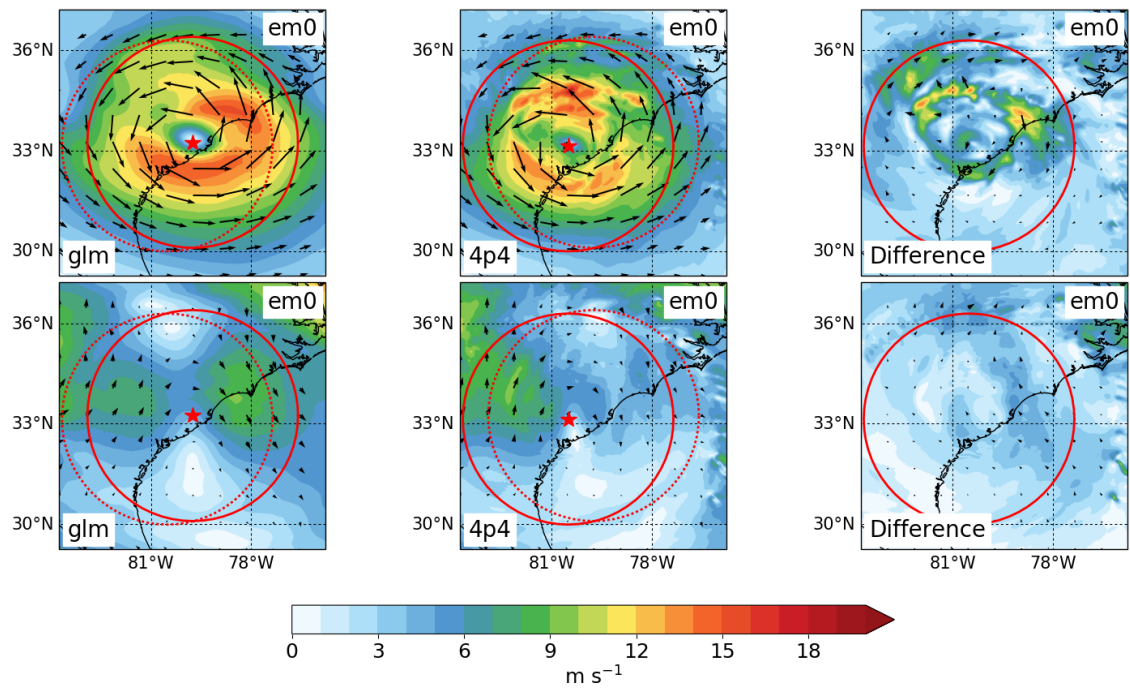
Figure 7.16: Comparison of winds averaged between 500 and 400 hPa for Hurricane Florence. The top figures show the original wind fields whilst the bottom panels show the storm removed winds. On the left is the global, middle the CP and right is the difference (calculated by subtracting the global u and v components from the CP). The time is 0000 UTC 16 September (T+60), all plots are for ensemble member 0. The solid red circle is the removal radius of 350 km, whilst the dashed circle is the removal radius in the other model. To calculate the difference the global is first recentred so that the centre of the storm is in the same location as the centre of the storm in the convection permitting forecast.

of the TC moving over land and the fact that Florence was weakening can impact the structure and symmetry of the TC. Further, the different science configurations likely lead to differences between global and CP forecasts in diabatic heating in the proximity of the storm. The PV-tendency approach of Wu and Wang (2000) could provide insight into the different contributions of diabatic heating to TC motion in the forecasts. Another approach would be to run a large sensitivity test which involves nudging parameters in the global and CP forecasts, to find out which aspect of the forecasts is causing the differences. Both of these were outside the scope of this study.

7.4   Summary and Conclusion

This chapter uses methods developed in Chapter 6 to investigate two further storms in which there were large differences between the global and CP forecasts. The aim has been to indentify any common themes between these storms and Hagupit which may lead to problematic CP TC track forecasts.

For Haiyan the differences were related to the early position of the TC in either forecast. The CP forecasts were positioned slightly to the south, and were, due to horizontal shear, embedded in a weaker easterly steering flow. In comparison the global forecsats did not initially intensify (or spin-up) into a TC. Rather the ensemble members forecasted a broad tropical disturbance which covered a greater horizontal area than the TC in the CP forecasts. In the global forecast this tropical disturbance was therefore influenced by the stronger easterly winds to the north. The reason that the CP forecasts were positioned slightly to the south is likely because this was a favourable environment for them to spin-up and intensify. To the south there was less vertical wind shear. In general vertical wind shear inhibits TC genesis. In reality Haiyan was already a TC by this initialisation point, however the weak intensity upon initialisation meant this was not the case in the model.

Hurricane Florence had some similar characteristics to Hagupit. Differences between global and CP ensemble members later in the forecast, specifically the location of

a northward turn, were related to east-west positional differences which developed between T+24 and T+72 in the forecasts initialised at 1200 UTC 13 September. The optimum steering flow of the TC in each type of simulation differed in its height but not its radius. The global forecasts, which did not propagate the storm as far to the west, had an optimal p_t of 400 hPa whilst the CP forecasts had an optimal p_t of 500 hPa. The difference between the averaged eastward component of the environmental wind vector in the CP forecast between T+24 and T+48 using a height of 400 hPa and a height of 500 hPa almost exactly matched the difference in the position of the storm during this time. Whilst this suggests there would be a difference in TC height between the two types of simulations, this was found not to be the case. Both sets of forecasts predicted the storm to be of similar intensity and depth. Some further analysis highlighted the complexity of Florence at this time. The storm was over land and there were many asymmetries in the structure. Between 500 and 400 hPa the weak steering flow did not fully embed the TC but rather formed a small channel just north of the TC centre. Accurately predicting the storm structure, including the asymmetries, seems vital at this point.

Neither Haiyan nor Florence were exactly the same as Hagupit. In the forecasts of Hagupit there were clear differences between the sets of simulations in how the TC reacted to vertical wind shear. In particular the large vertical wind shear caused the global forecasts to tilt and decrease in height. However, this was not the case in Haiyan or Florence. Despite this the presence of moderate to high vertical wind shear was present in each storm and did cause forecasting difficulties. For Haiyan these difficulties centred around where the CP would spin up in the model (the global forecasts were unable to spin up the TC until later in the forecast when vertical wind shear had decreased). Had Haiyan been initialised at the correct intensity this issue may have been avoided. The weak initial intensity was due to quality control dismissing the sea level pressure observations due to their large pressure gradients. It would be interesting to see the CP forecasts of the storm if these observations had not been omitted from the data assimilation process. For Florence the vertical wind shear, along with landfall, was the cause of the TC weakening. The difference in

motion between global and CP forecasts was related to the TC's interaction with winds at upper levels. However, a surprising result was that the structure of the TCs was broadly similar between each forecast and did not show any signal of the TC reacting differently in the different simulations.

Whilst a link between the storm motion differences and the vertical wind shear has been identified, the influence of vertical wind shear on TC structure has not been studied in detail. This is not a trivial question and is often studied with the aim of improving intensity forecasts. One common consequence of vertical wind shear is asymmetric convection in the eyewall of the storm. This can lead to asymmetries in the latent heat release due to convection. These asymmetries can influence the motion of the storm through advection of PV (e.g. Wu and Wang, 2000).

Chapter 8

Conclusion and Future Work

8.1 Introduction

The aim of this thesis is to improve our understanding of TC track predictability in both global and CP configurations of the MetUM. Whilst TC forecasts have improved considerably over the past decades, every year there are examples of TCs with large errors or large uncertainty in their track forecasts. Whilst these outlying cases are rare, they are problematic to decision makers whose job is to provide warnings to communities who are in danger of being affected by TCs. Understanding what causes uncertainty in track forecasts can reduce the impact of future cases and inform model development.

Typhoons Haiyan (2013) and Hagupit (2014) were two seemingly similar high-impact storms with large differences in the spread of the global operational MetUM track forecasts (Figures 1.4 and 1.5). The global track forecasts of Haiyan and Hagupit lead to the following research questions:

- Why were the track forecasts for Typhoon Haiyan and Typhoon Hagupit so different?

- How do Haiyan and Hagupit interact with their environment, and what impact does this have on their tracks?

The first part of this thesis addressed these questions by comparing global MetUM

track forecasts of Haiyan and Hagupit.

Regional CP forecasts of TCs are produced operationally at the Met Office over the western North Pacific. These CP forecasts are run at a higher resolution than global forecasts with different model physics (e.g. convection is allowed to develop freely rather than be parameterised). For TCs, the intensity and precipitation forecasts are improved in CP simulations (Short and Petch, 2018). Average CP TC track forecast errors remain approximately the same as average global TC track errors, however, there are significant positional differences between global and CP track forecasts (Figure 1.6). Sometimes one configuration performs better than the other and it is not always the case that CP forecasts are better than global forecasts. Global CP forecasts are the future of NWP (Bauer et al., 2015). Although this change will improve many aspects of TC predictions, it is not desirable to introduce errors in TC track forecasts that are not present in the current global simulations. Understanding why global and CP track forecasts differ for some storms is critical to the future development of CP models.

Systematic differences were present in the global and CP forecasts of both Haiyan and Hagupit. For Haiyan the motion of the TC was predicted too slowly in the CP forecasts, whilst each ensemble member of the CP forecasts of Hagupit predicted the storm to take a south-west turn, away from the best track. A third high-impact storm also caught the eye of model developers at the Met Office. Hurricane Florence (2018) made landfall over North Carolina, travelled inland and then turned north. Global forecasts predicted this motion well, however CP forecasts predicted the TC to track too far to the west before turning north. These differences in global and CP forecasts posed the final research question: What causes the differences in track forecasts between the global and CP simulations? To answer this question, the second part of the thesis analysed CP MetUM forecasts of Haiyan, Hagupit and Florence.

The key findings from this study are as follows:

- The uncertainty in the track forecasts of Hagupit was related to the storm's position in weak steering flow between two opposing anticyclones – one which

steered the TC to the north and one which steered the TC to the west. In comparison, Haiyan's track was well predicted as the storm was located to the south of the sub-tropical anticyclone and embedded in a strong easterly flow.

- Interactions between Hagupit's outflow and its environment, the strength of the two anticyclones either side of the TC and the upper level geopotential height to the south of the storm all influenced Hagupit's track and predictability. For example, forecasts which predicted Hagupit to turn to the north were associated with a stronger upper level anticyclone to the east earlier in the forecast. For storms embedded in both a weak steering flow and a deformation flow, accurately forecasting TC-environmental interactions is crucial to determining the future track forecast. As Haiyan was embedded in a much stronger steering flow, subtle differences in the TC-environment interactions between ensemble members have little impact on the TC track.

- Differences in TC track predictions between global and CP forecasts can be caused by differences in TC structure, particularly when the TC interacts with strong vertical wind shear. Convection permitting forecasts for Hagupit predict a strong TC vortex, even at upper levels, whilst the global forecasts predict a much weaker storm which tilts and dissipates at upper levels due to the vertical wind shear. Thus, whilst the CP forecasts are steered by the strong upper level winds, the global forecasts stall until the shear decreases. In addition to the TC structure, environmental differences were found between global and CP forecasts of Hagupit. These difference caused difference in the strength of the steering winds and were likely related to the representation of a broad region of convection to the south.

- A more systematic study of global and CP TC forecasts would lead to a greater understanding of differences between the two model configurations and highlight how CP forecasts can continue to be improved. As with this study, a systematic study should be conducted on forecasts using different configurations of the same model to ensure the impact of a change in resolution and science configuration is not conflated with, for example, the impact of a

different dynamical core or initial conditions.

The remainder of this chapter is structured as follows. In Section 8.2 the key results from each chapter are summarised. In Section 8.3 the general conclusions from the thesis are outlined. A discussion on avenues of future work is provided in Section 8.4.

8.2 Summary

8.2.1 Global Forecasts

The key results from this thesis were presented in Chapters 4 to 7. In Chapter 4 an overview of two TCs, Haiyan and Hagupit was given. Both Haiyan and Hagupit were high-impact storms which made landfall over the Philippines 13 months apart. Their similarities included the paths they followed across the Pacific prior to landfall, the intensities they reached and their size. However, the track forecasts were markedly different. Whereas global MetUM ensemble forecasts for Haiyan predicted the motion of the storm with a large amount of certainty, global track forecasts for Hagupit featured a large amount of variability in where the storm would move. Global forecasts initialised up to 60 hours before landfall failed to predict where, or indeed if, Hagupit would make landfall.

Motivated by the differences in the spread of these ensemble forecasts for both Haiyan and Hagupit, Chapter 5 investigated in detail the environments of both storms in the global forecasts. Hagupit's unpredictable track was linked to the weak environmental flow in which the storm was embedded. Whilst Haiyan was steered by a strong subtropical ridge, Hagupit was embedded in a much weaker steering flow and became positioned between two anticyclones. To the east an anticyclone pulled the storm to the north, and to the west an anticyclone steered the storm towards the Philippines. As Hagupit passed through the two anticyclones, the storm slowed and its forecasted tracks began to diverge.

The main contribution to the depth-averaged steering flow of Hagupit came from the upper levels (i.e. above 300 hPa). Statistically significant differences were found

in the 300 hPa geootential height field of ensemble members which predicted the TC to turn north and those which predicted the TC to continue to move to the west. For instance, north-turning ensemble members were associated with a stronger upper-level anticyclone to the east of the storm and an area of higher pressure to the south, when compared to the ensemble members which predicted Hagupit to continue west and make landfall. Earlier in the forecast, these environmental differences impacted Hagupit's steering flow, with ensemble members that would later predict the TC to turn north located to the east of landfall-predicting ensemble members.

The inherent uncertainty of Hagupit's environment was tested by calculating trajectories with slightly different initial positions using the storm-removed environmental winds. Trajectories were initialised at T+24 in a region consistent with the mean NWP track forecast errors. In forecasts for both Haiyan and Hagupit, the spread of the tracks in the original ensemble matched the spread of the trajectories. Whilst this method is far from perfect - it does not account for environmental differences between ensemble members, nor does it account for TC-environment interactions - it provides a computationally cheap and quick assessment of the unpredictability of a TC track forecast. This method has the potential to be used operationally to allow forecasters to understand the uncertainty of a single deterministic forecast without the need to run a full ensemble.

Large TC track errors are often associated with steering flow in which small perturbations to the TC location, or to the steering flow itself, can cause the TC to move into a drastically different position later in the forecast. This is usually due to a bifurcation point in the environmental flow (e.g. Grams et al., 2013; Torn et al., 2018). Hagupit's steering flow showed similarities to TCs located close to a bifurcation point. The east to west differences which formed whilst the TC entered the region between two anticyclones was key to whether or not Hagupit was predicted to make landfall or turn north. However, Hagupit differed from other case studies as the steering flow broke down and reached near-zero. The likelihood of Hagupit turning north (i.e. steered by the anticyclone to the west) or making landfall (i.e. steered by

the anticyclone to the east) depended on positional differences which developed after Hagupit became located between the two anticyclones. These positional difference developed because of environmental differences in the ensemble members leading to slight differences in the steering flows. Forecasting these differences is made more difficult due to the fact that Hagupit's own outflow interacts and influences the development of the environment.

Tang et al. (2020) studied three examples of TCs which enter a region of weak steering flow due to the break-up of the subtropical ridge - a similar synoptic set up to that of Hagupit. They highlighted the importance of accurately predicting the size of a TC and thus capturing its interactions with different synoptic features. In this study, similar uncertainty for track forecasts was found despite the size of the TC not changing between ensemble members. Whilst TC size is undoubtedly important to the forecasts, TC position, the strength and position of surrounding synoptic weather systems, TC outflow and interactions between the outflow of a TC and its environment can all impact the track.

8.2.2 Convection Permitting Forecasts

In Chapter 6, the differences between the CP and global forecasts of Typhoon Hagupit were investigated. Relative to the global forecasts, the CP forecasts produced more intense TCs, exhibited lower track spread and predicted Hagupit to turn to the south-west away from the best track.

There were two key differences which led to the deviation of CP and global track forecasts. First, the TC environments differed in important ways. In the CP simulations the geopotential height was lower at low-mid levels (850-500 hPa) in the region to the south of the storm compared to the global forecasts. This caused differences in the steering winds, with CP forecasts experiencing stronger easterly winds. Second, the storms reacted differently to the large vertical wind shear. As shear increased, the depth of the TC circulation in the global forecasts decreased. However, the TC vortex in the CP forecasts remained resilient to the vertical wind shear and was hence steered by the upper-level easterly winds. Each of these

differences contributed to the storm in the CP forecasts being steered further to the south-west relative to the global forecasts between 1200 UTC 4 December and 1200 UTC 6 December. The deviation in steering winds occurred before the storm in the global forecasts stalled and entered the region between two anticyclones. Consequently, the CP storm did not become positioned in this sensitive position, but rather was steered by the anticyclone to the west towards the Philippines.

Sensitivity tests identified the higher resolution, rather than the different scientific configurations, as the cause of intensity differences between CP and global forecasts, whilst both the higher resolution and the different science configuration were responsible for causing the systematic south-west turn in each ensemble member. The Par-Hi ensemble, where the global science configuration, GA6.1, was used to create a regional 4.4 km ensemble, was particularly interesting as it featured characteristics of both the global and CP ensembles. As the intensity of the TC vortex was similar to the CP forecasts the depth of Hagupit in the Par-Hi experiment did not decrease with wind shear. Therefore, the strong winds at heights of 300 hPa and above helped steer the Par-Hi ensemble (as they did in the CP forecasts), rather than shear the top of the storm away as in the global forecasts. However, the environment of the Par-Hi ensemble was almost identical to the global ensemble average, and did not feature the region of lower pressure to the south. As such the Par-Hi did not experience the stronger easterly winds like in the CP forecasts.

Chapter 7 investigated differences in the global and CP track forecasts of Typhoon Haiyan and Hurricane Florence. Haiyan in CP forecasts lagged behind the global equivalent, making landfall approximately 18 hours too late. In the case of Florence, the TC was predicted to move too far inland before turning north by the CP model, resulting in track errors. The global forecasts did not feature this error and turned to the north earlier than the CP forecasts.

Differences occurred in the initial intensification of Haiyan in the global and CP forecasts. The CP forecasts intensified the TC from the start of the forecast, however, the TC developed too far to the south where the vertical wind shear was decreased and was thus a more favourable environment for TC development. On the other

hand the strong vertical wind shear of up to $10\,\mathrm{m\,s^{-1}}$ between 850 and 400 hPa prevented the global forecasts from intensifying Haiyan and the forecasts predicted a broad tropical disturbance rather than a TC, until later in the forecast when shear decreased. The southwards position of Haiyan in the CP forecasts relative to Haiyan in the global forecasts caused differences in the steering flow experienced by the TCs in the different simulations. The TCs in the global forecasts were slightly to the north and thus embedded in a stronger easterly flow than the CP forecasts.

For Florence, differences in the average TC position in the CP and global forecasts developed between 1200 UTC 10 September (T+24) and 1200 UTC 12 September (T+72). During this 48 hour period, the CP forecasts predicted the TC to move further to the west than in the global forecasts. Both simulations predicted the northwards turn of Florence at the same time, however, the CP forecast had already predicted the storm to move too far inland. Between 1200 UTC 10 September and 1200 UTC 12 September, the optimum depth when computing the steering winds was between 850 and 400 hPa in the global forecasts and 850 and 500 hPa in the CP forecasts. When recalculated using an upper level pressure of 400 hPa as in the global model, the steering wind in the CP model almost exactly matched that in the global model. Therefore, the deviation of tracks was caused by differences in how the TC interacted with the upper-level winds in the CP and global forecasts.

For Haiyan and Hagupit, differences in the global and CP forecasts were related to the intensities and structure of the TCs. Both storms were initialised too weak in terms of minimum sea level pressure and near-surface wind speed. It would be interesting to see the impact of a better representation of the TCs at the initial time on the TC tracks in both the global and CP forecasts. In the global forecasts the central pressures of the TC were flagged during data assimilation due to the quality control procedures. This is because the global model was unable to capture the rapid intensification of the TC. Thus, the difference between the "background" forecast (i.e. the forecast used in the data assimilation process for the next forecast cycle) and the observed central pressure was deemed too large and the observations were not assimilated into the model (Heming, 2016). The CP forecasts are able to capture

rapid intensification better but they inherit initial conditions from the global model. Initial conditions for the CP forecasts, generated through the use of an assimilation specifically designed for the regional higher resolution forecasts, would likely have provided more accurate forecasts.

In all three cases vertical wind shear and differences in the storm's interaction with winds at different vertical levels were important to the TC track differences in global and CP forecasts. The impact of vertical wind shear on TCs is a well studied and challenging topic. It is well accepted that large vertical wind shear typically impedes TC genesis and intensification (e.g. Gray, 1968; Emanuel, 2003). However, there are also a number of cases where TCs intensify in spite of vertical wind shear (e.g. Molinari et al., 2004; Ryglicki et al., 2019). Vertical wind shear can cause a tilt in a TC, usually downshear and slightly to the left (e.g. Jones, 1995). The tilting typically causes a redistribution of convection, which in turn causes asymmetries in diabatic heating due to latent heat release from ascending air. Asymmetries in diabatic heating can have an impact on TC motion through the advection of PV (e.g. Wu and Wang, 2000). The contribution to TC motion by diabatic heating in the MetUM has not been studied, however, it may be important in situations such as Florence in which no obvious structural differences exist between global and CP simulations.

For each of the TCs studied, comparing the position of the CP ensemble average to the global ensemble average was useful in highlighting the first point in the forecast in which the tracks began to deviate. For Haiyan this highlighted the initial movement to the south in the CP forecasts, whilst for Hagupit and Florence it highlighted a 48-72 hour period in which the CP forecasts travelled further to the west. Simply considering the average position of one forecast with respect to another can be useful to a forecaster by highlighting a time at which an assessment can be made on the quality of either forecast.

The steering flow of the TC was discussed throughout the study. This flow was calculated using the vorticity inversion method of Galarneau and Davis (2013) with a couple of modifications. Before calculating the nondivergent wind from the relative

vorticity within the radius r_0 of the TC centre, the relative vorticity averaged across a longitudinal range was first removed from the total relative vorticity. This removal ensured that winds associated with a horizontally sheared environment were not removed when calculating the storm-removed environmental winds. Although the new method only differed slightly from that used in previous studies, the environmental vector was changed distinctly. It is something which should be adopted in future studies which use the TC removal method for calculating steering winds.

8.3 Conclusion

This thesis aimed to improve our understanding of TC track uncertainty in MetUM predictions. Results show that when a TC moves into an area of relatively weak environmental steering with two anticyclones either side, the track of the storm is likely to be difficult to predict. Slight differences in the strength and position of the anticyclones, the position of the storm and interactions between the outflow of the TC and its environment can all impact the future track. The complexities of accurately forecasting each of these processes highlights the unpredictable nature of TCs such as Hagupit, and motivates the use of ensemble forecasts.

Convection permitting track forecasts can deviate from the global equivalents in situations in which the TC structure is poorly predicted or in which there is large vertical wind shear. Deviations between global and CP forecasts are caused by either differences in the TC steering winds or differences in how the TC responds to the steering winds. The former is suggests there are slight differences in environments of the TC in global and CP simulations, which in the case of Hagupit are caused by the different science configurations, not the different resolutions. The TCs response to steering winds may be caused by differences in the TC structure and intensity.

The analysis of the cause of uncertainty in the global forecasts of Hagupit was limited by sparse observational data. Increased observations (i.e. from aircraft data) of TCs in weak steering flow and their surrounding environment would add confidence to the ensemble forecasts due to a reduction in potential errors in the assimilation

process, whilst also providing invaluable data to assess the quality of the forecast in hindsight and thus identify problems with the model. Similarly, repeating the study on a more well-observed case would yield better validation of the results through comparisons between the model and observations. This would be particularly useful when comparing the global and CP forecasts. In Chapter 6, both the environment and the TC structure were highlighted as differences between the global and CP forecasts. Comparisons to observations would allow conclusions to be made about which of the forecasts was closer to reality, whilst also highlighting any situations in which the forecast produces an accurate track prediction but for the wrong reasons.

The sparse observational data also exposes from difficulty of trying to improve one model based on a comparison to another model for just a handful of cases. There were a number of differences between the global and CP forecasts in each of the three storms discussed. Using a handful of metrics (i.e. track and intensity) to evaluate which forecast is best limits the amount of model validation which can take place. This can lead to situations in which errors are cancelled out and thus model deficiencies are missed. A more systematic comparison between global and CP forecasts would be needed to highlight exactly which processes are well represented in one compared to the other.

The CP forecasts will likely benefit from assimilating initial conditions rather than inheriting them from the global forecasts. Observations of a TC's minimum sea level pressure omitted from the global assimilation process as they are too unlike the background forecast need not be omitted from the CP forecasts where the higher resolution would provide a more intense TC in the background forecast.

8.4 Future Work

This study highlights many avenues of future work which will benefit both NWP development, forecasters and the research community. Tropical cyclones associated with uncertainty in track forecasts have been the subject of a number of case studies in the past. Track errors are often related to steering wind or positional

differences.

To discuss errors in steering flow it is necessary to first define what the steering flow of a TC is. Recently the method of TC removal through the inversion of relative vorticity associated with the TC, as used in this study, has become popular (e.g. Fowler and Galarneau, 2017; Torn et al., 2018; Huang et al., 2020). This method facilitates a comparison between ensemble members of the steering winds responsible for the TC motion. The steering wind can be defined with either a constant radius, r_0, and constant top pressure level, p_t, or these values can be allowed to vary in time. It makes conceptual sense that both r_0 and p_t should change in time as the size and structure of a TC will change in time. However, it is computationally more efficient, and allows for comparisons between different simulations, if the values are kept constant. Ideally a method would exist to accurately predict the optimum values of r_0 and p_t according the intensity and radius of a TC. A study comparing the Galarneau and Davis (2013) definition of steering flow to steering flow computed using PV inversion, or steering flow calculated in an idealised model where the TC-relative winds can easily be removed, may be of use in identifying a relation between r_0, p_t and various TC characteristics (e.g. intensity or radius of maximum winds). This would allow one to calculate an accurate TC steering flow whilst bypassing the computationally expensive optimisation process.

Case studies are useful at highlighting physical processes that may be contributing to TC track uncertainty. Some important examples include TCs embedded in deformation flow (e.g. Torn et al., 2018), TCs which interact with approaching upper level troughs (e.g. Grams et al., 2013) and TCs embedded in weak steering flow (e.g. this study on Typhoon Hagupit). Conclusions from these studies would be made more robust through the identification of many more cases. Composites may be formed to assess TC track variability in weak steering flow for a large number of TCs. Such a study may also identify common synoptic conditions affecting the TC tracks, for example the strength of an anticyclone to the east of the storm or the pressure to the south of the TC. Identifying these synoptic features could feed back into the observation and data assimilation community to identify regions in which

TC forecasts may benefit from better observations.

Currently there are few studies which compare the structure, track and intensity of TCs in global and CP forecasts from the same model. As CP forecasts begin to be more commonly used operationally, it is important that a thorough understanding of the representation of the structure of TCs in CP compared to global forecasts is gained and the possible implications of any differences on the track forecasts understood. Comparing the regional CP forecasts to the driving global simulations is of particular interest as the initial conditions of the regional forecasts are inherited from the global forecasts, and hence differences develop during the forecast due to different resolutions and science configurations. Whilst the intensity and structure of TCs are better represented in CP forecasts, it is important not to introduce track inaccuracies. In the three storms studied here it is shown that one cannot automatically assume a better track forecast in CP simulations. A potential link between high vertical wind shear and CP track errors was identified. Therefore, it would be of interest to investigate more cases of TCs in an environment of large vertical wind shear. Similarly, a systematic study of many TC cases, not necessarily embedded in large vertical wind shear, may lead to an identification of dynamical features which cause the global and CP forecasts to deviate.

As well as direct comparisons between global and CP forecasts, it is important to gain a better understanding of how well convection is resolved in TCs and their environments, and the potential impacts this can have on the storm tracks and intensity. A deeper understanding of the impact of allowing convection to develop freely could be gained through, for example, the use a diabatic tracers in the model. This would allow for an budget analysis of the different science configurations, gaining insight into how and why the environments and TCs are different in the different simulations. In this study, the intensity of the Par-Hi ensemble for Hagupit was similar to that of the CP ensemble, and much stronger than the global ensemble. This indicates that the resolution was more important in intensifying the storm than the science configuration. At higher resolutions the CP forecast would likely resolve more of the physical processes (such as downdrafts), investigating the impact of

increased CP resolution on the TC track and intensity would indicate how important fully resolving these processes is, and if there is a threshold at which increased resolution no longer benefits the forecast.

Investigating the impact of the differing TC structures in the global and CP forecasts in storms with a greater number of observations would allow for a better validation of results. In particular, data from aircraft reconnaissance missions can provide a detailed three-dimensional structure of TC winds through dropsonde data, doppler radar and *in-situ* measurements. This would be particularly useful for TCs which are embedded in strong vertical shear as it would allow for comparisons between observations, global forecasts and CP forecasts on TC height and TC tilt. The CP forecasts for Hagupit were more resilient to vertical wind shear, it would be interesting to compare a TC which has this same characteristic to detailed observations.

The problem of the weak initialisation of the TCs in the model is an area of active research (e.g. Liu et al., 2020). Three methods are generally used to initialise TCs: inserting a "bogus" TC into the initial state of the forecast by prescribing a vortex structure based on the observed position and intensity of the TC; including intensity and position estimates regularly in the assimilation process (and thus treating them in the same way as observations); and using a background model to spin up a realistic vortex and transfer this to the initial state of the forecast. Historically, the first two of these methods have been used to initialise the TC (e.g. the MetUM uses the second). However, the research community are building more advanced vortex assimilation techniques which will likely improve TC forecasts in the future. Each of the forecasts in this study would likely have benefited from better vortex initialisation, and it would be of interest to compare forecasts in the future.

Convection permitting ensemble forecasts would also benefit from perturbations targeted for the region and resolution of the domain. Currently, in the MetUM, initial conditions are inherited from the global model. These initial conditions are generated through an ETKF, where the fastest growing perturbations to the model analysis are identified. As these perturbations are made to the global forecast, the CP ensemble spread is limited and unlikely to be greater than the global spread. To

increase the spread of the TC forecasts, perturbations generated in an assimilation process focused on the regional CP domain should be made. Whilst this is an incredibly complex problem, it could help better represent the uncertainty in CP TC forecasts.

Magnusson et al. (2019) suggest a more systematic approach to understanding TC forecast errors, with institutions working together to investigate a greater number of case studies which can be recommended by operational centres. Such an approach would be of benefit to the research community as a whole. Future work should also include developing a greater understanding of how TC tracks are impacted by changes in model physics or resolution (i.e. not just TCs with large uncertainty in an ensemble forecasts, but TCs in which there are systematic differences in global and regional forecasts).

This thesis has identified weak steering flow as a cause of uncertainty in TC track forecasts. Additionally, differences in global and CP track forecasts can occur when there are discrepancies between the TC intensity and structure in the two types of simulation and in situations where there is large vertical wind shear impacting the storm. Whilst there are still a number of unknowns regarding TC track uncertainty, this study contributes to our growing understanding of difficult to predict TCs.

Bibliography

Alaka Jr, G. J., Zhang, X., Gopalakrishnan, S. G., Zhang, Z., Marks, F. D., and Atlas, R. (2019). Track uncertainty in high-resolution HWRF ensemble forecasts of Hurricane Joaquin. *Weather and Forecasting*, 34(6):1889–1908.

Alley, R. B., Emanuel, K. A., and Zhang, F. (2019). Advances in weather prediction. *Science*, 363(6425):342–344.

Ancell, B. and Hakim, G. J. (2007). Comparing adjoint- and ensemble-sensitivity analysis with applications to observation targeting. *Monthly Weather Review*, 135(12):4117–4134.

Arakawa, A. and Lamb, V. R. (1977). Computational design of the basic dynamical processes of the UCLA general circulation model. *General Circulation Models of the Atmosphere*, 17(Supplement C):173–265.

Archambault, H. M., Bosart, L. F., Keyser, D., and Cordeira, J. M. (2013). A climatological analysis of the extratropical flow response to recurving western north pacific tropical cyclones. *Monthly weather review*, 141(7):2325–2346.

Bagtasa, G. (2017). Contribution of tropical cyclones to rainfall in the Philippines. *Journal of Climate*, 30(10):3621–3633.

Bauer, P., Thorpe, A., and Brunet, G. (2015). The quiet revolution of numerical weather prediction. *Nature*, 525(7567):47–55.

Best, M., Pryor, M., Clark, D., Rooney, G., Essery, R., Ménard, C., Edwards, J., Hendry, M., Porson, A., Gedney, N., et al. (2011). The Joint UK Land

Environment Simulator (JULES), model description–Part 1: energy and water fluxes. *Geoscientific Model Development*, 4(1):677–699.

Bhatia, K., Vecchi, G., Murakami, H., Underwood, S., and Kossin, J. (2018). Projected response of tropical cyclone intensity and intensification in a global climate model. *Journal of Climate*, 31(20):8281–8303.

Bishop, C. H., Etherton, B. J., and Majumdar, S. J. (2001). Adaptive sampling with the ensemble transform Kalman filter. Part I: Theoretical aspects. *Monthly Weather Review*, 129(3):420–436.

Boutle, I., Eyre, J., and Lock, A. (2014). Seamless stratocumulus simulation across the turbulent gray zone. *Monthly Weather Review*, 142(4):1655–1668.

Bowler, N. E., Arribas, A., Beare, S. E., Mylne, K. R., and Shutts, G. J. (2009). The local ETKF and SKEB: Upgrades to the MOGREPS short-range ensemble prediction system. *Quarterly Journal of the Royal Meteorological Society*, 135(640):767–776.

Bowler, N. E., Arribas, A., Mylne, K. R., Robertson, K. B., and Beare, S. E. (2008). The MOGREPS short-range ensemble prediction system. *Quarterly Journal of the Royal Meteorological Society*, 134(632):703–722.

Brand, S., Buenafe, C. A., and Hamilton, H. D. (1981). Comparison of tropical cyclone motion and environmental steering. *Monthly Weather Review*, 109(4):908–909.

Brown, A., Beare, R., Edwards, J., Lock, A., Keogh, S., Milton, S., and Walters, D. (2008). Upgrades to the boundary-layer scheme in the Met Office numerical weather prediction model. *Boundary-Layer Meteorology*, 128(1):117–132.

Buizza, R., Houtekamer, P., Pellerin, G., Toth, Z., Zhu, Y., and Wei, M. (2005). A comparison of the ECMWF, MSC, and NCEP global ensemble prediction systems. *Monthly Weather Review*, 133(5):1076–1097.

Bush, M., Allen, T., Bain, C., Boutle, I., Edwards, J., Finnenkoetter, A., Franklin, C., Hanley, K., Lean, H., Lock, A., Manners, J., Mittermaier, M., Morcrette, C., North, R., Petch, J., Short, C., Vosper, S., Walters, D., Webster, S., Weeks, M.,

Wilkinson, J., Wood, N., and Zerroukat, M. (2019). The first met office unified model/JULES regional atmosphere and land configuration, RAL1. *Geoscientific Model Development Discussions*, 13:1–47.

Chan, J. C. (2005). The physics of tropical cyclone motion. *Annual Review of Fluid Mechanics*, 37:99–128.

Chan, J. C. and Gray, W. M. (1982). Tropical cyclone movement and surrounding flow relationships. *Monthly Weather Review*, 110(10):1354–1374.

Chan, J. C. and Williams, R. (1987). Analytical and numerical studies of the beta-effect in tropical cyclone motion. Part I: Zero mean flow. *Journal of the Atmospheric Sciences*, 44(9):1257–1265.

Charney, J. G. and Phillips, N. (1953). Numerical integration of the quasi-geostrophic equations for barotropic and simple baroclinic flows. *Journal of Meteorology*, 10(2):71–99.

Choy, C.-w., Chong, S.-n., Kong, D., and Cayanan, E. O. (2015). A discussion of the most intense tropical cyclones in the western North Pacific from 1978 to 2013. *Tropical Cyclone Research and Review*, 4(1):1–11.

Chu, P.-S., Kim, J.-H., and Ruan Chen, Y. (2012). Have steering flows in the western North Pacific and the South China Sea changed over the last 50 years? *Geophysical Research Letters*, 39(10).

Cinco, T. A., de Guzman, R. G., Ortiz, A. M. D., Delfino, R. J. P., Lasco, R. D., Hilario, F. D., Juanillo, E. L., Barba, R., and Ares, E. D. (2016). Observed trends and impacts of tropical cyclones in the Philippines. *International Journal of Climatology*, 36(14):4638–4650.

Clark, D., Mercado, L., Sitch, S., Jones, C., Gedney, N., Best, M., Pryor, M., Rooney, G., Essery, R., Blyth, E., et al. (2011). The Joint UK Land Environment Simulator (JULES), model description–Part 2: carbon fluxes and vegetation dynamics. *Geoscientific Model Development*, 4(3):701–722.

Clark, P., Roberts, N., Lean, H., Ballard, S. P., and Charlton-Perez, C. (2016).

Convection-permitting models: a step-change in rainfall forecasting. *Meteorological Applications*, 23(2):165–181.

Cusack, S., Edwards, J., and Crowther, J. (1999). Investigating k distribution methods for parameterizing gaseous absorption in the Hadley Centre Climate Model. *Journal of Geophysical Research: Atmospheres*, 104(D2):2051–2057.

Dawson, A. (2016). Windspharm: A high-level library for global wind field computations using spherical harmonics. *Journal of Open Research Software*, 4(1):e31.

DeMaria, M. (1985). Tropical cyclone motion in a nondivergent barotropic model. *Monthly Weather Review*, 113(7):1199–1210.

DeMaria, M., Sampson, C. R., Knaff, J. A., and Musgrave, K. D. (2014). Is tropical cyclone intensity guidance improving? *Bulletin of the American Meteorological Society*, 95(3):387–398.

Dong, K. and Neumann, C. J. (1986). The relationship between tropical cyclone motion and environmental geostrophic flows. *Monthly Weather Review*, 114(1):115–122.

Draper, D. W., Newell, D. A., Wentz, F. J., Krimchansky, S., and Skofronick-Jackson, G. M. (2015). The global precipitation measurement (GPM) microwave imager (GMI): Instrument overview and early on-orbit performance. *IEEE Journal of Selected Topics in Applied Earth Observations and Remote Sensing*, 8(7):3452–3462.

Eckstein, D., Künzel, V., Schäfer, L., and Winges, M. (2019). Global climate risk index 2020. *Bonn: Germanwatch*.

Edwards, J. and Slingo, A. (1996). Studies with a flexible new radiation code. I: Choosing a configuration for a large-scale model. *Quarterly Journal of the Royal Meteorological Society*, 122(531):689–719.

Emanuel, K. (2003). Tropical cyclones. *Annual Review of Earth and Planetary Sciences*, 31:75–104.

Emanuel, K. (2018). 100 years of progress in tropical cyclone research. *Meteorological Monographs*, 59:15.1–15.68.

Emanuel, K. et al. (2005). *Divine wind: The history and science of hurricanes.* Oxford University Press.

Emanuel, K. and Zhang, F. (2016). On the predictability and error sources of tropical cyclone intensity forecasts. *Journal of the Atmospheric Sciences*, 73(9):3739–3747.

Esteban, M., Valenzuela, V. P., Yun, N. Y., Mikami, T., Shibayama, T., Matsumaru, R., Takagi, H., Thao, N. D., De Leon, M., Oyama, T., et al. (2015). Typhoon Haiyan 2013 evacuation preparations and awareness. *International Journal of Sustainable Future for Human Security*, 3(1):37–45.

Evans, J. L., Holland, G. J., and Elsberry, R. L. (1991). Interactions between a barotropic vortex and an idealized subtropical ridge. Part I: Vortex motion. *Journal of the Atmospheric Sciences*, 48(2):301–314.

Evensen, G. (1994). Sequential data assimilation with a nonlinear quasi-geostrophic model using Monte Carlo methods to forecast error statistics. *Journal of Geophysical Research: Oceans*, 99(C5):10143–10162.

Fiorino, M. and Elsberry, R. L. (1989). Some aspects of vortex structure related to tropical cyclone motion. *Journal of the Atmospheric Sciences*, 46(7):975–990.

Food and Agriculture Organization (2014). Typhoon Haiyan. Technical Report November 2013.

Fortin, V., Abaza, M., Anctil, F., and Turcotte, R. (2014). Why should ensemble spread match the RMSE of the ensemble mean? *Journal of Hydrometeorology*, 15(4):1708–1713.

Fowler, J. P. and Galarneau, T. J. (2017). Influence of storm–storm and storm–environment interactions on tropical cyclone formation and evolution. *Monthly Weather Review*, 145(12):4855–4875.

Galarneau, T. J. and Davis, C. A. (2013). Diagnosing forecast errors in tropical cyclone motion. *Monthly Weather Review*, 141(2):405–430.

George, J. E. and Gray, W. M. (1976). Tropical cyclone motion and surrounding parameter relationships. *Journal of Applied Meteorology*, 15(12):1252–1264.

Grams, C. M., Jones, S. C., and Davis, C. A. (2013). The impact of Typhoon Jangmi (2008) on the midlatitude flow. Part II: Downstream evolution. *Quarterly Journal of the Royal Meteorological Society*, 139(677):2165–2180.

Gray, W. M. (1968). Global view of the origin of tropical disturbances and storms. *Monthly Weather Review*, 96(10):669–700.

Gray, W. M. (1975). Tropical cyclone genesis. *Atmospheric Science Paper*.

Gregory, D. and Rowntree, P. (1990). A mass flux convection scheme with representation of cloud ensemble characteristics and stability-dependent closure. *Monthly Weather Review*, 118(7):1483–1506.

Hamill, T. M., Whitaker, J. S., Fiorino, M., and Benjamin, S. G. (2011). Global ensemble predictions of 2009's tropical cyclones initialized with an ensemble Kalman filter. *Monthly Weather Review*, 139(2):668–688.

Heming, J. T. (2016). Met Office unified model tropical cyclone performance following major changes to the initialization scheme and a model upgrade. *Weather and Forecasting*, 31(5):1433–1449.

Heming, J. T., Prates, F., Bender, M. A., Bowyer, R., Cangialosi, J., Caroff, P., Coleman, T., Doyle, J. D., Dube, A., Faure, G., et al. (2019). Review of recent progress in tropical cyclone track forecasting and expression of uncertainties. *Tropical Cyclone Research and Review*, 8(4):181–218.

Hersbach, H., Bell, B., Berrisford, P., Hirahara, S., Horányi, A., Muñoz-Sabater, J., Nicolas, J., Peubey, C., Radu, R., Schepers, D., et al. (2020). The ERA5 global reanalysis. *Quarterly Journal of the Royal Meteorological Society*, 146:1999–2049.

Hodges, K. and Klingaman, N. (2019). Prediction errors of tropical cyclones in the western north pacific in the met office global forecast model. *Weather and Forecasting*, 34(5):1189–1209.

Holland, G. J. (1983). Tropical cyclone motion: Environmental interaction plus a beta effect. *Journal of the Atmospheric Sciences*, 40(2):328–342.

Holland, G. J. (1984). Tropical cyclone motion. A comparison of theory and observation. *Journal of the Atmospheric Sciences*, 41(1):68–75.

Hsu, L.-H., Kuo, H.-C., and Fovell, R. G. (2013). On the geographic asymmetry of typhoon translation speed across the mountainous island of Taiwan. *Journal of the Atmospheric Sciences*, 70(4):1006–1022.

Huang, L., Wan, Q., Liu, C., and Huang, H. (2020). Ensemble based diagnosis of the track errors of super Typhoon Mangkhut (2018). *Journal of Meteorological Research*, 34:353–367.

Ismail, P. and Siadari, E. L. (2017). Atmospheric conditions analysis of the heavy rain phenomenon in Biak (case study 4-5 December 2014). *Journal of Physics: Conference Series*, 795(1):012015.

Ito, K. (2016). Errors in tropical cyclone intensity forecast by rsmc tokyo and statistical correction using environmental parameters. *SOLA*, 12:247–252.

Jin, H., Peng, M. S., Jin, Y., and Doyle, J. D. (2014). An evaluation of the impact of horizontal resolution on tropical cyclone predictions using COAMPS-TC. *Weather and Forecasting*, 29(2):252–270.

Jones, S. C. (1995). The evolution of vortices in vertical shear. Part I: Initially barotropic vortices. *Quarterly Journal of the Royal Meteorological Society*, 121(524):821–851.

Jones, S. C., Harr, P. A., Abraham, J., Bosart, L. F., Bowyer, P. J., Evans, J. L., Hanley, D. E., Hanstrum, B. N., Hart, R. E., Lalaurette, F., et al. (2003). The extratropical transition of tropical cyclones: Forecast challenges, current understanding, and future directions. *Weather and Forecasting*, 18(6):1052–1092.

Kaplan, J., DeMaria, M., and Knaff, J. A. (2010). A revised tropical cyclone rapid intensification index for the atlantic and eastern north pacific basins. *Weather and forecasting*, 25(1):220–241.

Keller, J. H., Grams, C. M., Riemer, M., Archambault, H. M., Bosart, L., Doyle, J. D., Evans, J. L., Galarneau Jr, T. J., Griffin, K., Harr, P. A., et al. (2019).

The extratropical transition of tropical cyclones. Part II: Interaction with the midlatitude flow, downstream impacts, and implications for predictability. *Monthly Weather Review*, 147(4):1077–1106.

Kieu, C., Keshavamurthy, K., Tallapragada, V., Gopalakrishnan, S., and Trahan, S. (2018). On the growth of intensity forecast errors in the operational hurricane weather research and forecasting (HWRF) model. *Quarterly Journal of the Royal Meteorological Society*, 144(715):1803–1819.

Knapp, K. R., Kruk, M. C., Levinson, D. H., Diamond, H. J., and Neumann, C. J. (2010). The international best track archive for climate stewardship (IBTrACS) unifying tropical cyclone data. *Bulletin of the American Meteorological Society*, 91(3):363–376.

Knutson, T., Camargo, S. J., Chan, J. C., Emanuel, K., Ho, C.-H., Kossin, J., Mohapatra, M., Satoh, M., Sugi, M., Walsh, K., et al. (2020). Tropical cyclones and climate change assessment: Part ii: Projected response to anthropogenic warming. *Bulletin of the American Meteorological Society*, 101(3):E303–E322.

Kossin, J. P., Emanuel, K. A., and Camargo, S. J. (2016). Past and projected changes in western North Pacific tropical cyclone exposure. *Journal of Climate*, 29(16):5725–5739.

Kure, S., Jibiki, Y., Quimpo, M., Manalo, U. N., Ono, Y., and Mano, A. (2016). Evaluation of the characteristics of human loss and building damage and reasons for the magnification of damage due to Typhoon Haiyan. *Coastal Engineering Journal*, 58(01):1640008.

Lagmay, A. M. F., Agaton, R. P., Bahala, M. A. C., Briones, J. B. L. T., Cabacaba, K. M. C., Caro, C. V. C., Dasallas, L. L., Gonzalo, L. A. L., Ladiero, C. N., Lapidez, J. P., et al. (2015). Devastating storm surges of Typhoon Haiyan. *International Journal of Disaster Risk Reduction*, 11:1–12.

Landsea, C. W. and Cangialosi, J. P. (2018). Have we reached the limits of predictability for tropical cyclone track forecasting? *Bulletin of the American Meteorological Society*, 99(11):2237–2243.

Lee, Y.-S., Liou, Y.-A., Liu, J.-C., Chiang, C.-T., and Yeh, K.-D. (2017). Formation of winter supertyphoons Haiyan (2013) and Hagupit (2014) through interactions with cold fronts as observed by multifunctional transport satellite. *Transactions on Geoscience and Remote Sensing*, 55(7):3800–3809.

Lin, I.-I., Pun, I.-F., and Lien, C.-C. (2014). "Category-6" Supertyphoon Haiyan in global warming hiatus: Contribution from subsurface ocean warming. *Geophysical Research Letters*, 41(23):8547–8553.

Liu, Q., Zhang, X., Tong, M., Zhang, Z., Liu, B., Wang, W., Zhu, L., Zhang, B., Xu, X., Trahan, S., et al. (2020). Vortex initialization in the NCEP operational hurricane models. *Atmosphere*, 11(9):968.

Lock, A. (2001). The numerical representation of entrainment in parameterizations of boundary layer turbulent mixing. *Monthly Weather Review*, 129(5):1148–1163.

Lock, A., Brown, A., Bush, M., Martin, G., and Smith, R. (2000). A new boundary layer mixing scheme. Part I: Scheme description and single-column model tests. *Monthly Weather Review*, 128(9):3187–3199.

Lorenz, E. (1972). *Predictability: does the flap of a butterfly's wing in Brazil set off a tornado in Texas?* na.

Lott, F. and Miller, M. J. (1997). A new subgrid-scale orographic drag parametrization: Its formulation and testing. *Quarterly Journal of the Royal Meteorological Society*, 123(537):101–127.

Lum, T. and Margesson, R. (2014). Typhoon Haiyan (Yolanda): US and international response to Philippines disaster. *Current Politics and Economics of South, Southeastern, and Central Asia*, 23(2):209.

Magnusson, L., Bidlot, J.-R., Lang, S. T., Thorpe, A., Wedi, N., and Yamaguchi, M. (2014). Evaluation of medium-range forecasts for Hurricane Sandy. *Monthly Weather Review*, 142(5):1962–1981.

Magnusson, L., Doyle, J. D., Komaromi, W. A., Torn, R. D., Tang, C. K., Chan, J. C., Yamaguchi, M., and Zhang, F. (2019). Advances in understanding difficult

cases of tropical cyclone track forecasts. *Tropical Cyclone Research and Review*, 8(3):109–122.

Mei, W., Pasquero, C., and Primeau, F. (2012). The effect of translation speed upon the intensity of tropical cyclones over the tropical ocean. *Geophysical Research Letters*, 39(7).

Melhauser, C., Zhang, F., Weng, Y., Jin, Y., Jin, H., and Zhao, Q. (2017). A multiple-model convection-permitting ensemble examination of the probabilistic prediction of tropical cyclones: Hurricanes sandy (2012) and edouard (2014). *Weather and Forecasting*, 32(2):665–688.

Miller, W. and Zhang, D.-L. (2019). Understanding the unusual looping track of Hurricane Joaquin (2015) and its forecast errors. *Monthly Weather Review*, 147(6):2231–2259.

Molinari, J., Vollaro, D., and Corbosiero, K. L. (2004). Tropical cyclone formation in a sheared environment: A case study. *Journal of the Atmospheric Sciences*, 61(21):2493–2509.

Montgomery, M. T. and Smith, R. K. (2017). Recent developments in the fluid dynamics of tropical cyclones. *Annual Review of Fluid Mechanics*, 49:541–574.

Mori, N., Kato, M., Kim, S., Mase, H., Shibutani, Y., Takemi, T., Tsuboki, K., and Yasuda, T. (2014). Local amplification of storm surge by super Typhoon Haiyan in Leyte Gulf. *Geophysical Research Letters*, 41(14):5106–5113.

Munsell, E. B. and Zhang, F. (2014). Prediction and uncertainty of Hurricane Sandy (2012) explored through a real-time cloud-permitting ensemble analysis and forecast system assimilating airborne doppler radar observations. *Journal of Advances in Modeling Earth Systems*, 6(1):38–58.

Ngo-Duc, T., Mai, H. T., Kieu, C., et al. (2013). A study of the connection between tropical cyclone track and intensity errors in the WRF model. *Meteorology and Atmospheric Physics*, 122(1):55–64.

Nguyen, L. T., Molinari, J., and Thomas, D. (2014). Evaluation of tropical cyclone

center identification methods in numerical models. *Monthly Weather Review*, 142(11):4326–4339.

Nystrom, R. G., Zhang, F., Munsell, E. B., Braun, S. A., Sippel, J. A., Weng, Y., and Emanuel, K. (2018). Predictability and dynamics of Hurricane Joaquin (2015) explored through convection-permitting ensemble sensitivity experiments. *Journal of the Atmospheric Sciences*, 75(2):401–424.

OCHA (2014). Philippines: Typhoon Hagupit. Technical Report 29.

Paul, S., Ghebreyesus, D., and Sharif, H. O. (2019). Brief communication: Analysis of the fatalities and socio-economic impacts caused by Hurricane Florence. *Geosciences*, 9(2):58.

Peduzzi, P., Chatenoux, B., Dao, H., De Bono, A., Herold, C., Kossin, J., Mouton, F., and Nordbeck, O. (2012). Global trends in tropical cyclone risk. *Nature Climate Change*, 2(4):289–294.

Peng, X., Fei, J., Huang, X., and Cheng, X. (2017). Evaluation and error analysis of official forecasts of tropical cyclones during 2005–14 over the Western North Pacific. Part I: Storm tracks. *Weather and Forecasting*, 32(2):689–712.

Ramsay, H. (2017). The global climatology of tropical cyclones. In *Oxford Research Encyclopedia of Natural Hazard Science*.

Riemer, M. and Jones, S. C. (2010). The downstream impact of tropical cyclones on a developing baroclinic wave in idealized scenarios of extratropical transition. *Quarterly Journal of the Royal Meteorological Society*, 136(648):617–637.

Riemer, M. and Jones, S. C. (2014). Interaction of a tropical cyclone with a high-amplitude, midlatitude wave pattern: Waviness analysis, trough deformation and track bifurcation. *Quarterly Journal of the Royal Meteorological Society*, 140(681):1362–1376.

Riemer, M., Jones, S. C., and Davis, C. A. (2008). The impact of extratropical transition on the downstream flow: An idealized modelling study with a straight jet. *Quarterly Journal of the Royal Meteorological Society*, 134(630):69–91.

Rotunno, R., Chen, Y., Wang, W., Davis, C., Dudhia, J., and Holland, G. (2009). Large-eddy simulation of an idealized tropical cyclone. *Bulletin of the American Meteorological Society*, 90(12):1783–1788.

Ryglicki, D. R., Doyle, J. D., Hodyss, D., Cossuth, J. H., Jin, Y., Viner, K. C., and Schmidt, J. M. (2019). The unexpected rapid intensification of tropical cyclones in moderate vertical wind shear. Part III: Outflow-environment interaction. *Monthly Weather Review*, 147(8):2919–2940.

Scaife, A., Butchart, N., Warner, C., and Swinbank, R. (2002). Impact of a spectral gravity wave parameterization on the stratosphere in the Met Office Unified Model. *Journal of the Atmospheric Sciences*, 59(9):1473–1489.

Schade, L. R. and Emanuel, K. A. (1999). The ocean's effect on the intensity of tropical cyclones: Results from a simple coupled atmosphere–ocean model. *Journal of the Atmospheric Sciences*, 56(4):642–651.

Shea, D. J. and Gray, W. M. (1973). The hurricane's inner core region. Part I. symmetric and asymmetric structure. *Journal of the Atmospheric Sciences*, 30(8):1544–1564.

Short, C. J. and Petch, J. (2018). How well can the Met Office unified model forecast tropical cyclones in the Western North Pacific? *Weather and Forecasting*, 33(1):185–201.

Shu, S. and Zhang, F. (2015). Influence of equatorial waves on the genesis of Super Typhoon Haiyan (2013). *Journal of the Atmospheric Sciences*, 72(12):4591–4613.

Shutts, G. (2005). A kinetic energy backscatter algorithm for use in ensemble prediction systems. *Quarterly Journal of the Royal Meteorological Society*, 131(612):3079–3102.

Smagorinsky, J. (1963). General circulation experiments with the primitive equations: Part I. The basic experiment. *Monthly Weather Review*, 91(3):99–164.

Smith, R. K. (1991). An analytic theory of tropical-cyclone motion in a barotropic

shear flow. *Quarterly Journal of the Royal Meteorological Society*, 117(500):685–714.

Smith, R. K., Ulrich, W., and Dietachmayer, G. (1990). A numerical study of tropical cyclone motion using a barotropic model. Part I: The role of vortex asymmetries. *Quarterly Journal of the Royal Meteorological Society*, 116(492):337–362.

Smith, R. K. and Vogl, S. (2008). A simple model of the hurricane boundary layer revisited. *Quarterly Journal of the Royal Meteorological Society*, 134(631):337–351.

Smith, R. K. and Weber, H. C. (1993). An extended analytic theory of tropical-cyclone motion in a barotropic shear flow. *Quarterly Journal of the Royal Meteorological Society*, 119(513):1149–1166.

Smith, S. D. (1988). Coefficients for sea surface wind stress, heat flux, and wind profiles as a function of wind speed and temperature. *Journal of Geophysical Research: Oceans*, 93(C12):15467–15472.

Takagi, H. and Esteban, M. (2016). Statistics of tropical cyclone landfalls in the Philippines: unusual characteristics of 2013 Typhoon Haiyan. *Natural Hazards*, 80(1):211–222.

Takagi, H., Esteban, M., Shibayama, T., Mikami, T., Matsumaru, R., De Leon, M., Thao, N. D., Oyama, T., and Nakamura, R. (2017). Track analysis, simulation, and field survey of the 2013 Typhoon Haiyan storm surge. *Journal of Flood Risk Management*, 10(1):42–52.

Tang, C. K., Chan, J. C., and Yamaguchi, M. (2020). Effects of the outer size on tropical cyclone track forecasts. *Meteorological Applications*, 27(1):e1888.

Titley, H., Yamaguchi, M., and Magnusson, L. (2019). Current and potential use of ensemble forecasts in operational tc forecasting: Results from a global forecaster survey. *Tropical Cyclone Research and Review*, 8(3):166–180.

Titley, H. A., Bowyer, R. L., and Cloke, H. L. (2020). A global evaluation of multi-model ensemble tropical cyclone track probability forecasts. *Quarterly Journal of the Royal Meteorological Society*, 146(726):531–545.

Torn, R. D., Elless, T. J., Papin, P. P., and Davis, C. A. (2018). Tropical cyclone track sensitivity in deformation steering flow. *Monthly Weather Review*, 146(10):3183–3201.

Torn, R. D. and Hakim, G. J. (2008). Ensemble-based sensitivity analysis. *Monthly Weather Review*, 136(2):663–677.

Torn, R. D., Whitaker, J. S., Pegion, P., Hamill, T. M., and Hakim, G. J. (2015). Diagnosis of the source of GFS medium-range track errors in Hurricane Sandy (2012). *Monthly Weather Review*, 143(1):132–152.

Toth, Z. and Kalnay, E. (1993). Ensemble forecasting at NMC: The generation of perturbations. *Bulletin of the American Meteorological Society*, 74(12):2317–2330.

Toth, Z. and Kalnay, E. (1997). Ensemble forecasting at NCEP and the breeding method. *Monthly Weather Review*, 125(12):3297–3319.

Ulrich, W. and Smith, R. K. (1991). A numerical study of tropical cyclone motion using a barotropic model. Part II: Motion in spatially-varying large-scale flows. *Quarterly Journal of the Royal Meteorological Society*, 117(497):107–124.

Velden, C. S. and Leslie, L. M. (1991). The basic relationship between tropical cyclone intensity and the depth of the environmental steering layer in the Australian region. *Weather and Forecasting*, 6(2):244–253.

Vigh, J. L., Knaff, J. A., and Schubert, W. H. (2012). A climatology of hurricane eye formation. *Monthly Weather Review*, 140(5):1405–1426.

Wada, A., Kanada, S., and Yamada, H. (2018). Effect of air-sea environmental conditions and interfacial processes on extremely intense Typhoon Haiyan (2013). *Journal of Geophysical Research: Atmospheres*, 123(18):10–379.

Walters, D., Brooks, M., Boutle, I., Melvin, T., Stratton, R., Vosper, S., Wells, H., Williams, K., Wood, N., Allen, T., et al. (2017). The Met Office unified model global atmosphere 6.0/6.1 and JULES global land 6.0/6.1 configurations. *Geoscientific Model Development*, 10(4):1487–1520.

Wang, X. and Bishop, C. H. (2003). A comparison of breeding and ensemble

transform kalman filter ensemble forecast schemes. *Journal of the atmospheric sciences*, 60(9):1140–1158.

Wang, Y. and Holland, G. J. (1996). Tropical cyclone motion and evolution in vertical shear. *Journal of the Atmospheric Sciences*, 53(22):3313–3332.

Weatherford, C. L. and Gray, W. M. (1988). Typhoon structure as revealed by aircraft reconnaissance. Part II: Structural variability. *Monthly Weather Review*, 116(5):1044–1056.

Willoughby, H. (1998). Tropical cyclone eye thermodynamics. *Monthly Weather Review*, 126(12):3053–3067.

Willoughby, H. E. (1990). Gradient balance in tropical cyclones. *Journal of the Atmospheric Sciences*, 47(2):265–274.

Wilson, D. R. and Ballard, S. P. (1999). A microphysically based precipitation scheme for the UK Meteorological Office Unified Model. *Quarterly Journal of the Royal Meteorological Society*, 125(557):1607–1636.

Wilson, D. R., Bushell, A. C., Kerr-Munslow, A. M., Price, J. D., and Morcrette, C. J. (2008). PC2: A prognostic cloud fraction and condensation scheme. Part I: Scheme description. *Quarterly Journal of the Royal Meteorological Society*, 134(637):2093–2107.

Wood, N. and Mason, P. (1993). The pressure force induced by neutral, turbulent flow over hills. *Quarterly Journal of the Royal Meteorological Society*, 119(514):1233–1267.

Wood, N., Staniforth, A., White, A., Allen, T., Diamantakis, M., Gross, M., Melvin, T., Smith, C., Vosper, S., Zerroukat, M., et al. (2014). An inherently mass-conserving semi-implicit semi-Lagrangian discretization of the deep-atmosphere global non-hydrostatic equations. *Quarterly Journal of the Royal Meteorological Society*, 140(682):1505–1520.

Wu, L. and Wang, B. (2000). A potential vorticity tendency diagnostic approach for tropical cyclone motion. *Monthly Weather Review*, 128(6):1899–1911.

Wu, L., Wang, B., and Braun, S. A. (2005). Impacts of air–sea interaction on tropical cyclone track and intensity. *Monthly Weather Review*, 133(11):3299–3314.

Yablonsky, R. M. and Ginis, I. (2009). Limitation of one-dimensional ocean models for coupled hurricane–ocean model forecasts. *Monthly Weather Review*, 137(12):4410–4419.

Yamaguchi, M., Ishida, J., Sato, H., and Nakagawa, M. (2017). WGNE intercomparison of tropical cyclone forecasts by operational NWP models: A quarter century and beyond. *Bulletin of the American Meteorological Society*, 98(11):2337–2349.

Zhang, D.-L. and Altshuler, E. (1999). The effects of dissipative heating on hurricane intensity. *Monthly Weather Review*, 127(12):3032–3038.